The effects of pressure and doping on the structural, electronic, phonon, optical, thermoelectric, and superconducting properties of yttrium hydrogen selenide (YHSe): First Principles study

Tadesse Bekele Aredo

A PhD Dissertation Submitted to the department of Applied Physics,
School of Applied Natural Science

Presented in a Partial Fulfillment of the Requirement for the Degree of
Doctor of Philosophy in Applied Physics (Specialization in Material Physics)

Office of Graduate Studies
Adama Science and Technology University

June, 2025
Adama, Ethiopia

The effects of pressure and doping on the structural, electronic, phonon, optical, thermoelectric and superconducting properties of yttrium hydrogen selenide (YHSe): First-principles study

PhD Candidate :

Tadesse Bekele Aredo

Main Supervisor: Dr. Megersa Wodajo Shura (Associate Prof. of Physics)

Co-supervisor: Dr. Kumneger Tadele (Associate Prof. of Physics),

Co-supervisor: Dr. Fekadu Tolosa Maremi (Associate Prof. of Physics)

A PhD Dissertation Submitted to the Department of Applied Physics

School of Applied Natural Sciences

Presented in a Partial Fulfillment of the Requirement for the Degree of Doctor of Philosophy in Applied Physics (Material Physics)

Office of Graduate Studies

Adama Science and Technology University

June, 2025

Adama, Ethiopia

Declaration

I hereby declare that this PhD Dissertation entitled " **The effects of pressure and doping on the structural, electronic, phonon, optical, thermoelectric, and superconducting properties of yttrium hydrogen selenide (YHSe): First-principles study** " is my original work and has not been submitted for the award of any academic degree, diploma, or certificate in any other university. All sources of material used for this dissertation have been duly acknowledged through appropriate citations.

(Name of student)	Signature	Date

Recommendation

I/We, the supervisor(s) of this dissertation, hereby certify that we have read and revised the dissertation entitled " **The effects of pressure and doping on the structural, electronic, phonon, optical, thermoelectric, and superconducting properties of yttrium hydrogen selenide (YHSe): First-principles study** " prepared under our guidance by Tadesse Bekele Aredo in fulfillment of the requirements for the degree of Doctor of Philosophy in Applied Physics **(Material Physics)**. Therefore, we recommend the submission of the dissertation to the department for further review and defense.

(Major supervisor)	Signature	Date
(Co-advisor (1))	Signature	Date
(Co-advisor (2))	Signature	Date

Approval of Board of Examiners

We, the undersigned, members of the Board of Examiners of the dissertation open defense by **Tadesse Bekele Aredo** have read and evaluated the dissertation entitled " **The effects of pressure and doping on the structural, electronic, phonon, optical, thermoelectric, and superconducting properties of yttrium hydrogen selenide (YHSe): First-Principles study** " and examined the candidate during open defense. This is therefore to certify that the dissertation is accepted for the partial fulfillment of the requirement of the degree of Doctor of Philosophy in **Applied Physics (Specialization in Material Physics)**.

Chairperson	Signature	Date
Internal Examiner 1	Signature	Date
Internal Examiner 2	Signature	Date
External Examiner 1	Signature	Date
External Examiner 2	Signature	Date

Final approval and acceptance of the dissertation is contingent upon submission of its final copy to the Office of Postgraduate Studies (OPGS) through the Department Graduate Council (DGC) and College Graduate Committee (CGC).

Department Head	Signature	Date
College Dean	Signature	Date
Office of Postgraduate Studies, Dean	Signature	Date

Acknowledgments

First and foremost, I thank God Almighty for His countless blessings and constant guidance throughout this journey. I trust in His continued presence and will always praise Him.

The completion of this dissertation is a testament to the invaluable guidance and encouragement I received from my supervisors. I am immensely grateful to my major supervisor, **Dr. Megersa Wodajo Shura**, for his unwavering patience and insightful feedback. His generosity, immense support, and profound advice have been instrumental in shaping my understanding of the subject and the realization of this dissertation. This dissertation would not have materialized without his invaluable guidance, continuous assistance and steadfast motivation.

I sincerely appreciate the contributions of my co-supervisors, **Dr. Kumneger Tadele** and **Dr. Fekadu Tolosa**, for their invaluable guidance, insightful feedback, and unwavering support. Their expertise, patience, and motivation proved to be instrumental in developing both my scholarly and investigative growth. Their willingness to engage in discussions and provide constructive input has significantly enhanced the quality of this dissertation. I sincerely appreciate their mentorship, continuous support, and the friendly approach that made this journey enriching and fulfilling.

I sincerely thank **Dr. Mesfin Asfaw** for his early support and valuable guidance, which deepened my understanding of the subject. I am also grateful to **Dr. Tola Jabessa** for his consistent encouragement and technical support, and to **Dr. Getachew Mergia** for his ongoing mentorship, motivation, and generous financial assistance throughout my Ph.D.

Heartfelt thanks to my family especially my mother, sisters, and brother **Teshome Bekele Aredo** for their unwavering love and support. I especially honor my mother **Yeshe Mamo Dadi** and the memory of my father **Bekele Aredo Tura** for their sacrifices that made this journey possible. I also appreciate the encouragement from Zelalem Abera and Obsan Tadesse, and acknowledge the support of ASTU, BHU, and the Ministry of Education, particularly **Mrs. Lensa Abera**, for their vital contributions.

Contents

List of Tables

List of Figures

LIST OF ACRONYMS AND ABBREVIATIONS

DFT	Density Functional Theory
EPC	Electron-Phonon Couplings
BTE	Boltzmann Transport Equation
BZ	Brillouin Zone
DOS	Density of States
LDA	Local Density Approximation
GGA	Generalized Gradient Approximation
LSDA	Local Spin Density Approximation
PBE	Perdew–Burke–Ernzerhof
USPP	Ultrasoft Pseudopotentials
NCPP	Norm-Conserving Pseudopotentials
PAW	Projected Augmented-Wave
BFGS	Broyden-Fletcher-Goldfarb-Shanno
PhDOS	Phonon Density of States
TDF	Transport Distribution Function
RTA	Relaxation Time Approximation
CBM	Conduction Band Minimum
VBM	Valence Band Maximum
YHSe	Yttrium Hydrogen Selenide
BTT	Boltzmann Transport Theory
LEDs	Light Emitting Diodes
TM	Transition Metal
VESTA	Visualization for Electronic and Structural Analysis
XCrySDen	Crystalline Structures Visualizer
REMs	Rare Earth Metals
CTMHs	Complex Transition Metal Hydrides
BCS	Bardeen-Cooper-Schrieffer Theory

Abstract

Yttrium Hydrogen Selenide shows multifunctional behavior under high pressure and La doping, making it a promising material for next-generation superconducting, thermoelectric, and optoelectronic applications. This study explores the structural, electronic, phonon, optical, superconducting, and thermoelectric properties of YHSe under pressure and La doping using Density Functional Theory, Phonopy, Phono3py, BoltzTraP, and Python-based tools. With increasing pressure, structural analysis reveals a contraction of interatomic distances and a reduction in lattice parameters. Electronic band structure calculations indicate that, pressure-induced modulation of localized states drives a transition from an indirect to a direct band gap at high pressures. Phonon dispersion analysis shows an overall stiffening of lattice vibrations, although certain high-symmetry modes exhibit softening. Moreover, enhanced electron-phonon coupling under high pressure can lead to an increase in the superconducting transition temperature (T_c). Additionally, pressure induces notable modifications in most optical properties, particularly enhancing absorption in the UV region. Furthermore, pressure enhances thermoelectric performance, achieving a notable maximum Figure of merit (ZT) of 0.79. On the other hand, Lanthanum (La) doping modifies the crystal structure by causing lattice expansion along the c-axis, leading to an increased c/a ratio and structural anisotropy, which can influence electronic and transport behavior. La doping also raises the density of states near the Fermi level and introduces localized states within the band gap. Phonon mode softening induced by doping reduces the lattice thermal conductivity, thereby enhancing thermoelectric efficiency. Additionally, Lanthanum doping raises the superconducting critical temperature (T_c), providing a viable alternative to pressure-induced superconductivity. Moreover, optical analysis reveals that doping induces significant enhancements in the key optical parameters. Furthermore, thermoelectric calculations indicate enhanced performance, with the Figure of merit reaching, $ZT \approx 0.75$. These DFT results reveal crucial functional properties of the material relevant to optoelectronic, thermoelectric, and energy storage applications.

Keywords: DFT, Superconductivity, EPC, Phonon, Doping, YHSe

1

Introduction

1.1 Background of the Study

The development of next-generation materials is crucial for addressing challenges related to energy efficiency, environmental sustainability, and advanced technologies. As global concerns over energy consumption and climate change continue to grow, the search for innovative materials that enable sustainable solutions and technological advancements has become increasingly important (Khan et al., 2024).

Among these materials, Metal hydrides have gained popularity owing to their distinctive properties and wide range of applications, particularly in energy storage (Schlapbach & Züttel, 2001) superconductivity (Drozdov et al., 2019) optoelectronics (Grätzel, 2001) ,and photocatalytic applications (W. Ma et al., 2024). Metal hydrides such as LiH, $LiAlH_4$, MgH_2, $NaAlH_4$, $NaAlYH_4$, $LaNi_5H_6$, and $TiFeH_2$, etc are efficient hydrogen storage materials offering a promising solution for clean energy technologies (Schlapbach & Züttel, 2001 ;Liu et al., 2020). Their substantial hydrogen retention capability, reversibility and potential application in hydrogen fuel cells based on solid-state materials and advanced battery systems make them strong candidates for next generation energy storage (Schlapbach & Züttel, 2001 ;Liu et al., 2020).

Beyond their role in energy storage, metal hydrides are also considered strong candidates for high temperature superconductors. Notable experimental breakthroughs include the identification of superconductivity in hydrogen sulfide at 203 K (Drozdov et al., 2015), LaH_{10} ($\approx$ 250K at 170GPa (Drozdov.P.A. et al., 2019) $\approx$ 260K at 180 - 200GPa (Somayazulu .M.,et al.,2019), YH_9 at 243 K (Kong et al., 2019) CeH_9 ($\approx$ 100K at 130GPa (Chen.W.,et al., 2021), CaH_6(215K at 172GPa (Li.Z. et al., 2022) and YH_6 ($\approx$ 220K at 183GPa (Kong.P et al.,2021), all under extremely high pressures (90 - 201GPa). However, despite these advancements, achieving room temperature superconductivity under practical conditions remains challenging due to the requirement for extreme pressures,

which significantly limit real world applications. Moreover, the underlying mechanisms of hydrides superconductivity still require deeper theoretical and experimental investigation (Drozdov et al., 2019).

In addition to their superconducting potential, metal hydrides are gaining interest in photocatalysis and optoelectronics. Metal-organic frameworks (MOFs) containing metal hydrides have been widely researched for photocatalytic use because of their adjustable light absorption properties and large surface area (W. Ma et al., 2024).

Furthermore, some metal hydrides, particularly oxygen containing yttrium based hydride, titanium oxide, tungsten oxide, molybdenum oxide, and yttrium hydride, exhibit remarkable photochromic properties, making them valuable for smart materials that respond to light stimuli (Mongstad et al., 2011). The discovery of photochromic characteristics in yttrium hydride resulted from increased scientific activity (Van der Molen et al., 2001). This followed the finding of switchable optical characteristics in yttrium and lanthanum based hydrides (Van der Molen et al., 2001). These properties open new avenues for applications in adaptive optics, energy efficient windows, and data storage technologies (Sandrock & Bowman Jr, 2003).

Additionally, metal hydrides with tunable electronic and optical properties are being actively explored for their potential in next-generation optoelectronic devices, where they can significantly enhance charge carrier dynamics (Grätzel et al., 2001).

Among metal hydrides, those incorporating chalcogenide elements oxygen (O), sulfur (S), selenium (Se), tellurium (Te) have gained considerable attention in optoelectronics and photonics due to their rich electronic and optical characteristics, structural versatility, and environmentally friendly nature (Ab Rahman et al., 2015).

Transition metal based chalcogenides, in particular, stand out due to their variable oxidation states and stoichiometry, which enable diverse optical, catalytic, and electrical functionalities suitable for energy devices, sensors, and light-harvesting technologies (Ab Rahman et al., 2015). Binary and ternary chalcogenides such as Y_2Se_3, Er_2Se_3, KNi_2Se_2, and As_2Se_3 exhibit excellent thermal stability, high refractive indices, and facile synthesis, making them attractive for photonic and optoelectronic applications (Awada et al., 2020).

For example, Y_2Se_3 rock-salt cubic structure and octahedral coordination enable strong

light-matter interactions ideal for optoelectronics, while Er_2Se_3 is valued for infrared detection due to its narrow band gap and infrared sensitivity (Ikhioya, I. L., & Nkele, A. C., 2023).

Moreover, doping strategies have further enriched the toolbox for tailoring material properties, enabling precise control over electronic band structure, carrier density, and optical response. Lanthanum doping, in particular, has demonstrated remarkable effects by inducing lattice distortions and modulating band gaps, thereby enhancing charge transport and photocatalytic efficiency (Ali Khan & Tahir, 2021). La-based compounds possess high density, melting points, and electrical conductivity, attributes linked to their 4f electron configuration, enhancing their suitability for multifunctional applications (Boppella et al., 2018).

Additionally, La doping has also been shown to enhance thermoelectric performance in chalcogenide-based compounds, such as Bi_2Te_3, where La substitution effectively tunes the carrier concentration and reduces thermal conductivity, leading to improved power factors and higher figures of merit (ZT)(Amirkhizi et al., 2024; Terasaki et al., 1997).

Despite the advances in related hydrides and chalcogenides, YHSe remains virtually unexplored both computationally and experimentally. This presents a compelling research opportunity to systematically investigate its fundamental properties and technological potential.

Building upon these promising avenues, yttrium hydrogen selenide (YHSe) emerges as a novel compound bridging hydrides and chalcogenides, offering a rich platform for engineering multifunctional materials. The incorporation of hydrogen within the chalcogenide matrix provides additional tunability in bonding, carrier dynamics, and optical absorption. Introducing lanthanum doping at yttrium sites promises to further modulate the electronic structure, stabilize crystal symmetries, and introduce impurity states that may enhance optoelectronic and energy conversion efficiencies. Additionally, external pressure can serve as a powerful tool to fine-tune these properties, potentially unlocking superior performance.

Therefore, this study aims to comprehensively explore the structural, electronic, optical, phononic, superconducting, and thermoelectric characteristics of $Y_{1-x}La_xHSe$ ($x =$

0 to 0.5) and under varying external pressures using First-principles calculations. By combining lanthanum doping with pressure tuning, we seek to reveal novel pathways for optimizing multifunctional properties, advancing the frontier of sustainable materials science and technology.

La is chosen as a dopant due to its large ionic radius and ability to donate additional charge carriers, which can effectively modify the electronic structure of YHSe. La substitution at the Y-site is expected to introduce enhanced carrier concentration and band structure modulation, thereby improving the electrical conductivity and thermoelectric performance. Moreover, La-based compounds are well-known for their strong optical absorption and phonon-mediated superconducting behavior, as reported in several oxide and hydride systems. These characteristics make La a strategic choice for tuning the multifunctional properties of YHSe under doping and pressure.

Using First-principles calculations, we investigate the $Y_{1-x}La_xHSe$ composition series (where $x = 0$, 0.125, 0.25, 0.375, and 0.5) to examine how gradual La substitution influences the physical properties of YHSe. This dual approach combining La doping with applied pressure is designed to tailor the electronic structure and optimize the multifunctional properties of the YHSe system. Maintaining structural stability, especially under doping and pressure conditions, remains a key challenge one that this study also aims to address.

1.2 Statement of the Problem

Since the discovery of superconductivity, researchers have aimed to achieve the highest critical temperature, potentially surpassing room temperature. For decades, the critical temperature of conventional superconductors has stayed around 10 K (Giuseppe Grosso,et al.,2014). High critical temperature non-conventional superconductivity has been extensively explored, with a record critical temperature of 133 K at ambient pressure for Hg-Ba-Ca-Cu-O (Guo Ott Schilling, et al., 1993). However their pairing mechanism is still debated. Recent advancements in hydrogen-based superconductors have demonstrated promising characteristics, with superconducting critical temperatures (Tc) approaching or even surpassing room temperature (Drozdov et al., 2019). Despite these promising re-

sults, the underlying mechanisms governing superconductivity in hydrogen-based systems are still not fully understood and are therefore not addressed within the scope of this study. Furthermore, these extraordinary properties typically emerge under extreme pressure conditions far beyond current experimental capabilities raising fundamental questions about their practical applicability.

Despite significant advances in optoelectronic materials, the role of external pressure in tuning optical properties remains underexplored. Understanding how pressure-induced modifications influence optical behavior is crucial, as it may unlock new pathways for designing advanced optoelectronic devices and enhancing the performance of light-based technologies. Therefore, investigating these effects is essential for the development of materials with tailored and improved optical functionalities.

Furthermore, in many industrial processes, such as metal smelting and chemical production, a significant amount of heat is generated as a byproduct. However, most of this heat is not utilized and is instead released into the environment as waste heat, contributing to energy loss and thermal pollution. Thermoelectric materials have the potential to revolutionize energy harvesting by converting waste heat into electricity, offering a sustainable solution for energy efficiency. However, their low efficiency, at elevated temperatures prevent their widespread adoption in practical applications.

1.3 Research Questions

The study intends to answer the following questions:

1. how does pressure affect the electronic structure, phonon characteristics, optical properties, and superconducting behavior of YHSe ?
2. how does La doping influence the properties of the YHSe system, specifically the electronic structure, phonon behavior, optical properties, and superconductivity ?
3. how does temperature, pressure, and varying concentrations of La affect the thermoelectric properties of yttrium hydrogen selenide ?
4. What is the relationship between La concentration and the EPC parameter (λ) in the YHSe compound ?

1.4 Objectives

1.4.1 General Objective

- The general objective of this research is to investigate the effects of pressure and doping on the structural, electronic, phononic, optical, thermoelectric, and superconducting properties of the yttrium hydrogen selenide (YHSe) compound.

1.4.2 Specific Objectives

The specific objectives of this work are:

- to determine the electronic structure and phonon behavior at different lanthanum concentrations and under external pressure ;
- to evaluate the superconducting properties as a function of pressure and lanthanum doping ;
- to examine the optical responses influenced by lanthanum doping and pressure ;
- to compute the temperature-dependent thermoelectric properties under varying lanthanum concentrations and pressure.

1.5 Significance of the Study

Investigating the Consequence of La doping and pressure variations on the structure, phonons, thermoelectric, and superconducting characteristics of YHSe is essential for advancing material science and engineering. This research provides valuable insights into how external factors such as doping and pressure influence the fundamental properties of YHSe, enabling precise material manipulation for targeted applications. Understanding the impact of La incorporation can shed light on the tunability of superconducting behavior, potentially leading to the development of more efficient superconductors for high-performance electrical transmission and energy applications.

Moreover, exploring pressure-induced modifications in optical properties could pave the way for novel optoelectronic devices and improvements in light-based technologies. This

study also contributes to fundamental condensed matter physics by elucidating the complex relationships between doping, pressure, and material properties. The findings hold significant implications for thermoelectric applications, optoelectronic devices,fostering new technological advancements. Moreover, this research serves as a valuable reference for future studies focused on material enhancement and property optimization.

1.6 Scope of the Study

This work presents a comprehensive investigation of YHSe, employing first-principles DFT calculations to analyze its fundamental properties. Initially, the research examines the structural, electronic, optical, phonon, thermoelectric, and superconducting properties of pristine YHSe under varying pressure conditions. This analysis aims to establish a foundational understanding of the intrinsic behavior of YHSe, which is crucial for evaluating its potential applications in optoelectronic, thermoelectrics, and superconductivity. Subsequently, the study explores the effects of La doping on the structural, electronic, optical, phonon, thermoelectric, and superconducting characteristics of YHSe at a fixed pressure. This section specifically investigates how La incorporation modifies the electronic structure, alters phonon interactions, and influences light absorption capabilities critical factors for tuning the material's performance in optoelectronics, superconducting, and thermoelectric applications.

Unlike experimental studies, this work is entirely computational, relying on DFT based simulations and Boltzmann transport theory(BTT), as well as Phono3py, phonopy software, to predict and analyze material properties. A comparative analysis between pristine and La doped YHSe is conducted to clarify the specific role of doping in enhancing or modifying key physical characteristics. Finally, the study evaluates the interplay between doping, pressure, and phonon-mediated superconductivity, aiming to provide deeper insight into how external and intrinsic modifications influence the functional properties of YHSe. This analysis aims to establish a foundational understanding of the intrinsic behavior of YHSe, which is crucial for evaluating its potential applications in optoelectronics, thermoelectrics, and superconductivity.

1.7 Organization of the Dissertation

This dissertation systematically explores the structural, electronic, optical, phonon, thermoelectric and superconducting properties of yttrium hydrogen selenide under pressure variations and La doping, with structural analysis serving as the foundation for understanding its behavior. The dissertation is organized into five chapters: Chapter (1) introduces the research by outlining the background, motivation, research questions, objectives and scope of work. Chapter (2) provides a literature review that establishes the theoretical foundation by examining DFT, the role of phonons in superconductivity and heat transport, the influence of pressure on materials, and La's contributions to enhancing superconductivity, as well as its effects on photocatalysis and related phenomena. Chapter (3) Materials and Methods, including computational frameworks such as DFT, exchange-correlation functionals, pseudopotentials, Boltzmann transport theory and simulation tools. Chapter (4) presents the results and discussions derived different tools such as DFT, phonopy, phono3py emphasizing how pressure and La doping influence the fundamental properties of YHSe. Finally, Chapter (5) summarizes key findings, draws conclusions and provides recommendations for future research to advance the understanding and application of YHSe based materials.

2

Literature Review

2.1 Rare Earth Metal Hydrides

Rare-earth metal hydrides are compounds formed through the interaction of rare-earth elements with hydrogen, characterized by unique chemical, electronic, and structural properties. These unique properties have enabled their extensive application across various fields. Rare earth elements and their compounds play essential roles in traditional industries such as hydrogen storage, metallurgy, petroleum, textiles, and agriculture, as well as in rapidly emerging technological sectors (Kumari et al., 2015).

Importantly, rare earth metal hydrides are extensively utilized in hydrogen storage systems Due to their remarkable Capability to reversibly absorb and the process of hydrogen being produced or emitted under moderate conditions (Korst and Warf, 1966). They are also key materials in nickel-metal hydride (NiMH) batteries, where they function as negative electrode materials (Ovshinsky et al., 1993). Their superior hydrogen absorption characteristics further make them suitable for thermal management applications, such as hydrogen compressors and heat pumps (Sandrock, 1999). In the areas of magnetic refrigeration and permanent magnets, rare earth hydrides contribute significantly by enhancing and tuning magnetic properties (Gschneidner et al., 2005).

The superconductivity under high pressure highlights the importance of rare earth hydrides in cutting-edge in high-temperature superconductors and exploration of exotic quantum states (Flores-Livas et al., 2020).

However, despite their remarkable advantages, rare earth elements and their hydrides present significant challenges, including realizing and maintaining superconductivity under extreme conditions, such as ultra-high pressures, remains a complex and demanding task, limiting their immediate technological applications and requiring further fundamental research (Drozdov, A. P. et al., 2019).

2.1.1 Yttrium Hydride : Properties and Applications

YH_n is a compound composed of yttrium and hydrogen, with several known stoichiometric forms. The most frequent variant is the YH_2, which crystallizes in a face-centered cubic structure (FCC). Under high pressure, additional hydrogen atoms can be incorporated, leads to the creation of an insulating phase, approximately represented by YH_3, which adopts a hexagonal structure (Kume, Kenichi et al., 2011).

In 1996, Huiberts et al. demonstrated that the transition from YH_2 to YH_3 involves a metal to insulator transition, which can be exploited to modulate optical properties enabling smart windows that switch between opaque and transparent states (Huiberts et al., 1996). This groundbreaking discovery spurred extensive research into metal hydride based chromogenic materials and smart window technologies, including gasochromic windows devices controlled by external voltage (Van der Sluis et al., 2001).

Moreover, yttrium hydride containing a significant amount of oxygen has been shown to exhibit reversible photochromic behavior (Mongstad et al., 2001), further expanding its potential applications in optoelectronics, energy efficient building technologies, and sensors. This excellent switchable optical characteristics make them selective for a variety of technical uses, such as sensors, goggles, medical equipment, and smart devices. A study discovered that as the oxygen concentration in the film increases, the strength of the photochromic response decreases and the optical band gap widens (Moldarev, Dmitrii, et al., 2018).

2.2 Yttrium Selenide (Y_2Se_3) : Properties and Applications

Transition metal chalcogenides, including Y_2Se_3, Er_2Se_3, and As_2Se_3, have become a focus of research due are gaining attention for their unique properties (Ikhioya, I. et al., 2023). These features not only enhance their catalytic activity but also contribute to their affordability and efficiency in various applications.

Yttrium selenide (Y_2Se_3) has garnered significant attention for its potential applications in optoelectronics and photonics (Ikhioya, I. et al., 2023). As a member of the chalcogenide family, Y_2Se_3 exhibits unique properties that are heavily influenced by its

synthesis methods and material composition. These properties make it particularly sensitive to light, which is advantageous for structural designs in optical fibers. The variance Stoichiometry significantly impacts the optical and electrical properties of compounds (Ikhioya, I. et al., 2023).

Binary and ternary chalcogenides, such as Y_2Se_3, are known for their simple fabrication processes, unique structures, high refractive indices, and a wide range of deposition methods (Ikhioya, I. et al., 2023). These qualities make them very appropriate for use in optoelectronic devices. Additionally, these materials have promising uses for many technologies as solar cell,sensor and many more (Ikhioya, I. et al., 2023).

Yttrium selenide (Y_2Se_3) holds great potential for different technological uses, particularly in the area of optoelectronics, photovoltaics, thermoelectrics, and sensors (Ikhioya, I. et al., 2023). Continued research and exploration into the properties of Y_2Se_3 will open up new avenues for its use in cutting-edge applications (Ikhioya, I. et al., 2023).

Currently, there are no known studies on the properties or applications of Yttrium Hydrogen Selenide (YHSe), creating a significant gap in the literature. This is particularly notable given the growing interest in similar chalcogenides such as Yttrium Selenide Y_2Se_3, Er_2Se_3, and As_2Se_3, which have been explored for optoelectronics, photovoltaics, and sensors. Insights are mainly drawn from related hydrides and selenides, leaving the unique properties of YHSe largely unexplored. This presents an opportunity for this research to fill this gap.

2.3 Density Functional Theory (DFT)

DFT a quantum mechanical approach used in physics, chemistry, and material science to analyze and predict the physical properties of atoms, molecules, and solids (Dixon, 2016, Stanton, 2001). DFT approach is commonly used to determine the electronic structure of materials.

The theory proposes that a system's total energy can be described as a function of electron density, rather than electron wave function. DFT uses a wave function to describe electrons in a material and solves the Schrodinger equation for self-consistent behavior. This involves finding the wave function that minimizes the total energy of the system

(Anubhav Jain, Yongwoo 164 Shin,et al.,2016) subject to the constraint that the electron density is equal to the observed electron density of the material (Robert G Parr,1980). One of the key advantages of DFT is that it is computation-ally efficient, making it possible to study large systems with a high level of accuracy. It is also able to account for many-body effects, such as electron-electron interactions, which are important in understanding the properties of materials.

DFT has been used to a variety of materials, including superconductors, and has shown to be an effective method for understanding their electronic structure and superconducting characteristics. It has also been used to examine other characteristics of materials, such as their structural, optical, and magnetic properties (Eberhard Engel and Reiner M Dreizler,2011). The central equation in DFT is the Schrodinger equation, which explain the behavior of the electrons in a substance (Reiner M Dreizler and Eberhard KU Gross ,2012). In DFT, the Schrodinger equation is written as:

$$H\psi = E\psi \tag{2.1}$$

where $H[\psi]$ is the single-particle Hamiltonian operator, ψ is the wave function of the electrons, and E is the energy of the system. The single-particle Hamiltonian operator is given by

$$H = \frac{\hbar^2\nabla^2}{2m} + V[n] \tag{2.2}$$

where $\hbar$ is the reduced Planck constant, m is the mass of the electron, ∇^2 is the Laplacian operator, V[n] is the effective potential, which depends on the electron density n. To solve the Schrodinger equation self-consistently, the wave function ψ is iteratively updated until the total energy of the system is minimized, subject to the constraint that the electron density is equal to the observed electron density of the material. This is done using an iterative algorithm, such as the self-consistent field (SCF) method (Philip A Casey and Philip W Anderson, 2011). There are many different approximations that can be used to simplify the calculation of the effective potential V[n],such as the local density approximation (LDA) (Modarres .M, et al., 2005) and the generalized gradient approximation (GGA)(CA Ullrich and EKU Gross , et al.,1996). These approximations are used to ac-

count for the many-body effects that are important in understanding the properties of materials. In density functional theory (DFT), electron density is an important quantity that is used to calculate the properties of materials. The electron density is defined as

$$n(r) = \sum_i |\psi_i(r)|^2 \tag{2.3}$$

where $\sum_i$ indicates a sum over all the occupied electronic states,$\psi_i(r)$ is the wave function of the ith electronic state, and r is the position in space. The electron density is a measure of the number of electrons per unit volume at a given point in space (var Giaever and Karl Megerle, et al.,1961). It is related to the probability of finding an electron at a given point in space. The electron density can be used to calculate the total energy (Herbert Fröhlich, 1954) of a system using the following equation:

$$E[n] = T[n] + V[n] + E_H[n] + E_{xc}[n] \tag{2.4}$$

where T[n] is the kinetic energy of the electrons, V[n] is the potential energy of the electrons, $E_H[n]$ is the Hartree energy, and $E_{xc}[n]$ is the exchange-correlation energy. The kinetic energy of the electrons is given by

$$T[n] = \int n(r) \left(\frac{\hbar^2}{2m} \nabla^2 \varphi(r) \right) dr \tag{2.5}$$

where $\int$ indicates an integral over all space, n(r) is the electron density and $\varphi(r)$ is the single-particle wave function. The potential energy of the electrons is given by:

$$V[n] = \int n(r) V_{\text{ext}}(r)\, dr + \frac{1}{2} \int \int \frac{n(r)n(r')}{|r - r'|}\, dr\, dr' \tag{2.6}$$

Where $\int \int$ indicates a double integral over all space, $n(r)$ is the electron density, $V_{\text{ext}}(r)$ is the external potential, and $|r - r'|$ is the distance between the source and the point under consideration in space. The Hartree energy is given by:

$$E_H[n] = \frac{1}{2} \int \int \frac{n(r)n(r')}{|r - r'|}\, dr\, dr' \tag{2.7}$$

The exchange-correlation energy is given by

$$E_{xc}[n] = \int n(r)\, \epsilon xc(n(r))\, dr \tag{2.8}$$

where $\int$ represent an integral over all space, n(r) is the electron density, and ϵxc$(n(r)$ is the exchange energy. The time and position-dependent representation of the non-relativistic Schrödinger equation of the nuclei and electron system is given by

$$i\hbar \frac{\partial \Phi(R, r; t)}{\partial t} = \left(-\sum_{\mu} \frac{\hbar^2}{2M_\mu} \nabla^2_{R_\mu} - \frac{\hbar^2}{2m} \sum_{i} \nabla^2_{r_i} + V(R, r) \right) \Phi(R, r; t), \tag{2.9}$$

where

$$\begin{aligned} V(R, r) &= V_{\text{e–e}} + V_{\text{n–n}} + V_{\text{e–n}} \\ &= \sum_{i,\mu} \frac{Z_\mu e^2}{|r_i - R_\mu|} + \frac{1}{2} \sum_{i \neq j} \frac{e^2}{|r_i - r_j|} + \sum_{\mu \neq \nu} \frac{Z_\mu Z_\nu e^2}{|R_\mu - R_\nu|}. \end{aligned} \tag{2.10}$$

where $V_{\text{e–e}}$ is the electron–electron interaction energy, $V_{\text{n–n}}$ is the nucleus–nucleus interaction energy, and $V_{\text{e–n}}$ is the electron–nucleus interaction energy.

Here, $r = (r_1, r_2, \ldots, r_i)$ and $R = (R_1, R_2, \ldots, R_I)$ denote the positions of all electrons and nuclei, respectively. The indices i, j run over all electrons, and μ, ν run over all nuclei. m is the electron mass, M_μ is the mass of the μ-th nucleus, Z_μ is the atomic number of nucleus μ, and e is the elementary charge. I represents the total number of nuclei. $\Phi(R, r; t)$ is the many-body wave function of the full system. In short-hand notation, we can write Equation (2.10) as:

$$(T_{\text{n}} + T_{\text{e}} + V_{\text{e–e}} + V_{\text{n–n}} + V_{\text{e–n}})\Phi(R, r; t) = E_n \Phi(R, r; t), \tag{2.11}$$

where T_{n} and T_{e} represent the kinetic energy operators for nuclei and electrons, respectively, and E_n is the total energy eigenvalue of the system in the n-th quantum state.

The Born-Oppenheimer approximation relies on the idea that the significant mass difference between nuclei and electrons (i.e., $M \gg m$). For example, a proton (^{1}H) is approximately 1800 times heavier than an electron, and for elements like carbon, the mass

ratio exceeds 20,000. This disparity means that electrons respond to external perturbations much more rapidly than nuclei (Stanton, 2001). Consequently, the kinetic energy of nuclei T_{n} is neglected, and the nucleus–nucleus repulsion term $V_{\mathrm{n–n}}$ is treated as a constant. With this simplification, the electronic Schrödinger equation is solved in the first approximation.

2.3.1 The Hohenberg-Kohn Theorems

Hohenberg and Kohn's 1964 theorems established electron density as the key quantity for determining total energy, becoming the foundation of contemporary density-functional theory (Hohenberg, P., Kohn ,1964). They developed two theorems that serve as the foundation for the formulation of (i)] two theorems that serve as the foundation for the formulation of (i). The external voltage $V(\mathbf{r})$ and electron density n(r) have a unique one-to-one connection.

Using the variational principle, one may determine the ground state electron density. The variational principle states that the ground state energy E_0 in DFT is always less than or equal to the expected value determined with any trial electron density.

$$E_0 < \langle \Psi | \hat{H} | \Psi \rangle \tag{2.12}$$

The first theorem can be demonstrated by assuming that there exist two different external potentials, denoted as V_{ex1} and V_{ex2}, which produce the same ground state electron density $n_0(\mathbf{r})$. Consequently, the corresponding Hamiltonians, $\hat{H}_1$ and $\hat{H}_2$, will have different ground state wave functions, $\Psi_1(\mathbf{r})$ and $\Psi_2(\mathbf{r})$, respectively. Applying Equation (2.12), we obtain: The associated Hamiltonians, $\hat{H}_1$ and $\hat{H}_2$, will therefore have different ground state wave functions, $\Psi(r_1)$ and $\Psi(r_2)$. Using Equation (2.12), we have:

$$E_0 < \langle \Psi | \hat{H} | \Psi \rangle. \tag{2.13}$$

This implies that for each Hamiltonian:

$$E_{01} < \langle \Psi_2 | \hat{H}_1 | \Psi_2 \rangle. \tag{2.14}$$

$$E_{01} < \langle \Psi_2 | \hat{H}_1 + \hat{H}_2 - \hat{H}_2 | \Psi_2 \rangle. \tag{2.15}$$

$$E_{01} < \langle \Psi_2 | \hat{H}_1 | \Psi_2 \rangle = \langle \Psi_2 | \hat{H}_2 | \Psi_2 \rangle + \langle \Psi_2 | \hat{H}_1 - \hat{H}_2 | \Psi_2 \rangle. \tag{2.16}$$

Eq. (2.16) is simplified to

$$E_{01} < \langle \Psi_2 | \hat{H} | \Psi_2 \rangle = E_{02} + \int n(r)(V_{\text{ex1}} - V_{\text{ex2}})\, dr. \tag{2.17}$$

where E_{01} and E_{02} are the ground state energies of $\hat{H}_1$ and $\hat{H}_2$, respectively.

$$E_{02} < \langle \Psi_1 | \hat{H}_2 | \Psi_1 \rangle = E_{01} < \langle \Psi_2 | \hat{H}_2 + \hat{H}_1 - \hat{H}_1 | \Psi_2 \rangle. \tag{2.18}$$

$$E_{02} < \langle \Psi_1 | \hat{H}_2 | \Psi_1 \rangle = \langle \Psi_1 | \hat{H}_1 | \Psi_1 \rangle + \langle \Psi_1 | \hat{H}_2 - \hat{H}_1 | \Psi_1 \rangle. \tag{2.19}$$

$$E_{02} < \langle \Psi_1 | \hat{H}_2 | \Psi_1 \rangle = E_{01} + \int n(r)(V_{\text{ex2}} - V_{\text{ex1}})\, dr. \tag{2.20}$$

After adding Eq.(2.17)and Eq.(2.20) we get

$$E_{01} + E_{02} < E_{02} + E_{01} \tag{2.21}$$

This leads to a clear contradiction. Therefore, it is impossible for two different external potentials to produce the same electron density $n(\mathbf{r})$. As a result, the electron density $n(\mathbf{r})$ uniquely determines the external potential $V_{\text{ex}}(\mathbf{r})$ and all ground state properties. Consequently, the external potential V_{ex} can be conveniently expressed as a functional of the electron density.

$$V_{\text{ex}} = \int n(r_i) V(r)\, dr. \tag{2.22}$$

Thus, for a specified external potential, the total electronic energy E_e can be directly represented as a functional of the electron density $n(\mathbf{r})$:

$$E_e[n] = T[n] + V_{\text{ex}}[n] + V_{\text{ee}}[n]. \tag{2.23}$$

$$E_e[n] = \int n(r) v(r)\, dr + F_{\text{HK}}[n]. \tag{2.24}$$

where

$$F_{\mathrm{HK}}[n] = T[n] + V_{\mathrm{ee}}[n]. \tag{2.25}$$

Here, $F_{\mathrm{HK}}[n]$ depends solely on the electron density $n(\mathbf{r})$ and is independent of the external potential $v(\mathbf{r})$. Therefore, $F_{\mathrm{HK}}[n]$ is considered a universal functional of $n(\mathbf{r})$, meaning that its form remains the same for any system, regardless of the external potential applied. If the exact form of this functional were known, it would allow for an exact solution of the Schrödinger equation. However, the precise density dependence of $F_{\mathrm{HK}}[n]$ remains unknown. One of the central challenges in DFT is to determine the explicit form of this universal functional.

The second Hohenberg-Kohn theorem addresses how to verify whether a given electron density corresponds to the true ground-state density. It states that the total energy reaches its minimum value only when the electron density matches the ground-state density. Furthermore, the ground-state energy can be obtained through a variational principle, where the density that minimizes the total energy is identified as the exact ground-state density. This principle is consistent with the general variational method.

$$E_0 \leq E[n] = T[n] + V_{\mathrm{ex}}[n] + V_{\mathrm{ee}}[n]. \tag{2.26}$$

The problem of many-electron systems, initially described by 10^{23} variables in three dimensions, can now be simplified to a problem involving only a single variable in three dimensions. While these two theorems establish the existence of a universal functional, they do not offer any details about the nature of this functional or provide methods for calculating the ground-state density.

2.3.2 The Kohn-Sham Equations

Nearly one year after the Hohenberg-Kohn theorems were published, Kohn and Sham first applied DFT to practical electronic structure calculations in 1965. Their approach involves transforming the fully interacting system into an equivalent non-interacting one, similar to the Hartree-Fock approximation. However, unlike the Hartree-Fock method, the Kohn-Sham equations incorporate both electron correlation and exchange energy. As a result,

Kohn and Sham proposed that the energy functional can be written as: Their method focuses on transforming the complete interacting system into a virtual non-interacting one, akin to the Hartree-Fock approximation. However, the Kohn-Sham equations account for both electron correlation and exchange energy. Therefore, according to Kohn and Sham, the energy functional can be expressed as

$$\begin{aligned} E[n] &= \int n(r)V(r)\,dr + F_{HK}[n(r)] \\ &= \int n(r)V_{\text{ex}}(r)\,dr + T_s[n(r)] + \int\int \frac{n(r)n(r')}{|r-r'|}\,dr\,dr' + E_{\text{EX}}[n(r)] \end{aligned} \tag{2.27}$$

where $V_{\text{ex}}(\mathbf{r})$ denotes the external potential. The third term in Equation (2.27) represents the classical Coulomb interaction energy of the electron density with itself, commonly referred to as the Hartree energy. At the same time, the kinetic energy of non-interacting electrons, which collectively determine the exact ground-state density $n(\mathbf{r})$, is expressed as follows:

$$T_s(n) = -\frac{1}{2}\sum_{k=1}^{N}\int \phi_k^*(\mathbf{r})\,\nabla^2\phi_k(\mathbf{r})\,d\mathbf{r} \tag{2.28}$$

Where the effective potential energy functional can be written in separted form as:

$$V^{\text{eff}}[n(\mathbf{r})] = \int n(\mathbf{r})V_{\text{ex}}(\mathbf{r})\,d\mathbf{r} + \int\int \frac{n(\mathbf{r})n(\mathbf{r}')}{|\mathbf{r}-\mathbf{r}'|}\,d\mathbf{r}\,d\mathbf{r}' + E_{\text{XC}}[n(\mathbf{r})] \tag{2.29}$$

The exchange-correlation (XC) functional encompasses all factors not explicitly captured in Kohn-Sham (KS) theory. It includes the electron correlation energy resulting from electron-electron repulsion, the exchange energy that accounts for the effects of the Pauli exclusion principle on electron interactions, and the portion of the kinetic energy arising from these interactions and the component of kinetic energy resulting from these effects. These interactions are unified into a single term known as the exchange-correlation energy, denoted as $E_{\text{XC}}[n(\mathbf{r})]$. If the energy expression in Equation (2.27) is minimized with respect to the stationary density $n(\mathbf{r})$, the effective Kohn-Sham potential, which corresponds to

the minimization of the effective potential energy, can be written as:

$$v_{\text{eff}} = \frac{\delta V_{\text{eff}}}{\delta n} = \int \delta n(\mathbf{r}) V_{\text{ex}}(\mathbf{r})\, d\mathbf{r} + E_{\text{Hart}}[n(\mathbf{r})] + E_{\text{xc}}[n(\mathbf{r})]. = V(\mathbf{r}) + \int \frac{n(\mathbf{r}')}{|\mathbf{r} - \mathbf{r}'|}\, d\mathbf{r}' + V_{\text{xc}}(\mathbf{r}), \tag{2.30}$$

where, V_{xc} is the exchange-correlation potential. It is a variational derivative of the exchange-correlation energy, E_{xc},

$$V_{\text{xc}}(\mathbf{r}) = \frac{\delta E_{\text{xc}}[n(\mathbf{r})]}{\delta n(\mathbf{r})}. \tag{2.31}$$

This led to the basic equation in Kohn-Sham DFT, which is the one-electron Schrödinger-like equation expressed as:

$$\left(-\frac{\nabla^2}{2M_e} + v_{\text{eff}}\right)\phi_i = \epsilon_i \phi_i, \tag{2.32}$$

where the Kohn-Sham one-electron orbitals (ϕ_i) and the corresponding electron number density is given by

$$n(\mathbf{r}) = \sum_{i=1}^{N} |\phi_i|^2. \tag{2.33}$$

The total energy of system is given by

$$E_s = \sum_i \epsilon_i \tag{2.34}$$

Note that the V_{eff} depends on $n(\mathbf{r})$ through Eq.(2.29). A self-consistent iterative method starts with an initial electron density that can be used to determine the Kohn-Sham potential. Then, through solution of Eq.(2.32), and use of the relation in Eq.(2.33) we can obtain a new electron density. Eq.(2.33) reveals that the ground state density is the density that minimizes the total energy. Such a ground state density $n_0(\mathbf{r})$ can be found using an iterative scheme that approaches self-consistency. The self-consistent cycles are listed below:

1. Begin with an initial guess for the electron density.

2. Insert this guessed density into Equation (2.30) to construct a new effective potential $v_{\text{eff}}(\mathbf{r})$, which depends on the density $n(\mathbf{r})$.

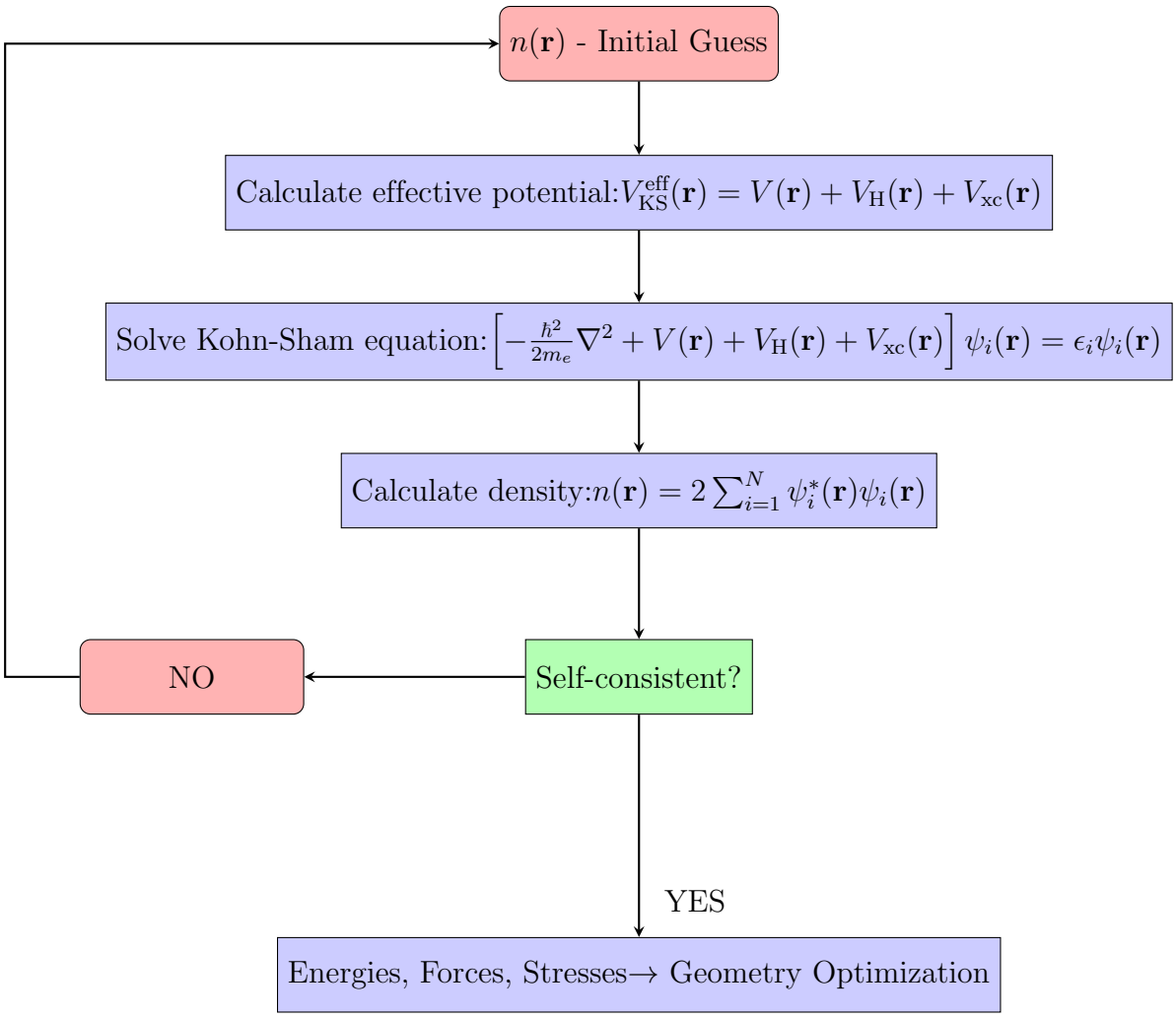

Figure 2.1: Self-consistent Kohn-Sham loop(Woods, N. D., Payne, M. C., & Hasnip, P. J.,2019).

3. Solve the Kohn-Sham orbital equation, Equation (2.32), using the effective potential $v_{\mathrm{eff}}[n(\mathbf{r})]$ obtained in the previous step.

4. Calculate the new electron density $n(\mathbf{r})$ using Equation (2.33).

Figure 2.1 illustrates the self-consistent Kohn-Sham loop. If the initial and new densities are identical, it indicates that the ground-state density has been reached, and the iterative process can be stopped. If they differ, a new trial density should be chosen by minimizing the total energy, and the iterative process should continue.

2.4 Estimation of the Exchange Correlation Energy (E_{XC})

In theory, the Kohn-Sham equations provide an exact method for determining the ground-state energy of an interacting system, provided the form of E_{XC} is known. However, since the exact form of E_{XC} is generally unknown, Equation (2.32) must be solved iteratively. Unfortunately, the specific form of E_{XC} is usually not known; therefore, Eq.(2.32) must be solved iteratively. In electronic structure calculations, the exchange-correlation energy E_{XC} is typically approximated using the Local Density Approximation (LDA) or the Generalized Gradient Approximation (GGA). The exchange-correlation energy is given by:

$$E_{\mathrm{xc}}[n] = \int n(\mathbf{r})\, \varepsilon_{\mathrm{xc}}(n)\, d^3r$$

where $n(\mathbf{r})$ is the electron charge density, and $\varepsilon_{\mathrm{xc}}(n)$ is the exchange-correlation energy per electron, which depends on the chosen functional. Different functionals approximate $\varepsilon_{\mathrm{xc}}(n)$ in different ways.

2.4.1 Local Density Approximation (LDA)

In this approximation, the contribution to E_{XC} from any given region of space depends only on the density within that region, which is why it is commonly known as the local density approximation (LDA). This approach assumes that an inhomogeneous system can be divided into infinitesimally small volumes, with the electron density treated as constant within each volume. Therefore, the exchange-correlation energy for the density in each volume is considered to be the same as that of a homogeneous electron gas at that density. In both the LDA and the local spin density approximation (LSDA) the exchange-correlation functionals are expressed solely as functionals of the density which allows them to be written as $E_{\mathrm{XC}}[n(\mathbf{r})]$.

$$E_{XC}[n] = \int \epsilon^{\mathrm{uniform}}(n(r))n(r)\, d^3r. \tag{2.35}$$

Here, $\epsilon_{\text{unif}}(n(\mathbf{r}))$ represents the exchange-correlation energy per particle of a uniform electron gas with density $n(\mathbf{r})$. This energy per particle is weighted by the probability $n(\mathbf{r})$ of finding an electron at position $\mathbf{r}$. The quantity $\epsilon_{\text{unif}}(n(\mathbf{r}))$ can be decomposed into exchange and correlation contributions.

$$\epsilon^{uniform}(n(r)) = \epsilon_X^{uniform}(n(r)) + \epsilon_C^{uniform}(n(r)). \tag{2.36}$$

The exchange component, denoted as $\epsilon_X^{\text{uniform}}$, represents the exchange energy of an electron within a uniform electron gas at a specific density, $n(\mathbf{r})$. The explicit form of $\epsilon_X^{\text{uniform}}[n(\mathbf{r})]$ is provided in

$$\epsilon_X^{\text{uniform}}[n] = -\frac{3}{4}\left(\frac{3}{\pi}\right)^{\frac{1}{3}} \int n(r)^{\frac{4}{3}}\, d^3r. \tag{2.37}$$

Equation (2.37) was originally derived by Bloch and Dirac in the late 1920s. However, the precise form of the correlation component, ϵ_{C}, is still not known. More precise estimates are typically obtained using quantum Monte Carlo simulations. The LDA tends to favor systems with greater homogeneity and provides reliable approximations for molecules and solids with orbitals primarily in the s or p states. Additionally, the E_{XC} per particle is considered spatially the same, meaning that the LDA depends solely on the electron density at a given point in space.

2.4.2 The Generalized Gradient Approximation (GGA)

A natural progression beyond the LDA is to incorporate both the electron density, $n(\mathbf{r})$, and point $\mathbf{r}$, as well as the gradient of the electron density, $\nabla n(\mathbf{r})$, in order to more accurately reflect the inhomogeneity of the real electron density. This methodology gives rise to the GGA, in which the exchange-correlation energy is modified to include these density variations. The GGA provides a more accurate representation than the LDA, and the exchange-correlation energy, $E_{\text{XC}}[n(r)]$, is expressed as:

$$E_{\text{XC}}^{\text{GGA}}[n] = \int f^{\text{GGA}}(n(r), \nabla n(r))\, d^3r. \tag{2.38}$$

Within GGA, the exchange energy, $\epsilon_X[n(r)]$, takes the form:

$$E_X^{\mathrm{GGA}}[n] = \int n(r)\epsilon_X^{\mathrm{uniform}}(n(r))F_X^{\mathrm{GGA}}(g)\, d^3r. \tag{2.39}$$

The term $F_X^{\mathrm{GGA}}(s)$ represents the exchange enhancement factor, which indicates the extent to which the exchange energy is increased compared to its value in the LDA for a given electron density $n(r)$. Here, g refers to the dimensionless reduced gradient. There exist various forms of this approximation owing to the flexibility in its parameterization. Among them, the Perdew-Burke-Ernzerhof (PBE) functional(Perdew.J.P, Burke.K et al.,1996) and its adaptation for solids, known as PBEsol (Perdew.J.P, Ruzsinszky.A, Csonka.I.G, et al.,2008) are two widely used approaches in solid-state physics.

2.5 K-Point Sampling and Brillouin Zone Integration

Physical quantities such as the electron density and total energy can be evaluated by integrating over the $\vec{k}$-points within the Brillouin zone (BZ). The precision of these evaluations strongly depends on selecting appropriate $\vec{k}$-points for the Brillouin zone integration. Ideally, this would require performing an integration over all $\vec{k}$-points to construct the electron density. However, due to the fact that the wave functions change slowly with respect to $\vec{k}$, the integration can be approximated by a discrete summation. Since electronic wave functions at nearby $\vec{k}$-points are almost the same, the wave function within a particular $\vec{k}$-space region can be sufficiently described by the wave function at a single $\vec{k}$-point. Consequently, only a finite set of $\vec{k}$-points is necessary to calculate the electronic potential. To achieve this, a regular grid of $\vec{k}$-points is commonly utilized, enabling efficient and accurate sampling of the BZ. Alternatively, a uniform mesh of $\vec{k}$-points can be produced using the Monkhorst-Pack scheme.

$$\vec{k}_{n_1,n_2,n_3} = \sum_{i=1}^{3} \frac{2n_i - N_i - 1}{2N_i}\vec{G}_i. \tag{2.40}$$

Where N_i represents the number of $\vec{k}$-points along each direction, and $n_i = 1, 2, \ldots, N_i$, denoting the index of the $\vec{k}$-points. In this work, a three-dimensional grid of $\vec{k}$-points is

constructed using the Monkhorst-Pack method (Monkhorst-Pack 1976) following a convergence test based on the total ground-state energy.

2.6 Pseudopotentials

In DFT, pseudopotentials are introduced to simplify the treatment of the electron nucleus interaction (Drut, J. E. et al.,2010). Core electrons are tightly bound to the nucleus, and their wave functions oscillate rapidly near the atomic core, which would require an extremely large number of plane waves to model accurately. However, since core electrons typically do not participate significantly in chemical bonding or other low-energy excitation, it is computationally efficient to replace their effects with a smoother, effective potential. This approach allows DFT calculations to focus on the chemically active valence electrons, drastically reducing computational cost while maintaining high accuracy (Vanderbilt, D., 1990).

In DFT calculations, pseudopotentials replace the complex Coulomb interactions between core electrons and valence electrons with a simplified potential, enabling a more efficient description of electronic properties while retaining the essential physics of the system. Choosing appropriate pseudopotentials is crucial for achieving accurate and reliable results (Garrity et al., 2014).

Within the framework of the Kohn-Sham (KS) equations of DFT, pseudopotentials specifically modify the external potential term $V_{\text{ext}}(\mathbf{r})$, which originally describes the true Coulomb attraction between electrons and nuclei. Instead of solving for the singular Coulomb potential, a smooth pseudopotential is introduced to represent the influence of both the atomic nucleus and the tightly bound core electrons on the valence electrons (Martin, R. M., 2020). This replacement leads to smoother valence wavefunctions, enabling efficient and accurate plane-wave-based DFT calculations.

Different types of pseudopotentials offer various trade-offs between accuracy and computational cost. Norm-Conserving Pseudopotentials (NCPPs) maintain a high degree of accuracy, especially in systems with critical chemical bonding or strong core valence interactions but they require high plane-wave cutoff energies, thus increasing computational demand (Martin, R. M., 2020). Additionally, norm-conserving pseudopotentials are gen-

erally transferable across different chemical environments, making them useful in diverse simulations (Kazanjian and Lucas, 1983). Ultrasoft Pseudopotentials (USPPs) relax the norm-conservation constraint, allowing lower plane-wave cutoffs and significantly reducing computational cost, making them suitable for metals and large or complex systems, although sometimes at the expense of accuracy for localized states. Projector Augmented-Wave (PAW) methods provide an even better balance between efficiency and accuracy by reconstructing the all-electron wavefunction from a pseudo-wavefunction, making PAW pseudopotentials widely applicable in many areas of materials science.

2.7 Doping

In materials science, impurities or foreign atoms are purposely introduced into semiconductors to improve their electrical, optical, or chemical properties (Chen et al., 2010). This carefully controlled process is essential for manufacturing electronic devices and developing advanced functional materials.

Although primarily associated with semiconductors, doping is also widely employed in ceramics, polymers, and metals (Chen et al., 2010). Dopants help separate and transport photo-induced charge carriers, reducing the over-potentials needed for energy-efficient redox processes. Beyond influencing electronic properties, doping can also alter structural characteristics and surface morphology. For instance, introducing lanthanum as a dopant has been shown to reduce particle size in host materials, improving photocatalytic activity (Sudrajat et al., 2019). Smaller particles reduce the distance that charge carriers must travel and leading to, faster involvement in this processes and a significant reduction in bulk recombination of electron-hole pairs.

Doping also introduces additional active sites within the material. When a metal interacts with a semiconductor, an electric field arises due to the mismatch in their Fermi levels. Electrons go a higher Fermi level to one with a lower Fermi level, causing band edge realignment and the creation of Schottky barriers at the metal/semiconductor junction.

Lanthanum is particularly effective as a dopant due to its favorable redox pair, which introduces intermediate energy levels within the semiconductor matrix, enabling efficient electron trapping and release. Additionally, lanthanum doping can shift the conduction

band (CB) to more negative potentials, improving photocatalytic activity (Khan et al., 2024). The 4f orbitals of La interact with Lewis base functional groups, forming coordination complexes that improve surface adsorption characteristics (Yu et al., 2015). Furthermore, La-induced structural changes facilitate the delocalization of photoexcited electrons within the conduction band, thereby promoting efficient hydrogen (H_2) production (Humayun et al., 2022).

2.8 Pressure Effects on Material Properties

Pressure is a key thermodynamic variable which profoundly affects the characteristics of condensed matter. By reducing atomic distances and modifying electronic structures, high pressure induces novel phases with unique characteristics that are rarely observed under ambient conditions (Duan & Liu, 2017).

One of the most notable effects of pressure is its ability to transform electronic band structures. It can drive indirect-to-direct bandgap transitions, as demonstrated in $LaAlO_3$ (Murtaza & Ahmad, 2012). Beyond band structure modifications, pressure can also induce insulator-to-metal transitions, fundamentally altering a material's electronic properties (Duan & Liu, 2017).

High pressures can create novel electronic states that do not exist under normal conditions (Paul, D. K. et al.,2024). According to Islam and Hossain (2020), new states may occur due to changes in lattice symmetry or hybridization effects. According to Islam and Hossain (2020), these factors can considerably impact on the DOS and band structure. High pressure can alter the hybridization patterns of different atomic orbitals (Connerade, J.P., 2009). In superconducting materials, pressure is a key factor that can increase the superconducting transition temperature (T_c). A striking example is observed in copper oxides, where T_c reaches 164 K at 31 GPa (Duan & Liu, 2017). Additionally, high-pressure conditions facilitate the synthesis of materials with remarkable magnetic, optical, thermoelectric, and superconducting properties (Brazhkin, 2007).

A particularly intriguing consequence of high pressure is its effect on alkali and alkali-earth metals, which begin to exhibit d-metal characteristics. This transformation enables the formation of intermetallic compounds such as K-Ni, K-Ag, and K-Pd, some of which

remain metastable upon decompression (Brazhkin, 2007). Expanding solid solution regions and leading to the emergence of metastable structures phases. These phases stabilized under elevated pressure exhibit superconducting transition temperatures of up to 11 K, nearly ten times that of pure aluminum (Brazhkin et al., 1993).

Moreover, pressure has been instrumental in the discovery of novel superconductors. For example, it has enabled the synthesis of Ba_8Si_4 clathrates, which exhibit unique superconducting properties (Yamanaka et al., 2000). Additionally, it has facilitated the growth of mercury-based high-temperature superconductors, which hold record T_c values approaching 150 K (Kuzemskaya et al., 1998).

2.9 Pressure Dependence of Superconductivity

The pressure dependence of Tc can be obtained from microscopic models of phonon-mediated superconductivity, such as the weak-coupling BCS model (Bardeen, Cooper, and Schrieffer, 1957) or the Eliashberg theory of strong-coupling superconductivity (Eliashberg, 1960). Understanding the pressure dependence of a superconductor's microscopic parameters, such as average phonon frequency (ω_D) and electronic density of states at the Fermi level $N(E_F)$, is crucial for estimating the superconducting transition temperature (T c) as a function of applied pressure (Lorenz & Chu, 2005). According to the weak-coupling BCS theory (Lorenz & Chu, 2005), the superconducting transition temperature Tc may be represented as

$$k_B T_C = 1.13\hbar\omega_D \exp\left(\frac{-1}{\lambda}\right) \tag{2.41}$$

where k_B and $\hbar$ are Boltzmann's and Planck's constants, respectively. The electron-phonon coupling constant is given by $\lambda = N(E_F)V_{\text{eff}}$, where V_{eff} is the effective interaction between electrons mediated by electron-phonon coupling. Since ω_D generally increases with pressure, representing the increase in the frequency of phonon modes, the typical decrease in T_c with pressure is primarily due to a reduction in λ (Lorenz, B., & Chu, C. W. 2005).

The average value of the electronic density of states is expected to decrease under

pressure due to the pressure-induced band broadening effect (Lorenz, B., & Chu, C. W. 2005). It should be noted that the BCS equation (2.41) applies only in the weak-coupling case when the electron-phonon coupling constant λ is small (Lorenz, B., & Chu, C. W. 2005). Most superconducting elemental metals (except Al) exhibit an intermediate to strong electron-phonon coupling with λ of the order of 1 or larger and their superconductivity is not well described by the weak-coupling BCS equation(2.41) (Lorenz, B., & Chu, C. W. 2005).

Extending the original BCS theory (Mattheiss.F.L, et al.,1966) Eliashberg developed the theory of strong-coupling superconductivity (Chu.W.C and Testardi.R.L, 1974) that provides, together with the pseudopotential treatment of the screened Coulomb interaction (Chu.W.C,et al.,1975) the fundamental equations describing the physics of superconductors with phonon mediated pairing of any coupling strength.

$$k_B T_c = \frac{\hbar\omega}{1.2} \exp\left\{-\frac{1.04(1+\lambda)}{\lambda - \mu^*(1+0.62\lambda)}\right\} \tag{2.42}$$

where μ^* is the Coulomb pseudopotential calculated as (Lorenz, B., & Chu, C. W. 2005):

$$\mu^* = \frac{N(E_F)V_c}{1 + N(E_F)V_c \ln\left(\frac{E_B}{\hbar\omega_0}\right)}. \tag{2.43}$$

Vc is the matrix element of the screened Coulomb interaction averaged over the Fermi surface, E_B is the electronic bandwidth and ω_0 is the cut-off (or maximum) phonon frequency. The electron-phonon coupling constant λ is given by McMillan (1967) (Lorenz, B., & Chu, C. W. 2005).

$$\lambda = 2\int \frac{d\omega\, \alpha^2(\omega)F(\omega)}{\omega} = \frac{N(E_F)\langle I^2\rangle}{M\langle\omega^2\rangle}. \tag{2.44}$$

$\alpha(\omega)$ and $F(\omega)$ are the strength of an average electron-phonon interaction and the phonon density of states, respectively. $\langle I^2\rangle$ is the average over the Fermi surface of the square of the electronic matrix element of the change of the crystal potential induced by a displacement of an atom. M stands for the atomic mass. $\langle\omega^n\rangle$ in equations (2), $n = 1$, and (4), $n = 2$,

is the n-th moment of the normalized weight function (Lorenz, B., & Chu, C. W. 2005):

$$\langle \omega^n \rangle = \frac{2}{\lambda} \int d\omega \, \alpha^2(\omega) F(\omega) \omega^{n-1}. \tag{2.45}$$

The ω parameter represents the frequency of phonons, while $\alpha^2 F(\omega)$ denotes the Eliashberg spectral function (Lorenz, B., & Chu, C. W. 2005).

From equations (2.42) to (2.45) it becomes obvious that the pressure dependence of Tc is very complex and depends on various parameters of the electron and phonon systems (Lorenz, B., & Chu, C. W. 2005). The McMillen formula (2.42) has been used successfully in a number of examples in deriving Tc(p) from first principle calculations of the pressure effect on the band structure and the phonon spectrum (Lorenz, B., & Chu, C. W. 2005). For example (Olsen et al.,1968) have demonstrated that equation(2.42) can be used to estimate the pressure dependence of Tc for a number of non-transition-metal superconductors in qualitative agreement with experiments (Lorenz, B., & Chu, C. W. 2005).

2.10 Role of Pressure in Modifying High-temperature Superconductivity

Superconductivity in the La-Ba-Cu-O system has been extensively investigated due to its potential for high-temperature applications (Lorenz, B., & Chu, C. W., 2005) with the discovery of unprecedentedly high superconducting transition temperatures around 35 K has reignited intense research.

The commonly observed enhancement of superconductivity under pressure in these newly developed materials has encouraged researchers to pursue the synthesis of compounds with even higher critical temperatures (T_c)(Lorenz, B., & Chu, C. W., 2005). Notably, the first p-dependent LBCO system yielded a remarkable outcome the superconducting Tc increased beyond 40K under applied pressure, exhibiting an unusually high rate of enhancement (Lorenz, B., & Chu, C. W., 2005).

The significant increase in $T_c(p)$ observed under pressures (with data at extreme condition deemed not valid due to the destruction of the system) and the absence of any signs

of T_c reaching saturation even higher Tc could be attained under extreme P and with further optimization of the samples. Moreover, it became apparent that the superconducting phase in those material corresponds to structure similar to K_2NiF_4, specifically $La_{2-x}Ba_xCuO_{4-\delta}$ (Lorenz and Chu, 2005).

In early 1987, the onset of superconductivity in these compounds was observed to increase under hydrostatic pressure, reaching a new record T_c of 52.5 K (Lorenz and Chu, 2005). Two key findings emerged from the initial studies of this new class of superconducting materials (i) Having a perovskite-like structure similar to K_2NiF_4, and (ii) the superconducting transition temperature, T_c, increased at an unusually rapid rate with pressure.

2.11 Superconductivity of Hydrides Under Pressure

Assessment of the critical temperature (T_c) throughout the 20th era can be categorized into three main phases. The first era began with Hg (Kamerlingh Onnes, 1911).

The second era centered around Nb-based superconductors, which remained the dominant materials until 1986, when the groundbreaking of Tc for Cu based material occurred (Bednorz.G.J and Müller.A.K.,1986). This discovery ushered in the third era, marked by an intense Look for materials that possess with even enhanced T_c value. It is capable of being characterized by the synthesis of novel materials with a fourth era, where the development of hydrogen-based materials and hydrides presents a promising avenue for achieving room-temperature superconductivity.

This discovery marked the third era, characterized by a rapid search for materials with even higher superconducting temperatures. Arguably, we have now entered a fourth era, where the synthesis of hydrogen-based materials and hydrides represents a promising route toward room-temperature superconductivity. This transition was strongly motivated by Ashcroft's theoretical prediction in 2004 that Hydrogen-dense materials under extreme pressure could exhibit high-Tc superconductivity (Ashcroft.W.N.,2004).

Hydrogen has the smallest atomic mass, leading to high phonon frequencies and, consequently, high critical temperatures in hydrogen compounds (Howie et al., 2012). However, achieving this requires high pressures, typically generated using diamond anvil cells. At

present, Hydrogen-dense materials are among the leading candidates for high Tc superconductivity. However, despite predictions, none of the materials surpasses Unalloyed hydrogen serving as a strong contender for aimed at enabling superconductivity under ambient conditions. Pristine hydrogen continues to be a central focus of ongoing research, with significant progress made in reaching pressures approaching 400 GPa (Howie et al., 2012). Figure 2.2 The maximum Tc attained in a mercury-based cuprate so far. As per BCS

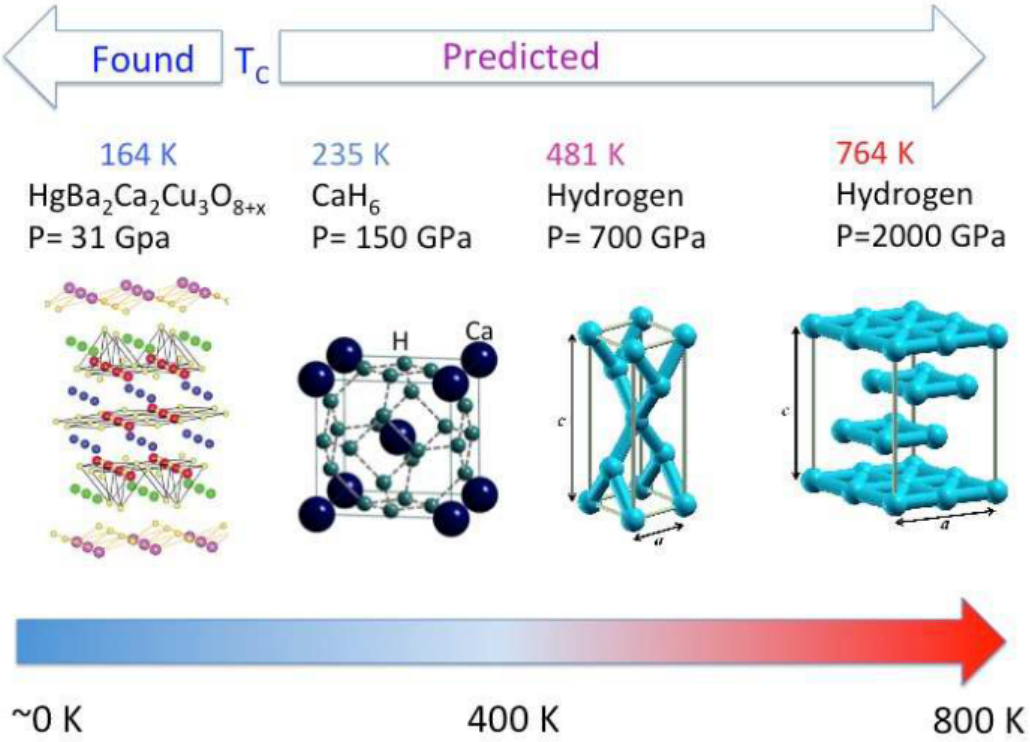

Figure 2.2: At 30 GPa, the highest Tc recorded in a mercury-based cuprate is 164 K (Howie et al., 2012) For CaH_6 at 150 GPa, Tc values approaching room temperature have been predicted, and in metallic hydrogen (atomic form), Tc values well exceeding room temperature are anticipated (Howie et al., 2012).

theory, compounds ormed from light elements, they hold the potential to display Elevated critical temperature, owing to the occurrence of high-frequency modes within quantized lattice excitation spectra. Ashcroft, during 1968, highlighted Hydrogen (H), known for its high-frequency phonons and a strong electron-phonon interaction in its condensed form (Shylin, S., 2017). As a result, the quest for conventional superconductors with high or even room-temperature superconductivity appears promising, as the Ginzburg interpre-

tation of BCS theory does not impose any formal limits on T_c. It was later anticipated that under pressure, hydrogen would undergo a transformation into a metallic super fluid liquid, a state that is likely to exhibit superconductivity (Shylin, S., 2017).

The metallization of hydrogen under high pressure (up to 300 GPa) and low temperatures (below 100 K) was not confirmed by experimental results (Shylin, S., 2017). Through the use of a diamond-anvil cell at room temperature, Eremets et al. showed that at pressures exceeding 200 GPa, the Raman vibration bands of hydrogen broadened and significantly shifted toward the low-frequency region, indicating pronounced intermolecular interactions (Shylin, S., 2017).

Hydrogen starts to metallize at pressures above 220 GPa, and at 260 GPa, it demonstrates metallic conductivity. The occurrence of a reverse transition at 200 GPa points to a hysteresis phenomenon at 60 GPa, in the context of the first phase transition. Advanced computational methods have predicted that hydrogen could become a critical temperature (T_c) ranging from 50 to 240 K for hydrogen, and roughly 300 to 350 K in the atomic phase at 500 GPa. However, studying electrical properties under such extreme pressures is highly challenging. Quantum chemical calculations have also suggested That hydrogen, along with hydrogen compounds such as SiH_4 and SnH_4 (hydrides of group IV elements), could exhibit superconductivity under high-pressure conditions (Shylin, S., 2017).

2.11.1 Alkali Metal Hydrides

Even with the relatively high Tc values in Cu and Fe-based superconductors. The Tc value remains well below 300K. Thus far, only lithium hydrides and potassium hydrides with hydrogen content greater than one have been predicted to exhibit superconductivity under pressure among the alkali metal hydrides (Jones.H, et al., 2008). LiH_2 and LiH_6 are insulating at 60GPa but become metallic around 100GPa. Their Tc are 38K for lithium hexa-hydride at 150GPa and 31K for lithium octa-hydride at 100GPa, mainly due to H_2 vibrations. While Tc increases with P for LiH_6, it remains nearly constant for Lithium octa-hydride (Jones.H,et al.,2008).

2.11.2 Alkaline Earth Metal Hydrides

Hydrides of alkaline earth metals, excluding strontium hydrides with n greater than 2, are predicted to exhibit high superconducting transition temperatures (Nishijima.S, 2013). Notably, the Tc of calcium hexahydride reaches between 220 and 235 K at 150 GPa, primarily due to the H_4 units (Narlikar.A., 2004). The metallic phases of magnesium tetrahydride and magnesium dodecahydride demonstrate superconductivity with Tc ranging from 29 to 37 K at 100 GPa and from 47 to 60 K at 140 GPa, respectively. Although both compounds have similar electron-phonon coupling (λ), the average logarithmic frequency of magnesium dodecahydride is greater than that of magnesium tetrahydride.

As a result, the Tc for magnesium decahydride is higher than that of magnesium tetrahydride. Recent theoretical studies have indicated that under compression, the stoichiometries of calcium tetrahydride, calcium hexahydride, and calcium decahydride become energetically stable (Tinkham, M., et al., 1988). Additional calculations show that the electron-phonon coupling (λ) and Tc are 2.69 and between 220 - 235 K at 150 GPa, respectively. The Tc value decreases as pressure increases (Morel.P and Anderson.P.W., 1962).

2.11.3 Hydrides of the Boron Group Elements

All boron group hydrides, except Tl, have been thoroughly investigated. The estimated Tc for diboron hexahydride and borane are 125 K and in the range of 14.1 K to 21.4 K, respectively, at high pressures (Ashcroft,N.W et al., 1748). Several studies have explored aluminum hydride, though its superconductivity remains a topic of debate. Gallium hydride stabilizes above 160 GPa, with a calculated superconducting transition temperature of 86 K (Drozdov, A.P., et al., 2015). In the case of indium hydrides, the superconducting transition temperatures of rhombohedral indium hydride and monoclinic indium hydride at 200 GPa and 150 GPa are in the ranges of 34.1 - 40.5 K and 22.4 - 27.1 K, respectively (Bednorz, J.G, et al., 1986). Aluminum hydride has received significant attention in high-pressure studies, and its superconducting properties have been extensively examined. For the Pm-3n phase of aluminum hydride, the superconducting transition temperature was

predicted to be 24 K at 110 GPa, but experimental confirmation of superconductivity was not achieved (Goncharenko I, et al., 2008).

2.11.4 Carbon Group Hydrides

The notion of chemical precompression was first proposed by doping hydrogen and its hydrides with IV-A group elements. Since then, hydrides composed of carbon group elements have remained a central focus of investigation. However, methane did not show favorable results in this context (Zhang LJ, Wang YC, Zhang X, et al., 2010). First-principles calculations confirmed that methane would not undergo metallization, even at pressures as high as 520 GPa (Zhang LJ, Wang YC, Zhang X, et al., 2010). However, there have been numerous studies suggesting that hydrides of other elements from the carbon group, such as silicon, germanium, tin, and palladium, may undergo metallization and potentially show superconductivity under pressure.

2.11.5 Phosphine, PH_3

Superconductivity was detected in phosphine following its liquefaction and compression elevated pressure conditions achieved using a DAC. Resistance measurements revealed Tc of 30 K at 83 GPa, which rose to 103 K at 207 GPa. Because phosphine behaves as a covalent hydride in normal conditions, the hydrogen atoms are already chemically compressed (Struzhkin, V. V., 2015). At these pressure levels, the phase behavior of phosphorus hydrides, from mono- to hexahydrides, was explored by different research groups using DFT (Struzhkin, V. V., 2015). The historical trends in T_c for various conventional and hydrogen based superconductors are shown in Figure 2.3.

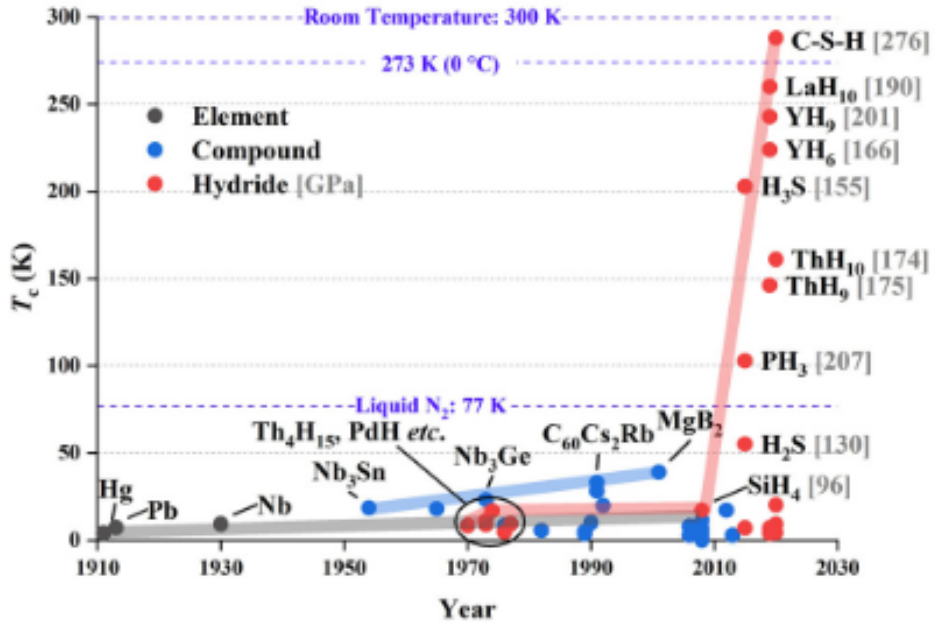

Figure 2.3: Chronological evolution of superconducting critical temperature (T_c) for various conventional superconductors (Lv, J., Sun, Y., Liu, H., & Ma, Y., 2020).

2.12 Phonon

Phonon represents the collective motion of atoms in a solid, behaving like a quasi-particle that carries energy and momentum (Blakemore, J. S., 1985). Phonon behavior plays a vital role in determining the heat transport, strength, characteristics of solids (Andreoni, W., & Yip, S., 2020). They can be broken down into various modes, with each mode corresponding to a particular energy (Smain, T. et al., 2024).

A unit cell containing N atoms possesses a total of 3N vibrational degrees of freedom, representing collective atomic vibrations. Phonons are categorized into acoustic and optical types. Acoustic phonons, consisting of three modes, exhibit low frequencies that approach zero at the BZ and correspond to long-wavelength vibrations where adjacent atoms move in phase. These are further subdivided into longitudinal (LA) and transverse (TA) modes, The direction of atomic vibrations whether longitudinal or transverse relative to the direction of wave propagation.

Optical phonons, which include $3N - 3$ modes, Possess greater vibrational rates and include adjacent atoms moving moving with a phase difference. Like acoustic phonons,

optical phonons are categorized into longitudinal optical (LO) or transverse optical (TO) modes based on the direction of oscillation. The characteristics of each mode can be analyzed by examining atomic displacements at the Γ point in reciprocal space. The angular frequencies of phonons (ω_q) can be calculated by analyzing the corresponding equations of motion for each wave vector q.

The phonon angular frequencies (ω_q) are obtained by solving the coupled equations of motion for each wave vector q as described by Hung, N. T. et al., (2022).

$$\sum_j D_{i\alpha,j\beta}(q)u_{j\beta}(q) = \omega_q^2 u_{i\alpha}(q) \quad (i_\alpha = 1, \ldots, 3N), \tag{2.46}$$

Here, N denotes atoms in the primitive cell; $\alpha(\beta)$ are spatial directions, and $u_{i\alpha}$, $u_{j\beta}$ describe respective atomic displacements.

$$D_{i\alpha,j\beta}(q)u_{j\beta}(q) = \frac{1}{\sqrt{M_i M_j}} F_{i\alpha,j\beta}(q) \tag{2.47}$$

The mass of the i^{th} and j^{th} atoms is denoted by M_i and M_j, E_{tot}, $(u_{i\alpha}, u_{j\beta})$ represents the IFC, symbolized as $F_{i\alpha,j\beta}$, is given by (Hung, N. T. et al., 2022).

$$F_{i\alpha,j\beta}(q) = \frac{\partial^2 E_{tot}}{\partial u_{i\alpha}(q)\partial u_{j\beta}(q)} \tag{2.48}$$

2.13 Phonons in Superconductivity and Thermal Transport

In conventional superconductors, phonons mediate the Mutual attraction involving electrons, Causing electrons to bind as Cooper pairs a fundamental mechanism (Bardeen et al., 1957). As electrons move through the lattice, they induce local distortions, generating phonons that attract other electrons and help overcome their natural repulsion. The strength of this interaction, known as the EPC constant, directly influences the superconducting Tc (Drozdov et al., 2019). Additionally, the PhDOS plays a crucial role in increasing EPC, significantly impacting Tc (Lugovskoi et al., 2019).

Materials with strong electron-phonon interactions, such as high-pressure hydrides, exhibit record-high Tc, demonstrating the profound influence of phonon dynamics on su-

perconductivity. Beyond superconductivity, phonons also a role particularly in semiconductors and insulators where electronic contributions to thermal conductivity are negligible (Tanaka, 2020). The effectiveness of phonon-mediated thermal energy flow is governed by their propagation and scattering mechanisms (Cahill et al., 2003). At elevated temperatures, phonon-phonon scattering becomes the dominant factor limiting thermal transport due to the anharmonic nature of interatomic interactions (Cahill et al., 2003). To control heat conduction, nanostructuring techniques such as introducing interfaces, defects, and engineered boundaries are widely employed. These approaches enhance phonon scattering, reducing thermal conductivity for improved thermoelectric performance while optimizing heat dissipation in microelectronics (Mahan et al., 1997).

2.14 Lattice Thermal Conductivity in Materials

When a thermal gradient is present, energy is transferred through diffusion of particles, convective currents, and emission of radiation (Müller, P. M., 2018).

As a result of the relatively low presence of free carrier, lattice vibration dominate the heat conduction in semiconductors (Srivastava.P.G, et al., 1990) thus, only phonon-mediated heat transport is relevant. Fourier's law provides the macroscopic definition of the thermal conductivity κ, which is represented as a second-order tensor (Czycholl.G, et al.,2008).

$$\mathbf{Q} = -\kappa \nabla T. \tag{2.49}$$

Heat transfer rate per unit area $\mathbf{Q}$ arises as a result of the presence of a thermal energy per particle T gradient ∇T, representing a non-equilibrium thermal process. When the temperature variation is sufficiently small over a local region, the formulation of heat flux can be expressed through the sum of phonon mode contributions (Müller, P. M.,2018).

$$\mathbf{Q} = \frac{1}{NV_0} \sum_{q,s} \hbar\omega_{qs} \left(n_{qs}(T)\right) \mathbf{v}_{qs}, \tag{2.50}$$

with N indicating the total count of unit cells V_0 denotes the spatial extent of an individual primitive cell, and $\hbar$ signifies the normalized Planck's constant, cell, $\hbar$ is the reduced

Planck constant, ω_{qs} stands for the vibrations of the phonon mode labeled by q and s, and $n_{qs}(T)$ indicates the phonon population at temperature (T). The symmetrical nature of the phonon dispersion relation results in an antisymmetric behavior of the group velocity (Müller, P. M.,2018).

Thus, under equilibrium conditions with a symmetric phonon occupation number $\langle n^0_{qs}\rangle = \langle n^0_{-qs}\rangle$, the net heat flux averages out to zero. A non-zero thermal flux can only emerge when the symmetry in the phonon momentum distribution is disrupted $\mathbf{q}$ since the Bose-Einstein distribution remains symmetric within the harmonic approximation, incorporating anharmonic effects becomes essential to induce asymmetry in the phonon population and enable a finite thermal flux. This asymmetry is introduced via a mode-specific correction term,which modifies the equilibrium phonon distribution (Müller, P. M.,2018).

$$\langle n_{qs}\rangle = \langle n^0_{qs}\rangle + \eta_{qs}. \tag{2.51}$$

The phonon distribution $\langle n_{qs}\rangle$ can be expressed as:

$$\langle n_{qs}\rangle = \frac{1}{\exp\left(\frac{\hbar\omega_{qs}}{k_B T} - \eta_{qs}\right) - 1}. \tag{2.52}$$

By expanding it in terms of the deviation η_{qs}, we obtain:

$$\langle n_{qs}\rangle = \langle n^0_{qs}\rangle - \left.\frac{\partial\langle n_{qs}\rangle}{\partial\eta_{qs}}\right|_{\eta_{qs}=0} \eta_{qs} + O(\eta^2_{qs}), \tag{2.53}$$

where $\langle n^0_{qs}\rangle$ is the equilibrium Bose-Einstein distribution. Substituting for the derivative, the expression becomes:

$$\langle n_{qs}\rangle = \langle n^0_{qs}\rangle + \eta_{qs}\frac{k_B T^2}{\hbar\omega_{qs}}\frac{\partial\langle n^0_{qs}\rangle}{\partial T} + O(\eta^2_{qs}). \tag{2.54}$$

The Taylor series expansion is limited to the first-order term, assuming that deviations from equilibrium are minimal. The non-equilibrium phonon distribution must satisfy the following conditions (Müller, P. M., 2018):

$$-\mathbf{v}_{qs}\nabla T\frac{\partial\langle n_{qs}\rangle}{\partial T}=-\frac{\partial\langle n_{qs}\rangle}{\partial t}\bigg|_{\text{scattering}}. \tag{2.55}$$

Eq(2.56) represents the spread of the distribution due to the applied temperature gradient. The right-hand side describes the alteration of the distribution due to scattering processes. At thermal equilibrium, where the phonon occupation numbers are symmetrical, i.e., $\langle n^0_{\mathbf{q}s}\rangle = \langle n^0_{-\mathbf{q}s}\rangle$, the resulting average thermal flux equals zero. A nonzero net thermal flux can only arise when the symmetry of the phonon distribution with respect to $\mathbf{q}$ is disturbed, so that $\langle n_{\mathbf{q}s}\rangle \neq \langle n_{-\mathbf{q}s}\rangle$. Since the Bose-Einstein distribution maintains symmetry within the harmonic approximation, it is essential to incorporate anharmonic effects to disrupt this symmetry and enable a nonzero heat flux. This symmetry disruption is introduced by applying a mode-dependent adjustment $\eta_{\mathbf{q}s}$, which alters the phonon distribution in the following manner:

$$\eta_{q's'}=0 \quad \text{for} \quad q's'\neq qs.$$

The scattering term for the rate at which the phonon occupation number changes can be approximated as:

$$\frac{\partial\langle n_{qs}\rangle}{\partial t}\bigg|_{\text{scattering}}\approx\frac{\langle n_{qs}\rangle-\langle n^0_{qs}\rangle}{\tau_{qs}}\approx\frac{\eta_{qs}}{\tau_{qs}}\frac{k_BT^2}{\hbar\omega_{qs}}\frac{\partial\langle n^0_{qs}\rangle}{\partial T}.$$

In the final step, the truncated Eq. (2.55) was substituted, and the relaxation time τ_{qs} was introduced. By using Eqs. (2.56) and (2.57), an expression for η_{qs} can be derived. This expression is then inserted into the phonon occupation number, which is subsequently substituted into Eq. (2.51) (Müller, P. M., 2018). The heat flux can be written as:

$$Q=-\frac{1}{V_0}\sum_{q,s}\frac{(\hbar\omega_{qs})^2}{k_BT^2}\tau_{qs}\langle n^0_{qs}\rangle\big(\langle n^0_{qs}\rangle+1\big)\boldsymbol{\nu}_{qs}\otimes\boldsymbol{\nu}_{qs}\nabla T. \tag{2.56}$$

By comparing this with Fourier's law, Eq. (2.50) gives the following expression for

thermal conductivity:

$$\kappa = \frac{1}{V_0}\sum_{q,s}\frac{(\hbar\omega_{qs})^2}{k_B T^2}\tau_{qs}\langle n^0_{qs}\rangle\big(\langle n^0_{qs}\rangle + 1\big)\boldsymbol{\nu}_{qs}\otimes\boldsymbol{\nu}_{qs} = \frac{1}{V_0}\sum_{q,s}\tau_{qs}c_{qs}\boldsymbol{\nu}_{qs}\otimes\boldsymbol{\nu}_{qs}. \tag{2.57}$$

To compute a scalar value, the thermal conductivity is determined as (Müller, P. M., 2018):

$$\kappa = \frac{1}{3}\,\mathrm{Tr}(\kappa).$$

The specific heat for each phonon mode, c_{qs}, is determined using equation (2.59), and the wave velocity ν_{qs} can be calculated using the harmonic assumption. The heat capacity at fixed volume, c_V, is then represented by (Lin, Y. H. et al., 2019):

$$c_V = \frac{1}{V}\frac{\partial E}{\partial T}\bigg|_V = \frac{1}{V}\sum_{q,s}k_B\left(\frac{\hbar\omega_{qs}}{k_B T}\right)^2\frac{\exp\left(\frac{\hbar\omega_{qs}}{k_B T}\right)}{\left(\exp\left(\frac{\hbar\omega_{qs}}{k_B T}\right)-1\right)^2}. \tag{2.58}$$

Based on Matthiessen's principle, the total inverse relaxation time is the sum of the separate scattering contributions:

$$\frac{1}{\tau_{qs}} = \frac{1}{\tau_{qs}^{\text{boundary}}} + \frac{1}{\tau_{qs}^{\text{mass defect}}} + \frac{1}{\tau_{qs}^{\text{phonon-phonon}}}. \tag{2.59}$$

In this analysis, boundary scattering is neglected under the assumption of an infinitely large crystal. Similarly, mass defect scattering is not considered, assuming a perfect crystal structure. Under these conditions, the relaxation time is approximated by the phonon lifetime (Müller, P. M., 2018). Nevertheless, under the harmonic approximation, the phonon lifetime becomes limitless due to the absence of scattering processes, resulting in an infinite mean free path (Müller, P. M., 2018). However, when anharmonic effects are incorporated, the phonon lifetime can be determined from the imaginary component of the self-energy, Γ_{qs} (Müller, P. M., 2018):

$$\tau_{qs} = \frac{1}{2\Gamma_{qs}}. \tag{2.60}$$

The imaginary contribution to the self-energy, Γ_{qs}, is given by (Wallace, C. D., 1972):

$$\begin{aligned}\Gamma_{qs} = \frac{18\pi}{\hbar^2}\sum_{s',s''}\int |\Psi_{s,s',s''}(\mathbf{q},\mathbf{q}',\mathbf{q}'')|^2 \Big\{ \\ \big(\langle n^0_{qs'}\rangle + \langle n^0_{qs''}\rangle + 1\big)\delta(\omega_{qs} - \omega_{qs'} - \omega_{qs''}) \\ + \big(\langle n^0_{qs'}\rangle - \langle n^0_{qs''}\rangle\big)\delta(\omega_{qs} + \omega_{qs'} - \omega_{qs''}) \\ + \big(\langle n^0_{qs''}\rangle - \langle n^0_{qs'}\rangle\big)\delta(\omega_{qs} + \omega_{qs''} - \omega_{qs'})\Big\},\end{aligned} \tag{2.61}$$

where the Fourier-transformed third-order potential constants $\Psi_{s,s',s''}(\mathbf{q},\mathbf{q}',\mathbf{q}'')$ are given by (Müller, P. M., 2018):

$$\begin{aligned}\Psi_{s,s',s''}(\mathbf{q},\mathbf{q}',\mathbf{q}'') =& \frac{1}{3!}\left(\frac{\hbar}{2N}\right)^{\frac{1}{2}} \frac{1}{\sqrt{\omega_{qs}\omega_{qs'}\omega_{qs''}}} \\ &\times \sum_{IJK}\sum_{\alpha\beta\gamma}\Psi_{IJK,\alpha\beta\gamma}\sqrt{\frac{1}{M_I M_J M_K}} e^{i\mathbf{q}\cdot\mathbf{R}_I} e^{i\mathbf{q}'\cdot\mathbf{R}_J} e^{i\mathbf{q}''\cdot\mathbf{R}_K} \\ &\epsilon_{ls\alpha}(\mathbf{q})\epsilon_{js'\beta}(\mathbf{q}')\epsilon_{ks''\gamma}(\mathbf{q}').\end{aligned} \tag{2.62}$$

The eigenvectors $\epsilon_{ls\alpha}(\mathbf{q})$ are obtained from the dynamical matrix. Finally, the force constants $\Psi_{IJK,\alpha\beta\gamma}$ can be computed through force calculations using the supercell and the finite difference approach (Müller, P. M., 2018).

At high temperatures, the dominant contribution from phonons corresponds to an energy of approximately $\hbar\omega_{\max}$. If this approximation is extended to all phonon modes, the phonon occupation number becomes directly in direct correlation with the temperature T. Consequently, the relaxation time exhibits an inverse dependence on temperature, scaling as T^{-1}, which results in thermal conductivity behaving accordingly (Landau, and Lifschitz, 2001):

$$\kappa \propto \frac{1}{T}. \tag{2.63}$$

2.15 Semiclassical Transport Theory

The original BoltzTraP program introduced a numerically stable and efficient approach for deriving analytic representations of quasi-particle energies (Madsen,G.K., et al., 2006). This approach has been extensively utilized for solving the Boltzmann transport equation (BTE) across various fields, including superconductors (Singh,D.J., et al., 2008), transparent conductors (Madsen, G. K., et al., 2006), intermetallic phases and thermoelectrics (Dolinšek,J.,Komelj, M., et al., 2009). From a theoretical standpoint, determining the DOS relies solely on the band energy dispersion $E_{n,\mathbf{k}}$ throughout the Brillouin zone. The electron velocity within a given band structure is expressed as (Hao, S. et al., 2016):

The velocity of an electron in a band structure is given by:

$$v_i(n,\mathbf{k}) = \frac{1}{\hbar}\frac{\partial E_{n,\mathbf{k}}}{\partial k_i} \tag{2.64}$$

Here, $E_{n,\mathbf{k}}$ signifies the energy of band n at wavevector $\mathbf{k}$, $\hbar$ represents the reduced Planck constant, and k_i is the component of the wavevector. The BoltzTraP program computes the transport distribution function (TDF) by performing a Fourier expansion of the band energies derived from DFT computations. Subsequently, the electrical conductivity matrix $\sigma_{\alpha\beta}$ and the Seebeck coefficient matrix $S_{\alpha\beta}$ are obtained from the TDF using semi-classical equations derived from the Boltzmann transport equation within the relaxation time approximation (RTA) (Mamani Gonzalo, F. et al., 2024). The Seebeck coefficient matrix $S_{\alpha\beta}(T;\mu)$, the electrical conductivity matrix $\sigma_{\alpha\beta}(T;\mu)$, and the electronic thermal conductivity matrix $\kappa^{\mathrm{el}}_{\alpha\beta}(T;\mu)$ are represented as follows:

$$S_{\alpha\beta}(T;\mu) = \frac{1}{eT}\frac{\int \sigma_{\alpha\beta}(\epsilon)(\epsilon-\mu)\left[-\frac{\partial f(T;\epsilon)}{\partial\epsilon}\right]d\epsilon}{\int \sigma_{\alpha\beta}(\epsilon)\left[-\frac{\partial f(T;\epsilon)}{\partial\epsilon}\right]d\epsilon}, \tag{2.65}$$

$$\sigma_{\alpha\beta}(T;\mu) = \frac{1}{\Omega}\int \sigma_{\alpha\beta}(\epsilon)\left[-\frac{\partial f(T;\epsilon)}{\partial\epsilon}\right]d\epsilon, \tag{2.66}$$

The electronic thermal conductivity matrix $\kappa^{\mathrm{el}}_{\alpha\beta}$ is computed using the Wiedemann-Franz

law, expressed as follows (Mamani Gonzalo, F. et al., 2024):

$$\kappa_{\alpha\beta}^{\mathrm{el}}(T;\mu) = \frac{1}{e^2T^2}\int_{-\infty}^{\infty}\sigma_{\alpha\beta}(\epsilon)(\epsilon-\mu)^2\left[-\frac{\partial f(T;\epsilon)}{\partial\epsilon}\right]d\epsilon, \tag{2.67}$$

Additionally, the quantities above are defined in terms of the transport distribution function (TDF) $\Sigma_{ij}(E)$, given by

$$\Sigma_{ij}(E) = \frac{1}{V}\sum_{n,\mathbf{k}} v_i(n,\mathbf{k})v_j(n,\mathbf{k})\tau_{n\mathbf{k}}\delta(E-E_{n,\mathbf{k}}), \tag{2.68}$$

where the summation runs over all bands n and all wavevectors $\mathbf{k}$ within the Brillouin zone (BZ). Here, $E_{n,\mathbf{k}}$ signifies the energy of band n at wavevector $\mathbf{k}$, and $v_i(n,\mathbf{k})$ denotes the i-th component of the band velocity at $(n,\mathbf{k})$, as defined in Eqs. (2.65).

2.15.1 Phonon Boltzmann Equation (PBE)

The core principle of inherent lattice heat conduction κ^i in semiconductors and insulators was initially proposed by Peierls, 1929. Since that time, the Boltzmann transport theory has been widely applied to explore lattice thermal conduction in semiconducting substances. Within the relaxation time approximation (RTA), the lattice thermal conductivity matrix is expressed by equation (2.70) (Jakhar, M. et al., 2024):

$$\kappa_{\alpha\beta} = \frac{1}{k_BT^2NV}\sum_{\lambda}(\hbar\omega_\lambda)^2 f_\lambda^0(1+f_\lambda^0)\nu_\lambda^\alpha\nu_\lambda^\beta\tau_\lambda \tag{2.69}$$

In this equation, $\kappa_{\alpha\beta}$ refers to the components of the lattice thermal conductivity matrix, with the indices α and β representing spatial directions such as x, y, or z. The constant k_B denotes the Boltzmann constant, which relates temperature to energy, while T is the absolute temperature. The quantity N represents the total number of phonon modes present in the material, and V is the system volume. The summation index λ runs over all phonon modes. The reduced Planck constant $\hbar$ links energy to frequency, and ω_λ corresponds to the angular frequency of phonon mode λ. The term f_λ^0 represents the equilibrium phonon distribution, generally described by Bose-Einstein statistics. The quantity ν_λ^α denotes the α-direction component of the group velocity of phonon mode λ,

and τ_λ is the relaxation time for that mode, indicating the average time between scattering events. Figure 2.4 depicts the computational procedure employed to assess lattice thermal conductivity using the real-space supercell approach for calculating force constants.

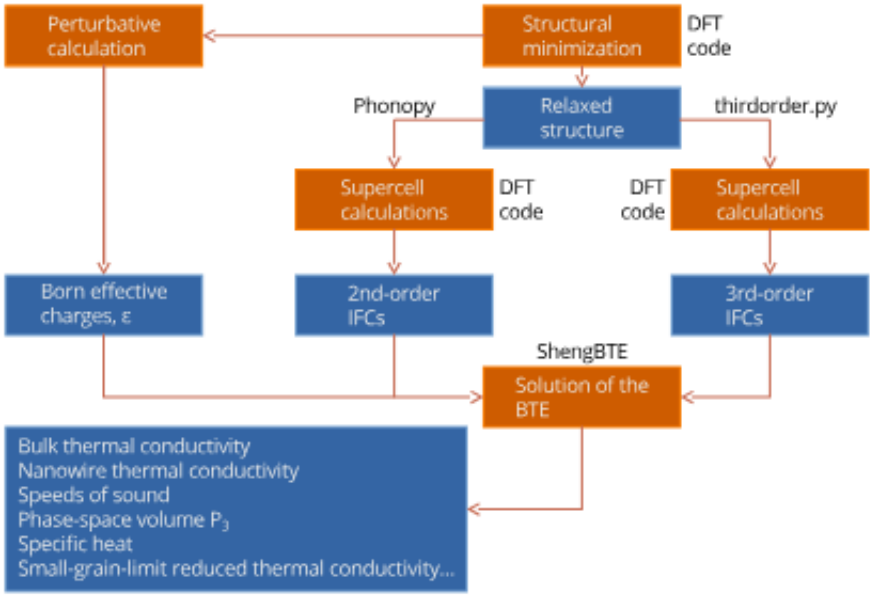

Figure 2.4: Procedure for calculating thermal conductivity using a real-space supercell method for force constants. Orange boxes illustrate the calculation steps, blue boxes indicate the outcomes of these steps, and software programs are represented as black text outside the boxes (Li, W., Carrete, J., Katcho, N. A., 2014).

2.16 Overview of the Figure of Merit (ZT)

The ability of a material to perform in thermoelectric applications is predominantly influenced by its dimensionless Figure of merit (Tritt, T. M., 2011).

$$ZT = \frac{S^2\sigma T}{\kappa} = \frac{S^2 T}{\rho\kappa}, \tag{2.70}$$

where the thermoelectric potential is denoted by S, σ is the electrical conductivity, ρ represents the electrical resistivity, and κ signifies the total thermal conductance. (Tritt, T. M., 2011):

$$\kappa = \kappa_p + \kappa_i, \tag{2.71}$$

Here, κ_p and κ_i are the contributions from vibrational thermal conductance and charge carrier thermal conductance, respectively. The energy conversion efficiency factor, $S^2\sigma T$ or equivalently $\frac{S^2 T}{\rho}$, is typically optimized through impurity inclusion in narrow-gap semiconductor materials as a function of carrier density (n) (generally approximately 10^{19} carriers cm^{-3}) to maximize the thermoelectric performance index (ZT) (Tritt, T. M., 2011). To maximize electrical conductance (σ) at a specific carrier density (n), carriers with high mobility are required. However, the ZT value of a single material has limited significance since practical thermoelectric systems or modules operate using several thermoelectric pairs. A thermoelectric pair comprises two distinct materials: an n-type and a p-type semiconductor, as illustrated in Figure 2.5.

Neglecting parasitic factors like contact resistance and radiative losses that degrade device efficiency, the effective ZT value for a thermoelectric couple can be expressed as:

$$ZT = \frac{(S_p - S_n)^2 T}{\left[(\rho_n\kappa_n)^{1/2} + (\rho_p\kappa_p)^{1/2}\right]^2}. \tag{2.72}$$

The thermoelectric potential of n-type charge carriers (S_n) is negative, while that of the positive charge carriers (holes) (S_p) is positive (Tritt, T. M., 2011). The performance factor (φ) during refrigeration operation and the thermoelectric performance (η_{TE}) during power generation are both intimately connected to the material's dimensionless merit index ZT.

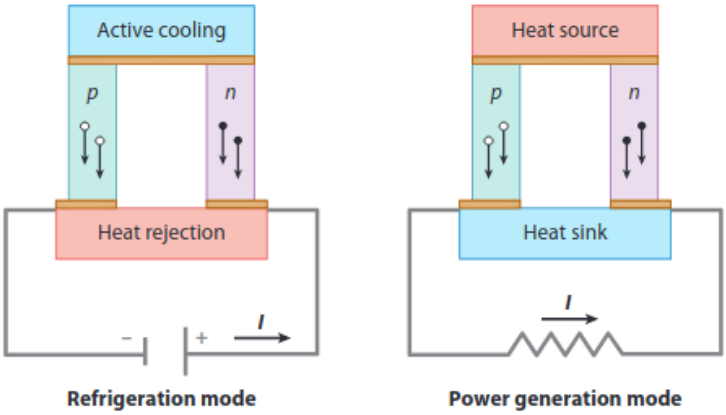

Figure 2.5: A general schematic of a thermoelectric pair composed of n-type and p-type thermoelectric materials (Sun, Y., Di, C. A., Xu, W., & Zhu, D. 2019).

This correlation is shown in Eq. (2.74) for the efficiency. Specifically, the thermoelectric performance (η_{TE}) of the thermoelectric pair is defined as the ratio of the electrical energy output (W) to the total thermal energy absorbed (Q_H), where Q_H denotes the thermal energy transferred from the hot reservoir to the cold sink:

$$\eta_{TE} = \frac{W}{Q_H} = \frac{T_H - T_C}{T_H} \left(\frac{(1 + ZT_M)^{1/2} - 1}{(1 + ZT_M)^{1/2} + T_C/T_H} \right), \tag{2.73}$$

Here, T_H represents the temperature on the hot side, T_C is the temperature on the cold side, and T_M denotes the average (mean) temperature. As a result, the thermoelectric performance (η_{TE}) is proportional to the Carnot efficiency (η_C), which is defined as:

$$\eta_C = \frac{T_H - T_C}{T_H}. \tag{2.74}$$

2.17 Approaches to Attain a High Efficiency Index

Over time, multiple methods have been utilized to enhance the merit measure (ZT) values in a variety of thermoelectric substances (Yang et al., 2018), with the most effective techniques concentrating on improving the electrical transport characteristics by optimizing charge carrier concentration (n) (Yang et al., 2018).

Sophisticated energy substances and band manipulation (Yang et al., 2018) can sepa-

rate electrical conductivity (σ) and Seebeck coefficient (S) to concurrently augment their values, thus attaining a high overall $S^2\sigma$. On the other hand, through nanoscale structure modification (Yang et al., 2018), thermal conductivity (κ) can be efficiently minimized without compromising the electrical transport properties of thermoelectric compounds (Yang et al., 2018), ultimately resulting in improved ZT.

2.17.1 Adjusting Carrier Concentration

Among all the factors that influence the thermoelectric behavior of substances, the Seebeck effect coefficient (S), electrical conductivity (σ), and electronic heat conductivity (κ_e) are intrinsically linked to charge carrier concentration (n) via the ensuing formulations (Chen et al., 2012):

$$S = \frac{8\pi^2 k_B^2}{3eh^2} m^* T \left(\frac{\pi}{3n}\right)^{2/3} \tag{2.75}$$

$$\sigma = \frac{1}{\rho} = ne\mu \tag{2.76}$$

$$\kappa_e = L\sigma T = ne\mu LT \tag{2.77}$$

Where m^* signifies the effective mass of the charge carrier, ρ denotes the electrical resistivity, e represents the elementary charge of an electron, k_B stands for the Boltzmann constant, μ indicates the carrier mobility, and L is the Lorenz constant. Such associations imply that n needs to be optimized to achieve both high electrical conductivity (σ) and thermoelectric power (S), while simultaneously minimizing the electronic thermal conductance (κ_e), making the regulation of n an essential approach for attaining elevated figure of merit (ZT) values.

2.17.2 Manipulating the Band Structure

The electrical conduction characteristics of a substance are primarily controlled by its electronic band configuration. Therefore, altering the electronic band structure is a vital approach to improve thermoelectric efficiency. By tuning the band gap, carrier concentration, and effective mass of the charge carriers, the electrical properties can be optimized for better performance. Additionally, the interaction between electrons and phonons within

the material can be manipulated through band engineering, further enhancing the material's thermoelectric response. Advanced techniques such as doping, strain engineering, and quantum confinement can be strategically used to tune the electronic band structure, which in turn can enhance the thermoelectric performance of materials, particularly by improving the ZT. In thermoelectric materials, the main methods of band structure engineering include: (1) enlarging E_g (Pei et al., 2011) to stabilize n; (2) tuning the effective mass (m^*) or achieving a resonant state in the proximity of the Fermi level (Heremans et al., 2012) to increase the Seebeck coefficient; and (3) achieving band convergence (Hong et al., 2016) to enhance the Seebeck coefficient (S) (Pei et al., 2011).

2.17.3 Tuning the Band Gap

At increased temperatures (T), thermal activation of minority charge carriers can augment the overall charge carrier density (n), which in turn diminishes (ZT) value. This happens because of a reduction in the thermopower (S) and a rise in the electronic component of heat conductivity (κ_e), as illustrated in Eqs. (2.76) and (2.78). Both theoretical (Boukhris et al., 2011) and empirical (Zhao et al., 2014) analyses demonstrate that the energy bandgap (E_g) of semiconductors can be efficiently adjusted by introducing dopants, and the widened Changes in (E_g) can modulate the thermal activation energy required for carrier excitation threshold of minority carriers to higher temperatures, thereby mitigating their impact (Zhu et al., 2017). Such doping techniques facilitate the fine-tuning of thermoelectric performance by regulating the concentration and thermal excitation of carriers, thereby enhancing the ZT values at elevated operating temperatures.

For instance, introducing Cd into PbTe (Pei et al., 2012) can increase the band gap (E_g), an increase in the band gap (E_g) shifts the thermal excitation of minority charge carriers to higher temperatures, thereby suppressing their contribution at lower temperatures, while also stabilizing the carrier concentration (n) in doped PbTe at elevated temperatures. The minority charge carriers also contribute to heat conduction, leading to bipolar thermal conductivity (κ_{bi}) (Bahk & Shakouri, 2014), which diminishes the value of ZT depends on the band gap (E_g) and temperature (T) (Bahk & Shakouri, 2014).

2.17.4 Tuning Effective Mass

For a specific carrier concentration (n), increasing the apparent mass of charge carriers in a crystal lattice (m^*) results in a higher Seebeck coefficient (S). The strategy for enhancing the effective mass (m^*) through doping involves boosting the apparent mass of charge carriers in a crystal lattice associated with a single valley in the band (m_b^*)(Pei et al., 2011).

$$m^* = N_v^{2/3} m_b^* \tag{2.78}$$

where N_v signifies the band degeneracy. Nevertheless, enhancing the effective mass (m^*) causes a decline in carrier mobility (μ), following the relationship provided by Pei, Y., Shi, X., LaLonde, A., et al., 2011.

$$\mu \propto m_b^{*-5/2} \tag{2.79}$$

Consequently, $S^2\sigma$ may be lowered due to the reduction in electrical conductivity (σ), as shown in Equation (2.77). This indicates that a higher effective mass (m^*) does not always correspond to an improved thermoelectric (ZT) (Pei et al., 2011). As the Fermi level moves closer to the resonant state, the effective mass (m^*) dramatically increases, driven by the enhanced density of states (DOS) (Heremans et al., 2012), which in turn results in an increased Seebeck coefficient, while the carrier concentration (n) remains unaffected (Pei et al., 2012). Figure 2.6 presents the workflow for evaluating the ZT, based on first-principles calculations rooted in DFT.

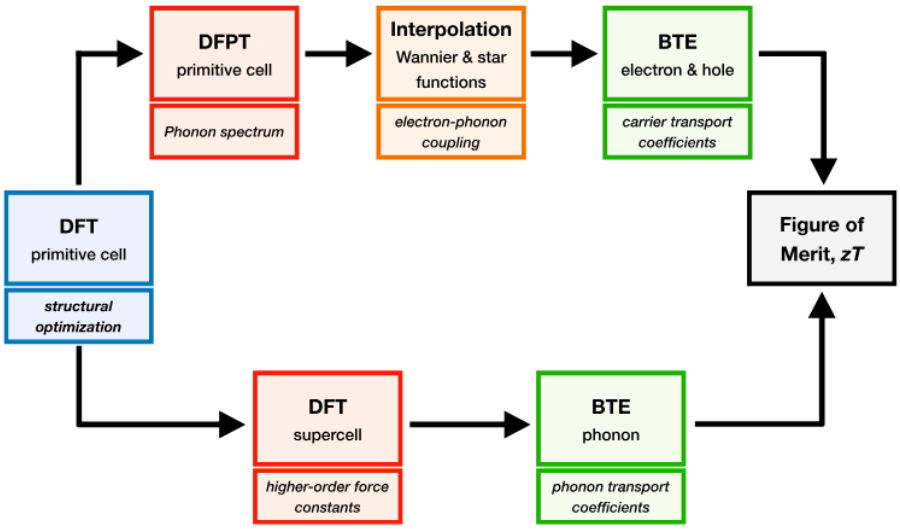

Figure 2.6: illustration of the simulation procedure employed to estimate the thermoelectric performance metric, ZT, through techniques derived from density functional theory (Chaves, A. S., Pizzochero, M., Larson, D. T., Antonelli, A., & Kaxiras, E., 2023)..

2.18 Optical properties

When electromagnetic radiation interacts with matter, various effects such as transmission, reflection, and scattering occur. At the microscopic level, photons interact with the electrons in the material, determining its optical features. These features are commonly divided into absorption, emission, and scattering. In semiconductors, both absorption and emission are governed by the energy of the incoming photons. When a photon's energy surpasses the semiconductor's band gap, it can excite an electron from the valence band to the conduction band, resulting in absorption.

The dielectric function shows the way a material reacts to an electromagnetic field, affecting its polarization and capacity to accumulate electrical energy (Kumar et al., 2009).

$$\epsilon(\omega) = \epsilon_1(\omega) + i\epsilon_2(\omega) \tag{2.80}$$

In this framework, $\varepsilon(\omega)$ expresses the frequency-dependent linear response of electrons and their optical transitions to incident photons. The real component $\varepsilon_1(\omega)$ corresponds to the polarizability of the crystal's electronic structure, while the imaginary part $\varepsilon_2(\omega)$ indicates energy dissipation. The imaginary part is obtained through momentum matrix

elements between occupied and unoccupied states across the first Brillouin zone, as noted by Okoye (2004). Additionally, using the Kramers-Kronig relation, one can derive the real part from the imaginary one for all positive frequencies, as discussed by Wu et al. (2016).

These dielectric components collectively determine a material's optical response to electromagnetic radiation, influencing its reflectivity, absorption coefficient, and energy-loss spectrum. In semiconductors and insulators, the onset of $\varepsilon_2(\omega)$ typically corresponds to the threshold for interband transitions, and its peak structure reveals details about the band structure and critical points. Meanwhile, $\varepsilon_1(\omega)$ governs light propagation and refractive index behavior, playing a key role in device applications such as photovoltaics and photodetectors.

$$\epsilon_2(\omega) = \frac{\pi e^2}{\epsilon_0 V}\frac{1}{q^2}\left[\psi_k e^{-iq\cdot r}\psi_{k'}\right]^2 \tag{2.81}$$

The variable e is used to express the negative charge associated with an electron ε_0 denotes the electric constant in free space V represents volume corresponding to a single unit cell, while q refers to the momentum shift during interaction, and k is the wave vector, with $k_0 = k + q$.

$$\epsilon_1(\omega) = 1 + \frac{2}{\pi}P\int \frac{\omega'\epsilon(\omega')}{\omega'^2 - \omega^2}d\omega' \tag{2.82}$$

The relative permittivity (ε) correlates with the square of the refractive index (N), which in turn is defined by the proportion of the light velocity in vacuum (c) to its propagation speed in a material (v), expressed as $\varepsilon = N^2$. This implies that the optical behavior of a material, such as how much it slows down electromagnetic waves, is directly governed by its dielectric response. The optical characteristics of a material are directly influenced by its dielectric constant, as described by equation (2.84).

$$N = \sqrt{\epsilon} = n + ik \tag{2.83}$$

Measurable optical properties such as the absorption coefficient (α) and reflectance (R) are commonly observed (Beal et al., 1976). These quantities provide valuable insights into how light interacts with the material. Once the complex dielectric function is acquired,

it allows for the calculation of both the absorption and reflectivity, using the formulas provided in Equations (2.85) and (2.86), respectively. This makes it possible to link microscopic material properties to macroscopic optical behaviors, such as the interaction of light with the material at different wavelengths.

$$\sigma = \frac{2\kappa\omega}{c} \tag{2.84}$$

$$r = \frac{(n-1)^2 + \kappa^2}{(n+1)^2 + \kappa^2} \tag{2.85}$$

which serves as the basis for computing n and κ through Eq.(2.86). These parameters are pivotal for analyzing the optical characteristics of the material, such as its light absorption and reflection properties.

$$n^2 = \frac{1}{2}\left([\epsilon_1^2 + \epsilon_2^2]^{\frac{1}{2}} + \epsilon_1\right); \quad \kappa^2 = \frac{1}{2}\left([\epsilon_1^2 + \epsilon_2^2]^{\frac{1}{2}} - \epsilon_1\right) \tag{2.86}$$

Eq.(2.87) shows that the imaginary part of the inverse dielectric tensor is directly linked to the loss spectrum of the material.

$$\mathrm{Im}\left[\frac{1}{\epsilon(\omega)}\right] = \frac{\epsilon(\omega)}{\epsilon_1^2 + \epsilon_2^2} \tag{2.87}$$

The non-imaginary portion associated with dielectric response or in other words, the complex-valued permittivity evaluated at imaginary angular frequencies $\epsilon(i\omega)$, is computed by applying using the causality-based relations,as illustrated in equation (2.89). This approach allows for the determination of the dielectric behavior as a function of frequency using known optical data.

$$\epsilon(i\omega) = 1 + \frac{2}{\pi}\int \frac{\omega'\epsilon_2(\omega')}{\omega'^2 + \omega^2} d\omega' \tag{2.88}$$

3

Materials and Methods

In this study, first-principles computations were carried out using Density Functional Theory (DFT), utilizing the Quantum ESPRESSO software package (Giannozzi et al., 2009, 2017). The Generalized Gradient Approximation `GGA` and `GGA+U` methods, in conjunction with the Perdew-Burke-Ernzerhof (PBE) exchange-correlation functional, were applied to model electron interactions.

The `GGA+U` approach was employed to more effectively consider on-site Coulomb interactions in confined d or f orbitals, where conventional `GGA` often underestimates electron interactions. By introducing a Hubbard `U` constant, `GGA+U` enhances the portrayal of intensely correlated systems for Y and La, and provides more precise electronic configurations for those materials with localized electrons.

First, convergence tests were conducted for k-points, cutoff energy (ecut), and lattice parameters. Subsequently, a variable-cell relaxation (vc-relax) calculation was performed. After performing structural optimization, self-consistent field (SCF) and non-self-consistent field (NSCF) calculations were conducted using a finer k-point mesh to improve the accuracy of the electronic structure. Following this, post-processing (PP) calculations were applied to derive the properties of YHSe. The electronic band structure was calculated along high-symmetry paths in the Brillouin zone: Γ-M-K-Γ-A-L-H.

Atomic positions within the crystal structure were optimized using the Broyden-Fletcher-Goldfarb-Shanno (BFGS) algorithm (Broyden, 1970; Fletcher, 2000; Goldfarb, 1970; Shanno, 1970) an iterative method that finds stationary points on the potential energy surface, corresponding to equilibrium atomic configurations. The total energy was calculated using the self-consistent field (SCF) approach, while forces were derived using the Hellmann-Feynman theorem.

Atomic positions were iteratively refined until the changes in energy and the components of the forces dropped below predefined convergence criteria. With the optimized

YHSe structure, the band structure, density of states (DOS), and other properties of YHSe were calculated. The DOS was computed using a finer k-point mesh compared to the self-consistent calculations, utilizing the tetrahedron method for precise integration over the Brillouin zone. The `Dos.x` utility was employed to process the extracted states. Additionally, the partial density of states (PDOS) was examined to assess the contributions from specific atomic orbitals.

A 12×12×12 k-point mesh was employed for Brillouin zone integration after performing convergence testing. The density of states (DOS) was calculated on a 24×24×24 k-point grid, while 350 k-points were used for band structure calculations. The plane-wave energy cutoff and charge density cutoff were set to 100 Ry and 400 Ry, respectively. The force and electronic convergence thresholds were fixed at 10^{-5} and 10^{-7} Ry, respectively. Norm-conserving pseudopotentials were utilized for both pristine and La-doped YHSe calculations.

For La doping, a 2×2×2 supercell was constructed, with 12.5%, 25%, 37.5%, and 50%, of the Y atoms replaced by La. The real and imaginary components of the dielectric function were calculated using momentum matrix elements and the Kramers-Kronig relations (Jia et al., 2019). A dense k-point mesh of 350 and 500 points within the irreducible Brillouin zone were employed for optical property calculations.

Superconducting characteristics were examined using Density Functional Perturbation Theory (DFPT), as implemented in Quantum ESPRESSO (Baroni et al., 2001). The matrix components for electron-phonon interaction were calculated on a 4×4×4 q-point grid, while separate electron-phonon interactions were assessed using a 32×32×32 k-point grid.

The thermoelectric characteristics of both pristine and La-doped YHSe were examined using `Quantum ESPRESSO` in combination with the `BoltzTraP` code. After completing the self-consistent field (SCF) calculation, a non-self-consistent field (NSCF) calculation was carried out using a finer **k**-point mesh to obtain more precise eigenvalues necessary for thermoelectric analysis. The results from the non-SCF calculation were then transformed into a `BoltzTraP`-compatible input file. Following this, thermoelectric parameters were determined using the `x_trans` command in `BoltzTraP`.

This method facilitated the evaluation of essential thermoelectric characteristics of both pristine and La-doped YHSe compounds. The phonon contribution to thermal conductivity was calculated using the RTA with the tetrahedron method, employing second and third-order force constants. These force constants were obtained through supercell displacements using the `Phono3py` software within a finite displacement framework.

The phonon band structure, $\omega(\mathbf{q})$, and the phonon DOS were calculated using supercell displacements with the `Phonopy` software. Additionally, various computational tools were used to assist with structural visualization, data processing, and graphical analysis. `XCrySDen` and `VESTA` were employed for visualizing crystal structures and generating supercells. These tools played a crucial role in analyzing the geometric characteristics of the materials, enabling the manipulation of atomic positions and the creation of supercells necessary for studying the material properties.

For graphical representation of the results, `Xmgrace` and `Gnuplot` were utilized to plot the data and produce clear visualizations of trends and relationships. These tools were instrumental in analyzing complex data sets, such as phonon spectra, band structures, and transport properties, by offering efficient methods to present the results in an understandable format.

`Python` was widely employed for both data processing and computational tasks. Specifically, Python's functionalities were essential for calculating the frequency-dependent electron-phonon coupling. Libraries such as `NumPy` and `SciPy` facilitated the management of large datasets, automating repetitive operations, conducting statistical analysis, and enabling detailed computational investigations of the system's properties. `Python` was also used for data manipulation, ensuring that calculations were executed efficiently and that the results could be processed and analyzed thoroughly.

4

Results and Discussion

4.1 Effects of Pressure on the Properties of YHSe

4.1.1 Structural Properties

The substance's arrangement is strongly related to its other properties; our first step involved optimizing the unit-cell dimensions of YHSe under the influence of varying pressure levels. a stability analysis was executed as a preliminary step in order to find the optimal lattice parameters for YHSe crystal. After careful analysis, the converged lattice parameters at 0 GPa were found to be $a = b = 3.80\,\text{Å}$ and $c = 3.88\,\text{Å}$. Following the convergence test, further structural optimization was performed. The refined optimized lattice parameters at zero pressure were calculated to be $a = b = 3.81\,\text{Å}$ and $c = 3.87\,\text{Å}$. This optimization process was then extended to applied pressures ranging from 0 to 200 GPa, revealing systematic changes in the lattice constants as pressure increased.

Figure. 4.1 demonstrates that the computed lattice constants of YHSe under extreme pressures reaching 200 GPa. The recorded reduction in lattice dimensions with increasing pressure in YHSe is due to the compressive effects induced by applied pressure on the crystal structure. As pressure rises, the distances between atoms in the crystal lattice reduce, leading to a shrinkage in the volume of the unit cell. This compression causes the atomic orbitals to overlap more, which enhances the bonding and leads to a reduction in the energy levels of these orbitals. Furthermore, as external pressure increases, atoms within the crystal lattice are compressed, leading to a reduction in interatomic spacing and consequently strengthening the overlap between the electron orbitals of neighboring atoms. This intensified orbital interaction can induce a rearrangement of the electronic charge distribution throughout the structure. These observations are consistent with prior findings reported by Mustapha et al. (2024), who identified a pressure-driven alteration in the band structure and improved optical characteristics in the quaternary Heusler alloy

TaAlCuCo.

As the external pressure exerted on YHSe increases from 0 to 200 GPa, the lattice parameters exhibit a decreasing trend, as shown in Fig. 4.1. The observed reduction in lattice parameters in this investigation signifies an increased atomic packing density within the crystal framework as the external pressure intensifies. This upper limit was chosen based on the results of phonon dispersion calculations, which indicated the emergence of dynamical instability beyond 200 GPa. Structural equilibrium at each pressure stage was verified through complete geometry optimization. The structure was obtained through full geometry optimization, ensuring the equilibrium lattice parameters and atomic positions were determined with high precision.

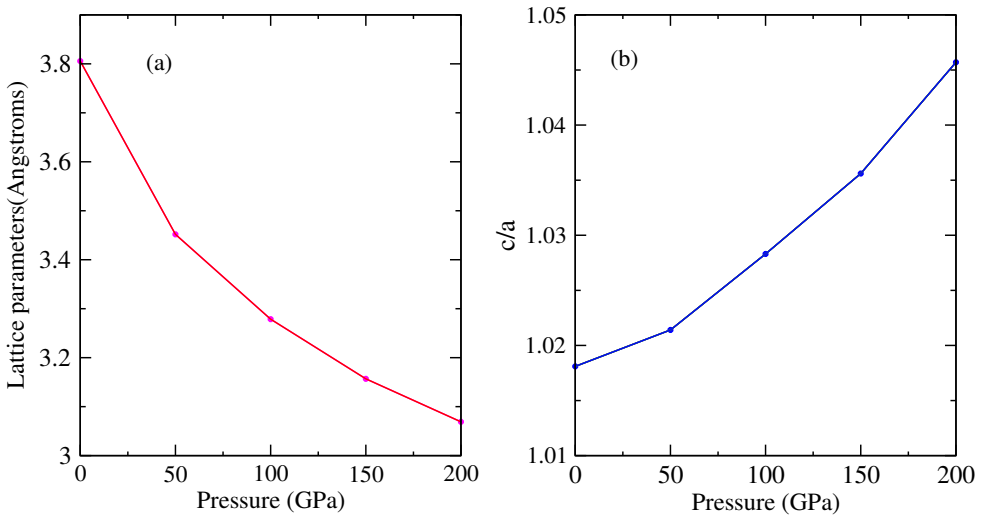

Figure 4.1: (a) Estimated lattice parameters (in Å) and (b) the c/a proportion of YHSe subjected to pressures up to 200 GPa.

4.1.2 Electronic Properties

In this section, we examine the electronic characteristics of YHSe under varying pressure conditions, with a focus on its band structure and density of states (DOS). The band structure of hexagonal YHSe, which crystallizes in the P$\bar{6}m2$ space group, was computed by selecting k-points along the high-symmetry path Γ-M-K-Γ-A-L-H (Setyawan & Curtarolo, 2010).

The results indicate that YHSe exhibits semiconducting behavior under pressure, as

predicted by both the Generalized Gradient Approximation (GGA) and the GGA+U approach. Within the GGA framework, the band gap decreases from 1.52 eV to 1.24 eV as pressure increases from 0 to 200 GPa. Similarly, when employing the GGA+U method, the band gap narrows from 1.66 eV to 1.37 eV across the same pressure range, further confirming the persistence of the semiconducting nature of YHSe under compression. At 0 GPa, the band structure shown in Fig. 4.2 (a) indicates that YHSe possesses an indirect band gap, with the valence band maximum (VBM) located at the A-point and the conduction band minimum (CBM) at the Γ-point. Since the VBM and the CBM occur at different **k**-points in the Brillouin zone, YHSe retains its indirect band gap nature under 0 GPa pressure conditions. A systematic analysis of the band structure at increasing pressures Fig. 4.2 (a) - Fig. 4.4 (e) demonstrates that the highest occupied state in the valence band consistently resides at the A-point across all examined pressures. At 0 GPa, the conduction band minimum is located at the Γ-point with an energy of 1.15 eV, which is lower than those at the K (1.83 eV) and A (1.53 eV) points under the GGA approximation. This trend persists up to 100 GPa.

However, a pressure-induced modification in the band structure is observed at 150 GPa, where the conduction band minimum shifts to the A-point. This alignment of the conduction band minimum and valence band maximum at the same high-symmetry location results in a transformation from an indirect to a direct band gap semiconductor. This result aligns with earlier investigations of indirect-to-direct energy gap conversions, as shown in the influence of compression on $LaAlO_3$ (Murtaza & Ahmad, 2012).

Figure 4.3 (d) provides a comprehensive visualization of the electronic band structure evolution under pressure. YHSe maintains an indirect band gap across all investigated pressures, except at 150 GPa, where it undergoes an indirect-to-direct band gap transition. Specifically, at this critical pressure, the highest filled state in the valence band and the minimum empty state in the conduction band coincide at the A high-symmetry point, leading to a direct energy gap. This transition is significant as it influences the optoelectronic properties of YHSe, making it a promising candidate for pressure-tunable semiconductor applications. Notably, at 200 GPa, the conduction band minimum relocates to the K-point (0.57 eV), which possesses less energy compared to the Γ (0.88 eV),

A (0.68 eV), L (5.34 eV), and H (6.44 eV) points in the conduction band under the GGA approximation.

Moreover, as illustrated in Fig. 4.4 (e), even at an elevated pressure of 200 GPa, the conduction and valence bands retain their separation, without any merging,indicating the sustained semiconducting nature despite the narrowed band gap. This observation further underscores the intriguing electronic properties of YHSe and its potential applicability in next-generation semiconductor technologies.A comparative examination of the band structure of YHSe at 0, 50, 100, 150, and 200 GPa, as as shown in Fig. 4.2 (a) through Fig. 4.4 (e), reveals a steady decline in the band gap with rising pressure an observation in agreement with earlier research on analogous compounds(Seo et al., 1998). The computed energy gaps of YHSe across a range of applied pressures were determined using the GGA approach. The energy band gaps of YHSe at various pressure levels, calculated using the GGA approximation, are 0 GPa (1.52 eV), 50 GPa (1.45 eV), 100 GPa (1.43 eV), 150 GPa (1.35 eV), and 200 GPa (1.24 eV). This progressive reduction in the band gap with rising pressure indicates significant pressure-driven alterations in the electronic structure of YHSe.

To address the limitations of GGA in predicting electronic properties, the DFT + U method is commonly employed (Orhan, O. K. et al., 2019). Yttrium, is a transition metal with the electronic configuration $[Kr]4d^15s^2$, has its valence electron primarily in the $4d$-orbital. Therefore, applying the Hubbard U to the $4d$-orbitals is ideal when modeling yttrium in YHSe.

The calculated Hubbard U parameter for yttrium in the $4d$ orbital of YHSe was set to 2.21 eV. This calculated value was selected based on reported U values for yttrium in various compounds, falling within the 2.0 to 8.5 eV range and closer to values reported for related compounds.

In this study, applying the GGA + U approximation improves predictions of both the band gap and electronic density of states for YHSe. The computed band gaps are at 0 GPa 1.66 eV ,at 50 GPa 1.54 eV , at 100 GPa 1.48 eV, at 150 GPa 1.45 eV , and at 200 GPa 1.37 eV. Table 2 summarizes the band gap values of YHSe under varying pressures, calculated using both GGA and GGA+U approximations.

Compared to standard GGA, the GGA+U method yields a slightly wider band gap and enhanced density of states, with the band gap ranging from 1.66 eV to 1.37 eV under increasing pressure, thereby reinforcing the semiconducting character of the YHSe material under compression.The inclusion of the Hubbard U term modifies the electronic structure of YHSe. As illustrated in Fig. 4.2 (2a) through Fig. 4.4 (2e), the electronic DOS reveals a notable shift in the Y- $4d$ states compared to the standard GGA results.

Table 2: Calculated energy band gaps of YHSe under various pressures using GGA and GGA+U methods.

P (GPa)	**GGA (eV)**	**GGA+U (eV)**
0	1.52	1.66
50	1.45	1.54
100	1.43	1.48
150	1.35	1.45
200	1.24	1.37

Overall, the characteristics of the calculated band structure and the band gap of 1.52 eV at 0 GPa pressure exhibit good agreement with values reported in established databases (e.g., E_g = 1.51 eV from the Materials Project). This close agreement validates the reliability and accuracy of the computational approach employed in this study.

Shifting from the evaluation of the band structure to the investigation of the density of states (DOS), we calculated both the total density of states (TDOS) and the projected density of states (PDOS) for YHSe across a broad pressure range from 0 GPa to 200 GPa, as shown in Fig. 4.2 (a) through Fig.4.4 (e). The TDOS provides insight into the overall electronic states available at different energy levels while the PDOS allows for a more detailed understanding of the contributions from individual atomic orbitals. As pressure increases, notable shifts in the DOS features are observed, reflecting significant modifications in the electronic structure. In these computations, the Fermi energy is defined as the reference energy at 0 eV in Fig.4.2 (a) - Fig.4.4 (e). Figure.4.4 shows the calculated electronic structure for YHSe presented at different pressures using both GGA and GGA+U approximations.

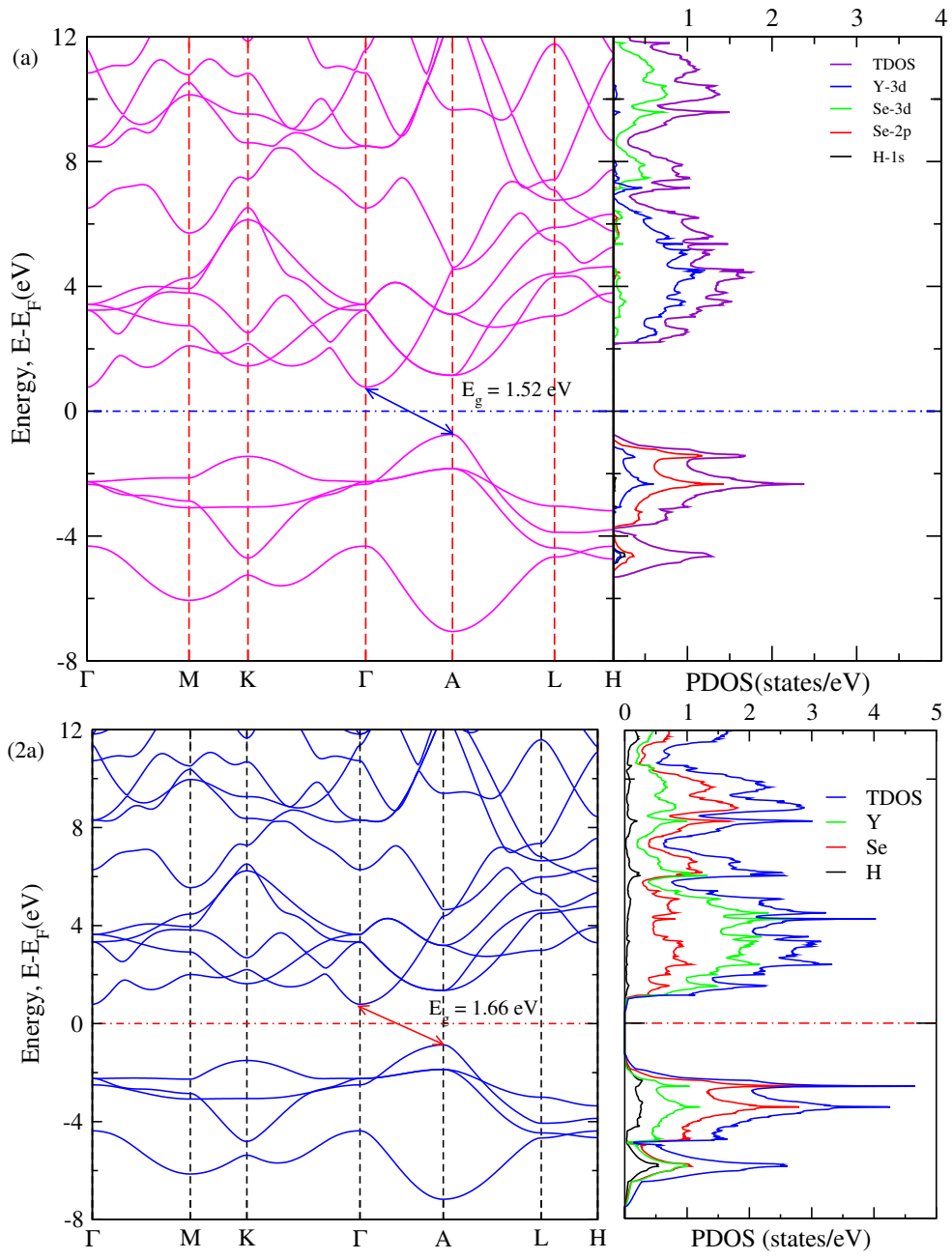
(a)
Energy, E-E$_F$(eV)
12
8
4
0
-4
-8
Γ
M
K
Γ
A
L
H
E$_g$ = 1.52 eV
1
2
3
4
TDOS
Y-3d
Se-3d
Se-2p
H-1s
PDOS(states/eV)
(2a)
Energy, E-E$_F$(eV)
E$_g$ = 1.66 eV
0
1
2
3
4
5
TDOS
Y
Se
H
PDOS (states/eV)

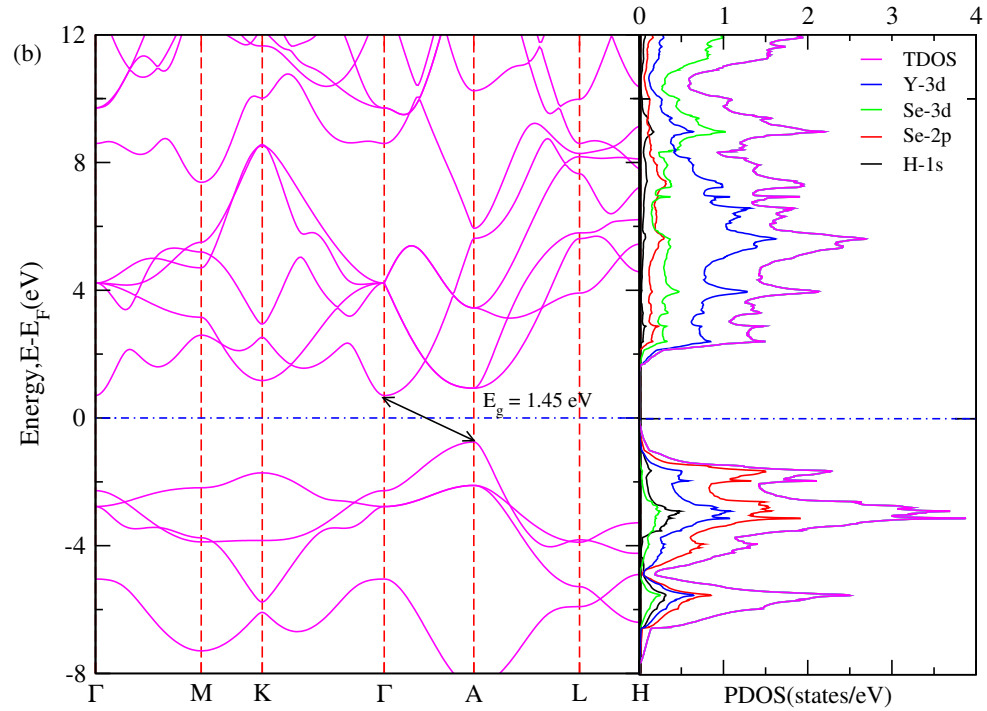
(b)
Energy,E-E$_F$(eV)
E$_g$ = 1.45 eV
Γ M K Γ A L H
PDOS(states/eV)
TDOS
Y-3d
Se-3d
Se-2p
H-1s

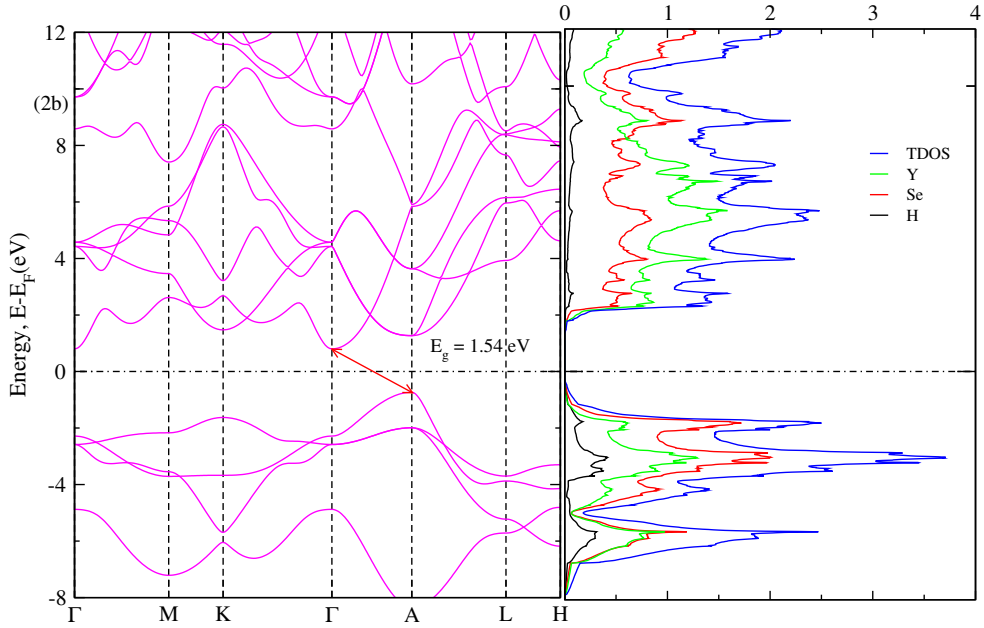
(2b)
Energy, E-E$_F$(eV)
E$_g$ = 1.54 eV
Γ M K Γ A L H
TDOS
Y
Se
H

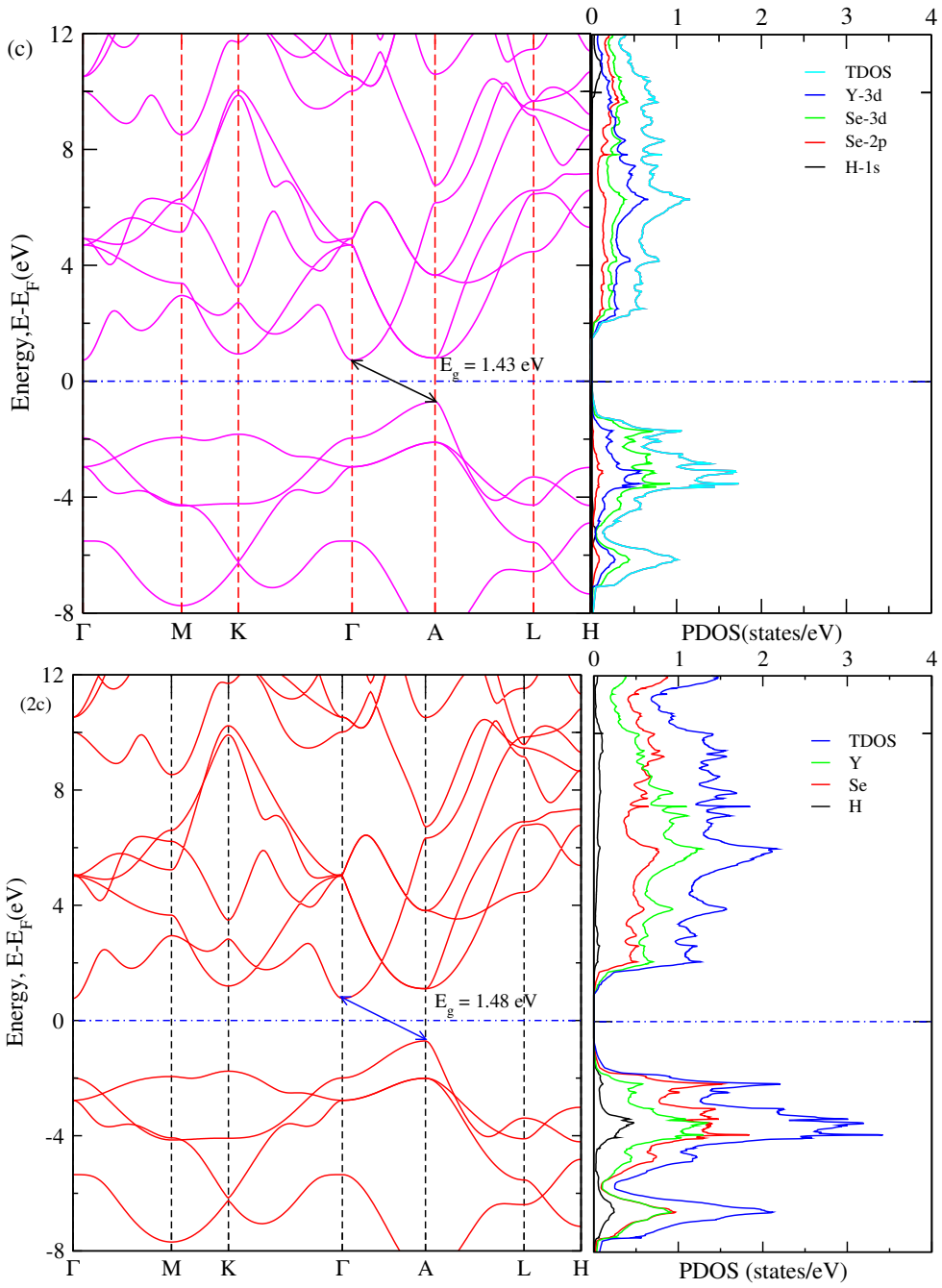

Figure 4.2: Band structures and electronic DOS for YHSe obtained using the GGA [(a) - (c)] and GGA+U [(2a) - (2c)] methods at pressures of (a) 0 GPa, (b) 50 GPa, (c) 100 GPa

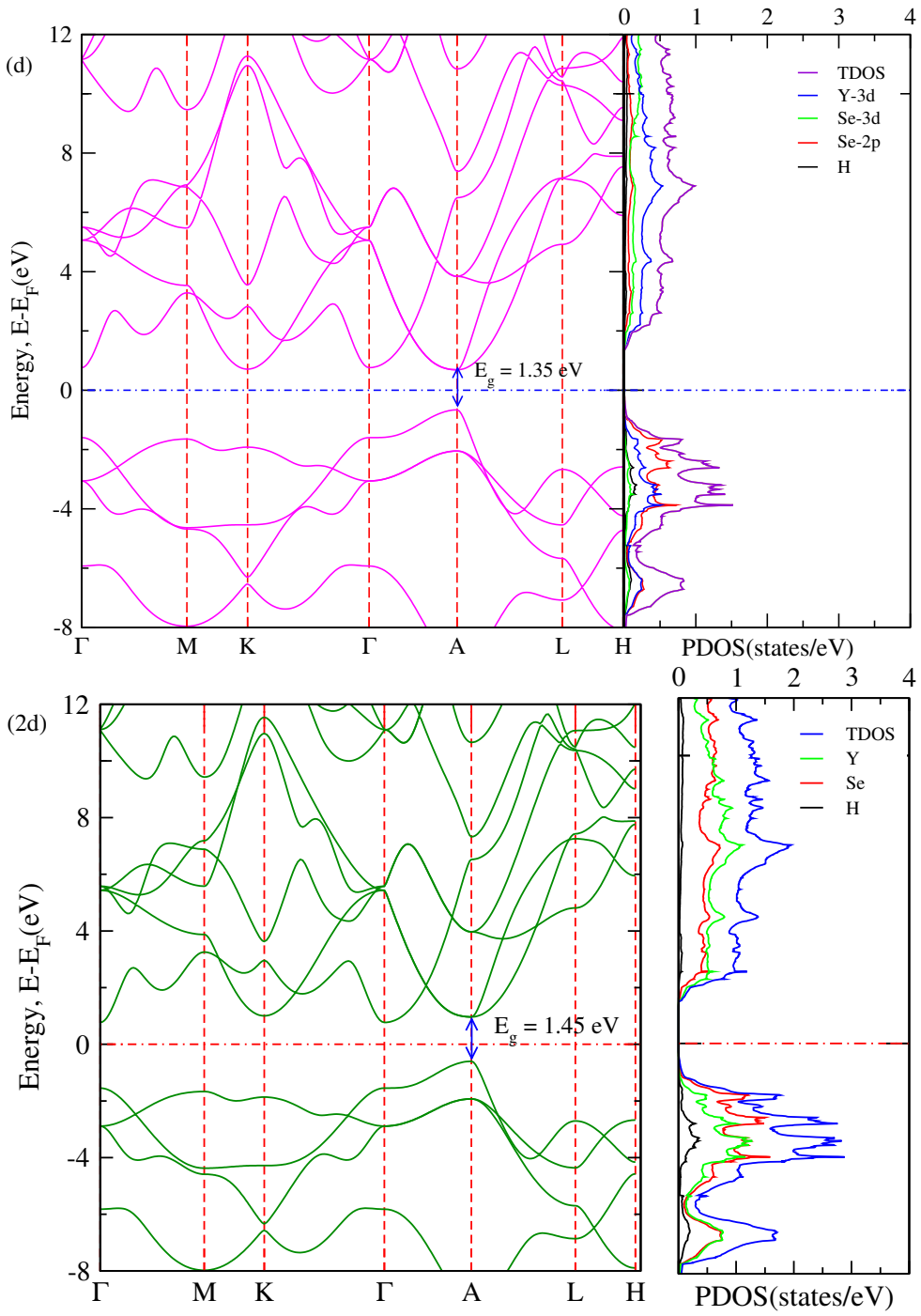

Figure 4.3: Band structures and electronic DOS for YHSe obtained using the GGA [d] and GGA+U [2d] methods at pressures of 150 GPa

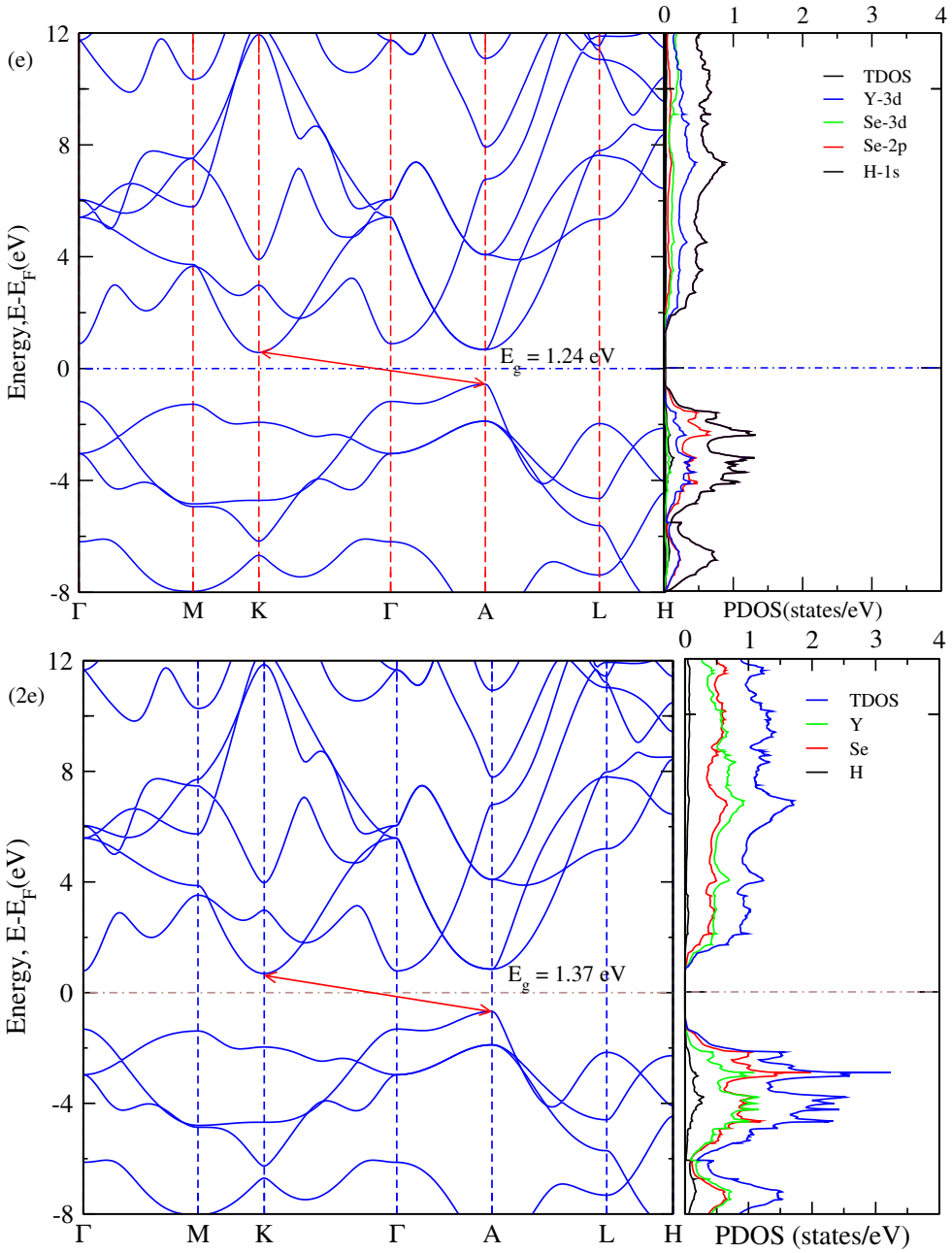

Figure 4.4: Band structures and electronic DOS for YHSe obtained using the GGA [e] and GGA+U [2e] methods at pressures of (e) 200 GPa.

The computed DOS analysis further confirms that YHSe retains its semiconductor characteristics across all examined pressures up to 200 GPa, as indicated by the zero DOS at the Fermi level. This observation aligns consistently with the band structure analysis, reinforcing the material's semiconducting nature under varying pressure conditions.

For more theoretical insight, the projected density of states for the individual atoms

Y, Se, and H in the YHSe structure has been analyzed and is depicted in Fig. 4.2 (a)–4.4 (e) and Fig. 4.2 (2a)–4.4 (2e), using the GGA and GGA+U approximations, respectively. At 0 GPa the Se atoms contribute more significantly to the total density of states in the valence band compared to Y and H atoms. Furthermore, among the Se states, the Se-2p orbitals exhibit a greater contribution than the Se-3d orbitals with the majority of states near the Fermi level primarily attributed to Se-2p orbitals. Conversely, in the conduction band, Y atoms contribute more substantially to the total density of states than Se and H atoms. Within the Y contributions, the Y-3d orbitals dominate over the Y-5p states, while in the Se contribution; the Se-3d orbitals exceed the Se-2p states. Notably, the highest density of states near the Fermi level in the conduction band is attributed to Y-3d orbitals. This trend persists across all examined pressures, although the degree of orbital overlap varies with increasing pressure. At 0 GPa the Se-3d and Se-2p bands exhibit overlap in the energy ranges of 4.39 - 6.025 eV and 6.35 - 8.305 eV. Moreover, hybridization between Y-3d and Se-3d orbitals is observed within the 7.28 - 7.299 eV and 9.27 - 9.47 eV energy ranges, suggesting the formation of covalent bonding between these orbitals. At 150 GPa, the overlap between Se-3d and Se-2p states occurs in the energy range of 6.86 - 9.043 eV. Furthermore, at 200 GPa, as shown in Fig. 4.4 (e) this overlap shifts to 7.814 - 8.96 eV energy range. In contrast, the interaction between Y-3d and Se-3d orbitals spans the energy ranges of -5.0 to 8 eV and -3.19 to -4.387 eV at 200 GPa.

Overall, the variations in orbital hybridization among Y $3d$, Se $2p$, and Se $3d$ states with increasing pressure indicate a pressure-dependent evolution of electronic interactions within the material for both GGA and GGA+U approaches. Furthermore, the total density of states near the Fermi level exhibits a decrease with increasing pressure. This consistent downward trend reflects a systematic reduction in the number of electronic states available for conduction. Such a decreasing behavior is consistent with previously reported findings in related systems (Murtaza & Ahmad, 2012), where pressure-induced changes in the electronic band structure result in a gradual depletion of states near the Fermi level.

According to these findings, the trends of the TDOS under varying pressures exhibit a consistent pattern, notably a reduction in the band gap as pressure increases. At lower

pressures, the relatively high density of states can be attributed to enhanced electronic hybridization and band broadening, which result in a greater availability of electronic states near the Fermi level. These observations are consistent with previous studies on pressure-induced electronic modifications in K_3C_{60} (Huang et al.,1993), where similar band gap narrowing and increased hybridization effects were reported. At lower pressures, the electronic states are more localized, and hybridization effects between orbitals can enhance the DOS near the Fermi level. As pressure increases, band broadening occurs due to the reduced inter atomic distances, which generally decline in the average DOS. The reference to Huang et al.,(1993) suggests that similar trends have been observed in other materials.

4.1.3 Vibrational Analysis

The phonon dispersion curves and projected phonon density of states for YHSe are presented in Fig.4.5 under different pressure conditions. The lack of imaginary phonon modes throughout the Brillouin zone verifies the dynamic stability of the YHSe structure. Accordingly, our findings confirm that YHSe remains dynamically stable across all examined pressures, as illustrated in Fig.4.5(a) to Fig.4.5(e). Phonon dispersion analyses at 0, 50, 100, 150, and 200 GPa further reinforce this structural stability. The phonon dispersion relations within the Brillouin zone offer valuable understanding of how phonon energy varies with the q-vector along high-symmetry paths, as illustrated in Fig.4.5(a) to Fig.4.5(e).

In this study, the primitive unit cell of the YHSe compound comprises three atoms, leading to a total of nine vibrational (phonon) modes. Among these modes, three represent acoustic branches, while the remaining six correspond to optical phonon modes. The phonon density of states $F(\omega)$, shown in Fig.4.5 under various pressure conditions, demonstrates the distribution of phonon frequencies within the YHSe compound, offering a detailed perspective of its vibrational characteristics. The unique features observed in the phonon spectrum, as depicted in Fig.4.5(a) to Fig.4.5(e), arise directly from the differing atomic masses of Y, Se, and H in the structure.

The phonon density of states (PhDOS) of YHSe indicates that low-frequency vibrational modes are primarily governed by the heavier Y and Se atoms, whereas the lighter H atoms contribute substantially to the high-frequency range. This disparity results in the

separation of the partial phonon density of states F(ω) into three distinct regions, each predominantly shaped by the vibrations of specific atomic constituents. This observation is consistent with previous findings reported for similar systems (Sadeghi & Esfarjani, 2024)

At 0 GPa and relatively low-pressure conditions, the PhDOS reveals distinct peaks at lower frequencies, predominantly originating from the vibrational modes of heavier Y and Se atoms. With increasing pressure, a gradual reduction in the intensity of the phonon density of states (PhDOS) is observed, indicating modifications in lattice dynamics caused by strengthened interatomic forces.

Figure 4.5(a) to Figure 4.5(e) reveals that the optical phonon density of states in the mid-frequency range exhibits a pronounced contribution from the lighter hydrogen atoms. As pressure increases, this contribution progressively shifts from higher to lower frequency regions, indicating pressure-induced redistribution of hydrogen-related vibrational modes. Conversely, the vibrational contributions of Y and Se atoms exhibit a noticeable shift toward higher frequencies. This pressure-induced redistribution of phonon modes indicates enhanced bonding strength and lattice stiffness, and is consistent with observations reported in previous investigations (Besson, 1989; Delaire et al., 2010). Overall the PhDOS exhibits a decreasing trend in magnitude with increasing pressure, accompanied by a noticeable shift toward higher frequencies.

The effect of pressure on the phonon dispersion curves of YHSe along selected high-symmetry directions in the Brillouin Zone (BZ) is illustrated in Fig. 4.5(a) to Fig. 4.5(e). At ambient pressure (0 GPa), the calculated phonon dispersion curves exhibit strong agreement with those obtained from inelastic neutron scattering experiments (Xie et al., 1999). The principal results related to YHSe from this investigation are summarized in Table 3, and are consistent with the experimental values reported at zero pressure (Xie et al., 1999).

As illustrated in Fig. 4.5(b), increasing pressure induces a noticeable upward shift in the phonon branches toward higher frequency regions. However, the extent of this frequency elevation varies across different points within the Brillouin Zone (BZ). Specifically, Fig. 4.5 (b) demonstrates that at 50 GPa, the phonon frequencies at the high-symmetry points

Table 3: Calculated phonon frequencies of hexagonal YHSe along selected high-symmetry paths at 0 GPa.

High Symmetry Point	**Phonon Frequencies (cm^{-1})**
Γ	209, 189.77
M	116.18, 134.29, 172.25, 174.64, 175.05, 228.97
K	148.59, 150.83, 163.89, 164.81, 201.20, 203.33
A	128.29, 138.48, 195.44
L	77, 127.74, 154.23, 154.58, 157.79, 166, 204.29, 209.61
H	126.85

Γ, M, K, A, L, and H are higher than those at the corresponding points under ambient pressure (0 GPa).

Moreover, across all examined pressure conditions, a distinctive characteristic is observed: two longitudinal optical phonon branches, primarily associated with the lighter hydrogen atoms, distinctly separate from the remaining optical modes by attaining significantly higher frequencies. This marked elevation in optical phonon frequencies at 0, 50, 100, 150, and 200 GPa is likely due to the dynamic contribution of hydrogen atoms, as supported by the phonon partial density of states. With increasing pressure, the partial density of states clearly indicates a shift of hydrogen-related vibrational modes toward the higher-frequency region.

From Fig.4.5, the other optical phonon modes associated with hydrogen atoms, initially located in the mid-frequency region exhibit a downward shift toward lower frequencies as the pressure increases. These modes gradually approach the optical phonon modes primarily generated by the heavier Y and Se atoms, indicating enhanced phonon coupling between the vibrations of light and heavy atoms under high-pressure conditions. Figure 4.5 presents the phonon dispersion relations and the corresponding projected phonon density of states (PhDOS) for YHSe under varying pressure conditions.

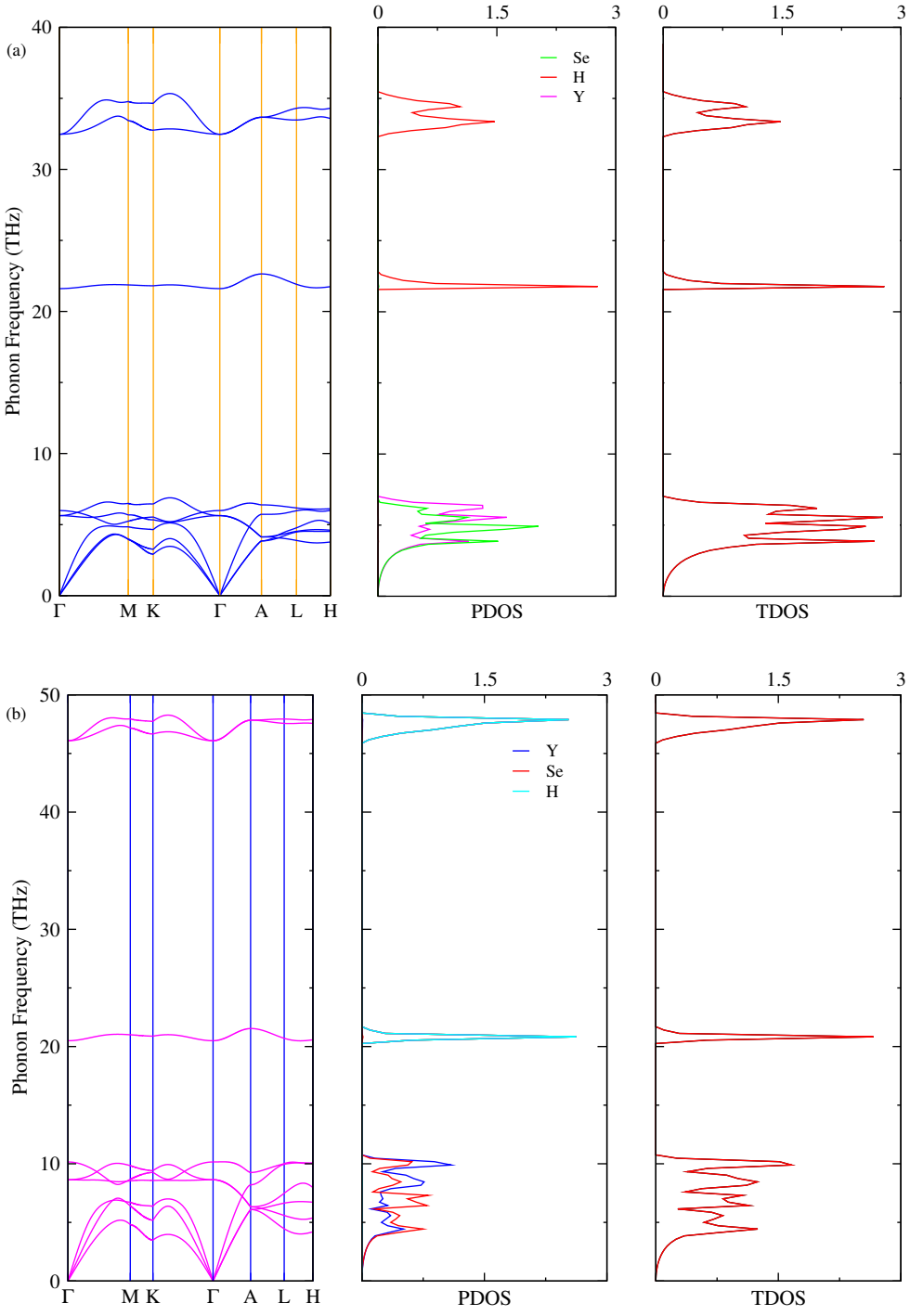
(a)
Phonon Frequency (THz)
40
30
20
10
0
Γ
M
K
Γ
A
L
H
0
1.5
3
Se
H
Y
PDOS
TDOS
(b)
50
40
30
20
10
0
Y
Se
H

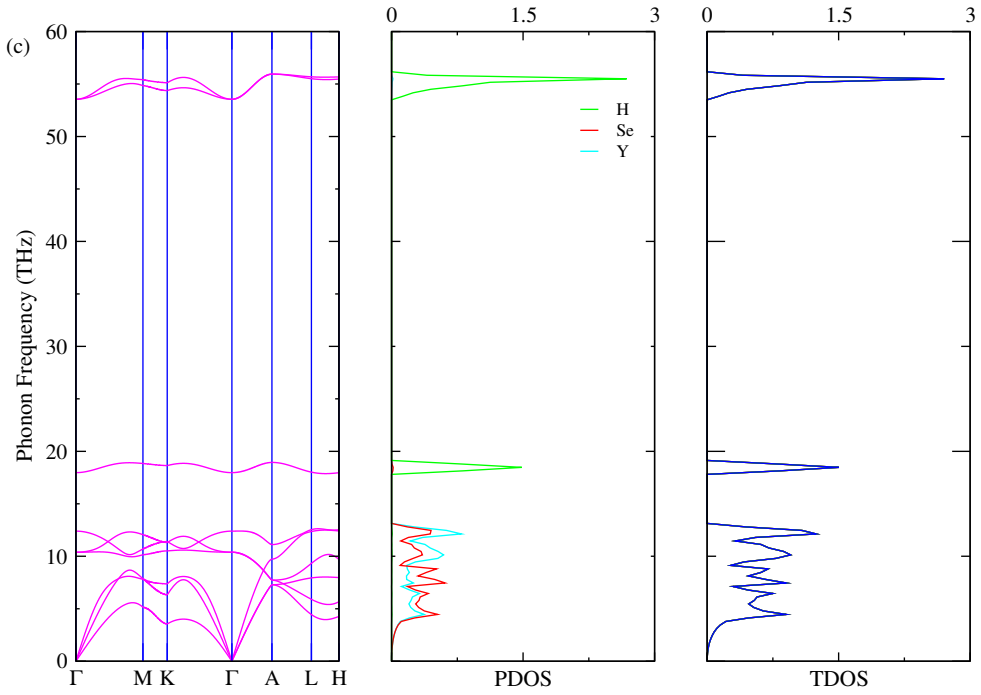
(c)
Phonon Frequency (THz)
60
50
40
30
20
10
0
Γ
M
K
Γ
A
L
H
0
1.5
3
H
Se
Y
PDOS
TDOS

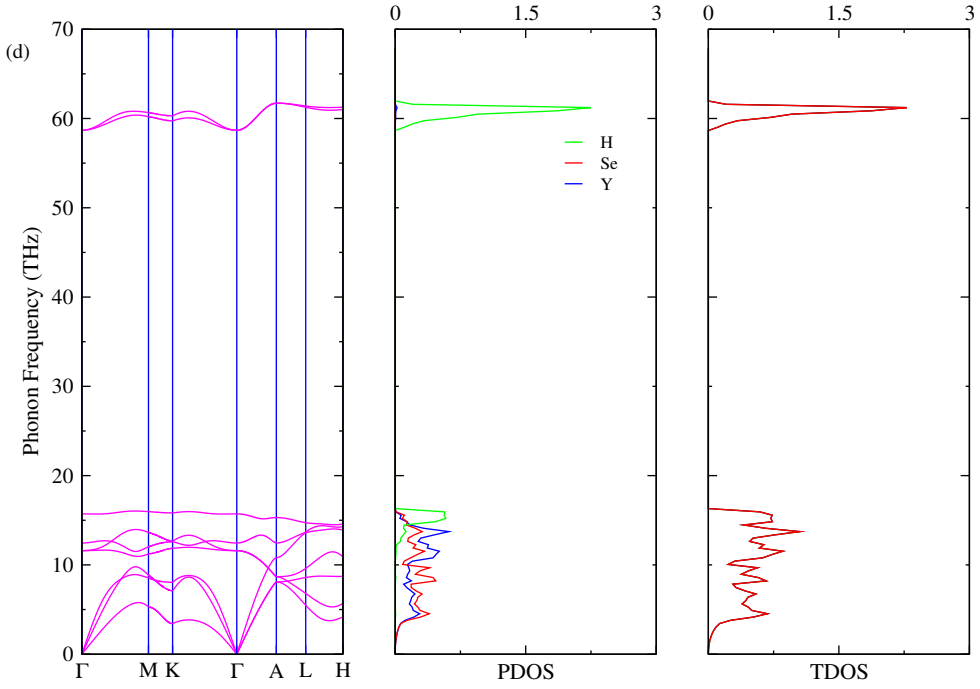
(d)
Phonon Frequency (THz)
70
60
50
40
30
20
10
0
Γ
M
K
Γ
A
L
H
0
1.5
3
H
Se
Y
PDOS
TDOS

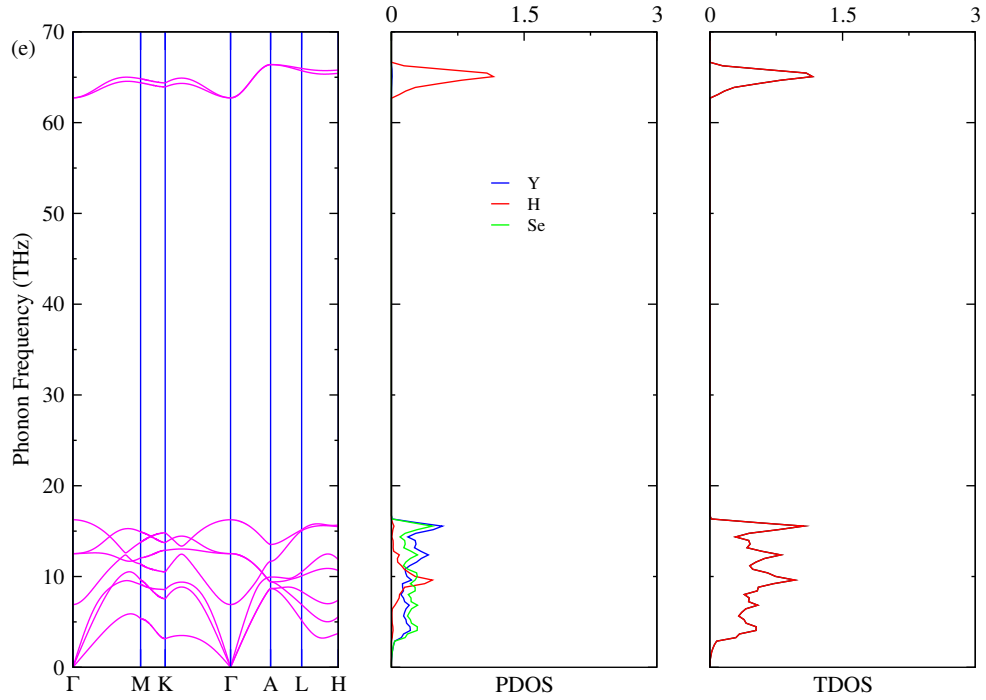

Figure 4.5: Phonon band structure and phonon DOS for hexagonal YHSe under various pressure conditions: (a) 0 GPa, (b) 50 GPa, (c) 100 GPa, (d) 150 GPa, and (e) 200 GPa.

The optical phonon frequencies corresponding to both the lighter hydrogen (H) atoms and the relatively heavier selenium (Se) and yttrium (Y) atoms at each high-symmetry point in the Brillouin Zone (BZ) show a consistent increase with pressure up to 200GPa, as depicted in Fig.4.6. This indicates that with increasing pressure, the optical phonon frequencies at each high-symmetry point experience a steady rise up to 200 GPa. The results of this study are consistent with previously reported data for related systems (Chen et al., 2004). This trend suggests a stiffening of the lattice dynamics under applied pressure. Phonon frequencies are influenced by the strength of the force constants that exist between atoms within a crystal lattice. When external pressure is increased, the atoms are pushed closer together, which enhances the force constants and results in elevated phonon frequencies (Allen & Dynes, 1975)

The optical phonon branches display a continuous increase in frequency as pressure increases. Figure 4.7 illustrates the change in acoustic phonon frequency as a function of pressure at various high-symmetry points in the Brillouin Zone (H, M, A, K, and L), with differently colored lines showing the phonon frequency trends for each point. Notably, the

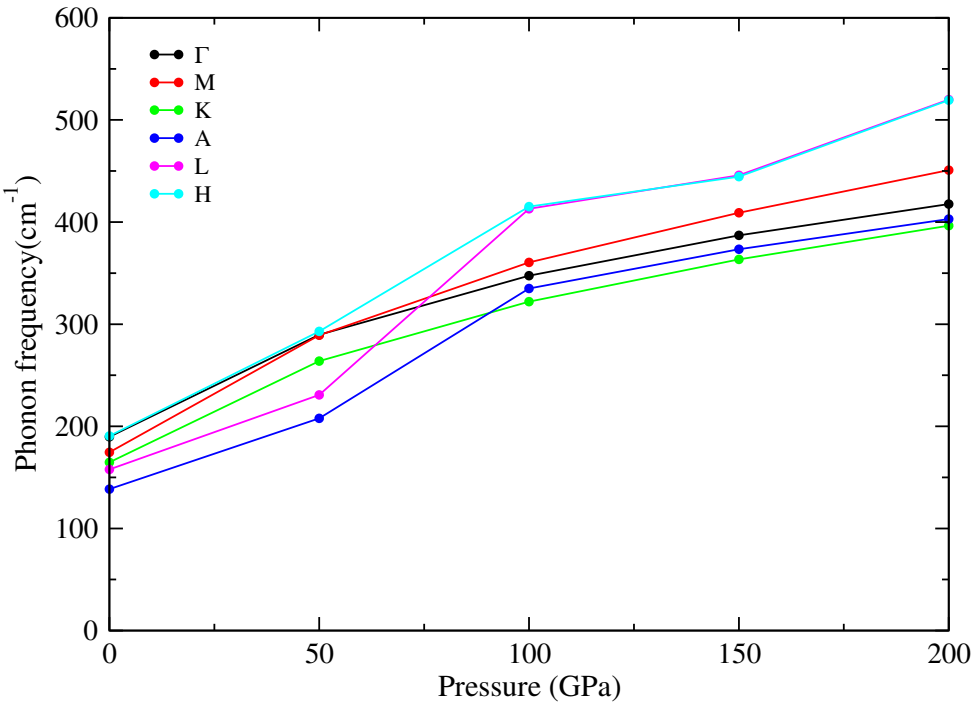

Figure 4.6: Variation of optical phonon frequencies with pressure at selected high-symmetry points (Γ, M, K, A, L, and H) in the Brillouin zone for YHSe.

acoustic phonon frequencies at the L and H high-symmetry points undergo a significant reduction at pressures of 150 and 200 GPa as shown in Fig.4.7 and Fig. 4.8, suggesting potential modifications in inter-atomic interactions.

Figure 4.8 presents the phonon band structure curves for YHSe at 0 GPa (red) and 200 GPa (blue). A comparative analysis of these dispersion curves reveals that the optical phonon modes exhibit a noticeable frequency increase at 200 GPa relative to 0 GPa, indicating lattice stiffening due to reduced inter-atomic distances under extreme compression. This stiffening suggests an increase in inter-atomic force constants, a phenomenon commonly observed in high-pressure studies.

However, the acoustic phonon frequencies associated with the heavier Y and relatively heavier Se atoms at the L and H high-symmetry points display a significant decrease under high pressure, implying alterations in the inter-atomic force constants and the possible emergence of anharmonic effects. Notably, phonon softening at these symmetry points is often linked with enhanced EPC, which could play a crucial role in facilitating superconductivity at 200 GPa in this study.

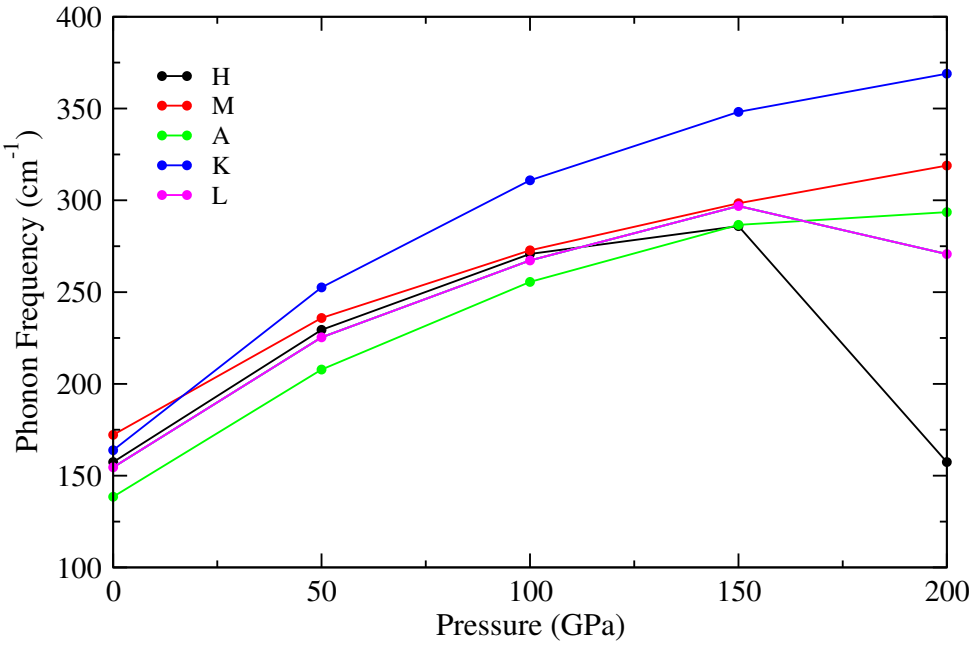

Figure 4.7: Acoustic phonon frequencies at high-symmetry points (M, K, A, L, and H) under different pressure conditions for YHSe.

The observed phonon softening at specific high-symmetry points implies a strengthening of the EPC, a key mechanism governing superconducting behavior. These findings align with prior investigations of similar high-pressure superconducting systems (Lian et al., 2017), further supporting the notion that pressure-induced modifications in phonon dynamics are instrumental in optimizing superconducting properties. The interplay between phonon softening, EPC, and Tc underscores the significance of high-pressure tuning in modulating the superconducting behavior of YHSe. Figure 4.9 shows the total phonon density of state for YHSe at different pressures.

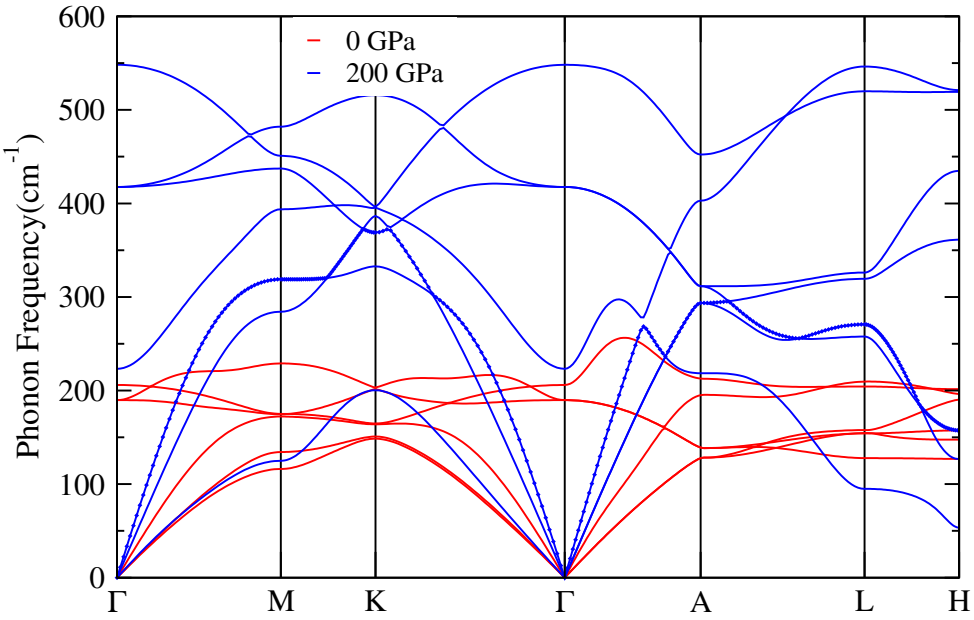

Figure 4.8: Comparison of phonon dispersion relations for YHSe at pressures of 0 GPa (red lines) and 200 GPa (blue lines).

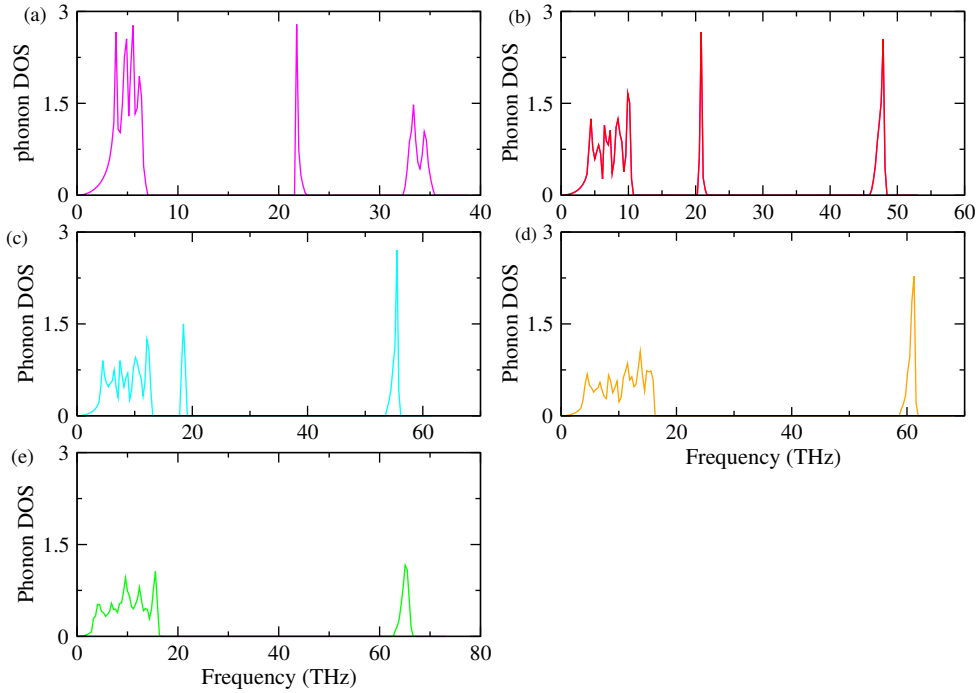

Figure 4.9: Overall phonon DOS for YHSe under various pressures: (a) 0 GPa, (b) 50 GPa, (c) 100 GPa, (d) 150 GPa, and (e) 200 GPa.

4.1.4 Superconducting Properties

In this investigation, the superconducting characteristics of YHSe are comprehensively explored through electron-phonon coupling $\lambda(\omega)$ calculations. The calculated non-monotonic relationship of the superconducting critical temperature (T_c), as shown in Fig. 4.10(a), together with the total electron-phonon coupling parameter $\lambda(\omega)$ in Fig. 4.10(b), offers valuable insights into the superconducting behavior of YHSe under extreme pressure conditions.

At 0 GPa, YHSe exhibits a superconducting critical temperature (T_c) of 28 K, highlighting its potential as a moderate superconductor compared to conventional superconducting materials. This relatively high T_c, compared to 100 GPa and 150 GPa, may be attributed to the substantial density of states near the Fermi level and the phonon density of states, which enhance electron-phonon interactions. As external pressure increases,T_c initially drops to 24.781 K at 50 GPa, suggesting a reduction in superconducting behavior. This reduction aligns with trends observed in similar systems and may be attributed to the decrease in both electronic and phonon densities of states (DOS), which leads to a relatively weakened electron-phonon interaction. Despite this decrease, T_c remains relatively high at 50 GPa due to the sustained density of states near the Fermi energy and phonon density of states, supporting strong electron-phonon interactions.

As the pressure increases to 100 GPa, the T_c further decreases to 15.8 K, indicating a continued suppression of superconductivity. This decrease suggests that the applied pressure modifies the material's electronic characteristics, weakening its superconducting behavior. A decline in T_c is mainly observed due to the reduction in EPC, which is influenced by lowered densities of both electronic states around the Fermi level and phononic states. Beyond 100 GPa, a reversal in this trend occurs, as T_c an upward trend in Tc is observed. At 150 GPa, the critical temperature Tc rises slightly to 15.9 K, indicating a minor improvement in superconducting behavior under high-pressure conditions. This increase is likely attributed to phonon softening at specific high-symmetry points (L and H), resulting in a reduction of the logarithmic average phonon frequency from 264 K to 250 K and thereby slightly strengthening the EPC.

Our investigation reveals that, similar to other documented hydrogen-based superconductors, the correlation between T_c and pressure (P) shows a consistent trend beyond 100 GPa, highlighting the complex interaction between structural changes and superconducting properties under high-pressure conditions, as illustrated by Drozdov, Eremets, and their colleagues in their research on hydrogen sulfide (Drozdov et al., 2015).

The pressure dependence of superconductivity is highly intricate and is influenced by various factors of the electron and phonon systems (Lorenz, B., & Chu, C. W., 2005). A lower electronic DOS near the Fermi level generally weakens electron-phonon coupling (EPC); however, the coupling constant (λ) is affected not only by the density of states near the Fermi energy but also by phonon-related aspects, particularly phonon frequencies and electron-lattice interactions.

Our analysis shows that, despite the reduction in the electronic DOS close to the Fermi level, as illustrated in Fig. 4.4 (a) - Fig.4.4 (e), the effectiveness of EPC improves at higher pressures due to modifications in phonon frequency and electronic structure. In this research, the decrease in phonon frequency depicted in Fig.4.7 and Fig.4.8 under high pressure results in a reduction in the logarithmic phonon frequency to 189.06 K, leading to a significant enhancement of the EPC constant, which reaches $\lambda = 2.63$ at 200 GPa.

This enhancement due to phonon softening aligns with findings from previous studies on related systems (Lian et al., 2017; Ma et al., 2021). The observed correlation between pressure (P) and the superconducting critical temperature (T_c) under extreme conditions is also in agreement with previous research on hydrogen-rich superconductors (Besedin et al., n.d.). In the YHSe system, T_c increases steadily from 15.8 K at 100 GPa, rises marginally to 15.9 K at 150 GPa, and then reaches 31.64 K at 200 GPa.

According to the McMillan equation, a reduction in logarithmic average phonon frequency leads to an increase in the EPC constant λ, which in turn contributes to a higher superconducting critical temperature (T_c) in the YHSe system at 200 GPa. This implies that pressure-induced phonon softening plays a pivotal role in enhancing the superconducting properties of YHSe at 200 GPa. Additionally, at extremely high pressures, the lattice structure of solids may undergo stabilization, fostering a more favorable environment for superconductivity (Tanaka et al., 2017). This stabilization can mitigate lattice

vibrations or distortions that might hinder Cooper pair formation, thus improving the superconducting critical temperature (T_c). Under extreme pressure conditions, the interactions between electrons and lattice vibrations (phonons) intensify, resulting in an increase in T_c (Kim.Y.D. et al., 2010; Eliashberg, 1960). Figure4.10 (a) presents the calculated superconducting critical temperature, Figure4.10 (b) shows the integral of λ, Figure 4.10(c) illustrates the logarithmic average phonon frequency, and Figure 4.10 as a function of pressure for YHSe.

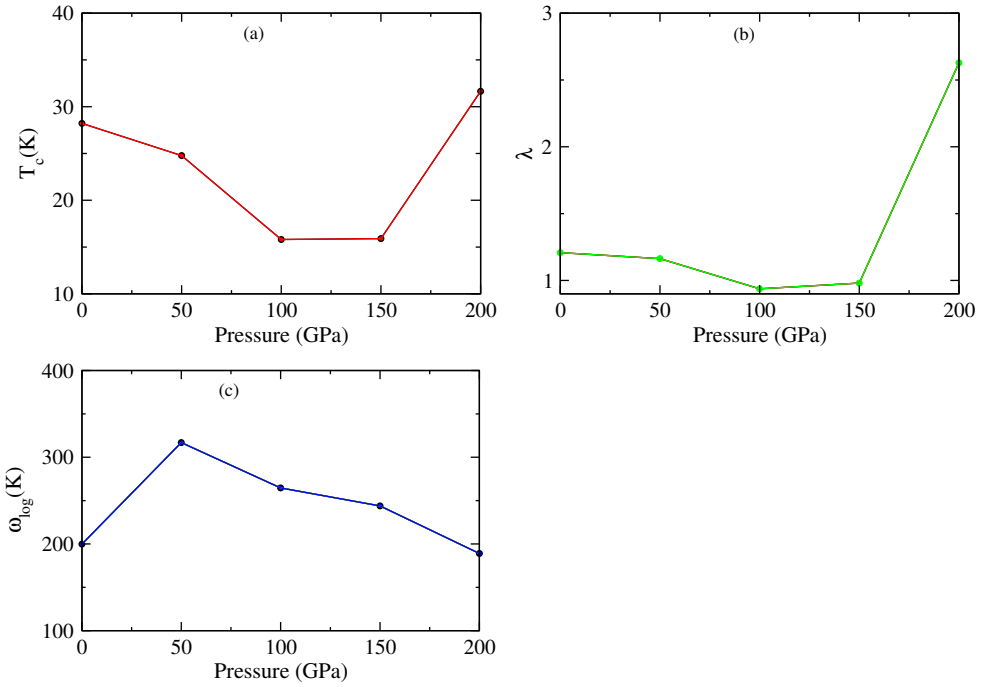

Figure 4.10: (a) Calculated superconducting critical temperature, (b) integral of λ, (c) logarithmic average phonon frequency as a function of pressure for YHSe.

Table 4: (a) Calculated superconducting critical temperature, (b) integral of λ, (c) logarithmic average phonon frequency as a function of pressure for YHSe

P (GPa)	T_c **(K)**	λ	$\omega_{\log}$ **(K)**
0	28.00	1.21	199.83
50	24.78	1.16	316.89
100	15.80	0.94	264.00
150	15.90	0.98	243.90
200	31.64	2.63	189.06

Extreme pressure could induce a lattice configuration that optimally supports strong EPC. This structural modification may enhance the efficiency of Cooper pair formation, leading to an increase in the superconducting critical temperature (T_c) (Kim et al., 2010; Lorenz & Chu, 2005).The changes in phonon frequency and electronic structure lead to an improvement in superconductivity properties(Tanaka et al., 2017)(Congeduti et al., 2001). The significant increase in the total EPC parameter, $\lambda(\omega)$, to 2.63 further reinforces this idea, indicating a remarkable enhancement in electron-phonon interactions that favor superconductivity.

The EPC constant (λ) at 0 GPa is determined to be 1.21, reflecting strong electron-phonon interaction strength. These interactions play a vital role in enabling superconductivity by supporting the formation of Cooper pairs. When the applied pressure is increased to 50 GPa, as illustrated in Fig. 4.11, λ decreases to 1.16, indicating a reduction in electron-phonon coupling (EPC) strength. This reduction is associated with the relatively lower density of states (DOS) near the Fermi level and a suppressed phonon density of states. Nevertheless, a further rise in pressure to 100 GPa, as shown in the same figure, causes λ to decline to 0.94, suggesting diminished electron-phonon interaction. This drop in the total electron-phonon coupling at 100 GPa is probably due to a continued decrease in both the electronic DOS and phononic states. In general, the coupling constant λ decreases from 1.16 to 0.94 between 50 GPa and 100 GPa. When this behavior is analyzed alongside the Coulomb pseudopotential ($\mu^* = 0.10$), it aligns with a reduction in the (T_c) from 24.78 K to 15.8 K within the same pressure interval. Thus, the observed decline in λ correlates well with the corresponding decrease in T_c over the pressure range from 50 GPa to 100 GPa.

As illustrated in Fig. 4.10(a) and Fig. 4.10(b), increasing the pressure beyond 150 GPa leads to a significant rise in the EPC constant (λ). Above this pressure point, the total EPC increases steadily, which corresponds to the enhancement of the superconducting critical temperature (T_c) observed in this study. At 150 GPa, λ increases to 0.98, showing a slight strengthening of the electron-phonon interactions. However, the overall coupling strength stays relatively low. Furthermore, at this pressure, the reduction in acoustic phonon frequencies at the L and H high-symmetry points results in phonon softening,

which lowers the logarithmic average phonon frequency from 264 K to 243.901 K. This phonon softening contributes to the observed enhancement of the EPC to 0.98. Figure 4.11 presents the frequency-resolved distribution of the EPC parameter for YHSe under various applied pressures.

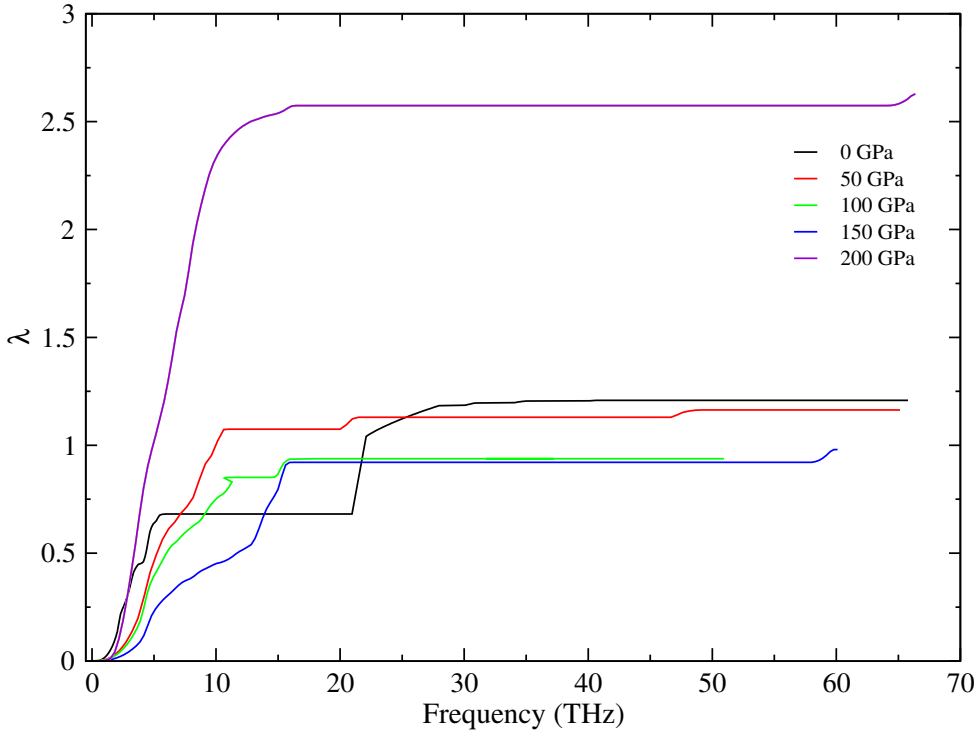

Figure 4.11: Variation of the electron-phonon coupling parameter with frequency under different pressure conditions.

Transitioning from the analysis of the total EPC strength (λ) to the ω_{log}, our study reveals a clear non-linear trend as pressure increases. Initially, the ω_{log} rises significantly from 199.83 K to 316.89 K at 50 GPa, reflecting intensified atomic interactions and the emergence of a more rigid lattice framework. This marked increase highlights the material's sensitivity to external compression, indicating its ability to structurally adapt. As pressure continues to rise, however, the phonon frequency demonstrates moderate fluctuations, remaining within the 264 K to 250 K range between 100 GPa and 150 GPa, as shown in Fig. 4.10(c). At even higher pressures, the logarithmic phonon frequency undergoes a sharp decline, falling to 189.06 K at 200 GPa. Overall, Fig. 4.10(c) reveals that the phonon frequency increases at lower pressures, peaks at 50 GPa, and subsequently decreases with

further compression.

Moreover, in this study, the Eliashberg spectral function $\alpha^2F(\omega)$ and the integrated EPC constant (λ) were calculated as functions of phonon frequency at 0 GPa, 50 GPa, 100 GPa, 150 GPa, and 200 GPa. These quantities were computed to examine the phonon spectrum and assess the electron-phonon interactions and lattice dynamics in the YHSe system. The $\alpha^2F(\omega)$ effectively characterizes the strength of electron-phonon interactions across various phonon frequencies (Uzunok et al., 2020). As such, it serves as a crucial tool for understanding how pressure-induced changes affect the EPC constant λ in YHSe, offering deeper insight into the superconducting behavior under different pressure conditions.

According to Fig. 4.12 (a) - (e), distinct peaks are observed at specific frequencies in the YHSe system. These peaks correspond to dominant phonon modes that significantly contribute to the electron-phonon coupling. At ambient pressure Fig. 4.12 (a), the moderate and highest peaks in the Eliashberg spectral function $\alpha^2F(\omega)$ appear within the frequency ranges of approximately 0.64 - 8.67 THz, 21.45 - 22.76 THz, and 34.00 - 34.54 THz, with corresponding peak values of 0.92, 0.91, and 0.93, respectively. This range highlights the frequencies where the most pronounced electron-phonon interactions occur under normal conditions.

As pressure increases, a fascinating trend emerges: the peak values of the Eliashberg spectral function vary within specific frequency regions, reflecting pressure-induced changes in the electron-phonon interaction landscape. Further analysis of Fig. 4.12 (a) - (e) reveals that the lower frequency range approximately 1.49 to 20 THz contributes most substantially to the overall EPC constant at all pressure levels. Beyond this range, particularly above 20 THz, the coupling constant stabilizes, suggesting that dominant electron-phonon interactions are confined to the 1.498 - 20 THz range. Within this range, however, the peak values of $\alpha^2F(\omega)$ exhibit noticeable pressure-dependent variations, underscoring the dynamic nature of the electron-phonon interactions under varying pressure conditions.

Figure 4.12 presents the $\alpha^2F(\omega)$ (green lines) along with the frequency dependence of the cumulative EPC parameter λ (red lines) for YHSe, calculated at (a) 0 GPa, (b)

50 GPa, (c) 100 GPa, (d) 150 GPa, and (e) 200 GPa.

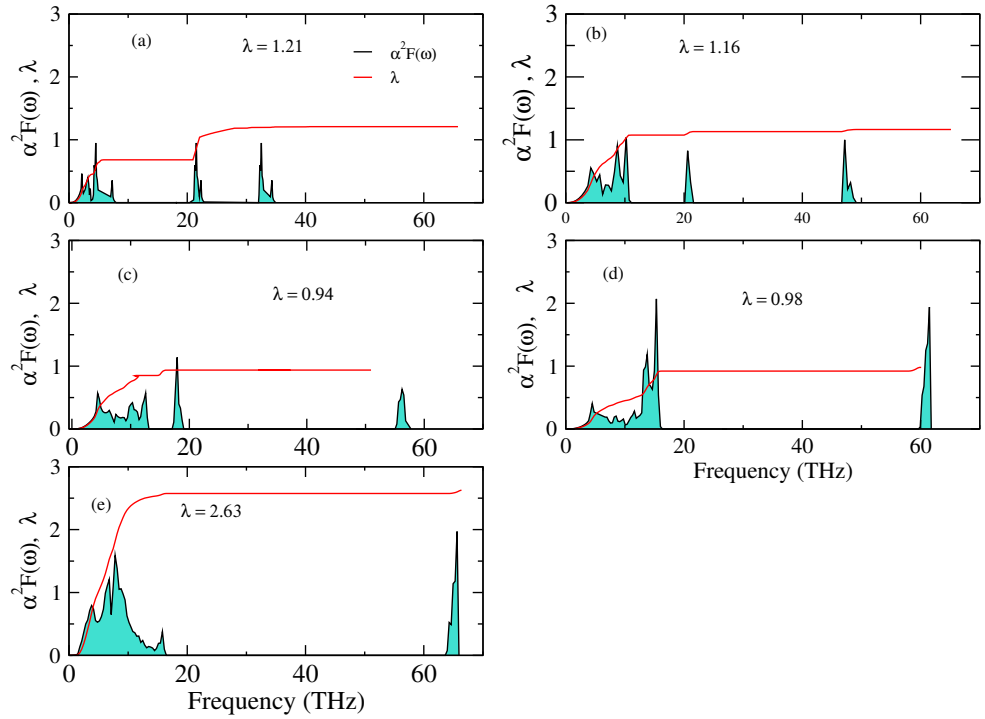

Figure 4.12: The $\alpha^2F(\omega)$ and the average EPC parameter λ for YHSe under different pressures: (a) 0 GPa, (b) 50 GPa, (c) 100 GPa, (d) 150 GPa, and (e) 200 GPa.

4.1.5 Optical Properties of YHSe

In this work, the complex dielectric function calculated for the material captures the electronic transitions induced by charge carriers interacting with electromagnetic fields. Our results reveal how these transitions vary across energy bands, providing detailed insights into the material's optoelectronic behavior.

The computed components of the complex dielectric response, $\varepsilon_1(\omega)$ and $\varepsilon_2(\omega)$, derived from TDDFT calculation, are depicted as functions of photon energy ranging from 0 to 15 eV under varying pressure conditions between 0 and 70 GPa as shown in Fig. 4.13(a) and Fig. 4.13(b). The imaginary part, $\varepsilon_2(\omega)$, which reflects the ability of the material to intake and lose electromagnetic energy, is presented in Fig. 4.13(a).This parameter is widely recognized as important for applications such as solar power harvesting and light-emitting technologies (Hasan & Hossain, 2021); however, a comprehensive conclusion requires considering additional parameters and results.

The $\epsilon_2(\omega)$ values rise from their initial levels at each pressure point. This behavior signifies interband electronic transitions, where the peak positions move toward lower photon energies with increasing pressure, suggesting a reduction in the band gap as a result of the applied pressure.

The intensity of the peaks also rises, indicating increased absorption at lower photon energies. These peaks, predominantly located within the 3 - 7 eV range, progressively shift toward lower energies as pressure increases, implying that pressure leads to band gap narrowing. Consequently, the region of maximum absorption transitions from the ultraviolet to the near-visible spectrum with increasing pressure. The computed complex dielectric functions of YHSe under various pressures are presented in Figure 4.13(a) and Figure 4.13(b).

Figure 4.13(a) displays the real component of the dielectric function, which indicates how the material reacts to an external electric field, thereby affecting optical characteristics such as refractive index, light transmission, and phenomena like reflection and refraction (Zhang, W., et al., 2016).

An upward trend is observed with increasing pressure, where the peak magnitude rises

from 21.51 at 0 GPa to 40.84 at 70 GPa, corresponding to a shift in photon energy from 1.0026 eV to 0.50 eV. A distinct peak consistently appears in the 1 - 3 eV range across all pressure levels, with its amplitude intensifying as pressure increases. This pattern indicates enhanced optical polarizability and stronger interactions between light and the material under elevated pressure. Beyond 7 eV, the curves exhibit a plateau, suggesting that high-energy photons interact less with the material, independent of the pressure applied. These observations align well with the results reported by Alouani.M and Wills.M.J (1996), who noted comparable optical behavior in Si, Ge, and GaAs subjected to hydrostatic pressure (Alouani & Wills, 1996).

The real part of the frequency-dependent dielectric function of YHSe reveals significant results. At 0 eV, the dielectric coefficient at each pressure represents the static dielectric constant. The calculated static dielectric constants, $\epsilon_1(0)$, for YHSe at different pressures are as follows: 20.27 at 0 GPa, 22.61 at 10 GPa, 25.22 at 20 GPa, 27.86 at 30 GPa, 30.55 at 40 GPa, 33.33 at 50 GPa, 36.23 at 60 GPa, and 39.24 at 70 GPa. This trend indicates that the static dielectric constant increases with pressure. The static dielectric constant elevates as the pressure intensifies, suggesting potentially enhanced charge separation abilities, which are essential for photocatalytic uses. The computed values for all prominent peaks in both the real and imaginary components of the dielectric function are presented with corresponding pressures in Table 6, covering the spectral range from 3 eV (0 GPa) to 1.5 eV (70 GPa).

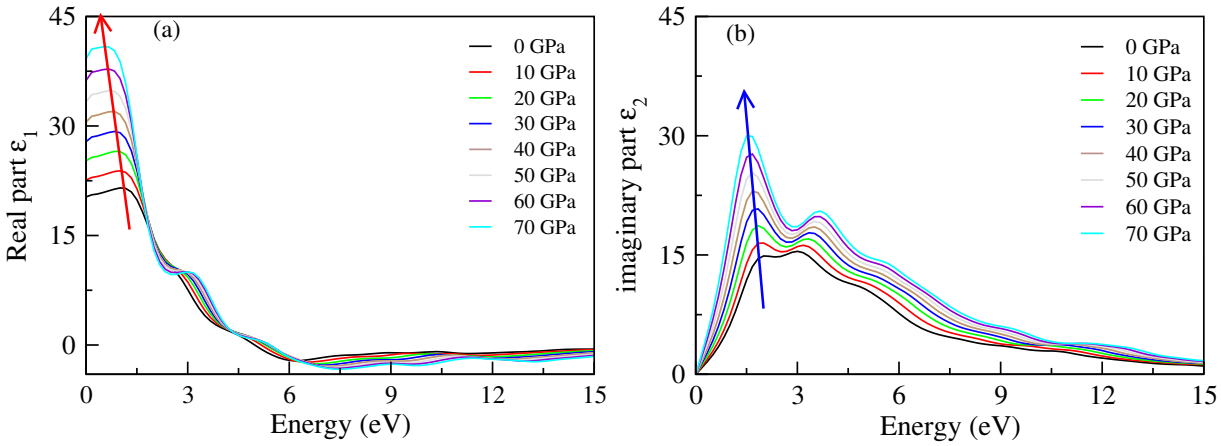

Figure 4.13: (a) Real part of the dielectric function; (b) Imaginary part of the dielectric function for YHSe under varying pressures (0, 10, 20, 30, 40, 50, 60, and 70 GPa)

The refractive index is a key optical parameter that governs how light propagates through a material, affecting its refraction, transmission, and absorption properties (Nastasenko, 2024). Figure 4.14(a) illustrates the refractive index of YHSe under various pressures. At ambient pressure, the real part of the refractive index is 4.7 at a photon energy of 1.17 eV. It increases progressively with pressure, reaching a peak value of 6.45 at 70 GPa across photon energies ranging from 0.84 to 1.17 eV. The refractive index analysis indicates that the YHSe crystal exhibits the highest refractive index of 6.45 at 70 GPa, potentially enhancing the interactions between light and the YHSe material. This rise in refractive index could improve the interactions between light and YHSe. The primary peak values at different pressures are provided in Table 6. At photon energies greater than 6 eV, the refractive index stabilizes, and the effect of pressure diminishes, suggesting that the interaction between high-energy photons and the material weakens as the energy increases. These results are consistent with previous research by Pan et al. (2014) and Iqbal.A.M. et al., (2024).

The rise in the refractive index under pressure suggests that as the pressure increases, the material becomes optically denser, leading to a further reduction in the speed of light as it traverses YHSe at lower photon energies. Based on this observation, the enhancement in refractive index with pressure can be attributed to the material's increased density, alterations in its electronic structure and polarizability, as well as enhanced optical confinement. As a result, the higher refractive index of YHSe under pressure at lower photon

energies makes it ideal for optical applications in high-pressure settings. This encompasses high-pressure sensors or optical equipment used in deep-sea or high-altitude environments where significant pressure variations occur (Runowski et al., 2019).

Additionally, the static refractive index is derived from the static dielectric constant $\varepsilon_1(0)$. The static part of the dielectric constant, $\varepsilon_1(0)$, is dependent on the material's electronic band gap, and its value at $\omega = 0$ is directly associated with $n(\omega)$ using the relation $n(0) = \sqrt{\varepsilon_1(0)}$ (Malki, S., 2024). The information provided in Table 5 reveals that the static refractive index increases as pressure is applied, reaching its peak at 70 GPa. This behavior suggests a consistent rise in the static refractive index with increasing pressure. Figure 4.14(b) presents the extinction coefficients of YHSe under various pres-

Table 5: Computed values of the $n(0)$ and $\varepsilon_1(0)$ for YHSe at various pressures.

P(GPa)	$n(0)$	$\varepsilon_1(0)$
0	4.50	20.27
10	4.75	22.61
20	5.02	25.22
30	5.28	27.86
40	5.53	30.55
50	5.77	33.33
60	6.02	36.23
70	6.26	39.24

sures examined in this study. The findings indicate that the extinction coefficient rises with increasing pressure, exhibiting a similar trend to the imaginary component of the dielectric function, with peaks observed between 5 and 15 eV. This implies that pressure enhances the material's light absorption capabilities. The primary peak values of the extinction coefficient at pressures ranging from 0 to 70 GPa are provided in Table 6 for the YHSe analysis. Table 6 lists the sharp peak values of optical properties under varying pressure conditions.

Table 6: Pressure-induced variations in the peak values of optical characteristics.

P (GPa)	$\alpha(\omega) \times 10^8$ (cm^{-1})	ε_1	ε_2	$n(\omega)$	$k(\omega)$	$R(\omega)$	$L(\omega)$
0.0	4.28	21.51	15.46	4.71	2.33	0.45	2.59
10	4.50	23.86	16.51	4.96	2.39	0.46	2.70
20	4.72	26.51	18.68	5.22	2.49	0.49	2.85
30	4.89	29.14	20.80	5.48	2.58	0.50	2.95
40	5.03	31.98	23.04	5.72	2.65	0.52	3.05
50	5.16	34.82	25.38	5.97	2.72	0.53	3.21
60	5.27	37.81	27.70	6.22	2.79	0.55	3.33
70	5.37	40.84	29.97	6.46	2.88	0.56	3.42

Figure 4.14(c) presents the absorption coefficient of YHSe under varying pressures studied in this research. The absorption coefficient is an important factor for evaluating how far electromagnetic radiation can penetrate a material. A thorough understanding of this coefficient is vital for analyzing the material's electronic properties and evaluating the effectiveness of electronic transitions across energy bands.

The analysis reveals prominent peaks in the absorption coefficient across all pressures, from 0 to 70 GPa. A notable rise is observed, with peak absorption occurring within the photon energy range of 5.844 – 7.1795 eV across all pressures. This trend suggests significant photon absorption attributed to electronic transitions.

Moreover, as pressure increases, the absorption coefficient shows a marked increase, particularly in the 5.844 – 7.1795 eV range, indicating enhanced optical absorption with higher pressure. Additionally, the absorption in the far-UV region for all pressure-induced phases shifts toward higher photon energies as pressure rises. The observed increase in absorption under pressure in this study aligns with prior investigations in other related system, including the work by Shakeel Ahmad (2023) as well as findings from Rehman et al. (2023) and Iqbal.A.M et al.,(2024).

Moreover, as pressure increases, the peak absorption coefficient shifts to higher photon energies in the UV region, indicating that pressure optimization enhances the material's optical behavior in this range. This key observation highlights the ability to dynamically

tune optical materials under pressure modulation. The observed increase in peak absorption coefficient suggests a fine-tuning process, where the optical behavior of YHSe evolves with changing pressure conditions. The major peaks computed at all pressures investigated in the study are listed in Table 6. These sharp peaks occur within the spectral range from 5.844 eV at 0 GPa to 7.1795 eV at 70 GPa.

The consistent presence of major peaks throughout this spectrum range suggests the strong absorption capabilities of YHSe material. Additionally, a sharp decrease in the absorption coefficient is observed in the high-energy region, which is characteristic of semiconductors (Hochbaum & Yang, 2010).

Figure 4.14(d) illustrates the influence of pressure on the reflectivity of YHSe. Reflectivity offers insight into how effectively a material's surface engages with electromagnetic radiation (Ahmad, Rehman, et al., 2023)(Hussain et al., 2020). Figure 4.14(d) validates the observed increase in reflectance with pressure, particularly at lower photon energies. This indicates enhanced electronic interactions and polarizability, leading to greater light reflection. Above 7 eV, a sharp decrease in reflectivity is observed, suggesting that less light is reflected at higher photon energies. At extremely high photon energies above 40 eV, reflectivity declines markedly for all pressures. This implies that the material becomes more transparent at these elevated photon energies, as its capacity to reflect light diminishes. Importantly, our results align with previous investigations on various systems by Rehman, et al. (2023), and Hussain et al. (2020). Table 6 presents a comprehensive summary of the highest peaks for different pressure levels and illustrates how reflectivity varies with pressure.

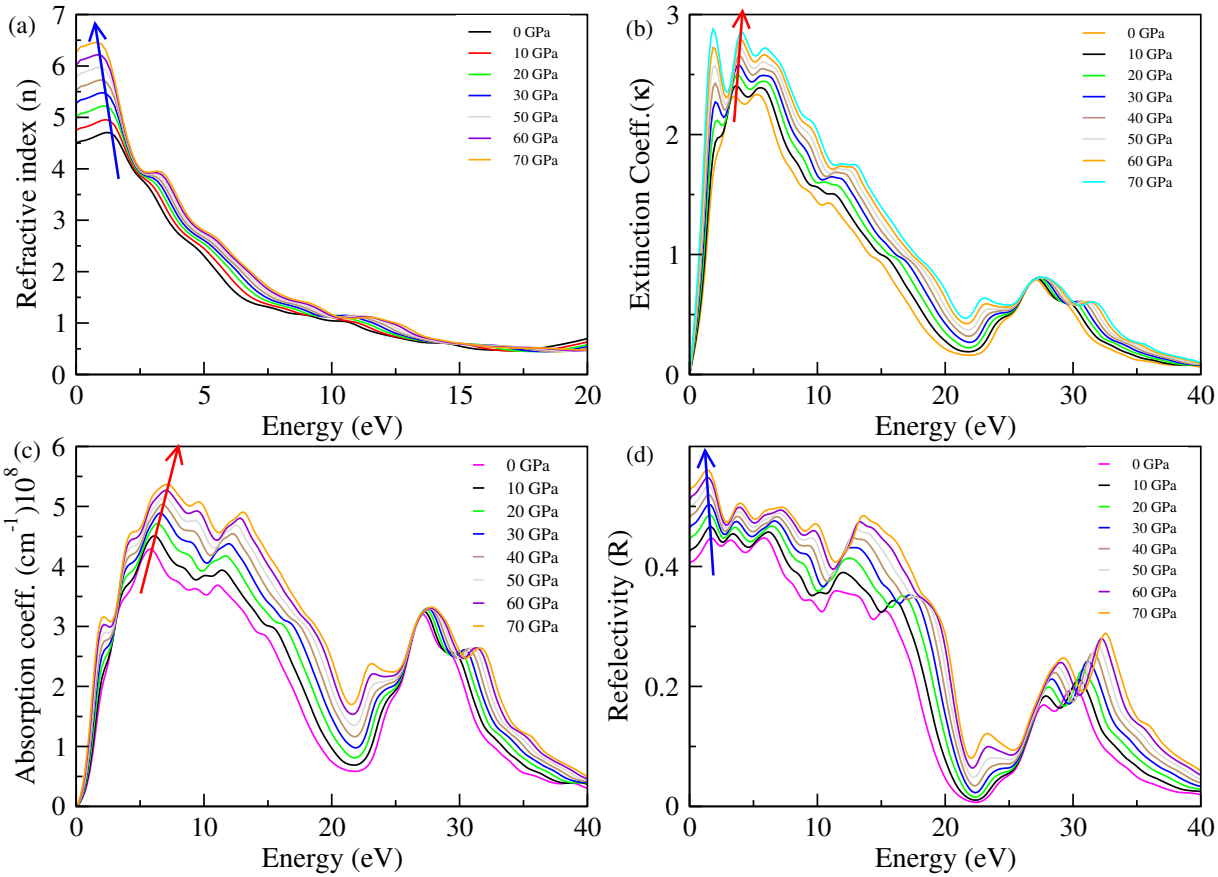

Figure 4.14: Illustration of the optical properties of YHSe under various pressures (0, 10, 20, 30, 40, 50, 60, and 70 GPa), including: (a) refractive index, (b) extinction coefficient, (c) absorption coefficient, and (d) reflectivity.

Figure 4.15 depicts the energy loss spectrum of YHSe under various applied pressures explored in this study. The loss function is essential for evaluating the energy dissipation of fast-moving electrons within a substance (Hussain et al., 2020). The location and strength of the peaks deliver important information about the material's electronic configuration and collective oscillations. Our results indicate that, within the photon energy interval from 0 eV to roughly 15 eV, the loss function remains comparatively low for all pressure values, implying limited energy dissipation in this domain. This implies that plasmonic excitation and related electronic interactions are less significant at lower photon energies. The loss function begins to rise gradually as photon energy nears 15 eV, indicating the initiation of electronic excitations that contribute to energy dissipation. A distinct peak emerges near 20 eV, indicative of a pronounced plasmon resonance, where considerable energy dissipation takes place due to collective oscillations of electrons within the com-

pound. With rising pressure, the magnitude of this peak tends to increase, accompanied by a slight displacement of the peak position toward elevated photon energy levels. This trend aligns with earlier findings by Shakeel Ahmad (2023) on the influence of uniform external pressure on the expansion of the band gap and on the mechanical, thermodynamic, and optical characteristics of rubidium niobate, explored through first-principles simulations for photocatalytic purposes (Rehman, et al., 2023) and (Iqbal.A.M. et al., 2024). This pattern implies that under compressive stress, the material exhibits greater susceptibility to plasmon excitation at high photon energies, with the spectral shift ascribed to variations in the electronic band structure and charge density. The dominant loss function peaks corresponding to each pressure level are detailed in Table 6. Additionally, in the present analysis, a higher ϵ_2 value corresponds to a lower energy loss function, which is a defining attribute of semiconducting materials. This conclusion corroborates prior work by Shakeel Ahmad (2023)(Ahmad, Rehman, et al., 2023).

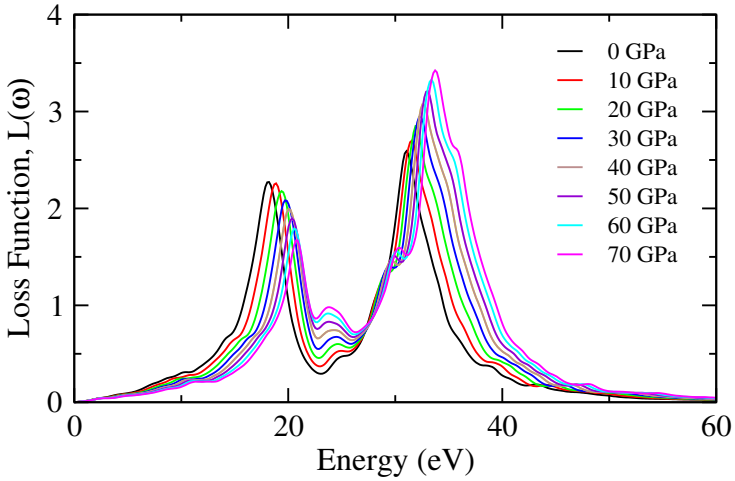

Figure 4.15: Electron energy loss function of YHSe under various applied pressures (0, 10, 20, 30, 40, 50, 60, and 70 GPa).

4.1.6 Thermoelectric Properties

The performance efficiency of thermoelectric compounds is generally quantified using the Seebeck coefficient, also referred to as thermopower (Pei et al., 2013). The dependence of the Seebeck coefficient (S) on temperature under various pressure scenarios is presented in Fig. 4.16. As depicted, the Seebeck coefficient of YHSe tends to rise with increasing temperature and eventually reaches a plateau at elevated temperatures due to the saturation in carrier excitation levels.

As depicted in Fig.4.16, the Seebeck coefficient diminishes with escalating pressure due to the increase in charge carrier density (n). This pattern is consistent with the results of (Kulwinder Kaur et al., 2016) regarding the pressure influences on the electronic and thermoelectric characteristics of magnesium silicide using density functional theory (Kaur & Kumar, 2016). At elevated pressures, the narrowing of the energy gap enhances the charge carrier density, resulting in a decreased Seebeck coefficient. This phenomenon is more pronounced at 200 GPa, where the energy gap is further diminished, rendering the material more conductive and leading to a reduced Seebeck coefficient.

The effective mass is inversely related to the curvature of the E versus k graph, implying that a more level band (lower curvature) leads to a higher effective mass, while a steeper band (higher curvature) corresponds to a smaller effective mass (Ashcroft, N. W., & Mermin, N. D., 1976).

The amplified Seebeck coefficient at 0 GPa is probably attributed to the greater effective mass of the carriers compared to 100 GPa, which arises from a less dispersive band (lower curvature) in the electronic structure of the YHSe system.

This higher effective mass compensates for the decrease caused by the higher carrier concentration, sustaining a higher Seebeck coefficient at lower temperatures. However, as the temperature rises, the Seebeck coefficients at 0 GPa and 100 GPa gradually converge, showing minimal fluctuation. Furthermore, the positive sign of the Seebeck coefficient indicates that YHSe is a P-type semiconductor, meaning that conduction primarily occurs due to the motion of holes. This implies that the majority charge carriers in this temperature range are holes, making the YHSe compound an excellent electrical charge

transport material, behaving as a p-type material within the temperature range of 50 - 800 K. Figure 4.16 illustrates the temperature dependence of the Seebeck coefficient of YHSe under varying pressures.

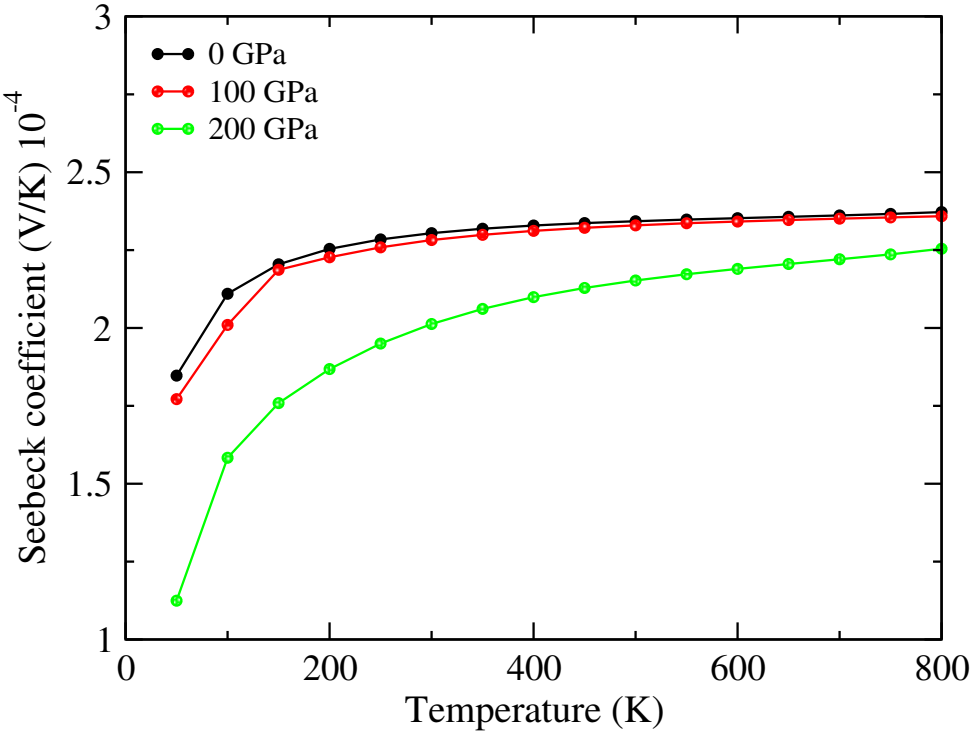

Figure 4.16: Seebeck coefficient (T) of YHSe subjected to different pressures.

Figure 4.17 shows how the electrical conductivity of YHSe varies with temperature at various pressures. Materials with high electrical conductivity are preferred for thermoelectric uses because they help reduce Joule heating (Wang & Yu, 2019). The electrical conductivity rises as both pressure and temperature increase from 50 to 800 K, since elevated temperatures supply energy to charge carriers, allowing more electrons and holes to traverse the band gap. This behavior likely results from the increased thermal excitation of charge carriers, enhancing conductivity as temperature rises. The positive correlation between temperature and electrical conductivity suggests that as temperature increases, conductivity also rises. In semiconductors, this trend typically arises from enhanced thermal excitation of charge carriers, which boosts conductivity (Marschall, 2014). Furthermore, higher pressure seems to improve the electrical conductivity of the material, which may be attributed to modifications in the electronic band structure or increased

carrier mobility under compression. This observation is consistent with earlier studies on how pressure influences the electronic and thermoelectric properties of magnesium silicide, as reported by Kulwinder Kaur and Ranjan Kumar (2016) through first-principles calculations (Kaur & Kumar, 2016).

Furthermore, a higher effective mass enhances the Seebeck coefficient but reduces carrier mobility (μ), lowering electrical conductivity. At 0 GPa, higher carrier concentration and effective mass result in lower mobility, whereas at 100 GPa, increased mobility compensates for lower carrier concentration, leading to slightly higher electrical conductivity.

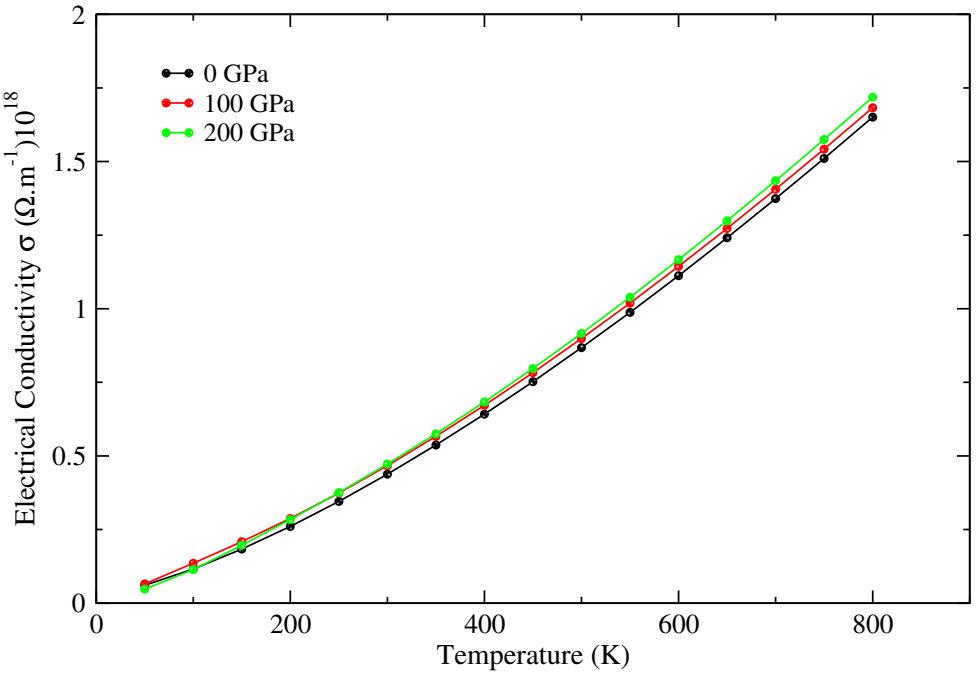

Figure 4.17: Electrical conductivity of YHSe as a function of temperature at different pressure levels.

Figure 4.18 demonstrates that the power factor rises as the temperature increases across all pressures, suggesting that pressure positively influences thermoelectric efficiency. The figure shows a steady rise in the power factor (PF) in relation to temperature approaches 800 K under all pressure conditions. This indicates that YHSe's thermoelectric efficiency improves at higher temperatures, making it well-suited for use in high-temperature applications. In this study, an increase in carrier concentration at 200 GPa results in a lower Seebeck coefficient, which in turn causes a decrease in the power factor. This pressure-induced degradation of thermoelectric performance, attributed to increased carrier concentration and reduced Seebeck coefficient, is consistent with the findings of Kaur and Kumar (2016), who reported a similar trend in magnesium silicide under high pressure using first-principles calculations (Kaur & Kumar, 2016). In semiconductors, overall thermal conductivity is determined by both electronic free carrier contributions and phonon (Y. Li et al., 2016).

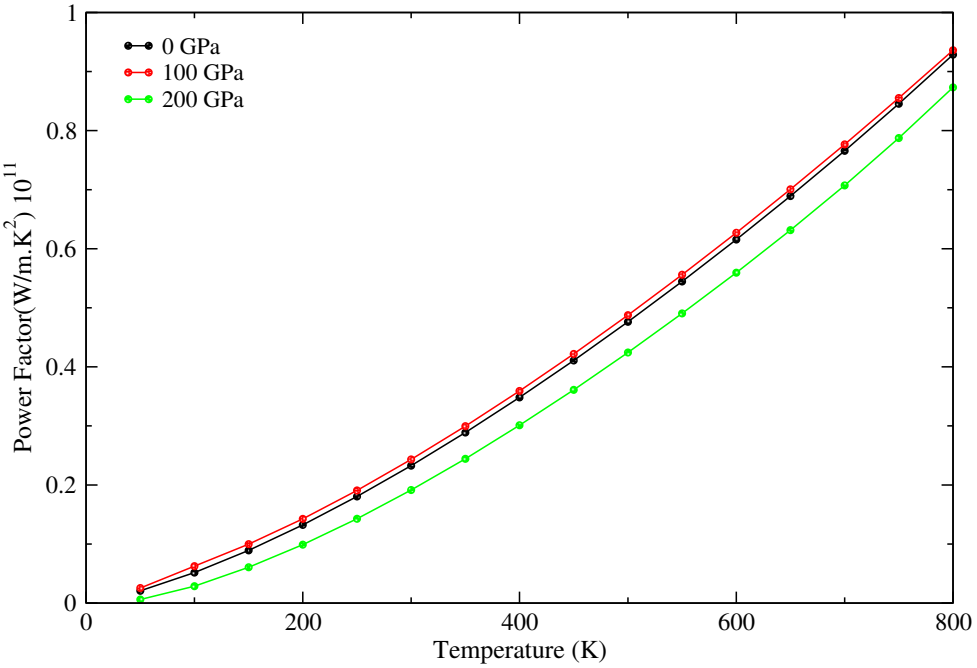

Figure 4.18: Power factor of YHSe as a function of temperature at different pressure levels.

Fig. 4.19 shows that the electronic heat conductivity (κ) increases with temperature at all pressures examined in this study, displaying an almost exponential growth for each

pressure level. This suggests that as the temperature rises, the material's capacity for heat conduction increases significantly. Moreover, the rise in electronic thermal conductivity increases with temperature because to increased carrier activity, which enhances the electronic contribution to heat conduction. The study reveals that, at low temperatures, the electronic thermal conductivity curves overlap, indicating that electronic thermal conductivity relatively unaffected by pressure in this regime. This suggests that the number of thermally activated charge carriers and the scattering mechanisms are not significantly influenced by pressure at low temperatures. The electronic thermal conductivity rises with temperature in a exponential manner. It is affected by carrier energy and scattering mechanisms, both of which increase as temperature rises. In this context, thermal conductivity is primarily determined by electronic structural characteristics and the Fermi density of states. This finding aligns with a recent investigation by Kulwinder Kaur and Ranjan Kumar (2016), which explored the effects of pressure on the electrical and thermoelectric properties of magnesium silicide through first-principles calculations.

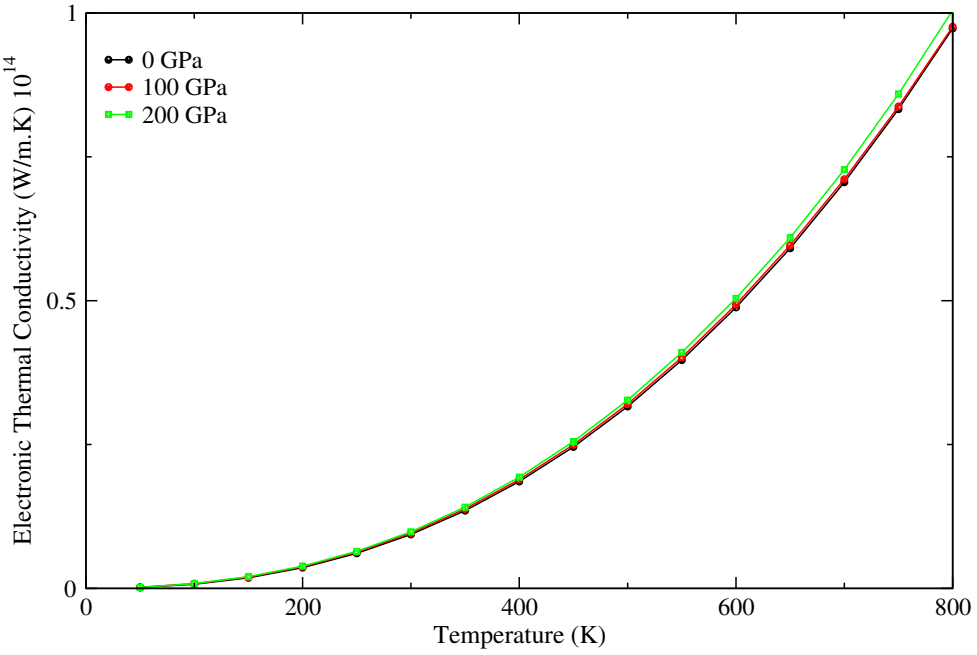

Figure 4.19: Electronic thermal conductivity versus temperature for YHSe under varying pressures.

The Fig.4.20 depicts the phononic impact on thermal conductivity in relation to temperature at three distinct pressures 0, 100, and 200 GPa. In Figure 4.20 (a) in temperatures near to 100 K the phonon heat conductivity is nearly zero. This behavior is expected due at low temperatures up to 100K, the available thermal energy is insufficient to excite a significant number of phonons. Since phonons are the primary heat carriers in insulators and semiconductors like YHSe, their limited presence results in minimal phonon heat conductivity. As the temperature rises, the growth in lattice thermal conductivity slows down, suggesting a possible saturation effect. In Figure4.20 (a), the lattice heat conductivity initially rises with temperature, reaching a peak, after which it decreases this is a result of increased phonon-phonon interactions at elevated temperatures. This temperature-dependent behavior, particularly the decline in thermal conductivity at elevated temperatures as a result of enhanced phonon scattering, is consistent with previous findings on pressure effects in bulk CdSe, as reported by Mamand et al. (2024).

Pressure significantly influences the alteration of phonon heat conductivity and other material characteristics (Hou et al., 2014). For 100 and 200 GPa at very low temperatures, lattice thermal conductivity starts with relatively high values and decreases sharply as the temperature increases. This behavior is typical for phononic thermal conductivity, as at low temperatures, phonon scattering is minimal, and the phonon mean free path is longer, leading to higher lattice thermal conductivity. From these findings, in Fig.4.20 (b), as scattering increases, it diminishes the phonon mean free path, leading to a subsequent effect and consequently decreasing the phonon heat conductivity. Our calculated results show that at 100GPa, phonon transport is more efficient than at 200GPa, though still significantly reduced compared to 0GPa. At 200GPa, the phonon thermal conductivity is more strongly suppressed, indicating enhanced phonon scattering as a result of increased pressure. This suppression reflects strong phonon-phonon interactions, likely driven by high anharmonicity under extreme compression. These findings are in good agreement with previous studies by Mamand et al. (2024), which reported pressure-induced suppression of phonon heat conductivity in CdSe due to intensified lattice vibration scattering mechanisms. The trends observed indicate that raising the pressure from 0 GPa to 200 GPa results in a notable decrease in lattice thermal conductivity.

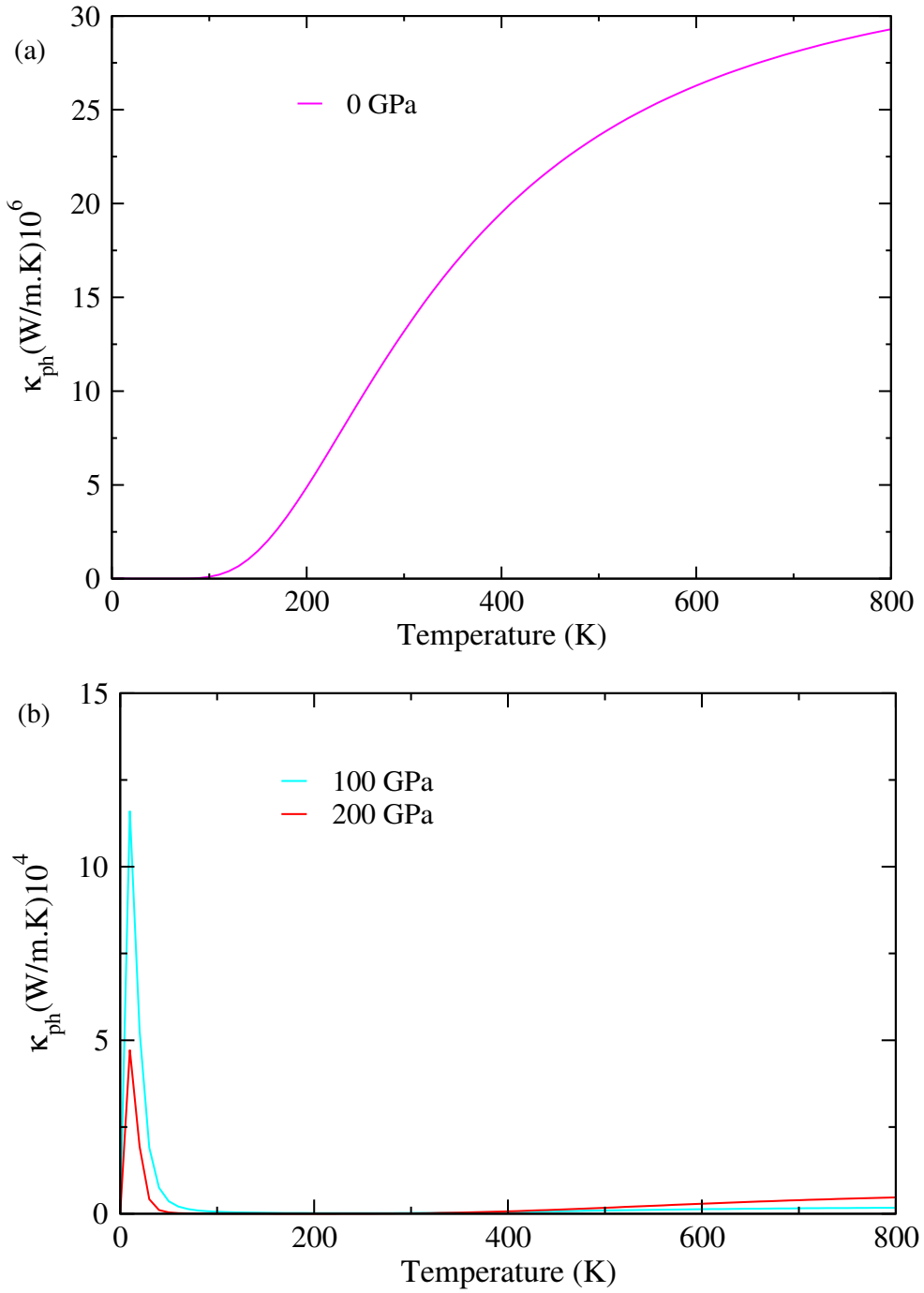

Figure 4.20: The phononic component of thermal conductivity for YHSe is shown under different pressures: (a) at 0 GPa, and (b) at 100 and 200 GPa.

Figure4.21 illustrates the ZT values in relation to temperature for Yttrium Hydrogen Selenide at pressures of 0, 100, and 200 GPa. The study examines the dimensionless thermoelectric ZT for YHSe under three different pressure scenarios, with calculations performed for temperatures ranging from 50 to 800 K. At lower temperatures, the ZT

values are generally low across all pressure levels. This is attributed to a lower Seebeck coefficient and electrical conductivity, along with a greater phonon contribution to thermal conductivity, which diminishes the overall thermoelectric efficiency. At 0 GPa, ZT slightly increases with temperature and stabilizes around 200 K, indicating balanced transport properties suitable for thermoelectric applications. Starting from relatively lower values at 0 GPa and 200 GPa, the ZT value raise with pressure and peaking at 0.78 at 100 GPa. This enhancement is primarily attributed to a reduction in carrier concentration, which improves the Seebeck coefficient and reduces the lattice heat conductivity.

However, at 200 GPa, ZT declines due to higher carrier concentration, which lowers the Seebeck coefficient. These findings, consistent with previous studies (Kaur & Kumar, 2016), highlight the potential for pressure optimization in thermoelectric materials.

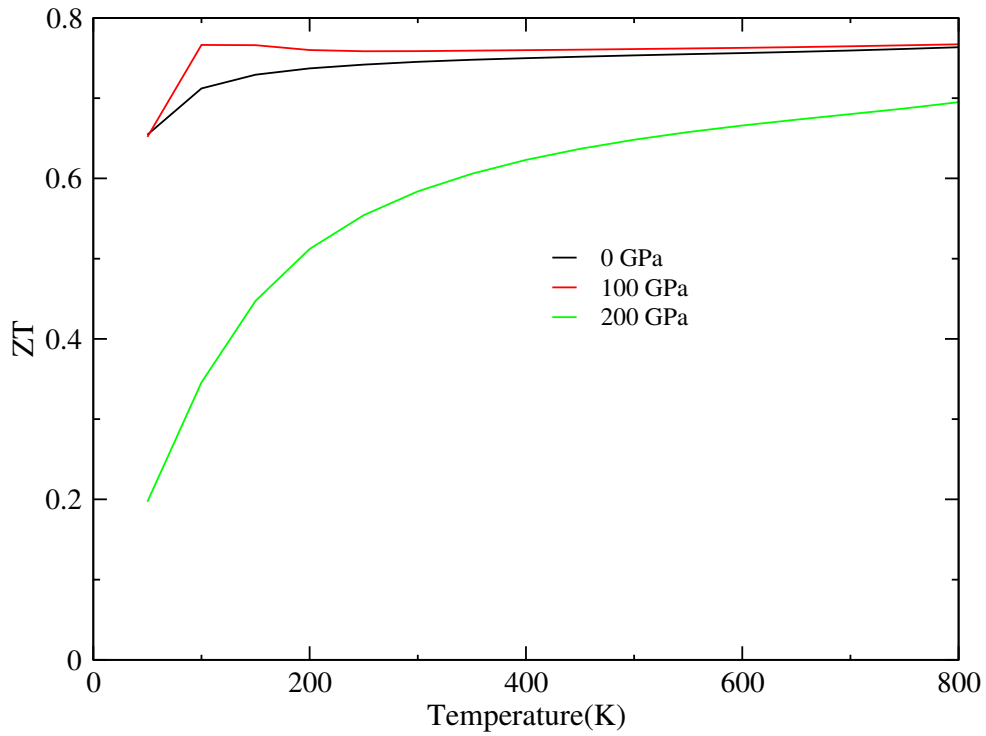

Figure 4.21: The relationship between temperature and the figure of merit (ZT) of YHSe is shown under different pressure conditions.

The impact of pressure on carrier concentration in materials can be significant, as pressure alters the electronic structure, lattice parameters, and other inherent characteristics of the substance (C. Li et al., 2022). Figure4.22 depicts that as pressure increases, the initial carrier concentration at low temperatures also increases. The rate of increase in carrier concentration with temperature diminishes as pressure increases, with the curve at 200 GPa showing minimal response to temperature. This behavior indicates that, under high pressure, the material's electronic properties become less sensitive to thermal excitation, leading to a more stable carrier concentration across a wide temperature range. The stabilization of carrier behavior due to pressure is in line with the results of (Guo et al., 2013), who observed a decrease in the temperature dependence of electronic transport properties when subjected to high-pressure conditions. At higher pressures, band gap narrowing increases carrier concentration. This effect is stronger at 200 GPa, where the band gap is further reduced, making the material more metallic and leading to increases a carrier concentration. In contrast, at a pressure of 100 GPa, the alterations in the band structure due to pressure lead to a decrease in the density of states close to the Fermi level, resulting in a minor reduction in carrier concentration.

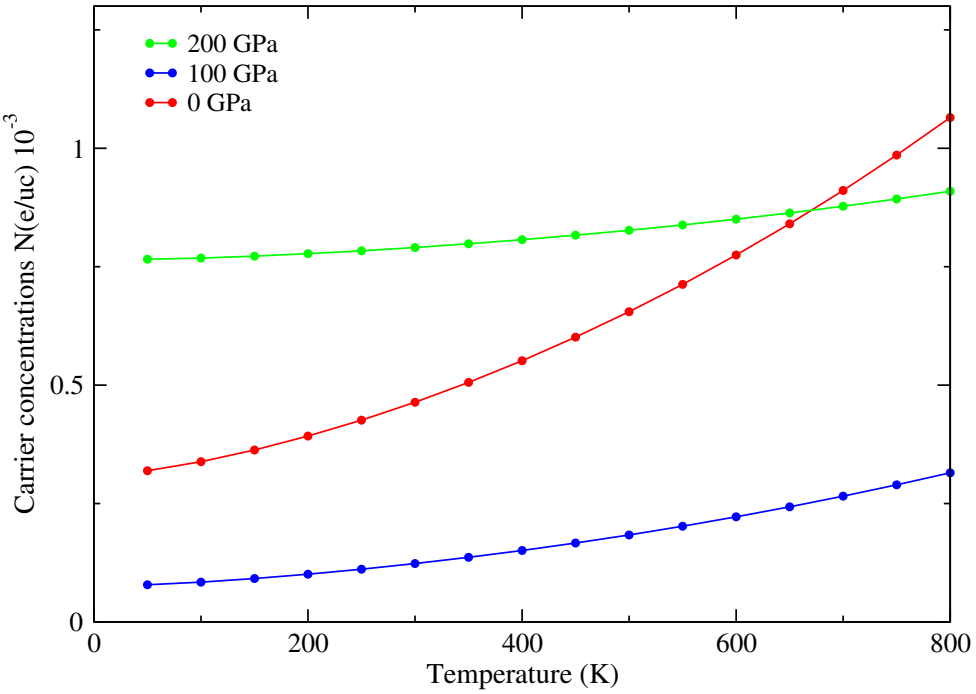

Figure 4.22: Carrier concentration versus temperature of YHSe under varying pressures.

Figure 4.23 illustrates how specific heat capacity varies with temperature at various pressures. As pressure rises from 0 to 200 GPa, the specific heat capacity values decrease. This pattern suggests that increased pressure compresses the lattice structure, which restricts the vibrational states available for energy storage, resulting in a lower specific heat capacity. When pressure is applied to YHSe, it alters the electronic structure, causing a decrease in the density of states (DOS) at the Fermi level. This decline in the density of states at the Fermi energy in YHSe is linked to the observed reduction in electronic specific heat (c) with higher pressure, as depicted in Fig. 4.23. The decline in DOS implies that fewer states are available for charge carriers, meaning less thermal energy can be absorbed, thus reducing the specific heat. This results in a lower capacity to store thermal energy. The reduced specific heat capacity at 100 and 200 GPa suggests that the material has a lower number of DOS at the Fermi level, as it absorbs less heat with increasing temperature.

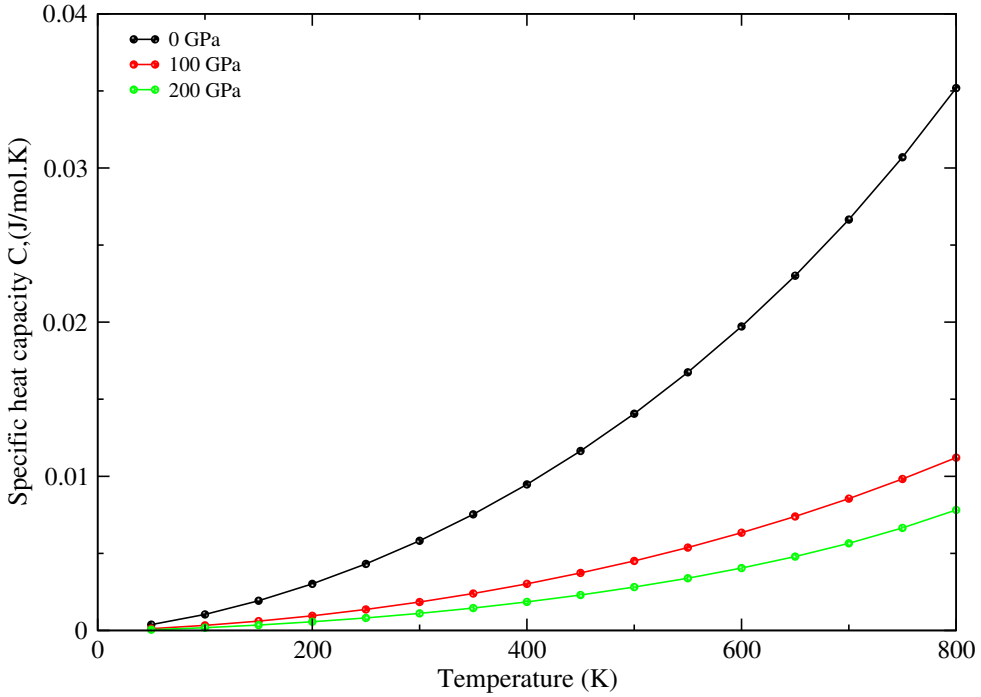

Figure 4.23: The specific heat capacity varies with temperature at different pressures.

4.2 The Effects of Doping on the Properties of YHSe.

4.2.1 Structural Properties

The optimized unit-cell parameters for the hexagonal crystal structure of YHSe at ambient pressure are found to be $a = b = 3.81\,\text{Å}$, $c = 3.87\,\text{Å}$, with a corresponding unit-cell volume of $V = 56.2\,\text{Å}^3$. Subsequently, the structural properties of $La_xY_{1-x}HSe$ (x = 0, 0.125, 0.25, 0.375, and 0.5) were optimized to investigate the effects of La doping on the lattice geometry. These results reveal systematic structural modifications with increasing La concentration, offering valuable insights into the influence of substitutional doping on the host lattice. Figure 4.24 displays the optimized crystal structures for various La concentrations: (a) at $x = 0\%$, (b) at $x = 12.5\%$, (c) at $x = 25\%$, (d) at $x = 37.5\%$, and (e) at $x = 50\%$, La concentration. As a relaxed parameter, the lattice parameters for YHSe with La dopants are optimized while fixing the pressure. The lattice parameter c

Table 7: Optimized lattice parameters and volume of La-doped YHSe at various La concentrations.

La (x)	$a = b$ **(Å)**	c **(Å)**	**Volume (Å^3)**
0.125	6.17	6.45	245.5
0.25	6.28	6.51	256.36
0.375	6.18	6.63	252.9
0.5	6.13	6.80	255.1

increases from 6.45 Å to 6.80 Å as the lanthanum concentration rises from 0.125 to 0.5. This data shows that the ratio of c/a increases with increasing La concentration. The increase in lattice parameters suggests that the introduction of La atoms, which are larger than Y atoms, induces a slight expansion of the unit cell. This expansion, especially along the c-axis, is associated with a greater distance between atoms. The rise in the c/a ratio due to La doping probably impacts the crystal's anisotropy, which may in turn influence its mechanical properties.

A higher c/a ratio often signifies material response variations to stress depending on the axis direction compared to the $a - b$ plane. This anisotropy could result in direction-

dependent mechanical properties, such as tensile strength or shear resistance, which may be advantageous for designing materials for specific structural applications.

Additionally, the expansion of the lattice could impact the material's thermal properties, particularly its thermal conductivity. Our results suggest that as the lattice expands, increased phonon scattering due to larger atomic spacing could contribute to the observed a significant decrease in heat conductivity. This interpretation is supported by the findings of (Chen.Z. et al., 2018), who reported a similar trend in which lattice expansion enhances phonon scattering, thereby lowering thermal conductivity.

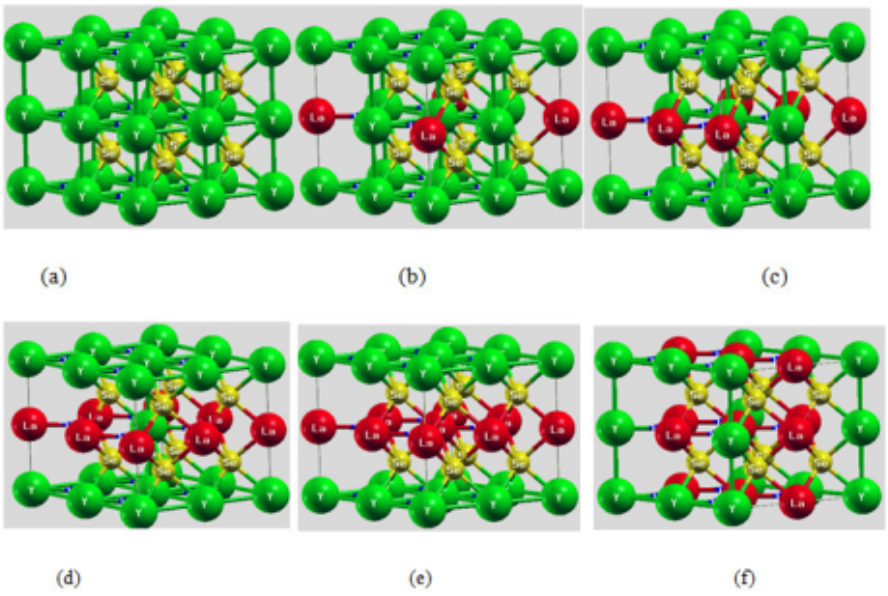

Figure 4.24: Optimized crystal structure of $La_xY_{1-x}HSe$ at (a) x = 0%, (b) x = 12.5%, (c) x = 25%, (d) x = 37.5%, and (e) x = 50% .

4.2.2 Electronic Structure

The electronic properties of a material are determined by the behavior of its electrons. The electronic band structure and the density of states characteristics of a material provide insight into its electronic response (Hochbaum & Yang, 2010). Figure A.1 (a) through Figure A.1 (f) (see Figure A.1 (a) through Figure A.1 (f) in Appendix) display the electronic band structures of both pristine and La-doped YHSe along main symmetry directions.

Our research, exemplified by the accompanying figures, centers on the electronic band structure of YHSe and La-doped YHSe materials, with emphasis on the valence and conduction bands' behavior. Notably, as shown in Fig. A.1 (a), the valence band maximum is located at the high-symmetry A point, while the conduction band minimum appears at the Γ point, confirming the presence of an indirect band gap. However, as illustrated in Fig. A.1 (b),(see Fig. A.1 (b) in Appendix) the material exhibits a direct band gap, indicated by the coincident wave vectors of the highest valence band and lowest conduction band energies.

La doping appears to induce a transition from an indirect to a direct band gap within YHSe, concurrently decreasing the band gap width. We employed GGA and GGA+U approximations to explore the influence of La concentration on the electronic properties and gain a deeper understanding of the underlying mechanisms. Using linear response theory, the Hubbard U parameters for yttrium and lanthanum were determined to be 2.00 eV and 1.28 eV, respectively. Density functional theory calculations employing the GGA functional predict a band gap of 1.52 eV for the undoped YHSe structure ($x = 0$). This value decreases with increasing La concentration, reaching 1.159 eV at $x = 0.125$ and continuing to diminish to 0.57 eV and 0.25 eV for $x = 0.25$ and $x = 0.5$, respectively. For the fully doped case ($x = 1$), the band gap increases to 1.87 eV. Similar calculations performed with the GGA+U approach, which accounts for on-site Coulomb interactions, yield consistently higher band gap values of 1.37 eV ($x = 0$), 1.17 eV ($x = 0.125$), 0.86 eV ($x = 0.25$), 0.51 eV ($x = 0.5$), and 2.01 eV ($x = 1$).

Electronic structure calculations employing the GGA+U method demonstrate a distinct shift in the conduction band minimum at $x = 0.375$ La concentration, indicating

a significant modification of the electronic structure under this correction scheme. This trend is consistent with previous findings, which indicate that the U parameter causes a shift in the conduction band minimum (Habura, K. H. et al., 2024). These results clearly demonstrate a systematic narrowing of the band gap with increasing La doping, indicating enhanced electronic delocalization and the potential for tuning the material toward semimetallic behavior. This trend indicates a significant modification in the electronic structure due to La doping, likely driven by enhanced hybridization between La states and the host material. The introduction of La atom into the system can create additional energy levels (localized energy state) within the band gap because of differences in electronic configuration and atomic size between La and Y. These new states can lead to bandgap narrowing of the pure YHSe crystal. The concentration of La, therefore, plays a critical role in determining the energy band gap of the material.

Unlike indirect band gaps, where momentum change is required for electronic transitions, a direct band gap allows efficient optical excitation, enhancing light absorption and emission. This property is vital for optoelectronic applications, including LEDs and laser technologies (Kovác et al., 2008), as direct band gap materials exhibit superior optical performance compared to their indirect counterparts.

The introduction of La into YHSe reduces the band gap due to the emergence of localized states, and at high La concentrations, the material exhibits narrow-gap characteristics and tends toward metallic behavior. This ability to tune the electronic properties is valuable for applications requiring precise control over the material's optical response. As illustrated in Fig. A.1 (b) - (e), doping with lanthanum at the yttrium site modifies the electronic band structure. Specifically, incorporating a heavier element at the A cation site leads to a decrease in the conduction band minimum and an increase in the valence band maximum (San et al., 2005). As the concentration of La increases from 0.125 to 0.5, the valence band maximum shifts towards higher energies, and the conduction band minimum shifts towards lower energies. Shifting from band structure analysis to the density of states provides insights into available energy states and elemental contributions to the electronic structure. Fig. A.1 (a) shows the partial DOS for pristine YHSe, serving as a reference. Fig. A.1 (b) through Fig. A.1 (e) then depict the PDOS with La doping at

Table 8: Calculated energy band gaps of La-doped YHSe at different La concentrations using GGA and GGA+U .

La (x)	**GGA (eV)**	**GGA+U (eV)**
0	1.52	1.66
0.125	1.16	1.17
0.25	0.57	0.86
0.375	0.54	0.75
0.5	0.25	0.51
1	1.87	2.01

constant pressure, revealing doping-induced changes.

In pure yttrium hydrogen selenide Fig. A.1 (a), Y atoms contribute more to the conduction band DOS than Se and H, suggesting Y's role in forming this band. Conversely, Se atoms dominate the valence band DOS, implying their key contribution to the valence band. The Y and Se overlap in the valence band indicates hybridization, suggesting some covalent bonding between these atoms. Doping of materials, in general, can change their electronic properties (Zunger & Malyi, 2021).

In Fig. A.1 (b), the total density of states is composed of contributions from Y, La, Se, and H atoms. Consistent with earlier observations, the total density of states generally increases as the La concentration rises from 0 to 0.125. At this lower concentration, the contribution of La to the electronic density of states in both the valence and conduction bands is relatively small compared to that of Y and Se.

However, as the La concentration is further increased, as illustrated in Fig. A.1 (b) through Fig. A.1 (f), La's contribution to the electronic density of states becomes progressively more significant in both the valence and conduction bands. This increasing La contribution results in an enhanced total electronic density of states near the Fermi energy in both the conduction and valence bands. For La concentrations exceeding (x = 0.25), La's contribution to the total electronic density of states in the conduction band becomes particularly prominent, leading to a substantial increase in the total electronic density of states specifically near the Fermi energy. This suggests that La doping modifies the electronic properties (Zunger & Malyi, 2021) and can significantly influence the material's

conductivity and other related characteristics. The ability of dopants to modify materials can be leveraged to tune electron transport (Kundu et al., 2023). In some instances, the Fermi level can be pinned within the valence band depending on impurity concentrations (Skipetrov et al., 2004).

Figure A.1 (a) - (e) show that for lanthanum concentrations ranging from 0 to 0.5, the total density of states at the Fermi energy remains zero, confirming a semiconducting nature. Furthermore, at elevated concentrations of La exceeding $x = 0.25$, the augmented contribution of La to the density of states, particularly within the conduction band, culminates in a reduction of the band gap. As the band gap diminishes, the material exhibits enhanced conductivity.

4.2.3 Optical Properties

The presence of a band gap in YHSe contributes to its unique optical properties. The addition of La doping in YHSe further modifies its optical characteristics for different uses. Figure 4.25 (a) illustrates the real part of the dielectric function of La-doped YHSe for different La concentrations: (a) $x = 0\%$, (b) $x = 12.5\%$, (c) $x = 25\%$, (d) $x = 37.5\%$, (e) $x = 50\%$. The real dielectric constant measures the slowing down of light as it moves through a substance, with greater values signifying potential uses in optical coatings (Awada et al., 2020). For the unaltered sample, the real component of the dielectric function reaches an outstanding peak value of ϵ_1 at a photon energy of 0. 1679 eV, as illustrated in Fig.4.25 (a). This prominent peak indicates robust interactions with external electric fields.

As La is added to YHSe, significant changes in the real component of the dielectric function are noted. The primary peak values of the real component of the dielectric function at varying La concentrations are shown in Table (4). These results imply that doping with La can cause fluctuations in the behavior of the real component of the dielectric function, influenced by specific electronic transitions and La's impact on the electronic structure. The incorporation of La modifies the electronic density and local bonding environment, subsequently affecting how electrons respond to the applied electric field.

The imaginary portions of the dielectric function of La-doped YHSe at various La

concentrations are shown in Fig.4.25(b): (a) $x = 0\%$, (b) $x = 12.5\%$, (c) $x = 25\%$, (d) $x = 37.5\%$, (e) $x = 50\%$. The imaginary dielectric constant quantifies a dielectric material's energy absorption and storage capacity in an electric field as a result of dipole movement (Awada et al. , 2020). A high imaginary dielectric constant suggests possible uses in charge storage capacitors (Awada et al., 2020). The imaginary component of the dielectric function for pure yttrium hydrogen selenide peaks at a value of $\epsilon_2 = 68.22$ at a photon energy of 1.17 eV. The imaginary part of the dielectric function shows significant changes when La is doped at percentages of $x = 12.5\%$, $x = 25\%$, $x = 37.5\%$, $x = 50\%$. The respective photon energy peaks are 5.51 eV, 5.009 eV, 3.67 eV, 3.34 eV. Compared to the pristine material, these numbers show a slow movement toward the low-energy region (red shift) as the La concentration increases, remaining inside the UV range. In addition, the imaginary curve's peak suggests an absorption band, which shows energy ranges in which the YHSe substance is more likely to absorb photons. Table (4) shows the primary peak values of the imaginary component of the dielectric function at various La concentrations. The observed trend in this study reveals that as La concentration increases, the imaginary part of the dielectric function rises, while the peak positions shift toward lower photon energies. This behavior is likely attributed to band gap narrowing and enhanced interband transitions induced by La incorporation.

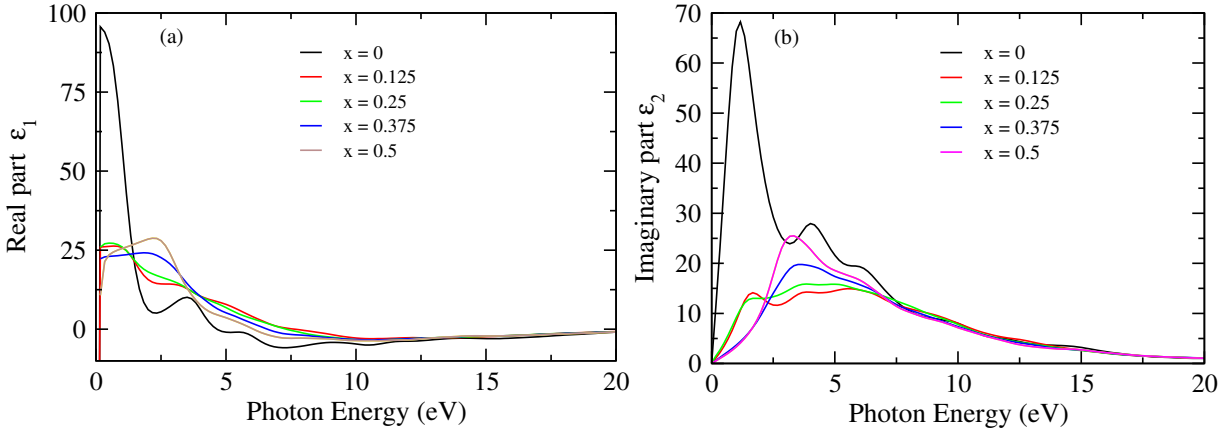

Figure 4.25: (a) Real and (b) imaginary parts of the dielectric function of La-doped YHSe at different La concentrations.

Figure 4.26 illustrate the absorption coefficient of La doped YHSe at various La concentrations. The absorption coefficient in the UV region is a crucial optical property, determining its suitability for different applications (Ijaz & Zafar, 2021). As the La concentration increases, the absorption coefficient fluctuates within the UV wavelength range. As La is incorporated into YHSe at concentrations of $x = 12.5\%$, $x = 25\%$, $x = 37.5\%$,and $x = 50\%$, the absorption coefficient exhibits notable variations. The peak values correspond to photon energies of 6.845 eV, 10.1 eV, 11.1 eV, and 9.87 eV respectively. These values are in the UV range but have small variations. The peak position on the absorption graph corresponds to electronic transitions from the valence to conduction bands. This trend implies that La doping has a major influence on the material's optical properties, most likely due to changes in the electronic structure and absorption mechanisms.

The main peak values of the absorption coefficient at different La concentrations are presented in Table (4).

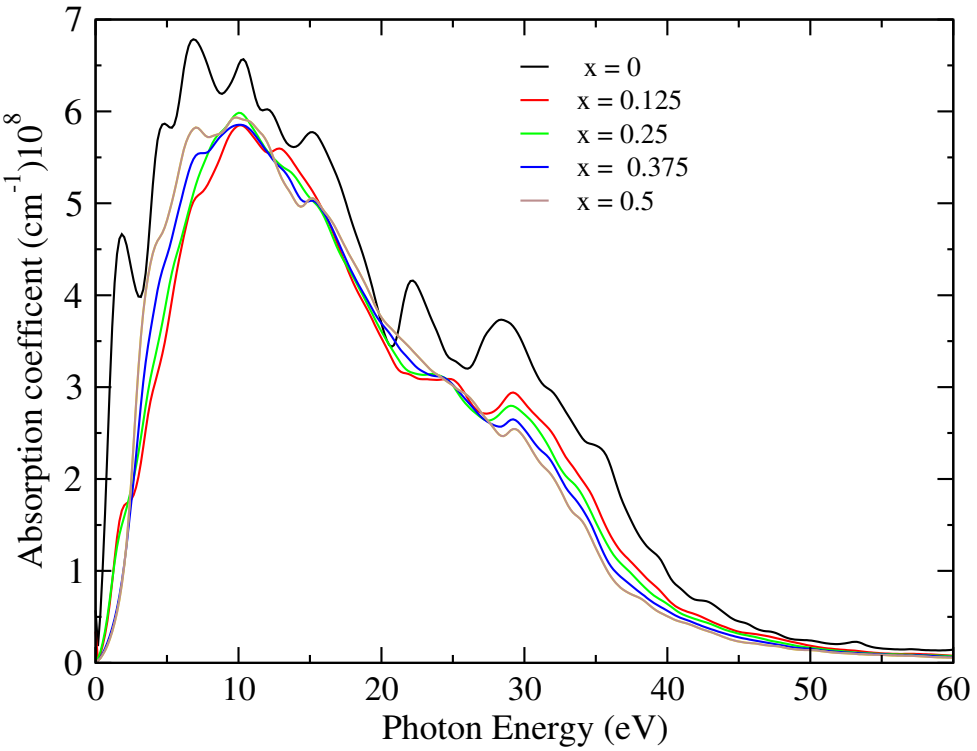

Figure 4.26: Absorption coefficient of La-doped YHSe at different La concentrations.

Figure4.27 shows the refractive index of La-doped YHSe at various La concentrations. In pristine YHSe, the real part of the refractive index (n) is notably high, reaching a peak value of 9.8 at a photon energy of 0.168 eV. This high refractive index indicates strong light-matter interaction and significant optical confinement, suggesting a dense and highly polarizable ectronic structure within the YHSe material. As La is incorporated into YHSe at concentrations of 0.125, 0.25, 0.375 and 0.5 the refractive index exhibits notable variations. The corresponding peak values are observed at 5.16 (0.84 eV), 5.24 (0.67 eV), 5.0094 (2.17 eV) and 5.53 (2.51 eV) respectively. This trend indicates a systematic shift in the peak positions of the refractive index with increasing La concentration, highlighting its dependence on photon energy. The main peak values of the refractive index at different La concentrations are presented in Table (4). Moreover, this enhancement of the refractive index could improve the interaction between light and YHSe, leading to enhanced photo absorption. applications.

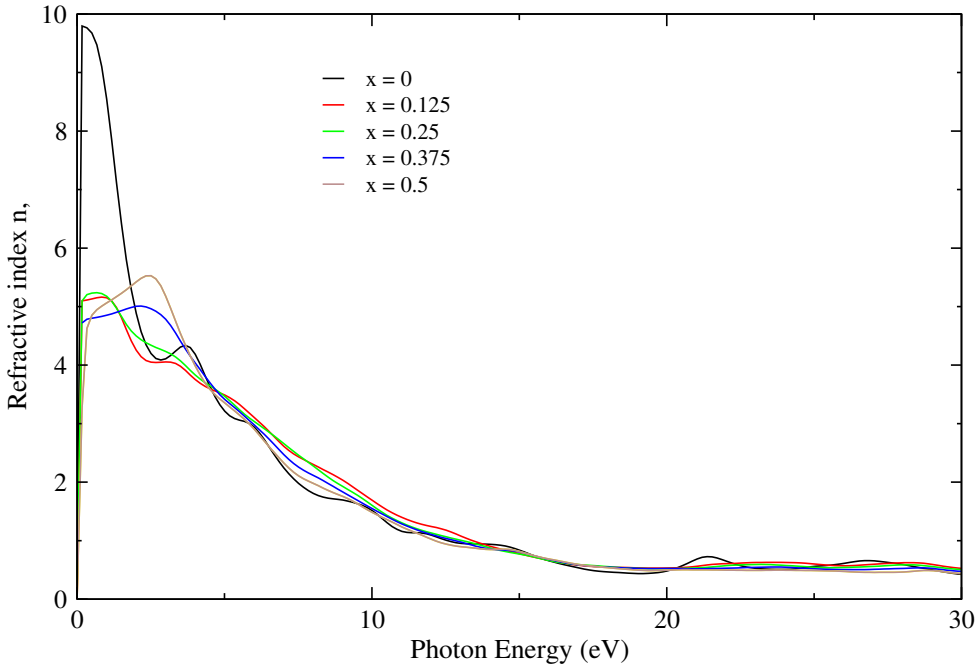

Figure 4.27: Refractive index of lanthanum-doped YHSe at different lanthanum concentrations.

According to Fig. 4.27, for photon energies beyond 20 eV, the refractive index stabilizes at approximately 0.937, 0.949, and 0.95 for La concentrations of 0, 0.125, and 0.25, respectively. This stabilization suggests that, at higher photon energies, the impact of La

doping on the refractive index becomes less pronounced, indicating a consistent optical behavior in this energy range. For photon energies beyond 20 eV, the refractive index for higher La concentrations of 0.375 and 0.5 exhibits slight variations, with values of 0.952, and 0.953 respectively. These results indicate that the addition of La at these concentrations has a minimal impact on the refractive index, suggesting that the optical properties of YHSe remain relatively stable despite the increased doping levels. This stability may indicate that the material maintains consistent optical characteristics in this energy range, which is beneficial for potential applications in optoelectronic devices.

Figure 4.28 illustrates the extinction coefficient of La-doped YHSe at different concentrations. The extinction coefficient (κ) of La-doped YHSe provides valuable insights into the material's optical properties, indicating the extent to which the material absorbs light at various La concentrations. In pristine YHSe, the extinction coefficient is significantly high, reaching $\kappa = 4.66$ at a photon energy of 1.503 eV. This finding aligns with prior research by Muhammad R. et al.,(2020), which investigated the electronic and optical characteristics of La doped perovskite using the DFT approach (Zhao et al., 2020).
The high extinction coefficient reflects strong light absorption at this concentration and energy level, aligning with the significantly strong absorption coefficient observed in this study. As La is incorporated into YHSe at concentrations of 0.125, 0.25, 0.375 and 0.5 the extinction coefficient exhibits significant variations, with values of 2.46 (6.85 eV), 2.54 (8.014 eV), 2.69 (6.78 eV), 2.89 (6.35 eV) respectively. These variations indicate that La doping significantly influences the optical absorption characteristics of YHSe, particularly in the low and mid-energy photon ranges. The observed shifts suggest modifications in electronic transitions and absorption mechanisms.

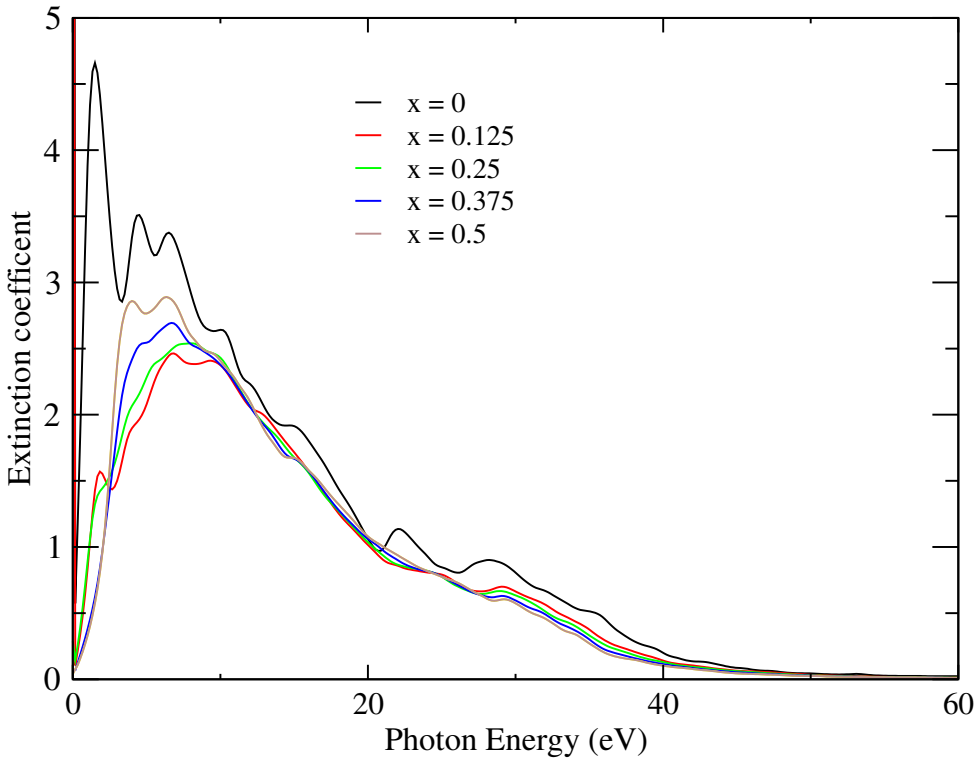

Figure 4.28: Extinction coefficient of La-doped YHSe at different La concentrations ranging from 0.0 to 0.5.

Figure4.29illustrates the reflectivity of La-doped YHSe at various concentrations. For La-doped YHSe, reflectivity at different La concentrations provides valuable insights into the material's optical behavior. For the pristine sample, the reflectivity peaks at $r = 0.9$ at a photon energy of 0.001 eV, indicating nearly perfect reflection of incident light at this energy level. This exceptionally high reflectivity suggests strong optical properties and efficient light reflection by the material. In the low photon energy range of 0 - 10 eV, the reflectivity remains high across all doping concentrations. However, between 10 - 30 eV, the reflectivity drops significantly across all concentrations, exhibiting noticeable oscillations. These oscillations may correspond to interband transitions, where the photon energy matches the energy gap between electronic bands, causing variations in reflectivity. While reflectivity for the pure material remains higher throughout this range, the curves for different doping concentrations begin to converge, suggesting that doping levels significantly alter the electronic structure and, consequently, the optical behavior of the material (Harrison, 2012). In the high photon energy range, all concentrations show a

steady decline in reflectivity. By around 50 eV, reflectivity reaches a lower stable level for all doping levels. The convergence of all curves at this high-energy range suggests that doping has a diminishing effect on reflectivity at higher photon energies, likely because photons at these energies possess sufficient energy to interact with deeper core levels or pass through the material with reduced interaction. This result is consistent with previous studies by Muhammad R. et al.,(2020) on the electronic and optical behavior of La-doped perovskite using the DFT approach (Rizwan et al., 2020b).

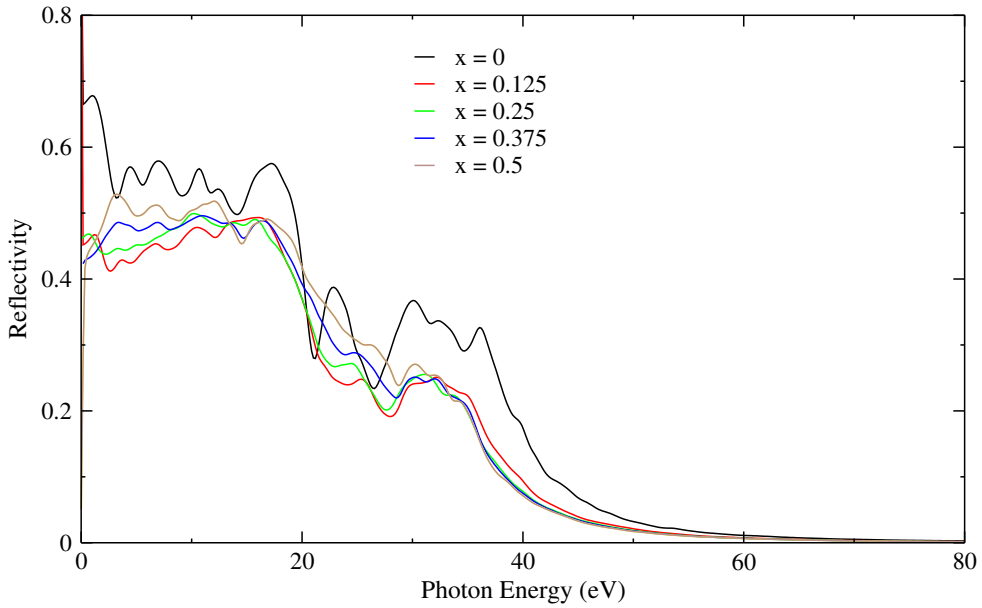

Figure 4.29: Reflectivity of La-doped YHSe at different La concentrations ranging from 0.0 to 0.5.

Figure 4.30,illustrates the electron energy loss function for La doping concentrations ranging from 0.0 to 0.5. The electron energy loss function of La-doped yttrium hydrogen selenide was examined across various La concentrations.The energy-loss spectrum is a valuable tool for investigating the electrical, structural, and vibrational properties of materials. As illustrated in Fig.4.30, the EELF remains relatively low across all doping concentrations within the 0 - 20 eV energy range. Although the curves exhibit slight fluctuations, no significant peaks are observed, indicating minimal energy loss due to electron excitations or plasmonic oscillations in this range. The absence of major peaks suggests that this region corresponds to lower energy transitions that do not result in significant energy loss. The pure material displays a higher peak, indicating stronger plasmonic inter-

actions compared to the doped materials. As the La concentration increases, the height of the peak decreases slightly, suggesting that doping reduces the strength of these collective oscillations. Beyond 40 eV, the loss function drops off for all concentrations, with no major peaks observed. This implies that at higher photon energies, the system does not exhibit strong plasmon resonance or other significant energy loss mechanisms. The convergence of the curves at higher photon energies further indicates that the effects of doping become less pronounced as photon energy increases, with all concentrations displaying similar loss characteristics.

Doping La alters the electrical structure of YHSe by redistributing electron densities and altering energy levels. These modifications can lead to a shift in plasmon resonance toward lower photon energies, as the electron cloud becomes less tightly bound, thereby reducing the energy required to excite collective electron oscillations (Harrison, 2012). These effects particularly the observed shift in plasmon resonance and the altered electronic structure are consistent with previous DFT studies on La doped perovskites, which reported similar electronic and optical behavior (Rizwan et al., 2020b). According to these findings, the higher the value of ϵ_2, the lower the energy loss function, which is an important feature of semiconductors.

Table 9: Sharp peaks of optical properties at various La concentrations (x)

(x)	$\mathbf{R}(\omega)$	$\boldsymbol{\alpha(\omega)} \times \mathbf{10^8}$ (cm^{-1})	$\mathbf{L}(\omega)$	$\mathbf{n}(\omega)$	$\boldsymbol{\epsilon_1(\omega)}$	$\boldsymbol{\epsilon_2(\omega)}$	$\boldsymbol{\kappa(\omega)}$
0.0	0.99	6.78	4.32	9.79	95.60	68.22	4.66
0.125	0.99	5.85	3.38	5.16	26.30	14.93	2.46
0.25	0.47	5.99	3.40	5.24	27.21	15.83	2.54
0.375	0.49	5.85	3.60	5.01	24.15	19.776	2.45
0.5	0.53	5.93	3.70	5.53	28.77	25.48	2.89

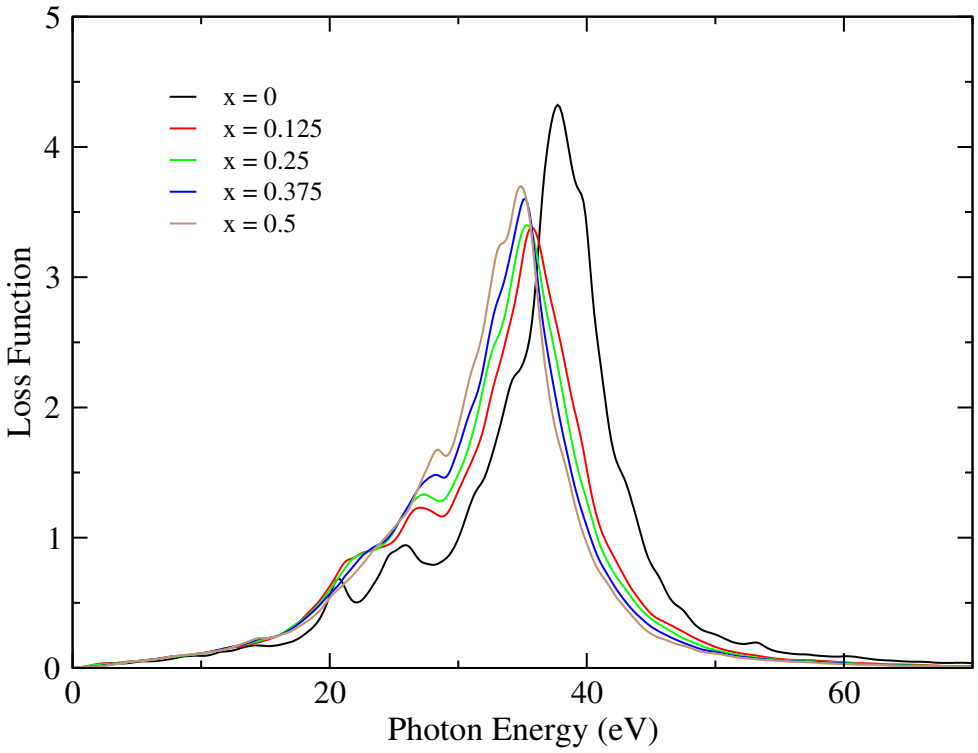

Figure 4.30: Electron energy loss function of La-doped YHSe at different La concentrations.

4.2.4 Vibrational Analysis

The phonon band structure curves demonstrate the dynamical stability of La doped YHSe, with no imaginary frequencies recorded across the Brillouin zone.

With increasing La concentration, low-frequency phonon modes exhibit a systematic redshift, attributed to the higher atomic mass of La compared to Y. This shift suggests a redistribution of vibrational energy, which directly impacts lattice dynamics and phonon-mediated interactions.

Figure 4.31 Phonon partial density of states analysis further elucidates the effects of La doping, revealing the emergence of additional low-frequency vibrational modes while inducing a slight upward shift in the Y and Se contributions. This trend aligns with previous findings in other related systems (Sadeghi & Esfarjani, 2024), where heavy-element substitution modulates phonon behavior through mass and bonding effects. Notably, at doping concentrations of $x = 0.3$ and $x = 0.5$, the total phonon density of states reaches its peak, indicating a maximization of available vibrational states in the frequency range

of 0.6 to 7 THz. At a La concentration of $x = 0.3$, the La atom significantly contributes to the phonon DOS, leading to an increase in the phonon DOS, as illustrated in the phonon partial density of states shown in Fig. 4.31(b) and Fig. 4.31(c). This increase suggests that La incorporation enhances phonon interactions, potentially strengthening EPC a critical factor in determining superconducting and thermal transport properties. Moreover, in La-doped YHSe, both the optical and acoustic phonon branches occur at lower frequencies compared to those of pristine YHSe, as shown in Fig.4.31 (a), Fig.4.31 (b), and Fig.4.31 (c). This suggests a softening of these modes due to the presence of the heavier La atom compared to yttrium. This reduction indicates a weakening of interatomic bonding, leading to lower lattice thermal conductivity as La concentrations increase. This observation aligns with previous research on other related systems (Sadeghi & Esfarjani, 2024)(Muchtar et al., 2021)

Furthermore, the material's softening likely enhances mechanical flexibility, potentially lowering shear and elastic moduli. This observation aligns with our current study on the phonon-related thermoelectric properties, specifically the impact of La concentration on lattice thermal conductivity. The reduction in lattice thermal conductivity is beneficial for thermoelectric materials, as it aids in sustaining a temperature gradient by limiting heat transfer, thus enhancing overall efficiency. The incorporation of La, due to its relatively high atomic mass, alters the phonon spectrum by shifting phonon frequencies and affecting phonon-phonon interactions. These changes influence the material's thermal and vibrational properties. Such behavior is consistent with prior studies on other systems (Sadeghi & Esfarjani, 2024).

Based on the phonon dispersion plot, additional optical phonon branches appear in the La-doped case at a La concentration of $x = 0.3$ compared to the pristine YHSe case. This suggests that La doping introduces new optical modes, likely due to changes in atomic mass, bonding strength, and structural distortions. Figure 4.33 illustrates the dependence of the longitudinal acoustic phonon frequency (LA) on La concentration at the high-symmetry points include M, K, A, L, and H.

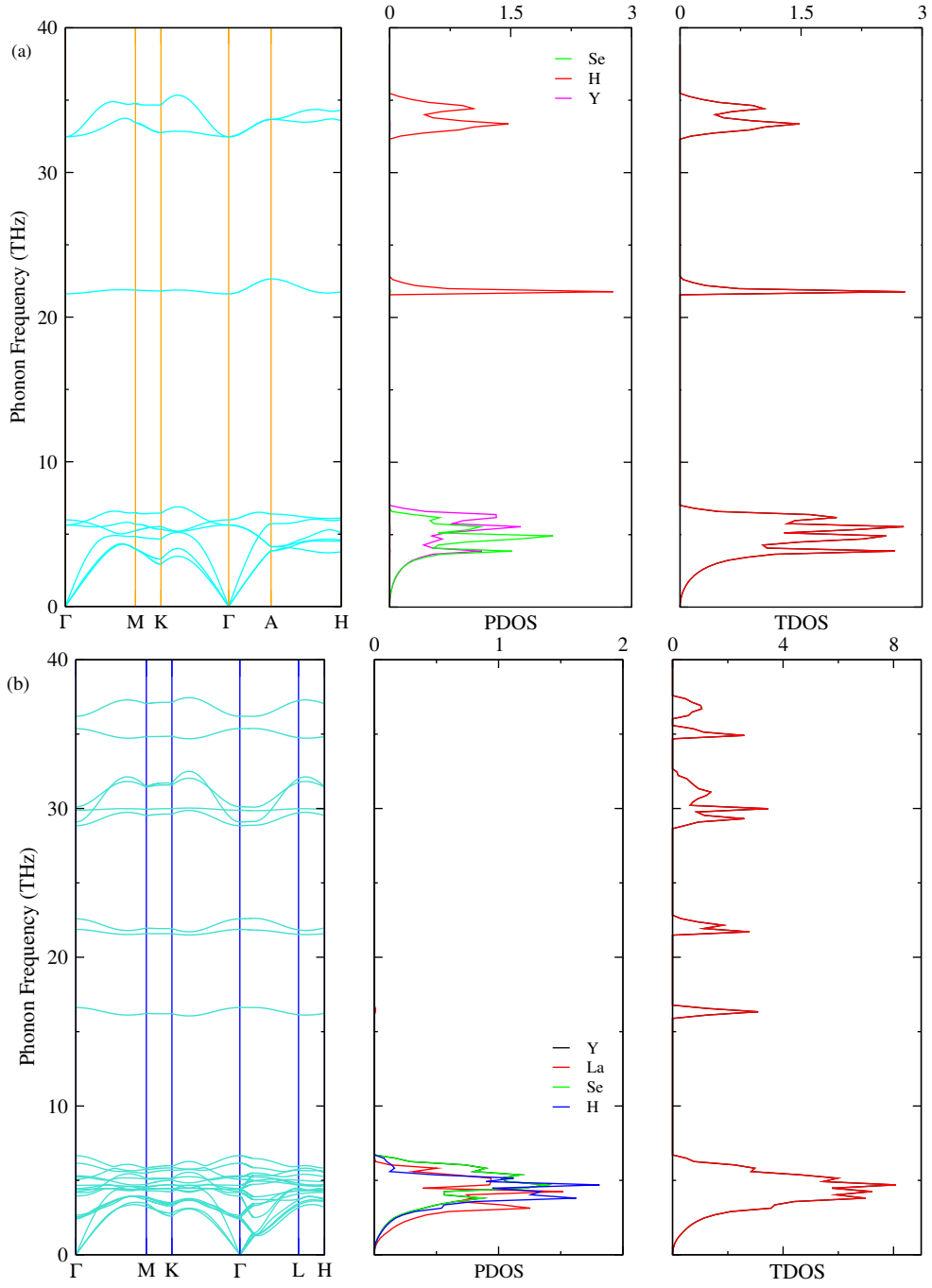

Figure 4.31 (a), 4.31 (b), and 4.31 (c) indicate that as the La concentration increases, both acoustic and optical phonon frequencies at all high-symmetry points generally decrease compared to the pristine case, indicating phonon softening. This finding is consistent with previous results in other related systems (Sadeghi & Esfarjani, 2024)(Muchtar et al., 2021). Figure 4.32 compares the phonon DOS across all studied doping concentrations, highlighting shifts and modifications in vibrational modes as the La content increases. No-

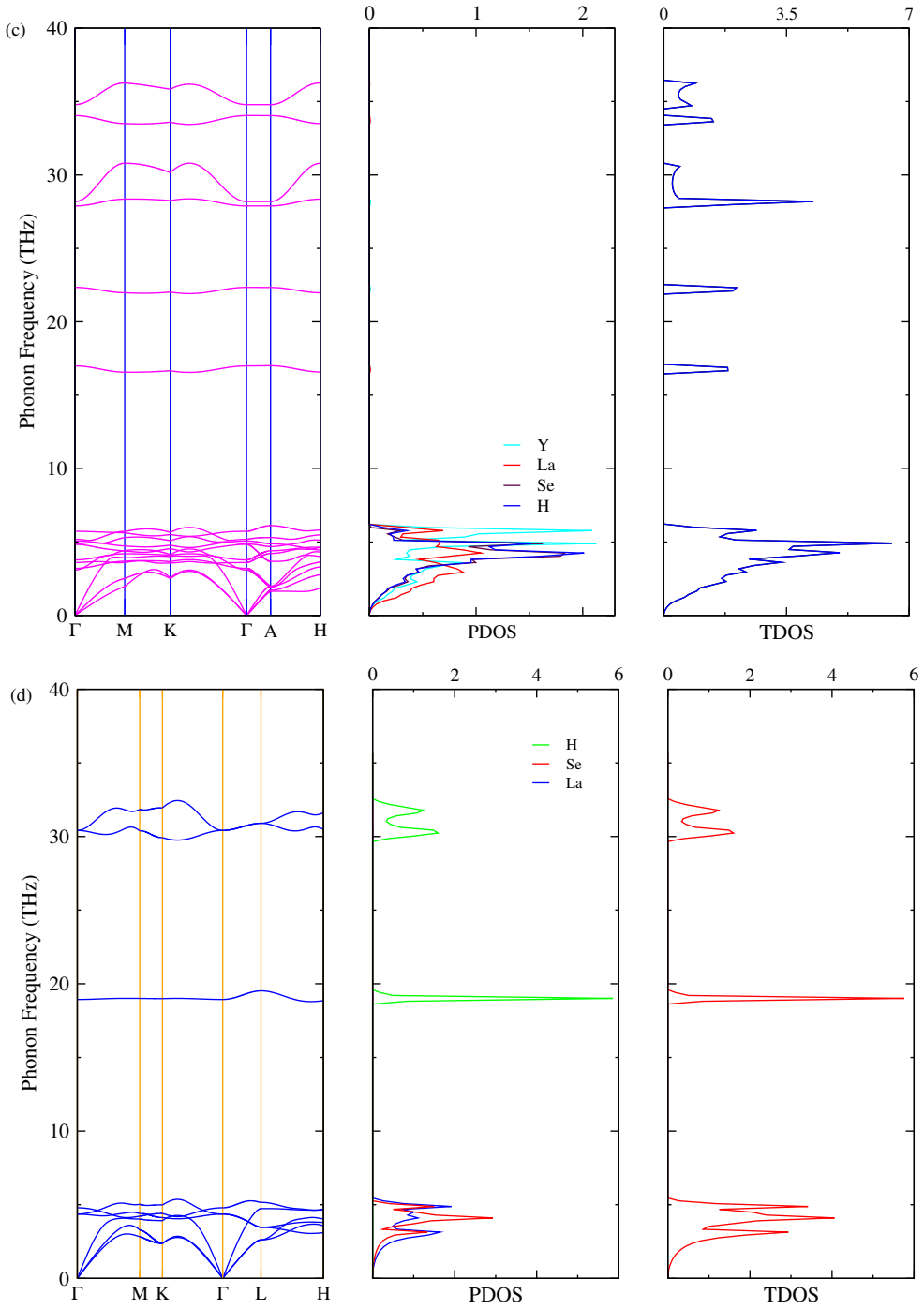

Figure 4.31: Phonon band structure and phonon DOS for La-doped YHSe at different La concentrations: (a) YHSe (b) $La_{0.3}Y_{0.7}HSe$, (c) $La_{0.5}Y_{0.5}HSe$, and (d) LaHSe.

tably, the total phonon DOS shows a pronounced increase at $x = 0.3$ and $x = 0.5$ in the low-frequency range, suggesting enhanced phonon activity and a potential improvement in superconducting properties at this doping level.

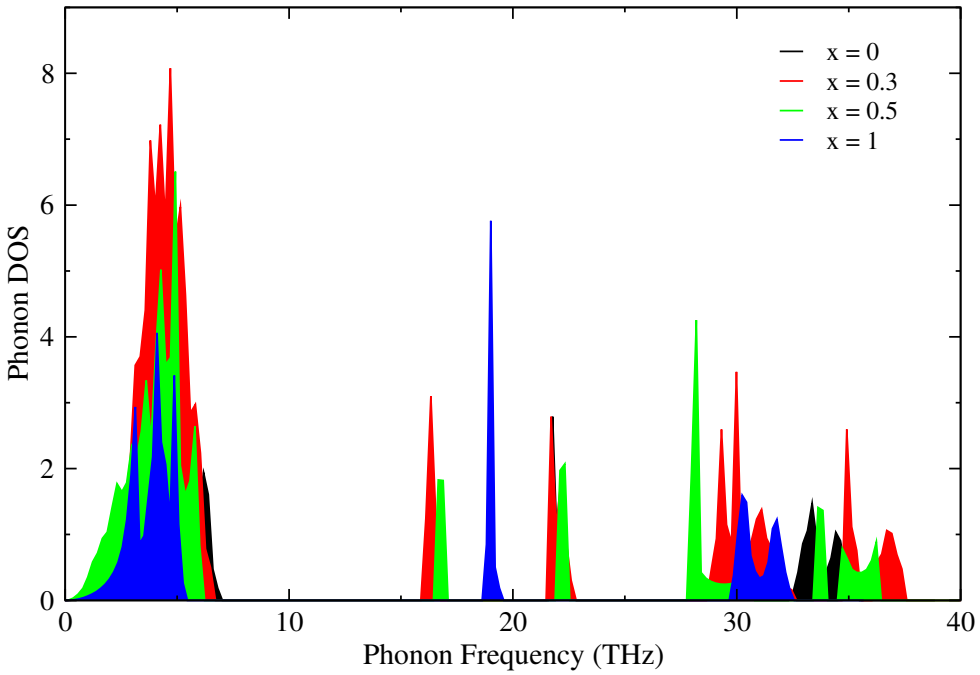

Figure 4.32: Total Phonon density of states for YHSe at various La concentrations (x).

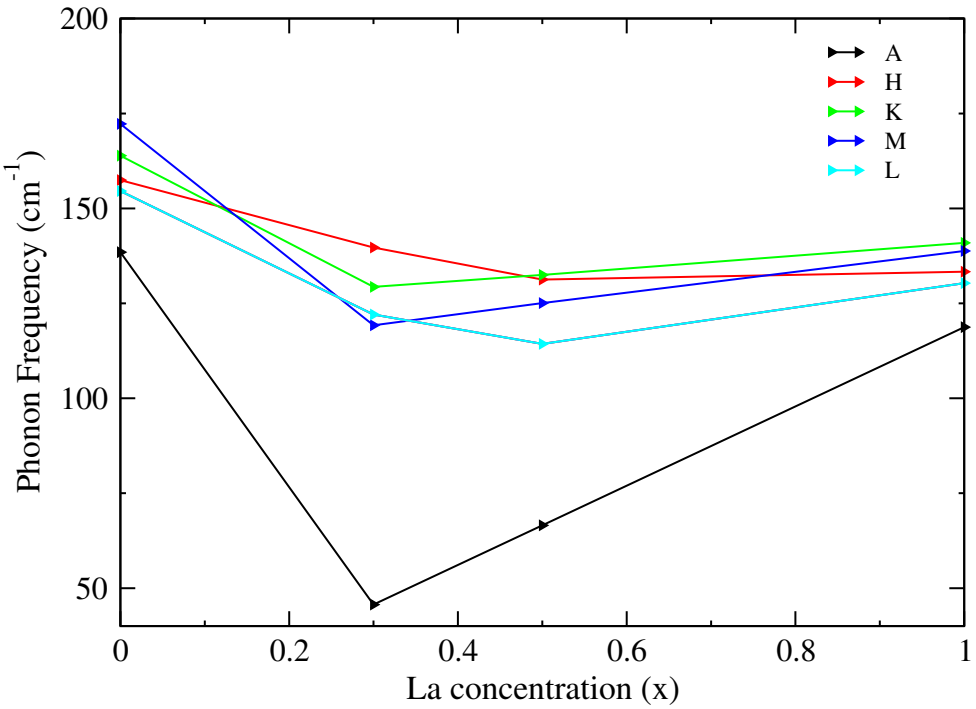

Figure 4.33: La concentration dependence of the longitudinal acoustic phonon frequencies (LA) at high symmetry points: M, K, A, L, and H.

As observed in Fig. 4.31 (b), and Fig. 4.31 (c), the low-frequency region (below approximately 7 THz) is dominated by vibrational contributions from all constituent atoms

Y, La, Se, and H. This collective participation suggests strong lattice interactions, particularly relevant for enhancing electron-phonon coupling.

From Fig.4.31(b), and Fig.4.31(c) Specifically, the La atoms introduce additional phonon states in the low-vibration mode, which contributes to the softening of phonon modes and enhances the phonon DOS. The yttrium atoms and lanthanum atoms both show prominent contributions in the mid-to-low frequency range, indicating active participation in lattice vibrations that couple to the electronic system. From partial phonon density of states the selenium atoms also contribute significantly across a broader frequency range, indicating their structural role and coupling with metallic elements.

The enhancement of the total phonon DOS in the low-frequency range, particularly due to La doping, supports the observed increase in EPC. This, in turn, justifies the rise in the superconducting critical temperature T_c with increasing La concentration.

4.2.5 Superconducting Properties

Superconducting properties were evaluated through electron-phonon spectral function analysis. The EPC constant and superconducting critical temperatures (T_c) were calculated at different doping levels. The preceding Fig.4.34 (a) and Fig.4.34 (b) indicate the calculated critical temperature (T_c) for superconductivity of La-doped YHSe and the integrated EPC constant. The results indicate that T_c increases with doping and reaches a maximum of 39.861 K at $x = 0.5$. Similarly, the total EPC constant (λ) follows the same trend, reaching a peak value of $\lambda = 1.3774$ at $x = 0.5$. The low frequency phonon modes contributes to enhance total EPC constant at this doping level. This finding is consistent with previous results in other system (Lian et al., 2017). However, excessive La incorporation ($x = 1$) leads to a decline in T_c due to reduced phonon density and relatively weaker electron-phonon interactions. This behavior aligns with previous studies on other systems, where optimal doping levels balance phonon softening and electronic interactions (Wu et al.,n.d.).

The superconducting critical temperatures (T_c) at different La concentrations (x) are as follows: $T_c = 28.321$ K for $x = 0$, $T_c = 35.399$ K for $x = 0.3$, $T_c = 39.861$ K for $x = 0.5$, and $T_c = 13.821$ K for $x = 1$. The higher T_c values at $x = 0.3$ and $x = 0.5$ are consis-

tent with their increasing total EPC constants, $\lambda = 1.3411$ and $\lambda = 1.3774$, respectively. Furthermore, calculations show that at La concentration $x = 0$, $\lambda = 1.21$, and at $x = 1$, $\lambda = 1.20$, both of which correspond to their relatively lower T_c values. Figure 4.34 (a) and Figure 4.34 (b) confirm that lanthanum substitution enhances the EPC constant (λ) and strengthens electron-phonon interactions, leading to raise in the superconducting critical temperature (T_c) up to a La concentration of 0.5. Figure 4.35 illustrates the

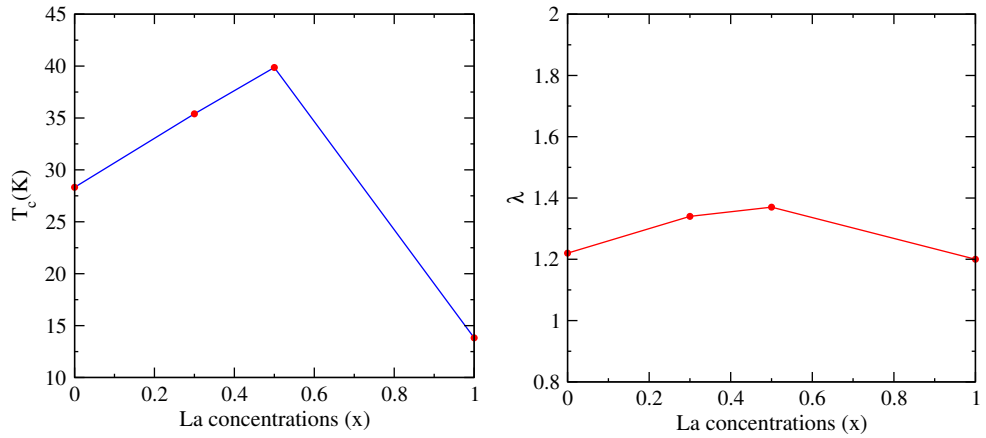

Figure 4.34: (a) The computed superconducting critical temperature (T_c) for La-doped yttrium hydrogen selenide. (b) The examination of EPC parameter (λ) for La doped YHSe.

Table 10: Tc, λ, and ω_{log} at different La concentrations in YHSe.

La (x)	T_c **(K)**	λ	$\omega_{\log}$ **(K)**
0	28.00	1.21	199.37
0.3	35.40	1.34	180.08
0.5	39.90	1.37	166.82
1	13.80	1.20	133.65

frequency-dependent distribution of the EPC parameter across various La concentrations. It indicates that increasing La concentration (x) leads to a higher EPC integral.

To investigate the source of the enhanced total EPC constant (λ) and critical temperature (T_c) due to La doping, we analyze the phonon spectra of $La_{0.3}Y_{0.7}HSe$ and $La_{0.5}Y_{0.5}HSe$ and compare them with those of other samples in Fig.4.32. The phonon density of states (PhDOS) plays a crucial role in phonon-mediated superconductors, as it

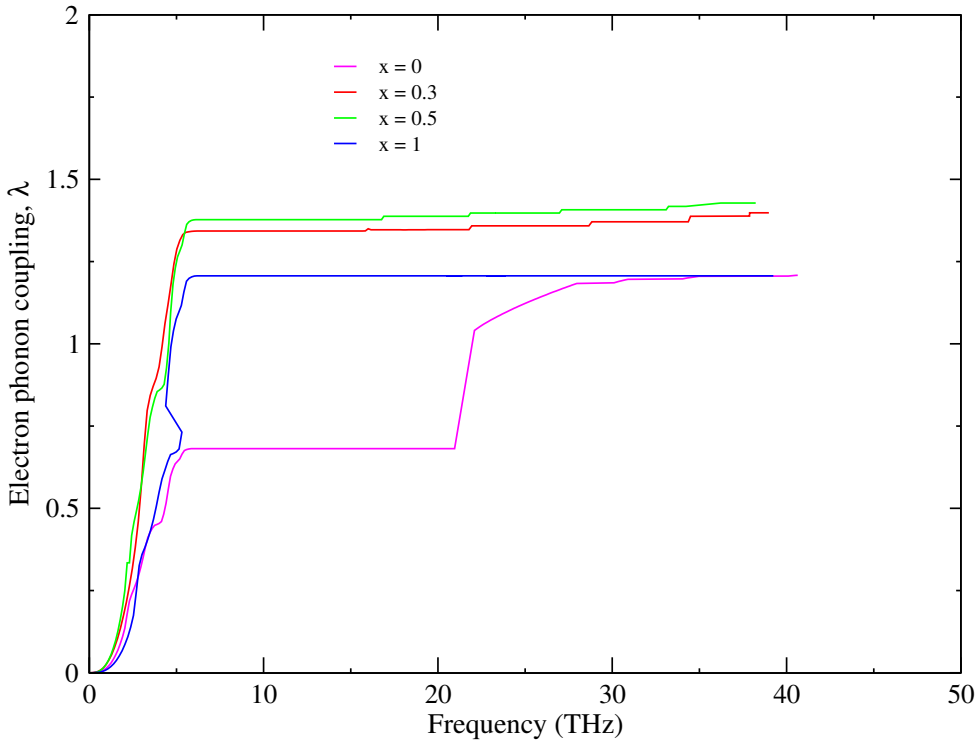

Figure 4.35: The frequency distribution of the EPC parameter (λ) for La-doped YHSe at varying La concentrations (x).

determines the strength of electron-phonon interactions, which influence the superconducting transition temperature (Babu & Guo, 2019). The graph shows significant differences in phonon DOS across different La concentrations ($x = 0, 0.3, 0.5, 1$), suggesting that doping alters the vibrational properties of the lattice. The peaks at higher frequencies indicate modifications in the phonon modes, likely due to changes in atomic mass and bond stiffness upon La doping. La doping introduces additional phonon states and shifts phonon frequencies, leading to an increase in the total EPC constant (λ) as the La concentration increases from $x = 0$ to $x = 0.5$. However, at a La concentration of $x = 1$, the total EPC constant (λ) decreases to 1.20, resulting in a lower T_c (13.8 K). This decline is attributed to the reduction in both the phonon density of states and the electronic density of states at the Fermi level, which weakens the overall electron-phonon interaction. This finding is consistent with previous results in other systems (Babu & Guo, 2019).

In the low-frequency region (0 to 8 THz), significant phonon contributions from La doping are observed, particularly at $x = 0.3$. These low-energy phonon modes play a crucial role in determining the strength of EPC, as lower energy phonons generally en-

hance EPC, thereby contributing to the increase in superconducting critical temperature (T_c).This finding is consistent with previous results in phonon and EPC in the YNi_2B_2C system (Weber et al., 2014). From Figure 4.35, the pristine YHSe exhibits the relatively lowest EPC constant (λ), which increases significantly with La substitution. Both $La_{0.3}Y_{0.7}HSe$ and $La_{0.5}Y_{0.5}HSe$ demonstrate higher values of the EPC constant, with the $La_{0.5}Y_{0.5}HSe$ composition achieving the highest coupling. The EPC increases sharply in the low-frequency range below 10 THz and saturates afterward.

Most doping elements tend to induce the softening of phonon modes, which enhances EPC, thereby improving the critical superconducting temperature (Yamashita et al., 2010). In this study, the increase in T_c with La doping is attributed to three factors: (i) the softening of the phonon spectrum, (ii) the enhancement of the phonon density of states (PhDOS) due to the contributions from all atoms in La-doped YHSe (Y, La, Se, and H) in the lower frequency region, approximately between 0.6 and 7 THz, and (iii) the rise in the electronic density of states near/at the Fermi level as the La concentration in YHSe increases.

In this work, La doping leads to phonon softening due to its larger atomic radius compared to yttrium,and increasing phonon density of states which enhances EPC. This coupling is a key factor in the formation of Cooper pairs, as stronger interactions between electrons and lattice vibrations facilitate superconductivity. This data provides strong evidence that La substitution effectively tunes the EPC in YHSe, contributing to enhanced superconductivity. This findings consistent with prior research on phonons and superconductivity in fcc and dhcp lanthanum (Bağcı et al., 2010) and phonon-mediated high T_c superconductivity in hole-doped diamond-like crystalline hydrocarbons (Lian et al., 2017). La doping increases the density of states near the Fermi level. This enhancement is crucial because a higher density of states allows more electrons to participate in superconductivity, thereby increasing the EPC strength. The increased density of states contributes to the formation of Cooper pairs, which are essential for superconductivity. This data provides strong evidence that La substitution effectively tunes the EPC constant in YHSe, contributing to enhanced superconductivity. Figure 4.36 illustrates the EPC characteristics and the electron-phonon spectral function for pristine and La-doped

YHSe at different La concentrations. The electron-phonon spectral function, denoted as $\alpha^2F(\omega)$, essentially characterizes the strength of the electron-phonon interaction at different phonon frequencies (Uzunok et al., 2020). Increasing La concentration systematically increases the overall $\alpha^2F(\omega)$ intensity at low frequencies. This trend aligns with the observed rise in EPC, supporting the notion that La doping strengthens phonon-mediated interactions critical for superconductivity. The electron-phonon spectral function confirms that La doping in YHSe modifies the phonon density of states, with a pronounced shift toward low-frequency phonons.

Moreover, the spectral function shows that the EPC strength is significant for La concentrations of $x = 0.3$ and $x = 0.5$ at a certain range of frequencies. Overall, these findings indicate that increasing La doping content enhances both the EPC constant and the intensity of the electron-phonon spectral function, particularly at $x = 0.3$ and $x = 0.5$, as depicted in Fig.4.37 . This finding aligns with previous study results on phonon-mediated high T_c superconductivity in hole-doped diamond-like crystalline hydrocarbons (Lian et al., 2017).

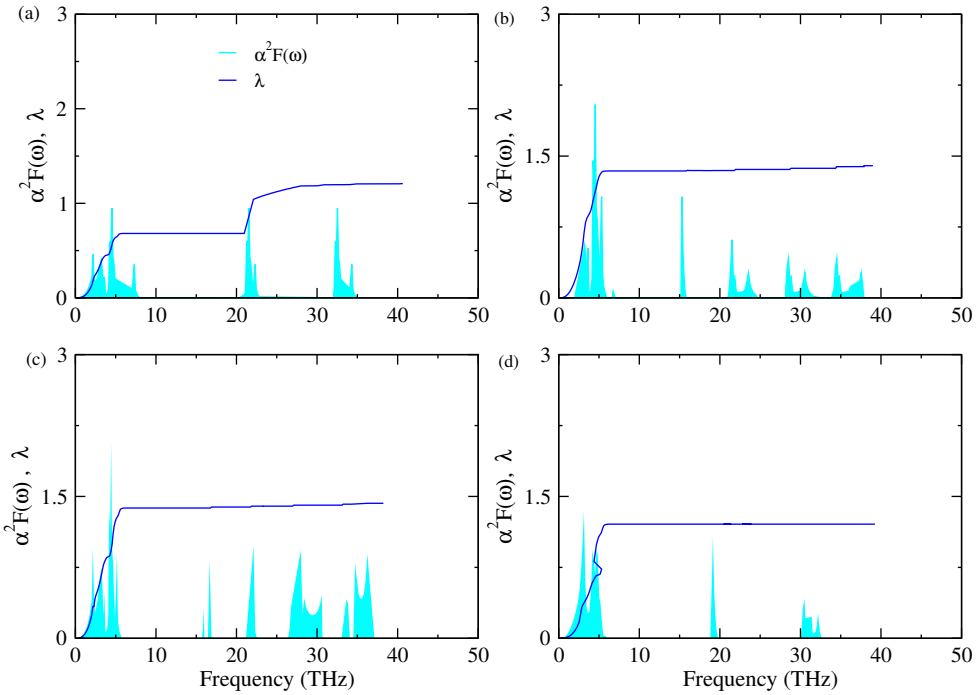

Figure 4.36: Eliashberg spectral function and frequency-dependent (λ) for La-doped YHSe. The plots are presented for (a) YHSe, (b) $La_{0.3}Y_{0.7}HSe$, (c) $La_{0.5}Y_{0.5}HSe$, and (d) LaHSe.

The variation of the logarithmic average phonon frequency (λ) with different La concentrations in the YHSe system at $x = 0$ (199.37 K), $x = 0.3$ (180.08 K), $x = 0.5$ (166.82 K), and $x = 1$ (133.65 K) reveals a decrease in the logarithmic average phonon frequency with increasing La concentration. This trend suggests that as more La is introduced into the YHSe system, the overall phonon frequencies shift toward lower values. This shift can be attributed to the heavier atomic mass of La compared to yttrium, leading to a softening of the phonon modes, particularly in the lower frequency range. As the phonon modes soften, the logarithmic average phonon frequency decreases, indicating that the vibrational spectrum of the material is being altered by the addition of La, which in turn affects the total EPC and the superconducting properties of the material. This finding aligns with previous study results on phonon-mediated high T_c superconductivity in hole-doped diamond-like crystalline hydrocarbons (Lian et al., 2017).

Figure 4.37 presents the electron-phonon spectral function of La-doped YHSe at different La concentrations, offering a comparative analysis of its evolution with increasing doping levels. Notably, the enhanced phonon density of states in the frequency range of 1.5 THz to 8 THz significantly contributes to the total EPC integral within this region, as shown in Fig. 4.37. As a result, both $La_{0.3}Y_{0.7}HSe$ and $La_{0.5}Y_{0.5}HSe$ exhibit a marked improvement in the total EPC constant.

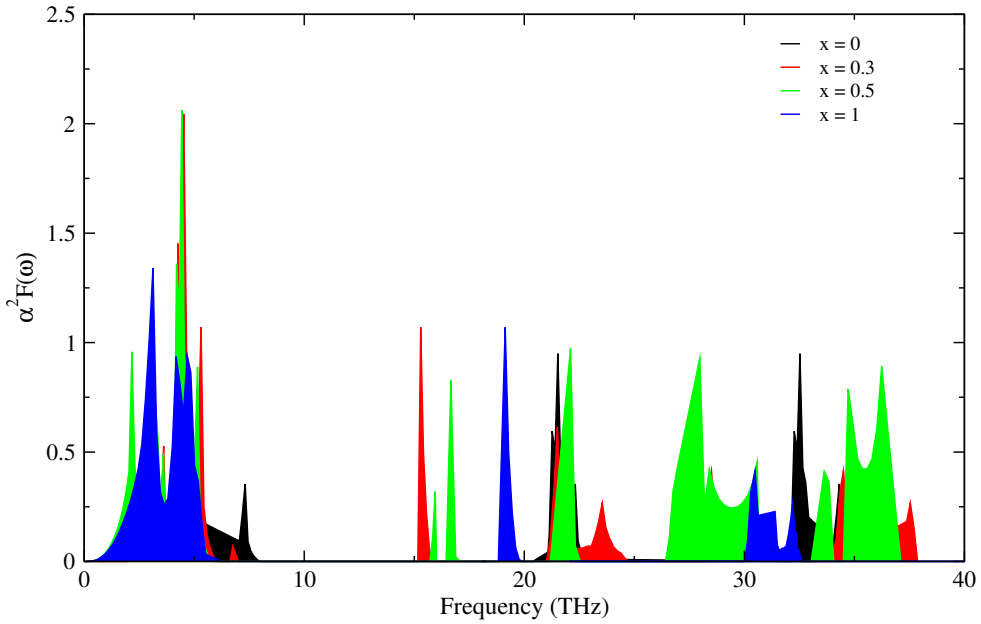

Figure 4.37: Eliashberg spectral functions of YHSe with varying La doping levels

4.2.6 Thermoelectric Properties

In this section, we systematically investigate the thermoelectric properties of La-doped YHSe across varying La concentrations. Key parameters, including carrier concentration (n), electrical conductivity (σ), electronic thermal conductivity (κ_e), lattice thermal conductivity (κ_p), Seebeck coefficient (S), electronic heat capacity (c), power factor (PF), and the figure of merit (ZT), are analyzed to gain deeper insights into their dependence on La doping.

Figure 4.38 shows that the Seebeck coefficient of La doped YHSe at different La concentrations. We observe that for pristine, to low-doped samples (x = 0 and 0.125), the Seebeck coefficient is relatively high and remains relatively stable up to 800K. This suggests that low doping levels enhance thermoelectric performance over a wide temperature range, making them suitable for high-temperature applications, such as power generation from industrial waste heat in the YHSe system. For low doping levels (x = 0.125), the carrier concentration (n) is higher than in the pristine material.

However, based on the band structure curvature of the La doped YHSe system, the transition to a less dispersive or more flattened band with increasing La concentration leads to a higher effective mass of the carriers. The findings of this study are consistent

with previous research on La-doped $NaTaO_3$, where the effective masses increase with higher doping concentrations (Khan et al., 2024). This enhancement in effective mass offsets the effect of higher carrier concentration on the Seebeck coefficient, resulting in a higher Seebeck coefficient compared to the pristine material.

At higher doping levels ($x = 0.5$), the carrier concentration (n) starts at a very low value and increases exponentially with temperature. Hence, for higher doping at $x = 0.5$, the Seebeck coefficient starts at a relatively high value and remains stable up to 350 K. Beyond this temperature, the Seebeck coefficient decreases with increasing temperature due to the generation of more excited carriers, which reduces the Seebeck coefficient. This means that as the carrier concentration increases, the Seebeck coefficient decreases. This inverse relationship explains why higher doping which increases (n), generally leads to a lower Seebeck coefficient. The present observations align well with the prior investigation by K. Imasato et al. (2018), La-doped $Mg_3Sb_{1.5}Bi_{0.5}$(Imasato et al., 2018).

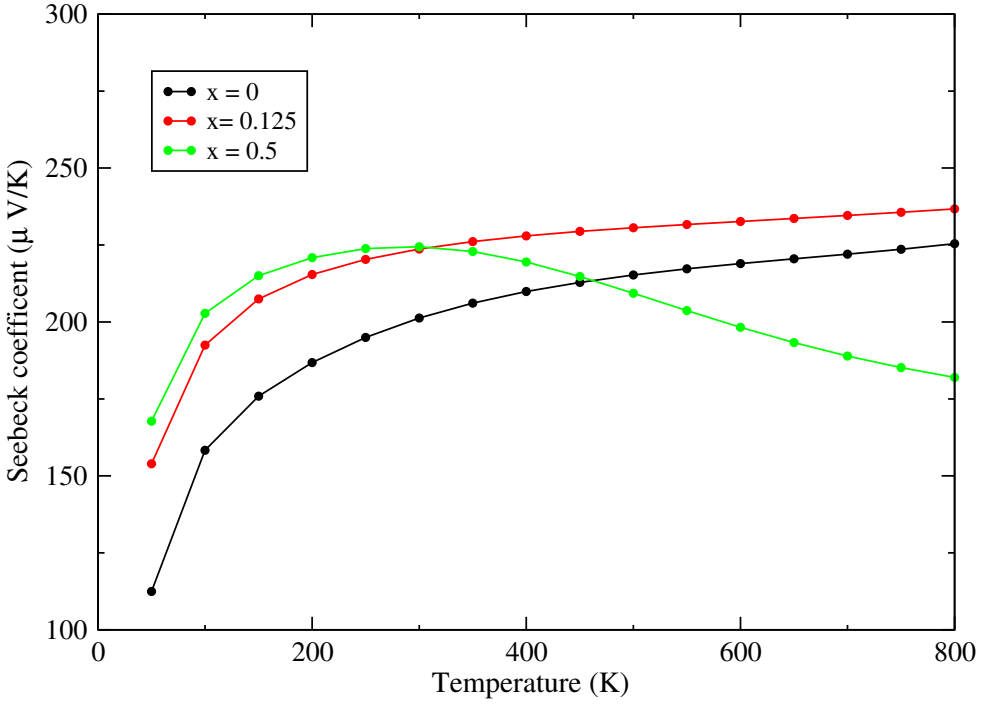

Figure 4.38: Seebeck coefficient of La doped YHSe at varying La concentrations.

Figure 4.39 illustrates the variation of electrical conductivity versus temperature at different La concentrations in YHSe. Increasing La concentration reduces the band gap, gradually shifting the material from a semiconductor toward a metallic state. This band

gap narrowing results in more thermally excited electrons at increased temperatures, which boosts the electrical conductivity in the La doped YHSe system. As the system approaches metallic behavior, the density of states at the Fermi level also increases, allowing for more charge carriers actively involved in the conduction process at elevated temperatures (Kaur & Kumar, 2016). With a smaller band gap, thermally activated carriers are less necessary for conduction, and more charge carriers can directly contribute to the current flow as temperature rises. Consequently, the conductivity increases more rapidly with temperature for higher La concentrations due to the abundance of accessible electronic states. The findings of this study are in strong agreement with the earlier research on the Bi_2Te_3 compound by M. Yaprintsev et al. (2018), which employed an experimental approach (Yaprintsev et al., 2018). Additionally, as the La concentration increases from Fig. 4.39 (a) to Fig.4.39 (d), it is evident that conductivity also increases with higher La concentrations. The La doped YHSe with concentrations of x = 0, 0.125, and 0.5 shows semiconducting behavior.

Figure 4.40 illustrates the power factor for La doped YHSe at varying La concentrations. Thermoelectric materials that exhibit high electrical conductivity, a large Seebeck coefficient, and low thermal conductivity lead to an enhanced power factor performance (Dehkordi et al., 2015). The power factor of YHSe increases with temperature across all concentrations, indicating an improvement in the material's thermoelectric performance at higher temperatures. At a doping concentration of $x = 0.5$, the material exhibits superior thermoelectric performance compared to other concentrations at low temperatures. This is as a result of the higher Seebeck coefficient.

This reduction in the Seebeck coefficient as results of an enhanced carrier concentration (n), which in turn lowers the efficiency of YHSe in converting waste heat into electricity. These findings suggest that a La concentration of x = 0.5 provides optimal thermoelectric performance, as indicated by the high power factor shown in Fig. 4.40.

Figure 4.41 shows the electronic thermal conductivity (κ_e) of La-doped YHSe at varying La concentrations. In semiconductors, thermal conductivity arises from two contributions: phonons and electrons (Pei et al., 2013). According to Fig.4.41 and 4.42, the electronic heat conductivity is lower than the phonon heat conductivity at low temperatures. The

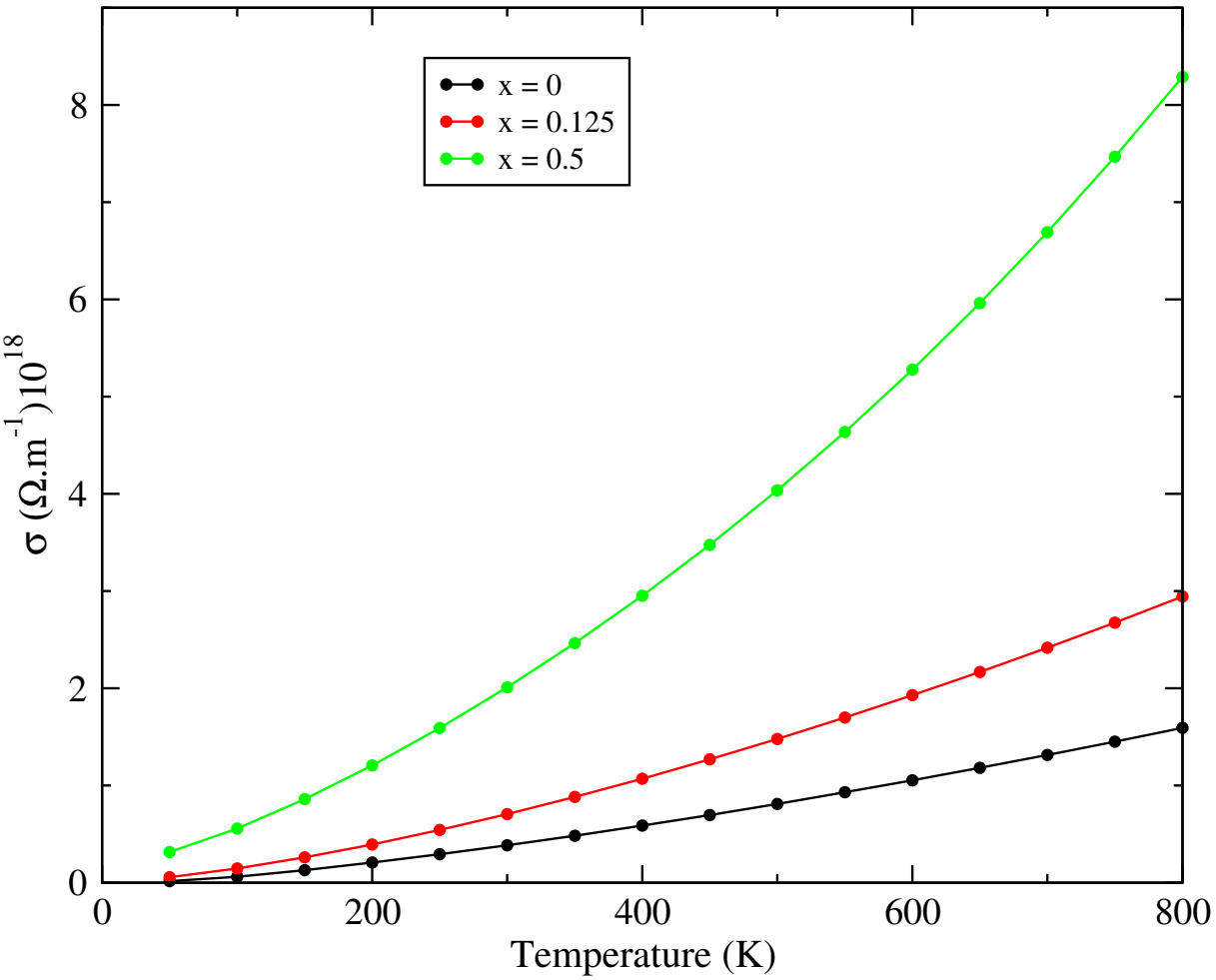

Figure 4.39: Electrical conductivity of La-doped YHSe at varying La concentrations:

observed increase in the electronic part of heat conductivity of La doped YHSe with rising temperature can be ascribed to improved carrier mobility and an increase in the number of thermally activated charge carriers. These findings indicate that in La doped YHSe, as temperature increases, more electrons gain sufficient energy to contribute to conduction, resulting in higher electronic thermal conductivity. This increase is as a result of the rising carrier concentration, which is directly proportional to electronic thermal conductivity. As the concentration of La increases, it introduces more charge carriers into the system, which enhances the material's heat conductivity. Overall, both the temperature and La concentration positively influence the electronic thermal conductivity of YHSe by facilitating enhanced charge carrier contributions and improving mobility. These results agree well with the previous work, La-doped $Mg_3Sb_{1.5}Bi_{0.5}$ by Imasato et al., (2018) (Imasato

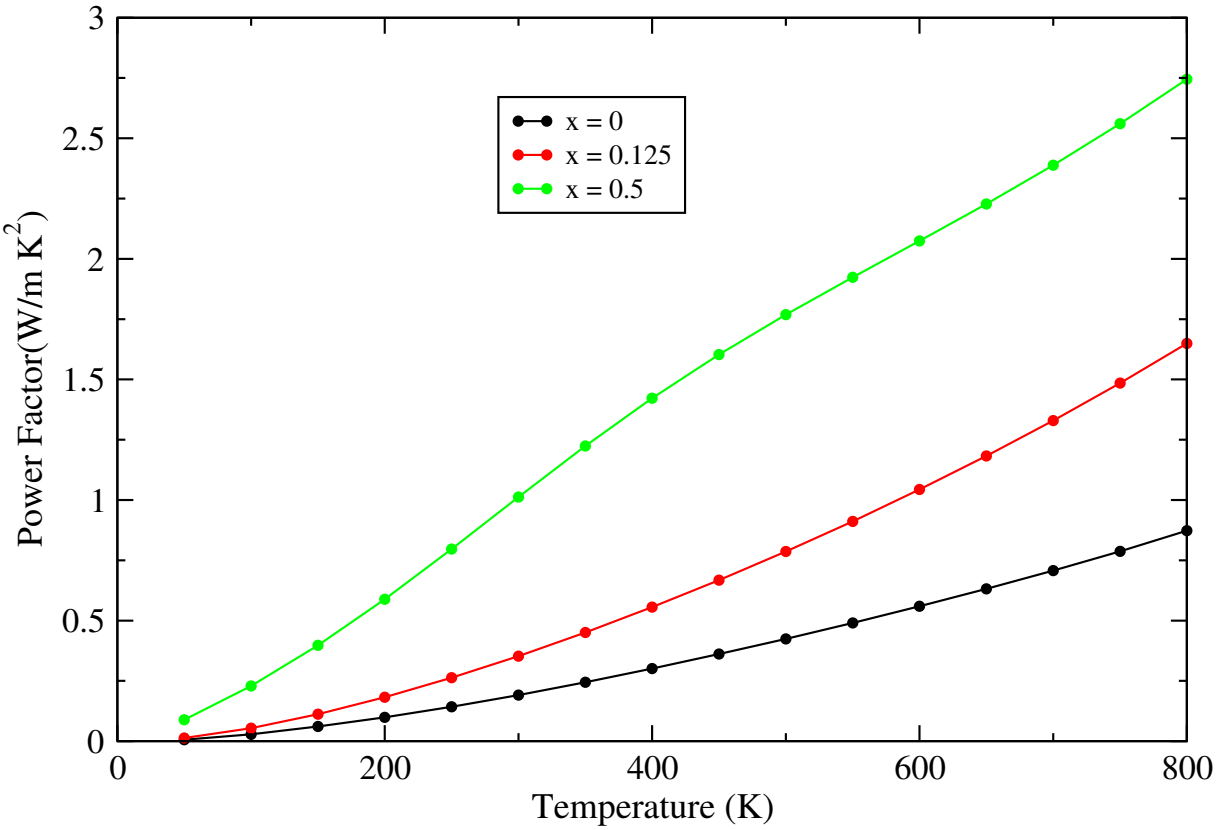

Figure 4.40: Power factor of La-doped YHSe at varying La concentrations.

et al., 2018).

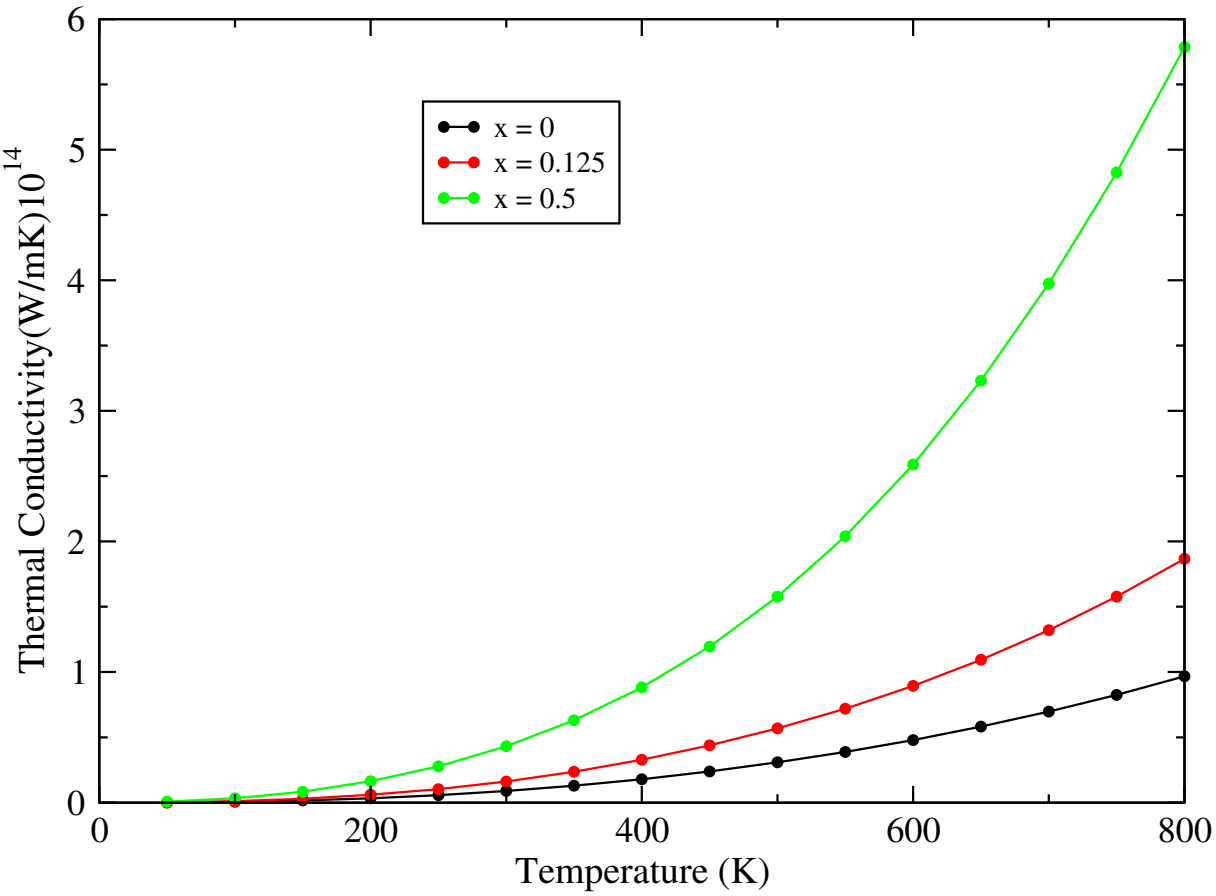

Figure 4.41: Electronic heat conductivity (κ_e) of La-doped YHSe at varying lanthanum concentrations.

Figure 4.42 (a), Figure 4.42 (b), and Figure 4.42 (c) depict the phononic contribution to heat conductivity for different La concentrations. Phonon thermal conductivity is initially high at low temperatures for all dopant levels but decreases rapidly and remains relatively low beyond 200 K. This suggests significant phonon-phonon scattering at elevated temperatures. The phonon contribution to heat conductivity of La-doped YHSe exhibits a pattern comparable to that of the pristine material, but its overall value declines notably with increasing La content. This suggests that at low doping levels, phonon scattering is less effective, allowing better heat conduction. The decreasing in phonon heat conductivity is expected as a result of increased phonon-defect scattering caused by La doping. With increased dopant levels, mass disorder and lattice distortion further intensify phonon scattering, leading to a greater reduction in lattice thermal conductivity (Y. Li et al., 2016). The substantial atomic mass difference between La and Y in YHSe creates mass disor-

der, which scatters low-frequency acoustic phonons, the primary heat carriers, thereby reducing lattice thermal conductivity. In our study, we observe that La doping in YHSe significantly reduces the lattice thermal conductivity, especially at higher doping levels. This decrease is ascribed to intensified phonon scattering processes, mainly resulting from the significant atomic mass disparity between La and Y.The heavier La atoms introduce mass disorder in the lattice, which preferentially scatters low-frequency acoustic phonons the dominant carriers of heat in crystalline solids. This observation is well-supported by the findings of (Nishino et al., 2006), who reported that the substitution of heavier atoms in a host lattice contributes to the suppression of lattice thermal conductivity. Their work emphasizes that atomic mass contrast enhances phonon scattering, which is a desirable feature for thermoelectric materials as it promotes a low lattice thermal conductivity while maintaining a high Seebeck coefficient. Our results are in line with this principle, showing that the La substitution acts as an effective strategy to suppress lattice heat transport in YHSe, thereby improving its thermoelectric performance.

Our calculated results indicate a notable decrease in lattice thermal conductivity with increasing La doping concentration in YHSe. This trend can be attributed to two primary mechanisms: the significant mass and size difference between La and Y atoms, and the potential increase in grain boundary scattering.

The substitution of Y with heavier La atoms introduces point defects and mass disorder, which enhance phonon scattering and reduce thermal transport. This mechanism is consistent with the results reported by Y. Li et al. (2016), who showed that the introduction of dopant ions lowers phonon heat conductivity by Promoting greater phonon scattering caused by variations in size and mass of atoms.

Moreover, La doping may influence the microstructure, potentially leading to reduced grain size and increased grain boundary density both of which further suppress phonon transport. Thus, the mechanisms proposed by Li et al., 2016 provide strong theoretical backing for the observed reduction in Lattice heat transport as examined in our research, supporting the idea that both mass disorder and microstructural changes contribute to improved thermoelectric performance in La-doped YHSe. Thus, the lattice thermal conductivity is primarily explained by mass difference scattering, meaning that doping with

heavier elements like La more effectively shortens the phonon mean free path in YHSe. As temperature increases, Umklapp phonon-phonon scattering processes become dominant, further reducing lattice thermal conductivity. These results are consistent with earlier research on the superior thermoelectric efficiency of oxyselenides, especially the naturally low thermal conductivity reported in calcium-doped BiCuSeO (Pei et al., 2013; Amirkhizi et al., 2024).

According to Fig.4.41 and Fig.4.42, as La concentration increases, the phononic contribution to heat transport decreases, while the electronic contribution increases. The suppression of lattice thermal conductivity at higher doping levels enhances thermoelectric performance by increasing the ZT, most significantly at lower thermal conditions, as shown in Fig. 4.42. La doping effectively modulates lattice thermal conductivity, suggesting that optimizing doping concentration can improve thermoelectric efficiency.

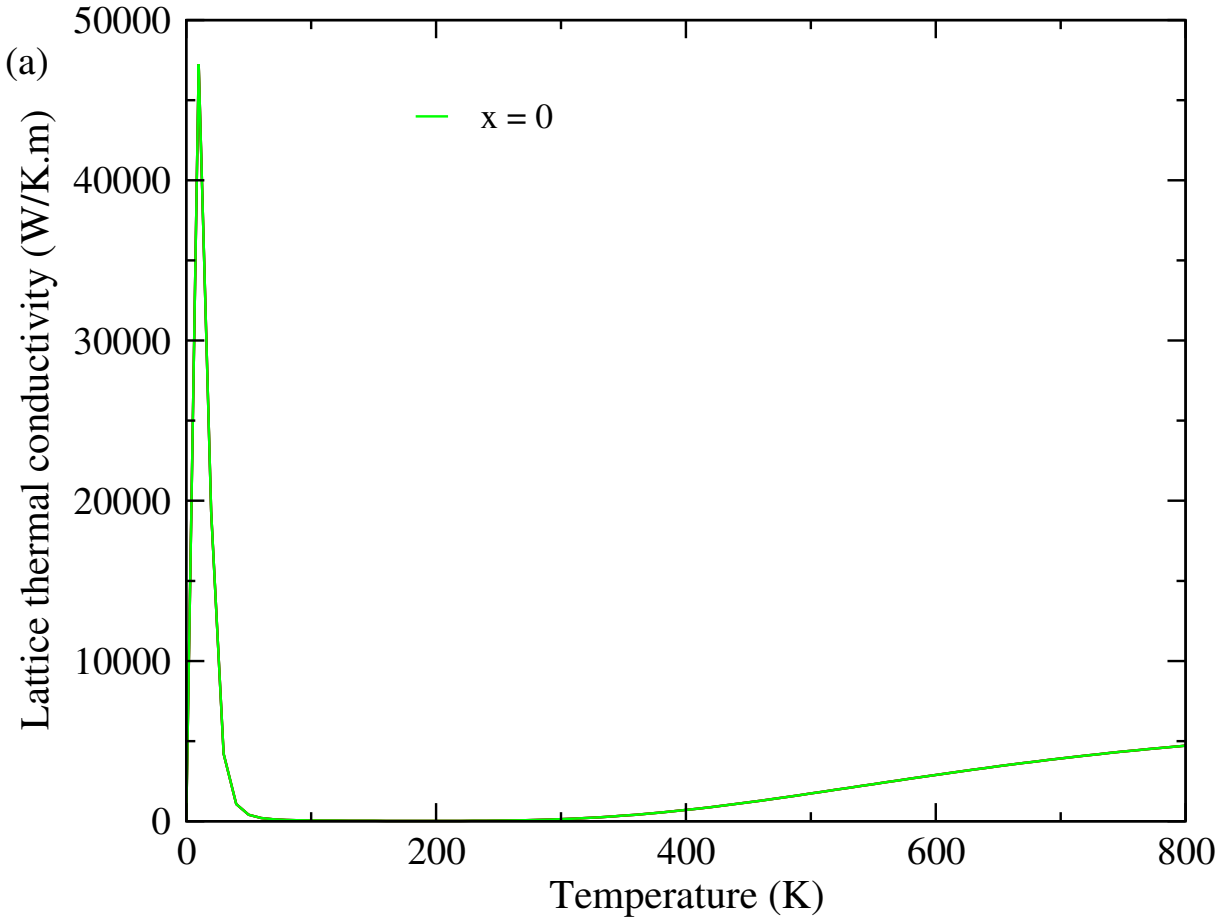

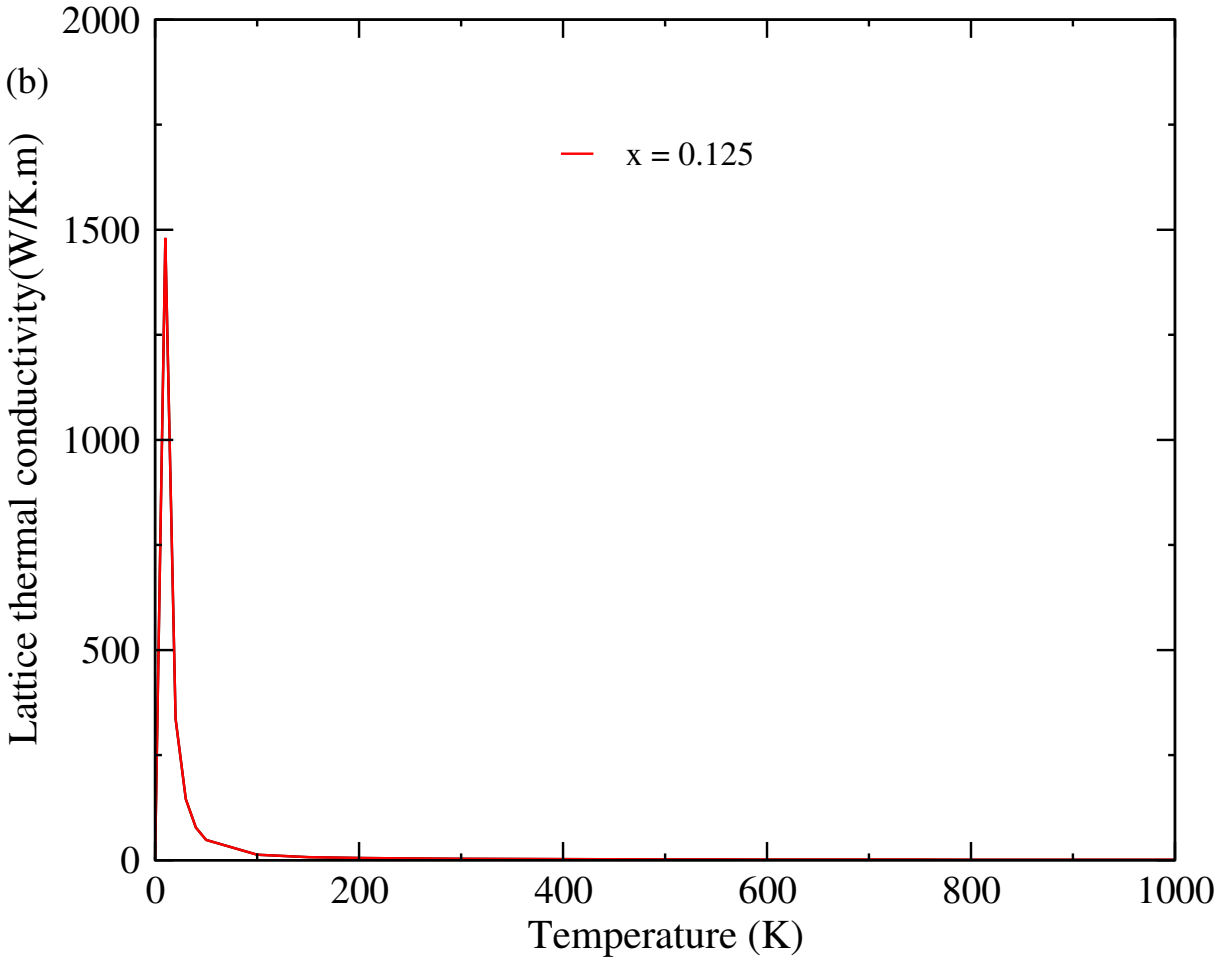
(b)
x = 0.125
Lattice thermal conductivity(W/K.m)
Temperature (K)
2000
1500
1000
500
0
0
200
400
600
800
1000

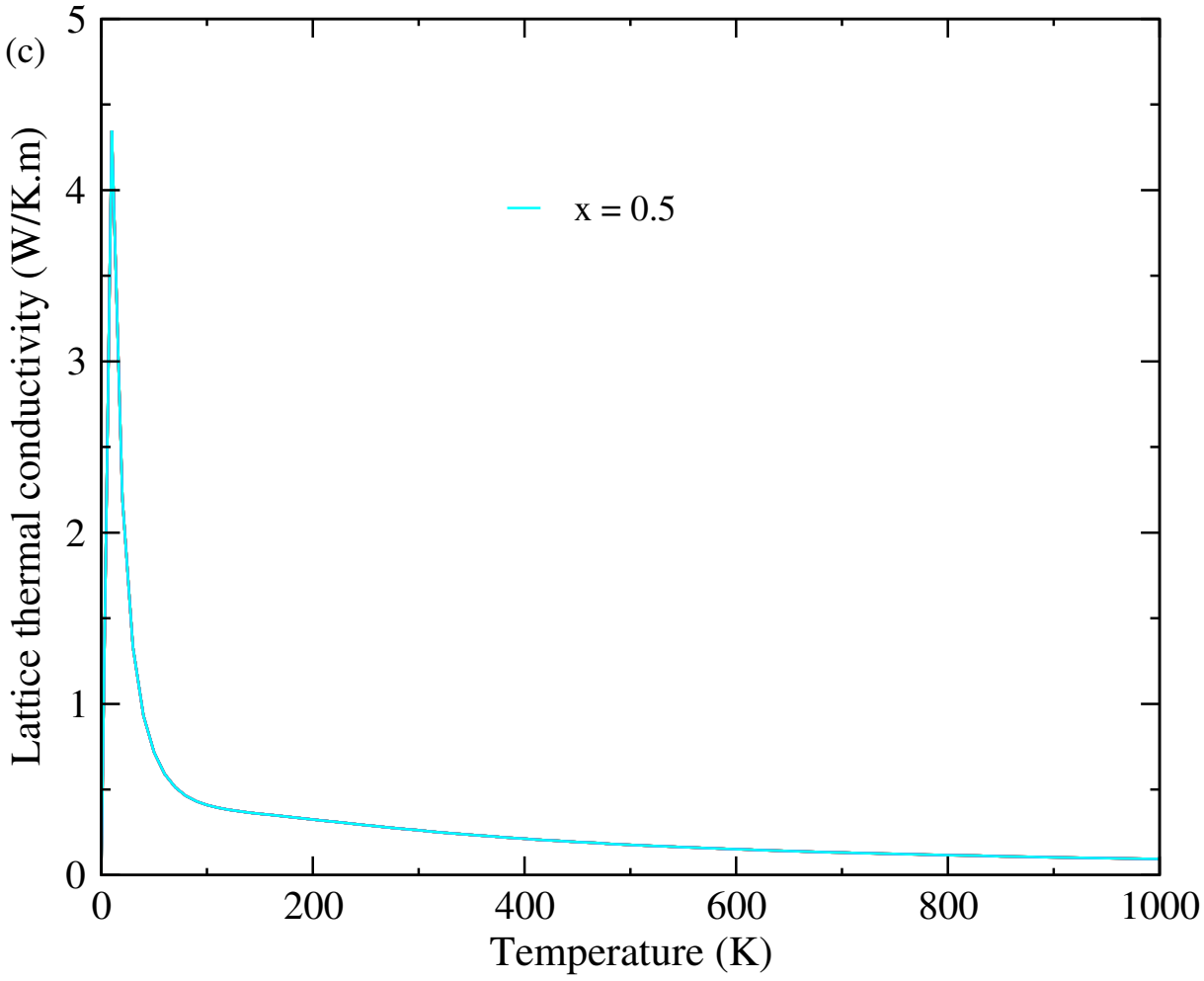

Figure 4.42: Lattice thermal conductivity (κ_{ph}) of La-doped YHSe at different La concentrations: (a) $x = 0$, (b) $x = 0.125$, and (c) $x = 0.5$.

Figure 4.43 shows the dimensionless thermoelectric ZT for YHSe at various La doping concentrations (x = 0, 0.125, and 0.5). The investigation focuses on how ZT varies with temperature across these doping levels. For pristine YHSe, the figure of merit gradually increases with temperature, reaching a maximum around 800 K. This trend suggests that intrinsic YHSe maintains reasonable thermoelectric performance over a wide temperature range. At low La doping ($x = 0.125$), ZT is consistently higher than that of the pristine case across all temperatures, indicating that moderate La doping enhances thermoelectric performance. The increase is more pronounced at lower temperatures, after which the curve stabilizes at higher temperatures. At higher La doping ($x = 0.5$), ZT rises rapidly at lower temperatures, reaching a peak around 350 K before declining at higher temperatures. This behavior is attributed to the initially low carrier concentration at $x = 0.5$. The small carrier concentration at moderate temperatures (50 - 350 K) enhances the ZT, reaching approximately 0.75. The Seebeck coefficient decreases as the temperature rises, due to the generation of additional excited carriers, which lowers the Seebeck coefficient. This trend suggests that the material with $x = 0.5$ doping may exhibit favorable thermoelectric properties at moderate temperatures but loses efficiency at higher temperatures.

Our results for La doped YHSe follow this same behavior, emphasizing the need to optimize doping levels to balance n and S. Unlike undoped or moderately doped samples (e.g., $x = 0.125$), where a favorable balance is achieved.

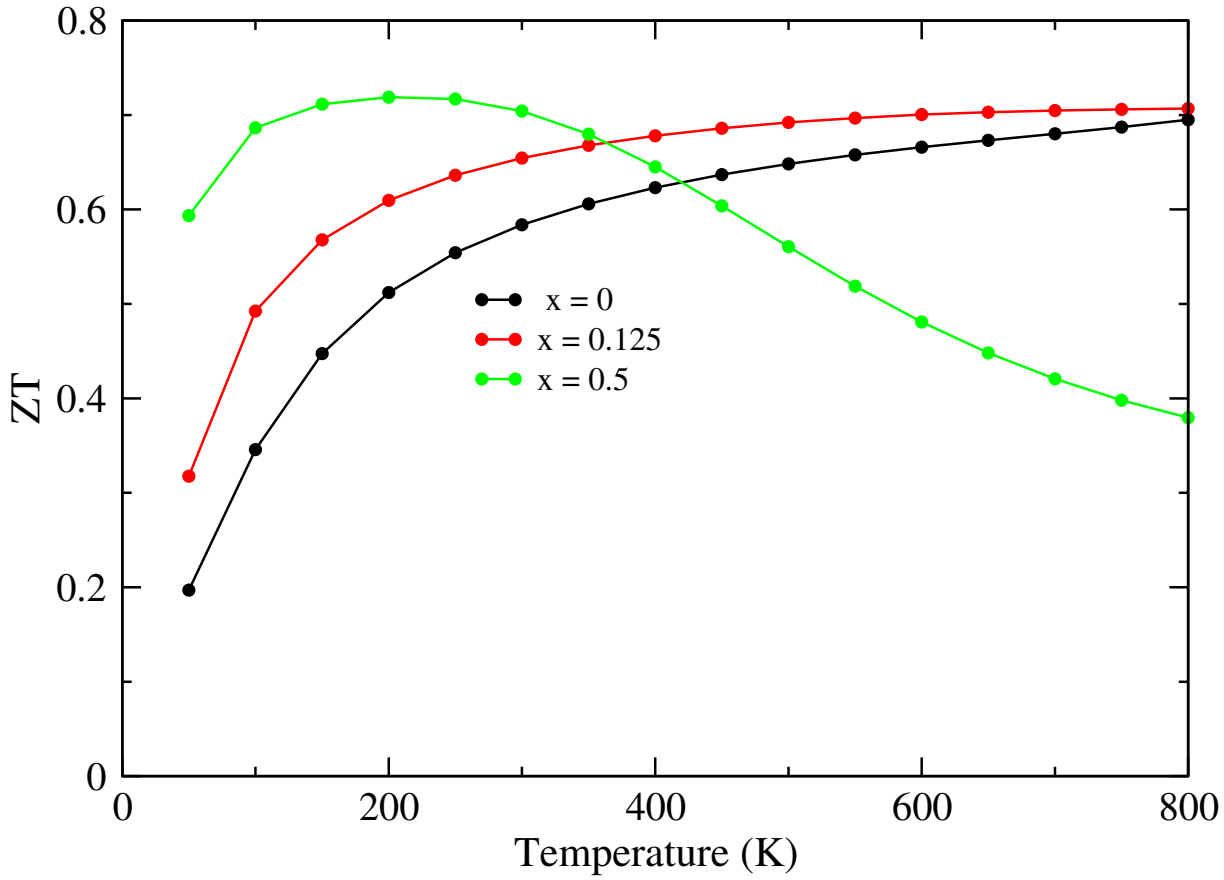

Figure 4.43: Figure of merit (ZT) of La-doped YHSe at different La concentrations.

Figure 4.44 shows the carrier concentration as a function of temperature for Yttrium Hydrogen Selenide (YHSe) at various La doping concentrations ($x = 0, 0.125, \text{and } 0.5$). Doping is a critical factor influencing the electronic properties of materials, as it introduces extra charge carriers and perturbs the band structure (shklovskii ,2013). In our study, the incorporation of lanthanum, a trivalent element, into the YHSe lattice (where Y is also trivalent but La has a larger atomic radius and a more diffuse electron cloud) leads to a significant increase in carrier concentration. This increase is clearly observed in Fig. 4.44, where higher La content correlates with a rise in carrier density across the temperature range. This behavior aligns well with previous findings in rare-earth-doped semiconductors such as La-doped Y_2O_3 (Zhang, L. et al., 2020) and La-doped Bi_2Se_3 (li,et al., 2017), where La doping similarly introduced donor states and enhanced electron concentration. By introducing dopants such as La into the YHSe lattice, significant alterations in carrier concentration can be observed in this study.

From Fig. 4.44, as the La doping concentration increases, the carrier concentration in YHSe also rises. This can be attributed to the higher availability of majority holes and minority electrons, as La-doped YHSe is a p-type semiconducting material, as indicated by the sign of the Seebeck coefficient in this study, which facilitates electrical conduction. The Seebeck coefficient values of all calculated samples are positive, indicating that holes are the majority carriers in La-doped YHSe. As the La concentration increases from 0 to 0.5, the carrier concentration becomes significantly higher than that of pristine YHSe and increases more prominently with temperature. This suggests that La doping enhances carrier density, while temperature-dependent excitation further amplifies this effect. At higher doping levels ($x = 0.5$), the carrier concentration starts at a low value and increases exponentially with temperature. This low initial concentration enhances the Seebeck coefficient at moderate temperatures up to 350 K, suggesting a more significant impact of temperature on carrier generation, likely due to a reduced band gap at higher doping levels.

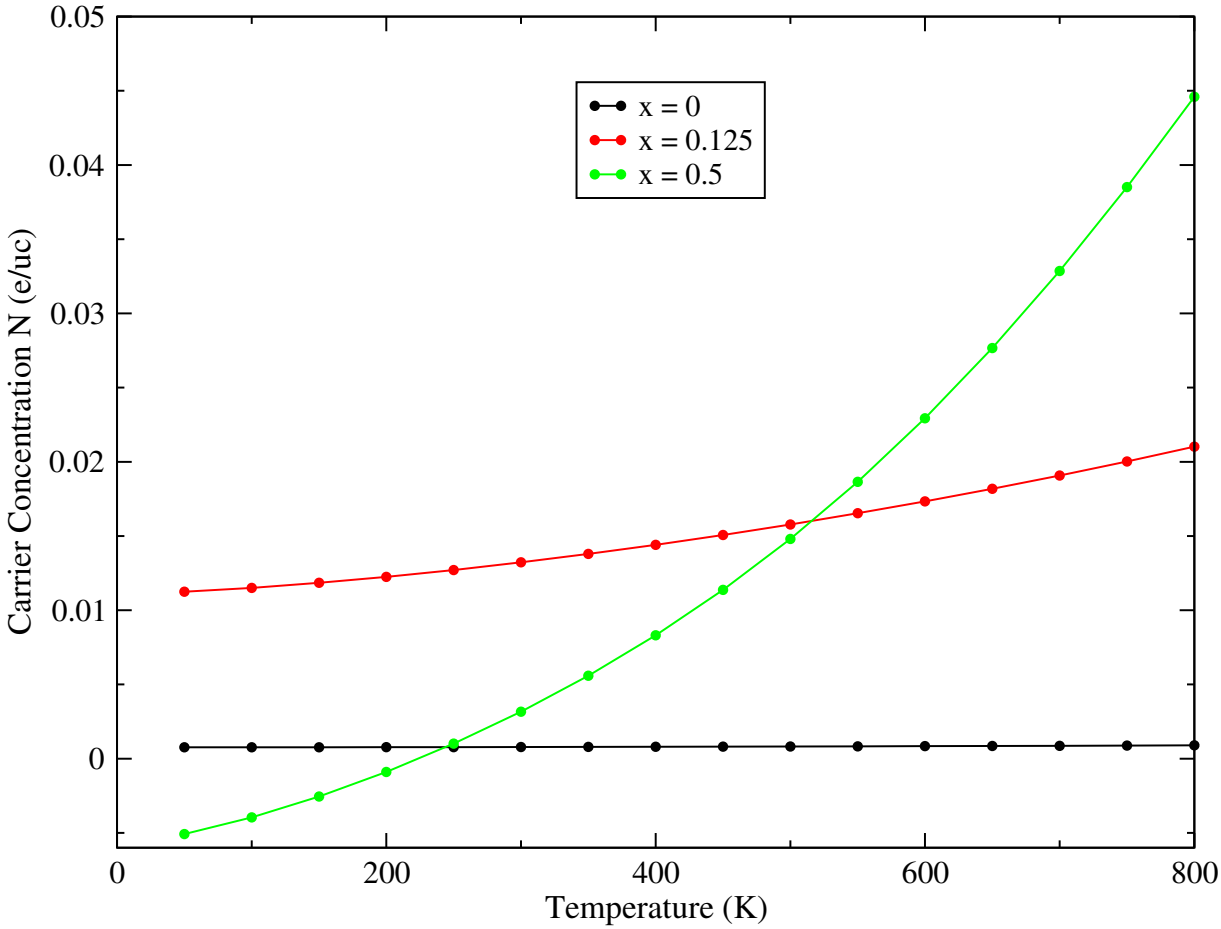

Figure 4.44: Carrier concentration of La-doped YHSe at varying lanthanum concentrations

Figure 4.45 shows the specific heat capacity (c) of La-doped YHSe across varying La concentrations. While it is known that the DOS at the Fermi level influences electronic specific heat, our results reveal a direct correlation between La doping and the enhancement of electronic specific heat (c). Specifically, as La concentration increases, the DOS at the Fermi level also increases, leading to a noticeable rise in electronic specific heat. Specifically, as La concentration increases, the DOS at the Fermi level also increases, leading to a noticeable rise in electronic specific heat. This trend suggests that La doping not only modifies the electronic structure but also significantly enhances the material's capacity to store thermal energy via electronic excitation. This behavior is particularly important in applications requiring efficient thermal management or electronic tuning, indicating that La doping can be used as a tool to engineer thermal properties in YHSe-based devices.

Increasing the La concentration leads to a rise in the DOS at the Fermi energy, which sub-

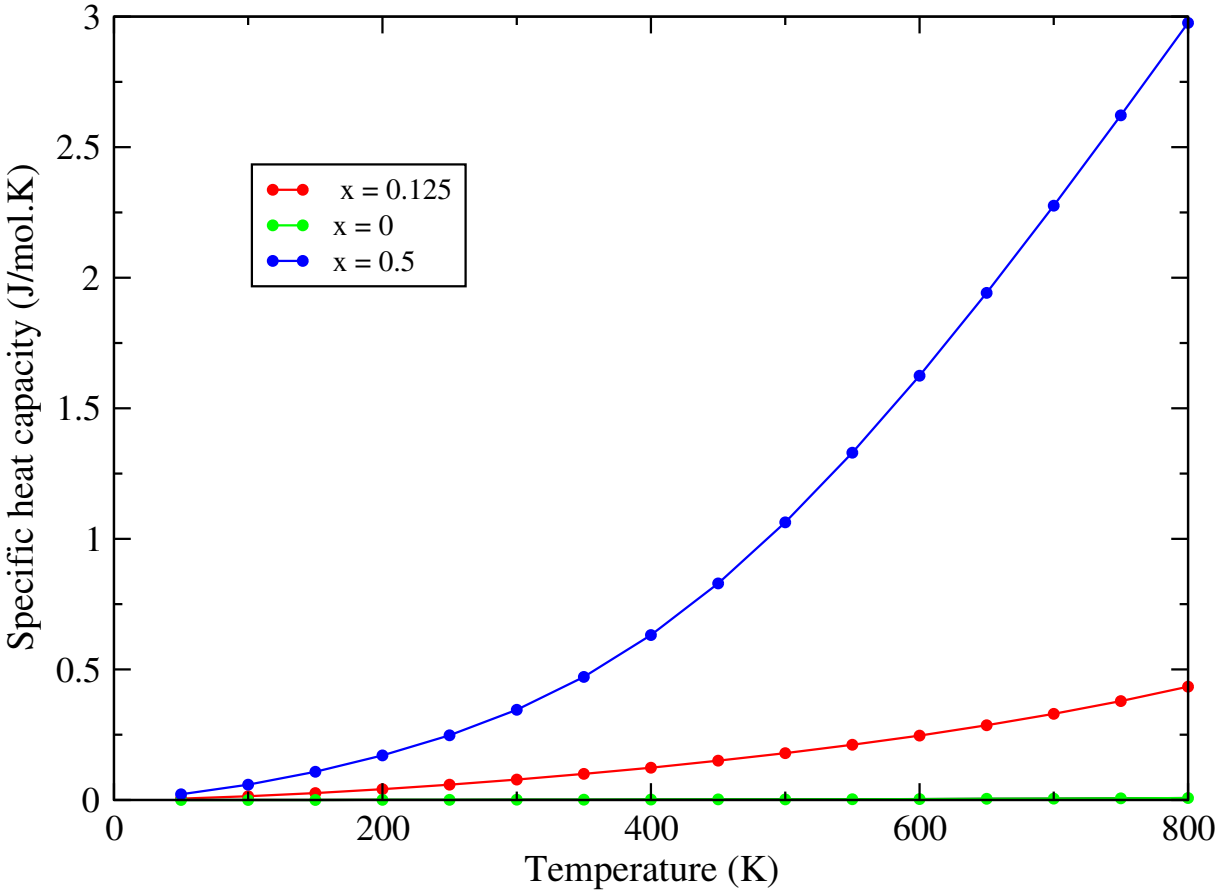

Figure 4.45: Specific heat capacity of La-doped YHSe at varying lanthanum concentrations.

sequently enhances the electronic specific heat capacity. This trend aligns with the findings of Siham Malki et al., (2020), who reported a similar relationship between increased DOS at the Fermi level and enhanced electronic specific heat in VbS_2 using DFT calculations (Malki & Farh, 2020). In both cases, the introduction of dopants (La in YHSe and a transition metal in VbS_2) modified the electronic structure, increasing the DOS near the Fermi level. This directly contributes to a higher value of the Sommerfeld coefficient (γ), which is proportional to the DOS at E_F, and hence to the electronic part of the specific heat. The rise in DOS implies that more states are available for the charge carriers, which means more thermal energy can be absorbed, thus increasing the specific heat capacity. In addition to increasing the DOS, doping typically affects carrier concentration.

5

Conclusions and Recommendations

5.1 Conclusions

This dissertation comprehensively investigates the structural, electronic, optical, phonon, thermoelectric, and superconducting properties of yttrium hydrogen selenide (YHSe) under varying pressures and lanthanum (La) doping. Both the Generalized Gradient Approximation (GGA) and the GGA+U method were employed for electronic structure calculations. The results demonstrate that the GGA+U approach significantly improves the prediction of band gaps and electronic density of states (DOS) compared to the standard GGA, providing a more accurate description of the electronic behavior in both pristine and La-doped YHSe.

Building on this improved electronic description, our findings reveal that external pressure has a pronounced effect on the functional properties of YHSe. It modifies the electronic band structure, reduces the band gap, and can induce a semiconductor-to-metal transition. Notably, pressure transforms YHSe from an indirect to a direct band gap semiconductor, which is favorable for optoelectronic applications due to improved light absorption and emission capabilities. Moreover, modifications in the electronic structure caused by pressure result in variations in the DOS around the Fermi level, which in turn affect carrier transport behavior. Such alterations contribute positively to thermoelectric performance by improving the Seebeck coefficient and electrical conductivity, while also aiding in the reduction of lattice heat conductivity.

Additionally, pressure reduces the lattice parameters, which strengthens interatomic bonding and increases orbital overlap, resulting in modified mechanical properties. It also enhances Phonon-phonon scattering, which diminishes the lattice contribution to heat conductivity and increases anharmonic effects. Under extreme pressure conditions, enhanced EPC and enhance the superconducting behavior of YHSe, consistent with observations in other hydrogen-based superconductors. Beyond pressure effects, this study explores

the role of La doping in enhancing the intrinsic properties of YHSe. Our results indicate that La serves as a crucial dopant, enhancing the superconducting critical temperature without requiring external pressure. This behavior distinguishes it from previous studies. Furthermore, La doping significantly enhances thermoelectric performance by lowering phonon contribution to heat conductivity, which in turn boosts the ZT. The optical properties of YHSe also benefit from La incorporation, as evidenced by improved absorption characteristics.

Moreover, La doping profoundly influences the electrical properties of YHSe. As the doping concentration increases, ultimately closing the band gap and increasing the DOS at the Fermi level . Additionally, La doping modifies the band structure, further facilitating the transition of YHSe from an indirect to a direct semiconductor. This transition enhances the material's optoelectronic performance, making it highly effective for applications requiring strong light absorption and emission.

Moreover, increasing La concentration shifts the CBM to lower energies and the VBM to higher energies. The La-doped YHSe semiconductor exhibits a broad spectral response, effectively extending the photo-response from the near-visible light region into the upper ultraviolet (UV) range across various doping concentrations.

La doping introduces phonon softening, which affects the superconducting, and thermal properties of the YHSe material. It intensifies phonon-phonon scattering, thereby reducing the phonon-driven component of heat transport, which is crucial for enhancing thermoelectric efficiency. Furthermore, La doping considerably increases the lattice parameter along the c-axis, resulting in a higher c/a ratio and, consequently, greater structural anisotropy. This structural modification influences both the mechanical and electronic properties of the material, further contributing to its potential for advanced technological applications.

Overall, this research highlights the multifaceted impact of pressure and La doping in tailoring the properties of YHSe, positioning it as a promising material for energy conversion, superconductivity, and advanced optoelectronic applications. To fully exploit its potential, further studies on mechanical stability and possible phase transitions under extreme conditions are necessary.

In conclusion, the synergistic effects of pressure and La doping underscore YHSe's

potential as a transformative material for various technological applications. Continued exploration under diverse conditions will be essential in unlocking the full capabilities of YHSe and its doped derivatives.

5.2 Recommendations

To advance the understanding and application of YHSe-based materials, the following research directions are recommended:

- Investigate diverse dopants, co-doping strategies, and the role of intrinsic defects to tailor electronic and optical properties.
- Explore 2D forms, heterostructures, and strain-engineered systems for enhanced thermoelectric performance.
- Experimental Synthesize and characterize YHSe compounds to confirm theoretical predictions and evaluate real-world performance.
- Building on DFPT-based analysis, future work could explore many-body approaches or experimental validation to gain deeper insight into the superconducting mechanism and improve accuracy in T_c prediction.
- Extend the current analysis by exploring nanostructuring, interface engineering, and anharmonic effects to further enhance the thermoelectric performance beyond the included lattice thermal conductivity.

List of Publications

A. Articles Published in Reputable Journals

1. **Effect of Pressure Variation on Electronic Structure, Phonon, and Superconductivity Properties of YHSe Compound** *Wiley Journal of Advances in Condensed Matter Physics*, Article ID 8722867, 15 pages.
   https://doi.org/10.1155/2024/8722867

2. **Tuning and Enhancing Photochromic Behavior in YHSe through Pressure Variations and Doping**, *Wiley Journal of Advances in Condensed Matter Physics*, Article ID 8831998, 18 pages.
   https://doi.org/10.1155/2024/8831998

B. Manuscript Under Review

3. **Doping Effects on Phonon and Superconductivity of Yttrium Hydrogen Selenide at Different Lanthanum (La) Concentrations** *(Second Revision).*

C. Ready Manuscript

4. **Doping Effects and Pressure Variations on Thermoelectric Properties of Yttrium Hydrogen Selenide Compound**

Bibliography

Abrahams, S. C., Ginsberg, A. P., & Knox, K. (1964). Transition metal-hydrogen compounds. II. The crystal and molecular structure of potassium rhenium hydride, K2ReH9. Inorganic Chemistry, 3(4), 558-567.

Agamah, C., Vuori, S., Colinet, P., Norrbo, I., de Carvalho, J. M., Okada Nakamura, L. K., ... & Lastusaari, M. (2020). Hackmanite The natural glow-in-the-dark material. "Chemistry of Materials", 32(20), 8895-8905.

Ali, A., Khan, T., & Tahir, M. (2021). Synergistic effect of Co/La in oxygen vacancy rich ternary CoAlLa layered double hydroxide with enhanced reductive sites for selective photoreduction of CO2 to CH4. "Energy Fuels", 35, 8922–8943.

Amritha, A., Sundararajan, M., Rejith, R. G., & Mohammed-Aslam, M. A. (2019). La-Ce doped TiO2 nanocrystals: A review on synthesis, characterization and photocatalytic activity. "SN Applied Sciences", 1(11), 1441.

Ashcroft, N. W. (1968). Metallic hydrogen: A high-temperature superconductor. "Physical Review Letters", 21(26), 1748.

Atta, R. M. (2011). Solar water condensation using thermoelectric coolers. "International Journal of Water Resources and Arid Environments", 1(2), 142.

Ahmad, S., Ur Rehman, J., Tahir, M. B., Alzaid, M.,& Shahzad, K. (2023). Investigation of external isotropic pressure effect on widening of bandgap, mechanical, thermodynamic, and optical properties of rubidium niobate using first-principles calculations for photocatalytic application. Optical and Quantum Electronics, 55(4), 346.

Ali Khan, A., & Tahir, M. (2021) Synergistic effect of Co/La in oxygen vacancy rich ternary CoAlLa layered double hydroxide with enhanced reductive sites for selective photoreduction of CO2 to CH4. Energy & Fuels, 35(10), 8922–8943.

Allen, P. B., & Dynes, R. C. (1975) Superconductivity and phonon softening: II. Lead alloys. Physical Review B, 11(5), 1895.

Alouani, M & Wills, J. M. (1996). Calculated optical properties of Si, Ge, and GaAs under hydrostatic pressure. Physical Review B, 54(4), 2480.

Amirkhizi, P., Madre, M. A., Dura, O. J., Torres, M. A., Sotelo, A., Kovalevsky, A. V., & Rasekh, S. (2024). Enhancing thermoelectric performance of CaMnO3 through a Y- and La- dual-doping strategy. Ceramics International, 51(7), 9421–9428. https://doi.org/10.1016/j.ceramint.2024.12.375

Awada, C., Whyte, G. M., Offor, P. O., Whyte, F. G., Kanoun, M. B., Goumri-Said, S., Alshoaibi, A., Ekwealor, A. B. C., Maaza, M., & Ezema, F. I. (2020). Synthesis and studies of electro-deposited yttrium arsenic selenide nanofilms for opto-electronic applications. Nanomaterials, 10(8), 1–15. https://doi.org/10.3390/nano10081557

Bahk, J. H., & Shakouri, A. (2014). Enhancing the thermoelectric figure of merit through the reduction of bipolar thermal conductivity with heterostructure barriers. "Applied Physics Letters", 105(5).

Babón, J. C., Esteruelas, M. A., & López, A. M. (2022). Homogeneous catalysis with polyhydride complexes. Chemical Society Reviews, 51(23), 9717-9758.

Bardeen, J., Cooper, L. N., & Schrieffer, J. R. (1957). Theory of superconductivity. "Physical Review", 108(5), 1175.

Barachevsky, V. A. (2017). Negative photochromism in organic systems. "Review Journal of Chemistry", 7, 334-371.

Baroni, S., De Gironcoli, S., Dal Corso, A., & Giannozzi, P. (2001). Phonons and related crystal properties from density-functional perturbation theory. "Reviews of Modern Physics", 73(2), 515.

Babu, K. R., & Guo, G. Y. (2019). Electron-phonon coupling, superconductivity, and nontrivial band topology in NbN polytypes. Physical Review B, 99(10), 1–12. https://doi.org/10.1103/PhysRevB.99.104508

Bağcı, S., Tütüncü, H. M., Duman, S., & Srivastava, G. P. (2010). Phonons and superconductivity in fcc and dhcp lanthanum. Physical Review B—Condensed Matter and Materials Physics, 81(14), 144507.

Bashir, A., Bashir, F., Sultan, M., Mubeen, M., Iqbal, A., & Akhter, Z. (2020). Influence of nickel and lanthanum ions co-doping on photocatalytic properties of TiO 2 for effective degradation of reactive yellow 145 in the visible region. Journal of Sol-Gel Science and Technology, 93, 438–451.

Ben Mahmoud, C., Anelli, A., Csányi, G., & Ceriotti, M. (2020). Learning the electronic density of states in condensed matter. Physical Review B, 102(23), 235130.

Besedin, S., Eremets, M., Troyan, I., & Irodova, A. (n.d.). Search for CaH6 in X-ray diffraction measurements at pressures up 200 GPa.

Besson, J. M. (1989) Pressure dependence of Tc and electron phonon interaction in MBa2Cu3O7 systems. Journal de Physique, 50(12), 1433–1443.

Blakemore, J. S.(1985) Solid state physics. Cambridge university press.

Boppella, R., Choi, C. H., Moon, J., & Kim, D. H. (2018). Spatial charge separation on strongly coupled 2D-hybrid of rGO/La2Ti2O7/NiFe-LDH heterostructures for highly efficient noble metal free photocatalytic hydrogen generation Applied Catalysis B: Environmental, 239, 178-186.

Bednorz, J. G., & Müller, K. A. (1986) Possible high Tc superconductivity in the Ba-La-Cu-O system. "Zeitschrift für Physik B Condensed Matter", 64(2), 189-193.

Beal, A. and Liang, W. (1976) Reflectivity spectra of some first row transition metal intercalates of nbs. Philosophical Magazine, 33(1):121-131.

Bhuiya, M. M. H., Kumar, A., & Kim, K. J. (2015) Metal hydrides in engineering systems, processes, and devices: a review of non-storage applications. International Journal of Hydrogen Energy, 40(5), 2231-2247.

Boukhris, N., Meradji, H., Ghemid, S., Drablia, S., & Hassan, F. E. H. (2011). Ab initio study of the structural, electronic and thermodynamic properties of PbSe1 xSx, PbSe1 xTex and PbS1 xTex ternary alloys. "Physica Scripta", 83(6), 065701.

Bouas-Laurent, H., & Dürr, H. (2001). Organic photochromism (IUPAC technical report). "Pure and Applied Chemistry", 73(4), 639-665.

Callaway, J. (1959). Model for lattice thermal conductivity at low temperatures. Physical Review, 113(4), 1046.

Cao, T., Shi, X.-L., Li, M., Hu, B., Chen, W., Liu, W.-D., Lyu, W., MacLeod, J., & Chen, Z.-G. (2023). Advances in bismuth-telluride-based thermoelectric devices: progress and challenges. EScience, 3(3), 100122.

Chen, X.-J., Struzhkin, V. V, Kung, S., Mao, H., Hemley, R. J., & Christensen, A. N. (2004). Pressure-induced phonon frequency shifts in transition-metal nitrides. Physical Review B, 70(1), 14501.

Chen, Y.-C., Yu, C.-Y., Fan, Y.-L., Hung, L.-I., Chen, C.-P., & Ting, C. (2010). Low-bandgap conjugated polymer for high efficient photovoltaic applications. Chemical Communications, 46(35), 6503–6505.

Chen, Y., Yang, H., Liu, X., & Guo, L. (2010). Effects of cocatalysts on photocatalytic properties of La doped Cd2TaGaO6 photocatalysts for hydrogen evolution from ethanol aqueous solution. International Journal of Hydrogen Energy, 35(13), 7029–7035.

Chen, Z., Zhang, X., Lin, S., Chen, L., & Pei, Y. (2018). Rationalizing phonon dispersion for lattice thermal conductivity of solids. National Science Review, 5(6), 888–894.

Chen, W., Semenok, D. V., Huang, X., Shu, H., Li, X., Duan, D., ... & Oganov, A. R. (2021). High-temperature superconducting phases in cerium superhydride with a T c up to 115 K below a pressure of 1 megabar. Physical Review Letters, 127(11), 117001.

Congeduti, A., Postorino, P., Caramagno, E., Nardone, M., Kumar, A., & Sarma, D. D. (2001). Anomalous high pressure dependence of the Jahn-Teller phonon in La 0.75 Ca 0.25 MnO 3. Physical Review Letters, 86(7), 1251.

Chen, Y. C., Yu, C. Y., Fan, Y. L., Hung, L. I., Chen, C. P., & Ting, C. (2010). Low-bandgap conjugated polymer for high efficient photovoltaic applications. "Chemical Communications", 46(35), 6503-6505.

Chu, C. W., & Testardi, L. R. (1974). Direct observation of enhanced lattice stability in V3Si under hydrostatic pressure. "Physical Review Letters", 32(14), 766.

Coperet, C., Estes, D. P., Larmier, K., & Searles, K. (2016). Isolated surface hydrides: formation, structure, and reactivity. Chemical reviews, 116(15), 8463-8505.

Cui, Y., Ke, Y., Liu, C., Chen, Z., Wang, N., Zhang, L., ... & Long, Y. (2018). Thermochromic VO2 for energy-efficient smart windows. "Joule", 2(9), 1707-1746.

Dehkordi, A. M., Zebarjadi, M., He, J., & Tritt, T. M. (2015). Thermoelectric power factor: Enhancement mechanisms and strategies for higher performance thermoelectric materials. Materials Science and Engineering: R: Reports, 97, 1–22.

Ding, Y. C., Xiang, A. P., Xu, M., & Zhu, W. J. (2008). Electronic structures and optical properties of -Si3N4 doped with La. Physica B: Condensed Matter, 403(13–16), 2200–2206.

Drozdov, A. P., Eremets, M. I., Troyan, I. A., Ksenofontov, V., & Shylin, S. I. (2015). Conventional superconductivity at 203 kelvin at high pressures in the sulfur hydride system. Nature, 525(7567), 73–76.

Drozdov, A. P., Kong, P. P., Minkov, V. S., Besedin, S. P., Kuzovnikov, M. A., Mozaffari, S., Balicas, L., Balakirev, F. F., Graf, D. E., & Prakapenka, V. B. (2019). Superconductivity at 250 K in lanthanum hydride under high pressures. Nature, 569(7757), 528–531.

Dixon, D. A. (2016). Density functional theory. "Encycl. Earth Sci. Ser.", pages 1–7.

Drozdov, A. P., Eremets, M. I., & Troyan, I. A. (2015). Superconductivity above 100 K in PH3 at high pressures. "arXiv preprint arXiv:1508.06224".

Du, J., Yang, Z., Lin, H., & Poelman, D. (2024). Inorganic photochromic materials: Recent advances, mechanism, and emerging applications. "Responsive Materials", 2(2), e20240004.

Dürr, H. (1989). Perspectives in Photochromism: A Novel System Based on the 1,5-Electrocyclization of Heteroanalogous Pentadienyl Anions. "Angewandte Chemie International Edition in English", 28(4), 413-431.

Delaire, O., Lucas, M. S., Dos Santos, A. M., Subedi, A., Sefat, A. S., McGuire, M. A., ... & Egami, T. (2010). Temperature and pressure dependence of the Fe-specific phonon density of states in Ba (Fe 1 x Co x) 2 As 2. Physical Review B—Condensed Matter and Materials Physics, 81(9), 094504.

Eliashberg, G. M. (1960). Interactions between electrons and lattice vibrations in a superconductor. Sov. Phys. JETP, 11(3), 696–702.

Egranov, A. V., Sizova, T. Y., Shendrik, R. Y., & Smirnova, N. A. (2016). Instability of some divalent rare earth ions and photochromic effect. "Journal of Physics and Chemistry of Solids", 90, 7-15.

Ekimov, E. A., Sidorov, V. A., Bauer, E. D., Mel'Nik, N. N., Curro, N. J., Thompson, J. D., & Stishov, S. M. (2004). Superconductivity in diamond. "Nature", 428(6982), 542-545.

Emme, H. & Hupperz, H. (2004). Acta Cryst., 60, 117-119.

Flores-Livas, J. A., Boeri, L., Sanna, A., Profeta, G., Arita, R., and Eremets, M. "A perspective on conventional high-temperature superconductors at high pressure: Methods and materials." Physics Reports 856 (2020): 1–78. https://doi.org/10.1016/j.physrep.2020.02.003

Fujishima, A., & Honda, K. (1972). Electrochemical photolysis of water at a semiconductor electrode. Nature, 238(5358), 37–38.

Garrity, K. F., Bennett, J. W., Rabe, K. M., & Vanderbilt, D. (2014). Pseudopotentials for high-throughput DFT calculations. "Computational Materials Science", 81, 446-452.

Ge, M., Cao, C., Huang, J., Li, S., Chen, Z., Zhang, K.-Q., Al-Deyab, S. S., & Lai, Y. (2016). A review of one-dimensional TiO2 nanostructured materials for environmental and energy applications. Journal of Materials Chemistry A, 4(18), 6772–6801.

Giannozzi, P., Andreussi, O., Brumme, T., Bunau, O., Buongiorno Nardelli, M., Calandra, M., Car, R., Cavazzoni, C., Ceresoli, D., Cococcioni, M., Colonna, N., Carnimeo, I., Dal Corso, A., De Gironcoli, S., Delugas, P., Distasio, R. A., Ferretti, A., Floris, A., Fratesi, G., Baroni, S. (2017). Advanced capabilities for materials modelling with Quantum ESPRESSO. Journal of Physics Condensed Matter, 29(46), 1–31.

Grätzel, M. (2001). Photoelectrochemical cells. nature 414.

Gor'kov, L. P., & Kresin, V. Z. (2018). Colloquium: high pressure and road to room temperature superconductivity. Reviews of Modern Physics, 90(1), 011001.

Gschneidner, K. A., Pecharsky, V. K., and Tsokol, A. O. "Recent developments in magnetocaloric materials." Reports on Progress in Physics 68, no. 6 (2005): 1479–1539. https://doi.org/10.1088/0034-4885/68/6/R04

Guo, H., Yang, T., Tao, P., Wang, Y., & Zhang, Z. (2013). High pressure effect on structure, electronic structure, and thermoelectric properties of MoS2. Journal of Applied Physics, 113(1).

Guo Ott Schilling, Cantoni. Superconductivity above 130 k in the hg-ba-ca-cu-o system. Phys. Rev. B, 363, May 1993.

Grockowiak, A. D., Ahart, M., Helm, T., Coniglio, W. A., Kumar, R., Glazyrin, K., ... & Tozer, S. W. (2022). Hot hydride superconductivity above 550 K. "Frontiers in Electronic Materials", 2, 837651.

Harrison, W. A. (2012). Electronic structure and the properties of solids: the physics of the chemical bond. Courier Corporation.

Hasan, M., & Hossain, A. K. M. A. (2021). Structural, electronic and optical properties of strontium and nickel co-doped BaTiO3: A DFT based study. Computational Condensed Matter, 28, e00578.

Hemley, R. J., Ahart, M., Liu, H., & Somayazulu, M. (2019). Road to room-temperature superconductivity: Tc above 260 K in lanthanum superhydride under pressure. arXiv preprint arXiv:1906.03462.

Hochbaum, A. I., & Yang, P. (2010). Semiconductor nanowires for energy conversion. Chemical Reviews, 110(1), 527–546.

Hou, H., Yang, J., Hu, F., Zhang, S., & Yang, S. (2014). Structural, elastic and thermodynamic properties of rock-salt structure CdSe at high temperature and high pressure,". Chalcogenide Letters, 11(3), 121–128.

Huang, M.-Z., Xu, Y.-N., & Ching, W. Y. (1993). Pressure dependence of the band structure, density of states, Fermi surfaces, and optical properties of superconducting K 3 C 60. Physical Review B, 47(13), 8249.

Humayun, M., Ullah, H., Usman, M., Habibi-Yangjeh, A., Tahir, A. A., Wang, C., & Luo, W. (2022). Perovskite-type lanthanum ferrite based photocatalysts: Preparation, properties, and applications. Journal of Energy Chemistry, 66, 314–338.

Huo, J., Wang, L., & Yu, H. (2009). Polymeric nanocomposites for electromagnetic wave absorption. Journal of Materials Science, 44, 3917–3927.

Hussain, M. I., Khalil, R. M. A., Hussain, F., Rana, A. M., Murtaza, G., & Imran, M. (2020). Probing the structural, electronic, mechanical strength and optical properties of tantalum-based oxide perovskites ATaO3 (A= Rb, Fr) for optoelectronic applications: First-principles investigations. Optik, 219, 165027.

He, T., & Yao, J. (2006). Photochromism in composite and hybrid materials based on transition-metal oxides and polyoxometalates. "Progress in Materials Science", 51(6), 810-879.

Hohenberg, P., & Kohn, W. (1964). Density functional theory (DFT). "Phys. Rev.", 136, B864.

Howie, R. T., Guillaume, C. L., Scheler, T., Goncharov, A. F., & Gregoryanz, E. (2012). Mixed molecular and atomic phase of dense hydrogen. "Physical Review Letters", 108(12), 125501.

Ijaz, M., & Zafar, M. (2021). Titanium dioxide nanostructures as efficient photocatalyst: Progress, challenges and perspective. International Journal of Energy Research, 45(3), 3569–3589.

Ikhioya, I. L., & Nkele, A. C. (2023). A novel synthesis of hydrothermally-prepared yttrium selenide and erbium selenide nanomaterials doped with magnesium. Results in Optics, 13, 100555.

Imasato, K., Wood, M., Kuo, J. J., & Snyder, G. J. (2018). Improved stability and high thermoelectric performance through cation site doping in n-type La-doped Mg 3 Sb 1.5 Bi 0.5. Journal of Materials Chemistry A, 6(41), 19941–19946.

Iqbal, M. A., Javeed, S., Bakhsh, S., Arellano-Ramírez, I. D., Khalid, M., Morsy, K., Shati, A. A., & Choi, J. R. (2024). Pressure induced mechanical, elastic, and optoelectronic characteristics of Cd0.75Zn0.25Se alloy. Frontiers in Chemistry, 12(August), 1–12. https://doi.org/10.3389/fchem.2024.1405315

Islam, J., & Hossain, A. A. (2020). Semiconducting to metallic transition with outstanding optoelectronic properties of CsSnCl3 perovskite under pressure. Scientific reports, 10(1), 14391.

Iqbal, N. (2021). Tailoring g-C3N4 with lanthanum and cobalt oxides for enhanced photoelectrochemical and photocatalytic activity. Catalysts, 12(1), 15.

Jakhar, M., Chauhan, P., Kumar, A., & Pandey, R. (2024). Theoretical advances in predicting the thermoelectric performance of materials. 2D Materials, 12(1), 013001.

Joost, U., Sutka, A., Oja, M., Smits, K., Döbelin, N., Loot, A., ... & Nõmmiste, E. (2018). Reversible photodoping of TiO2 nanoparticles for photochromic applications. "Chemistry of Materials", 30(24), 8968-8974.

Jia, W., Niu, Y., Zhou, M., Liu, R., Zhang, L., Wang, X., & Ji, W. (2019). Effects of vacancy defects on the electronic structure and optical properties of GaN:Fe. Superlattices and Microstructures, 133, 1–9.

Jones, H. (2008). Superconductors in the transmission of electricity and networks. "Energy Policy", 36(12), 4342-4345.

Kanda, H. (2001). Colored high pressure high temperature (HPHT) synthetic diamonds. "Radiation Effects and Defects in Solids", 156(1-4), 163-172.

Kato, H., Asakura, K., & Kudo, A. (2003). Highly efficient water splitting into H2 and O2 over lanthanum-doped NaTaO3 photocatalysts with high crystallinity and surface nanostructure. "Journal of the American Chemical Society", 125(10), 3082-3089.

Kazanjian, H. and Lucas, G. (1983). Richard, M.Khenata, R., Bouhemadou, A., Sahnoun, M., Reshak, A. H., Baltache, H., and Rabah, M.(2006). Elastic, electronic and optical properties of ZnS, ZnSe and ZnTe under pressure. Comput. Mater. Sci., 38(1):29-38.

Kaur, K., & Kumar, R. (2016). Effect of pressure on electronic and thermoelectric properties of magnesium silicide: A density functional theory study. Chinese Physics B, 25(5), 56401.

Khan, A. A., Partho, A. T., Arnab, M. H., Khyam, M. A., Kumar, N., & Tahir, M. (2024). Recent advances in Lanthanum-based photocatalysts with engineering aspects for photocatalytic hydrogen production: A critical review. Materials Science in Semiconductor Processing, 184(May), 108809. https://doi.org/10.1016/j.mssp.2024.108809

Kim, D. Y., Scheicher, R. H., Mao, H., Kang, T. W., & Ahuja, R. (2010). General trend for pressurized superconducting hydrogen-dense materials. Proceedings of the National Academy of Sciences, 107(7), 2793–2796.

Kim, M., DiMaggio, C., Yan, S., Wang, H., Salley, S. O., & Ng, K. Y. S. (2011). Performance of heterogeneous ZrO2 supported metaloxide catalysts for brown grease esterification and sulfur removal. Bioresource Technology, 102(3), 2380–2386.

Kong, P. P., Minkov, V. S., Kuzovnikov, M. A., Besedin, S. P., Drozdov, A. P., Mozaffari, S., Balicas, L., Balakirev, F. F., Prakapenka, V. B., & Greenberg, E. (2019). Superconductivity up to 243 K in yttrium hydrides under high pressure. ArXiv Preprint ArXiv:1909.10482.

Kovác, J., Jakabovic, J., & Kytka, M. (2008). Advanced light emitting devices for optoelectronic applications. Photonics, Devices, and Systems IV, 7138, 537–542.

Kokalj, A. (1999) XCrySDen-a new program for displaying crystalline structures and electron densities. Journal of Molecular Graphics and Modelling, 17(3–4), 176–179.

Kumar, S., Parashari, S. S., and Auluck, S. (2009). Disorder effects on electronic and optical properties of the ternary gaxin1- xp (x= 0.25, 0.50,and 0.75) alloy. physica status solidi (b), 246(10):2294–2300.

Kumari, A., Panda, R., Jha, M. K., Kumar, J. R., & Lee, J. Y. (2015). Process development to recover rare earth metals from monazite mineral: A review. Minerals Engineering, 79, 102-115.

Kuroiwa, H., Inagaki, Y., Mutoh, K., & Abe, J. (2019). On-demand control of the photochromic properties of naphthopyrans. "Advanced Materials", 31(2), 1805661.

Labbé, J. (1968). Relation between superconductivity and lattice instability in the -W compounds. "Physical Review", 172(2), 451.

Lai, Z., He, Q., Tran, T. H., Repaka, D. M., Zhou, D. D., Sun, Y., ... & Zhang, H. (2021). Metastable 1T-phase group VIB transition metal dichalcogenide crystals. Nature Materials, 20(8), 1113-1120.

Leonov, V. (2011). Thermoelectric energy harvester on the heated human machine. "Journal of Micromechanics and Microengineering", 21(12), 125013.

Lee, P. A., Nagaosa, N., & Wen, X. G. (2006). Doping a Mott insulator: Physics of high-temperature superconductivity. Reviews of modern physics, 78(1), 17-85.

Li, W., Carrete, J., Katcho, N. A., & Mingo, N. (2014). ShengBTE: A solver of the Boltzmann transport equation for phonons. "Computer Physics Communications", 185(6), 1747-1758.

Liu, H., Naumov, I. I., Hoffmann, R., Ashcroft, N. W., & Hemley, R. J. (2017). Potential high-Tc superconducting lanthanum and yttrium hydrides at high pressure. "Proceedings of the National Academy of Sciences", 114(27), 6990-6995.

Li, C., Liu, R., Zhao, T., Li, Z., Yue, L., Lin, T., Zhang, X., Li, Q., & Liu, B. (2022). Pressure-induced photoconductivity enhancement and positive–negative switch in bulk silicon. Applied Physics Letters, 121(4).

Li, Y., Liu, J., Zhang, Y., Zhou, Y., Li, J., Su, W., Zhai, J., Wang, H., & Wang, C. (2016). Enhancement of thermoelectric performance of Sr 0 . 7 Ba 0 . 3 Nb 2 O 6 À ceramics by lanthanum doping. 42, 1128–1132. https://doi.org/10.1016/j.ceramint.2015.09.041

Lian, C., Wang, J., Duan, W., & Chen, C. (2017). superconductivity in hole-doped diamond-like crystalline hydrocarbon. Scientific Reports, October 2016, 1–6. https://doi.org/10.1038/s41598-017-01541-6

Liu, Y., Li, H.-W., & Huang, Z. (2020). Metal Hydride-Based Energy Storage and Conversion Materials. In Frontiers in chemistry (Vol. 8, p. 675). Frontiers Media SA.

Li, Z., He, X., Zhang, C., Wang, X., Zhang, S., Jia, Y., ... & Jin, C. (2022). Superconductivity above 200 K discovered in superhydrides of calcium. Nature communications, 13(1), 2863.

Lorenz, B., & Chu, C. W. (2005). High pressure effects on superconductivity. In Frontiers in Superconducting Materials (pp. 459–497). Springer.

Lv, J., Sun, Y., Liu, H., & Ma, Y. (2020). Theory-orientated discovery of high-temperature superconductors in superhydrides stabilized under high pressure. Matter and Radiation at Extremes, 5(6).

Ma, J., Xu, L., Yin, Z., Li, Z., Dong, X., Song, Z., Chen, D., Hu, R., Wang, Q., & Han, J. (2024). “One stone four birds” design atom co-sharing BiOBr/Bi2S3 S-scheme heterojunction photothermal synergistic enhanced full-spectrum photocatalytic activity. Applied Catalysis B: Environment and Energy, 344, 123601.

Ma, W., Yu, L., Kang, P., Chu, Z., & Li, Y. (2024). Modifications and Applications of Metal-Organic-Framework-Based Materials for Photocatalysis. Molecules, 29(24), 5834.

Malki, S., & Farh, L. El. (2020). First - Principles Investigation on Thermoelectric Properties. 1–9.

Mamand, S. M., Qader, I. N., & Omar, M. S. (2024). Pressure Impact on Lattice Thermal Conductivity and Its Related Parameters in CdSe Bulk, Nanowires, and Thin Film. Journal of Nanotechnology, 2024(1), 4727716.

Marschall, R. (2014). Semiconductor composites: strategies for enhancing charge carrier separation to improve photocatalytic activity. Advanced Functional Materials, 24(17), 2421–2440.

Miao, S., Liang, K., Zhu, J., Yang, B., Zhao, D., & Kong, B. (2020). Hetero-atom-doped carbon dots: Doping strategies, properties and applications. Nano Today, 33, 100879.

Moldarev, D., Primetzhofer, D., You, C. C., Karazhanov, S. Z., Montero, J., Martinsen, F., Mongstad, T., Marstein, E. S., & Wolff, M. (2018). Composition of photochromic oxygen-containing yttrium hydride films. Solar Energy Materials and Solar Cells, 177, 66–69.

Mahan, B. (1997). Sales, and J. Sharp. Phys. Today, 50(3), 42-47.

Madsen, G. K., & Singh, D. J. (2006). BoltzTraP. A code for calculating band-structure dependent quantities. Computer Physics Communications, 175(1), 67-71.

Mahitha, P. M., Nakul, S., Kumar, M., Kulkarni, N. V., Kharissova, O. V., & Kharissov, B. I. (2024). Photochromic molecules and materials: design and development. In Handbook of Emerging Materials for Sustainable Energy (pp. 237-254). Elsevier.

Mattheiss, L. F. (1966). Band structure and Fermi surface for rhenium. Physical Review, 151(2), 450.

McMillan, W. L. (1968). Transition temperature of strong-coupled superconductors. Physical Review, 167(2), 331.

McGrady, G. S., & Guilera, G. (2003). The multifarious world of transition metal hydrides. Chemical Society Reviews, 32(6), 383-392.

Meer, E. (1876). Ueber Dinitroverbindungen der Fettreihe. Justus Liebigs Annalen der Chemie, 181(1), 1-22.

Mazierski, P., Mikolajczyk, A., Bajorowicz, B., Malankowska, A., Zaleska-Medynska, A., & Nadolna, J. (2018). The role of lanthanides in TiO2-based photocatalysis: A review. Applied Catalysis B: Environmental, 233, 301-317.

Meng, D., Sakata, M., Shimizu, K., Iijima, Y., Saitoh, H., Sato, T., ... & Orimo, S. I. (2019). Superconductivity of the hydrogen-rich metal hydride L i 5 Mo H 11 under high pressure. Physical Review B, 99(2), 024508.

Misra, P. K. (2010). 2.1. 3 Normal modes of a one-dimensional chain with a basis. Physics of Condensed Matter; Academic Press: Cambridge, MA, USA, 44.

Mongstad, T., Platzer-Björkman, C., Maehlen, J. P., Mooij, L. P. A., Pivak, Y., Dam, B., Marstein, E. S., Hauback, B. C., & Karazhanov, S. Z. (2011). A new thin film photochromic material: Oxygen-containing yttrium hydride. Solar Energy Materials and Solar Cells, 95(12), 3596–3599.

Momma, K., & Izumi, F. (2011). VESTA 3 for three-dimensional visualization of crystal, volumetric and morphology data. Journal of Applied Crystallography, 44(6), 1272–1276.

Mortazavi, B., Novikov, I. S., Podryabinkin, E. V., Roche, S., Rabczuk, T., Shapeev, A. V., & Zhuang, X. (2020). Exploring phononic properties of two-dimensional materials using machine learning interatomic potentials. Applied Materials Today, 20, 100685.

Mustapha, E., Soufiane, H., Abdellah, B., & Naji, M. (2024). Pressure - induced band gap shift and enhanced optical properties of quaternary Heusler TaAlCuCo: DFT study. Optical and Quantum Electronics, 56(9), 1–26. https://doi.org/10.1007/s11082-024-07374-8

Muchtar, A. R., Srinivasan, B., Tonquesse, S. Le, Singh, S., Soelami, N., Yuliarto, B., Berthebaud, D., & Mori, T. (2021). Physical Insights on the Lattice Softening Driven Mid-Temperature Range Thermoelectrics of Ti/Zr-Inserted SnTe—An Outlook Beyond the Horizons of Conventional Phonon Scattering and Excavation of Heikes' Equation for Estimating Carrier Properties. Advanced Energy Materials, 11(28), 2101122.

Müller, P. M. (2018). Thermal Conductivities of Group IV and Group III-V Compound Semiconductors from First Principles (Doctoral dissertation, Technische Universität Berlin).

Murtaza, G., & Ahmad, I. (2012). Shift of indirect to direct bandgap and optical response of LaAlO3 under pressure. Journal of Applied Physics, 111(12).

Muramatsu, T., Wanene, W. K., Somayazulu, M., Vinitsky, E., Chandra, D., Strobel, T. A., ... & Hemley, R. J. (2015). Metallization and superconductivity in the hydrogen-rich ionic salt BaReH9. The Journal of Physical Chemistry C, 119(32), 18007-18013.

Nastasenko, V. (2024). New Physical Meaning and Principle of Determining the Speed of Light Constant. Adv Theo Comp Phy, 7(2), 1–11.

Nejad, M. A. F., Ranjbar, S., Parolo, C., Nguyen, E. P., Álvarez-Diduk, R., Hormozi-Nezhad, M. R., & Merkoçi, A. (2021). Electrochromism: An emerging and promising approach in (bio) sensing technology. Materials Today, 50, 476-498.

Nishijima, S., Eckroad, S., Marian, A., Choi, K., Kim, W. S., Terai, M., ... & Izumi, M. (2013). Superconductivity and the environment: A roadmap. Superconductor Science and Technology, 26(11), 113001.

Nishino, Y., Deguchi, S., & Mizutani, U. (2006). Thermal and transport properties of the Heusler-type Fe 2 VAl 1. 1–6. https://doi.org/10.1103/PhysRevB.74.115115

Ohko, Y., Tatsuma, T., Fujii, T., Naoi, K., Niwa, C., Kubota, Y., & Fujishima, A. (2003). Multicolour photochromism of TiO2 films loaded with silver nanoparticles. Nature Materials, 2(1), 29-31.

Okoye,C. (2004). Structural, electronic, and optical properties of beryllium monochalcogenides. The European Physical Journal B-Condensed Matter and Complex Systems, 39(1):5–17.

Ovshinsky, S. R., Fetcenko, M. A., and Ross, J. "A nickel metal hydride battery for electric vehicles." Science 260, no. 5105 (1993): 176–181.https://doi.org/10.1126/science.260.5105.176

Paul, D. K., Chaudhry, W. T., Mamun, S. N., Rahman, M. L., Haider, A. Y., & Haque, F. H. (2024). Impact of doping and hydrostatic pressure on structural, electronic, optical, and mechanical properties of novel double halide perovskite Cs2LiGaBr6. ChemPhysMater, 3(4), 422-430.

Parker, L. J., Atou, T., & Badding, J. V. (1996). Transition element-like chemistry for potassium under pressure. Science, 273(5271), 95-97.

Pan, D., Wan, Q., & Galli, G. (2014). The refractive index and electronic gap of water and ice increase with increasing pressure. May, 1–6. https://doi.org/10.1038/ncomms4919

Patial, S., Hasija, V., Raizada, P., Singh, P., Singh, A. A. P. K., & Asiri, A. M. (2020). Tunable photocatalytic activity of SrTiO3 for water splitting: strategies and future scenario. Journal of Environmental Chemical Engineering, 8(3), 103791.

Pei, Y., He, J., Li, J., Li, F., Liu, Q., Pan, W., Barreteau, C., Berardan, D., Dragoe, N., & Zhao, L. (2013). High thermoelectric performance of oxyselenides: intrinsically low thermal conductivity of Ca-doped BiCuSeO. November 2012. https://doi.org/10.1038/am.2013.15

Pei, Y., LaLonde, A., Iwanaga, S., & Snyder, G. J. (2011). High thermoelectric figure of merit in heavy hole dominated PbTe. Energy & Environmental Science, 4(6), 2085-2089.

Pei, Y., Wang, H., & Snyder, G. J. (2012). Band engineering of thermoelectric materials. Advanced Materials, 24(46), 6125-6135.

Perdew, J. P., Burke, K., & Ernzerhof, M. (1996). Generalized gradient approximation made simple. Physical Review Letters, 77(18), 3865-3868.

Piela, L. (2020). Ideas of Quantum Chemistry. Elsevier, Warsaw, Poland, 2nd edition.

Prabhavathy, S., & Arivuoli, D. (2022). Visible light-induced Silver and Lanthanum co-doped BiVO4 nanoparticles for photocatalytic dye degradation of organic pollutants. Inorganic Chemistry Communications, 141, 109483.

Popova, S. V., Sazanova, O. A., Brazhkin, V. V., Kalyaeva, N. V., Kondrin, M. B., & Lyapin, A. G. (2006). High-pressure phases in the GaSb-Mn system. Physics of the Solid State, 48, 2177-2182.

Ran, J., Zhang, J., Yu, J., Jaroniec, M., & Qiao, S. Z. (2014). Earth-abundant cocatalysts for semiconductor-based photocatalytic water splitting. Chemical Society Reviews, 43(22), 7787-7812.

Raza, A. H., Farhan, S., Yu, Z., & Wu, Y. (2024). Double S-scheme ZnS/ZnO/CdS heterostructure photocatalyst for efficient hydrogen production. Acta Physico-Chimica Sinica, 40(11), 2406020.

Reiser, A., Bogdanović, B., & Schlichte, K. (2000). The application of Mg-based metal-hydrides as heat energy storage systems. International Journal of Hydrogen Energy, 25(5), 425-430.

Reiner, M. D., & Gross, E. K. U. (2012). Density functional theory: An approach to the quantum many-body problem. Springer Science & Business Media.

Richardson, T. J., Slack, J. L., Armitage, R. D., Kostecki, R., Farangis, B., & Rubin, M. D. (2001). Switchable mirrors based on nickel–magnesium films. Applied Physics Letters, 78(20), 3047–3049.

Rizwan, M., Usman, Z., Shakil, M., Gillani, S. S. A., Azeem, S., Jin, H. B., Cao, C. B., Mehmood, R. F., Nabi, G., & Asghar, M. A. (2020a). Electronic and optical behaviour of lanthanum doped CaTiO3 perovskite. Materials Research Express, 7(1), 15920.

Runowski, M., Sobczak, S., Marciniak, J., Bukalska, I., Lis, S., & Katrusiak, A. (2019). Gold nanorods as a high-pressure sensor of phase transitions and refractive-index gauge. Nanoscale, 11(18), 8718–8726.

Santos, T., Ventura, T., & do Carmo Lopes, M. (2021). A review on radiochromic film dosimetry for dose verification in high energy photon beams. Radiation Physics and Chemistry, 179, 109217.

Sadeghi, S. N., & Esfarjani, K. (2024). Anomalous mass dependence of phonon thermal transport in lanthanum monopnictides and its origin in the nature of chemical bonding. Journal of Materials Chemistry A, 12(37), 25067–25075.

Sandrock, G., & Bowman Jr, R. C. (2003). Gas-based hydride applications: recent progress and future needs. Journal of Alloys and Compounds, 356, 794–799.

Sandrock, G. "A panoramic overview of hydrogen storage alloys from a gas reaction point of view." Journal of Alloys and Compounds 293–295 (1999): 877–888. https://doi.org/10.1016/S0925-8388(99)00423-9

Schlapbach, L., & Züttel, A. (2001). Hydrogen-storage materials for mobile applications. Nature, 414(6861), 353–358.

Schultze, M., Bothschafter, E. M., Sommer, A., Holzner, S., Schweinberger, W., Fiess, M., Hofstetter, M., Kienberger, R., Apalkov, V., & Yakovlev, V. S. (2013). Controlling dielectrics with the electric field of light. Nature, 493(7430), 75–78.

Schönberg, A., Elkaschef, M., Nosseir, M., & Sidky, M. M. (1958). Experiments with 4-Thiopyrones and with 2, 2', 6, 6'-Tetraphenyl-4, 4'-dipyrylene. The Piezochromism of Diflavylene. Journal of the American Chemical Society, 80(23), 6312-6315.

Seo, D.-K., Gupta, N., Whangbo, M.-H., Hillebrecht, H., & Thiele, G. (1998). Pressure-induced changes in the structure and band gap of CsGeX3 (X= Cl, Br) studied by electronic band structure calculations. Inorganic Chemistry, 37(3), 407–410.

Setyawan, W., & Curtarolo, S. (2010). High-throughput electronic band structure calculations: Challenges and tools. Computational Materials Science, 49(2),299–312.https://doi.org/10.1016/j.commatsci.2010.05.010

Shklovskii, B. I., & Efros, A. L. (2013). Electronic properties of doped semiconductors (Vol. 45). Springer Science & Business Media.

Sheppard, D. A., Paskevicius, M., Humphries, T. D., Felderhoff, M., Capurso, G., Bellosta von Colbe, J., ... & Buckley, C. E. (2016). Metal hydrides for concentrating solar thermal power energy storage. Applied Physics A, 122, 1-15.

Singh, D. J., & Du, M. H. (2008). Density Functional Study of LaFeAsO1-xFx: A Low Carrier Density Superconductor Near Itinerant Magnetism. Physical Review Letters, 100(23), 237003.

Smith, F. T., & Chu, W. C. (1967). Phys. Rev., 159, 353.

Sinha, T. K. (2022). Morphology-dependent visible light photocatalysis. In Nanostructured materials for visible light photocatalysis (pp. 375-412). Elsevier.

Somayazulu, M., Ahart, M., Mishra, A. K., Geballe, Z. M., Baldini, M., Meng, Y., ... & Hemley, R. J. (2019). Evidence for superconductivity above 260 K in lanthanum superhydride at megabar pressures. Physical review letters, 122(2), 027001.

Sudrajat, H., Kitta, M., Ichikuni, N., & Onishi, H. (2019). Double doping of NaTaO3 photocatalysts with lanthanum and manganese for strongly enhanced visible-light absorption. ACS Applied Energy Materials, 2(10), 7518–7526.

Stathatos, E., Petrova, T., & Lianos, P. (2001). Study of the efficiency of visible-light photocatalytic degradation of basic blue adsorbed on pure and doped mesoporous titania films. Langmuir, 17.

Stishov, M. S., & Popova, V. S. (1961). Geokhimiya, 10, 837 (Geochem., 1961, 10, 923).

Struzhkin, V. V. (2015). Superconductivity in compressed hydrogen-rich materials: Pressing on hydrogen. Physica C: Superconductivity and its Applications, 514, 77-85.

Sudrajat, H., Kitta, M., Ichikuni, N., & Onishi, H. (2019). Double doping of NaTaO3 photocatalysts with lanthanum and cerium for enhanced photocatalytic activity. Journal of Photochemistry and Photobiology A: Chemistry, 378, 1-10.

T Hung, N., Nugraha, A. R. T., Yang, T., Zhang, Z., & Saito, R. (2019). Thermoelectric performance of monolayer InSe improved by convergence of multivalley bands. Journal of Applied Physics, 125(8).

Takahashi, H., & Takahashi, Y. (2018). Photochromism of organic compounds: A review. Chemical Reviews, 118(12), 6340-6370.

Tse, J. S., & Klug, D. D. (2011). High-pressure phase transitions in hydrogen. Physical Review Letters, 106(15), 155701.

Tan, Y., Li, Z., Tian, Y., Hu, S., Jia, L., Chi, B., Pu, J., & Li, J. (2017). Charge-compensated (Nb, Fe)-codoped La2Ti2O7 photocatalyst for photocatalytic H2 production and optical absorption. Journal of Alloys and Compounds, 709, 277–284.

Tilley, R. J. D. (2020). Colour and the optical properties of materials. John Wiley & Sons.

Tian, H., & Wang, Y. (2019). Recent advances in photochromic materials for smart windows. Materials Today, 21(1), 1-12.

Tanaka, K., Tse, J. S., & Liu, H. (2017). Electron-phonon coupling mechanisms for hydrogen-rich metals at high pressure. Physical Review B, 96(10), 100502.

Terasaki, I., Sasago, Y., & Uchinokura, K. (1997). Large thermoelectric power in NaCo 2 O 4 single crystals. Physical Review B, 56(20), R12685.

Uzunok, H. Y., BaÇcl, S., Karaca, E., Tütüncü, H. M., & Srivastava, G. P. (2020). First-principles calculations of physical properties and superconductivity of orthorhombic ScRuSi and ZrRhSi. Physical Review B, 102(13). https://doi.org/10.1103/PhysRevB.102.134508

Van der Molen, S. J., Nagengast, D. G., Van Gogh, A. T. M., Kalkman, J., Kooij, E. S., Rector, J. H., & Griessen, R. (2001). Insulating fcc YH 3 stabilized by MgH 2. Physical Review B, 63(23), 235116.

Vanderbilt, D. (1990). Soft self-consistent pseudopotentials in a generalized eigenvalue formalism. Physical review B, 41(11), 7892.

Wang, H., & Yu, C. (2019). Organic thermoelectrics: materials preparation, performance optimization, and device integration. Joule, 3(1), 53–80.

Wang, H., & Wang, Y. (2020). Recent advances in the design of photochromic materials. Advanced Materials, 32(18), 1908231.

Wang, J., & Zhang, Y. (2021). Thermoelectric materials: A review of recent advances. Materials Today, 45, 1-12.

Wang, Y., & Zhang, H. (2019). Photocatalytic water splitting: Recent advances and future perspectives. Chemical Society Reviews, 48(10), 2635-2655.

Wang, Q., Pan, J., Guo, J., Hansen, H. A., Xie, H., Jiang, L., ... & Chen, P. (2021). Ternary ruthenium complex hydrides for ammonia synthesis via the associative mechanism. Nature Catalysis, 4(11), 959-967.

Weber, F., Pintschovius, L., Reichardt, W., Heid, R., Bohnen, K.-P., Kreyssig, A., Reznik, D., & Hradil, K. (2014). Phonons and electron-phonon coupling in YNi 2 B 2 C. Physical Review B, 89(10), 104503.

Wen, H. (2024). Structural, Electronic, and Optical Properties of Halide Perovskite Cs3Bi2I9: Density Functional Calculations. Russian Journal of Physical Chemistry A, 98(13), 3144–3151.

Wu, Z., Sun, Y., Durajski, A. P., Zheng, F., & Antropov, V. (n.d.). Effect of doping on the phase stability and Superconductivity in LaH10.

Xie, J., Chen, S. P., Tse, J. S., de Gironcoli, S., & Baroni, S. (1999). High-pressure thermal expansion, bulk modulus, and phonon structure of diamond. Physical Review B, 60(13), 9444.

Yang, Y., Liu, G., Irvine, J. T. S., & Cheng, H.-M. (2016). Enhanced photocatalytic H2 production in core–shell engineered rutile TiO2. Advanced Materials.

Yaprintsev, M., Lyubushkin, R., Soklakova, O., & Ivanov, O. (2018). Effects of Lu and Tm Doping on Thermoelectric Properties of Bi 2 Te 3 Compound. Journal of Electronic Materials, 47, 1362–1370.

Yamamoto, T., & Takahashi, H. (2017). Photochromic properties of organic compounds: A review. Journal of Photochemistry and Photobiology A: Chemistry, 344, 1-12.

Yu, L., Yang, X., He, J., He, Y., & Wang, D. (2015). One-step hydrothermal method to prepare nitrogen and lanthanum co-doped TiO2 nanocrystals with exposed 0 0 1 facets and study on their photocatalytic activities in visible light. Journal of Alloys and Compounds, 637, 308–314.

Zhang, H., & Wang, Y. (2020). Recent advances in thermoelectric materials. Materials Today, 45, 1-12.

Zhao, J., Ross, N. L., Wang, D., Rizwan, M., Usman, Z., Shakil, M., Gillani, S. S. A., Azeem, S., & Jin, H. B. (2020). Electronic and optical behaviour of lanthanum doped CaTiO3 perovskite Electronic and optical behaviour of lanthanum doped CaTiO 3 perovskite.

Zhang, L., Yang, J., Yu, H., & Pan, W. (2020). High performance of La-doped Y 2 O 3 transparent ceramics. Journal of Advanced Ceramics, 9, 493-502.

Zhang, W., Eperon, G. E., & Snaith, H. J. (2016). Metal halide perovskites for energy applications. Nature Energy, 1(6), 1-8.

Zhou, Y., & Zhang, Y. (2021). Advances in photochromic materials for smart windows. Materials Today, 45, 1-12.

Zhong, Y., Xia, X., Shi, F., Zhan, J., Tu, J., & Fan, H. J. (2016). Transition metal carbides and nitrides in energy storage and conversion. Advanced Science, 3(5), 1500286.

Zou, X., Yuan, C., Dong, Y., Ge, H., Ke, J., & Cui, Y. (2020). Lanthanum orthovanadate/bismuth oxybromide heterojunction for enhanced photocatalytic air purification and mechanism exploration. Chemical Engineering Journal, 379, 122380.

A

Supplementary Figures

The electronic band structure for pristine and La-doped YHSe is presented in Figure GGA [(a) - (g)] and GGA+U [(2a) - (2g)] to illustrate the effect of La doped YHSe on the electronic properties of the YHSe material.

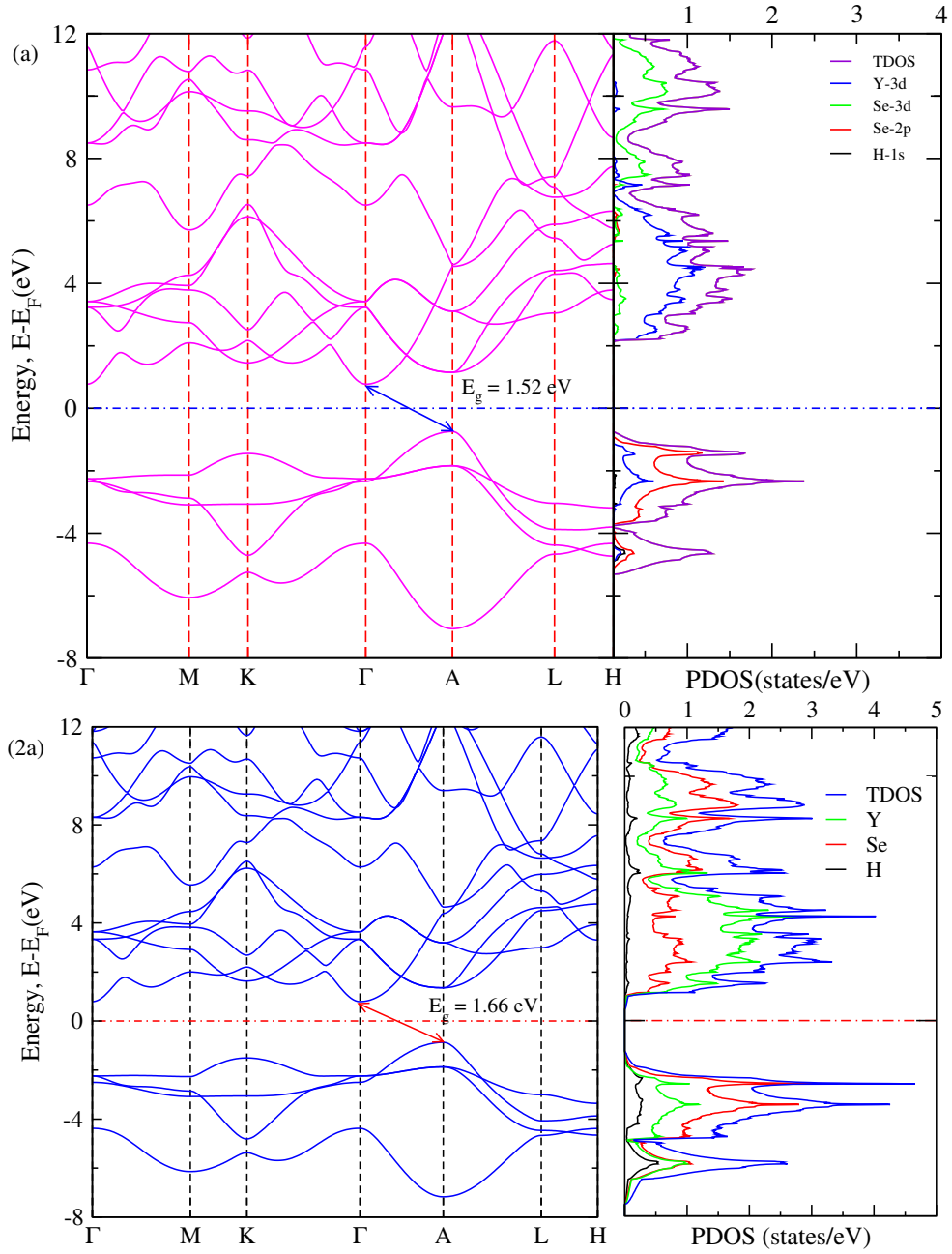

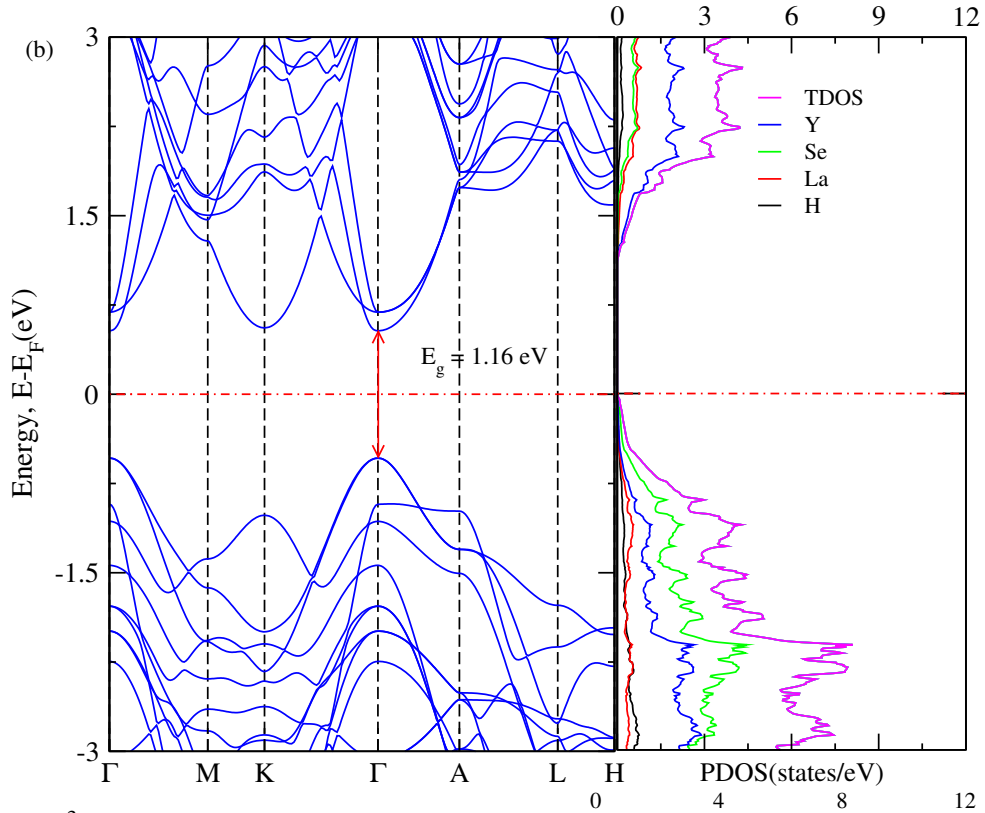
(b)
Energy, E-E$_F$(eV)
3
1.5
0
-1.5
-3
E$_g$ = 1.16 eV
Γ
M
K
Γ
A
L
H
0
3
6
9
12
TDOS
Y
Se
La
H
PDOS(states/eV)

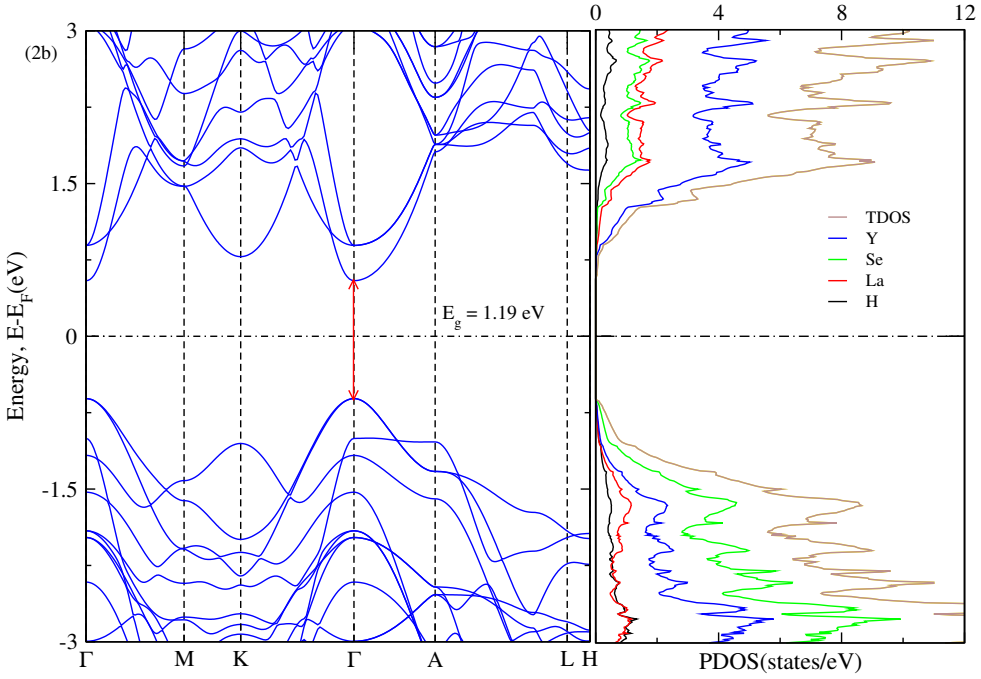
(2b)
Energy, E-E$_F$(eV)
3
1.5
0
-1.5
-3
E$_g$ = 1.19 eV
Γ
M
K
Γ
A
L
H
0
4
8
12
TDOS
Y
Se
La
H
PDOS(states/eV)

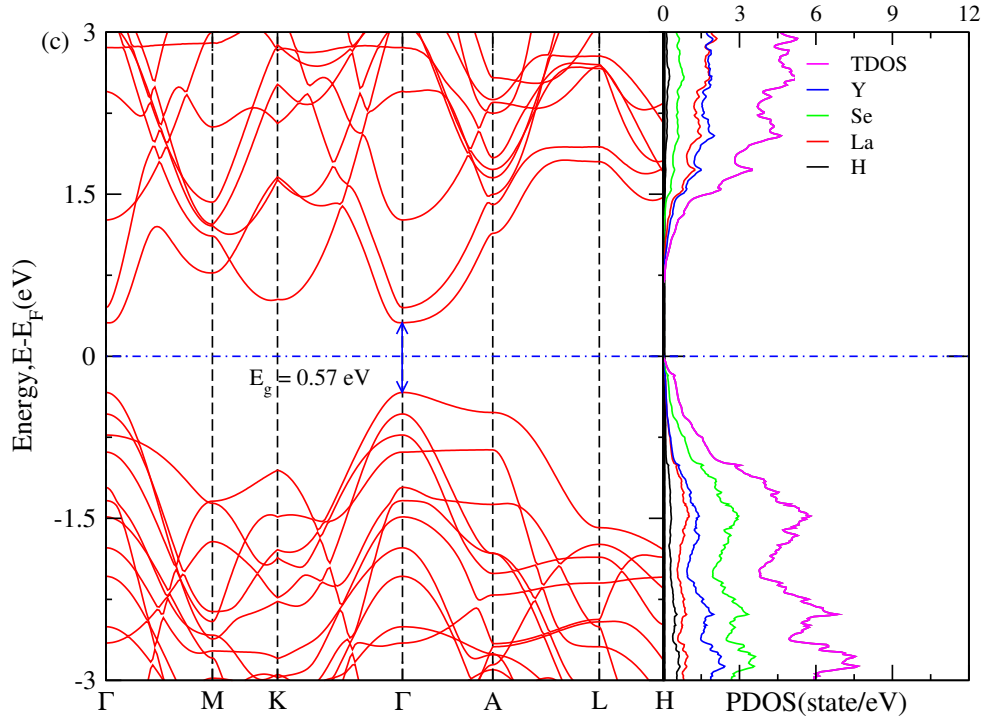
(c)
Energy,E-E$_F$(eV)
E$_g$ = 0.57 eV
Γ M K Γ A L H
PDOS(state/eV)
TDOS
Y
Se
La
H

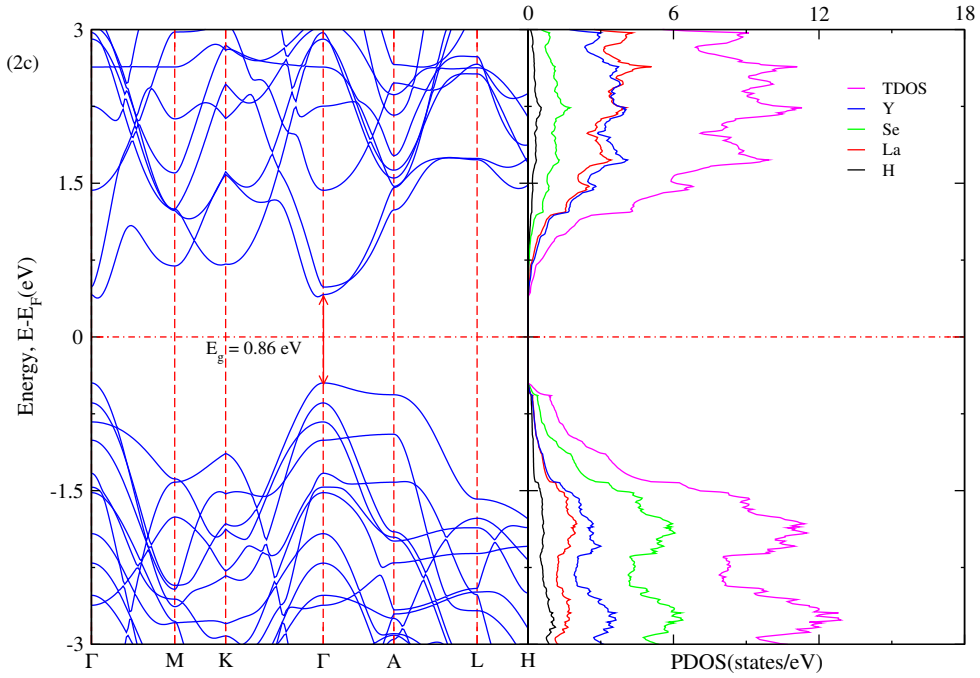
(2c)
Energy, E-E$_F$(eV)
E$_g$ = 0.86 eV
Γ M K Γ A L H
PDOS(states/eV)
TDOS
Y
Se
La
H

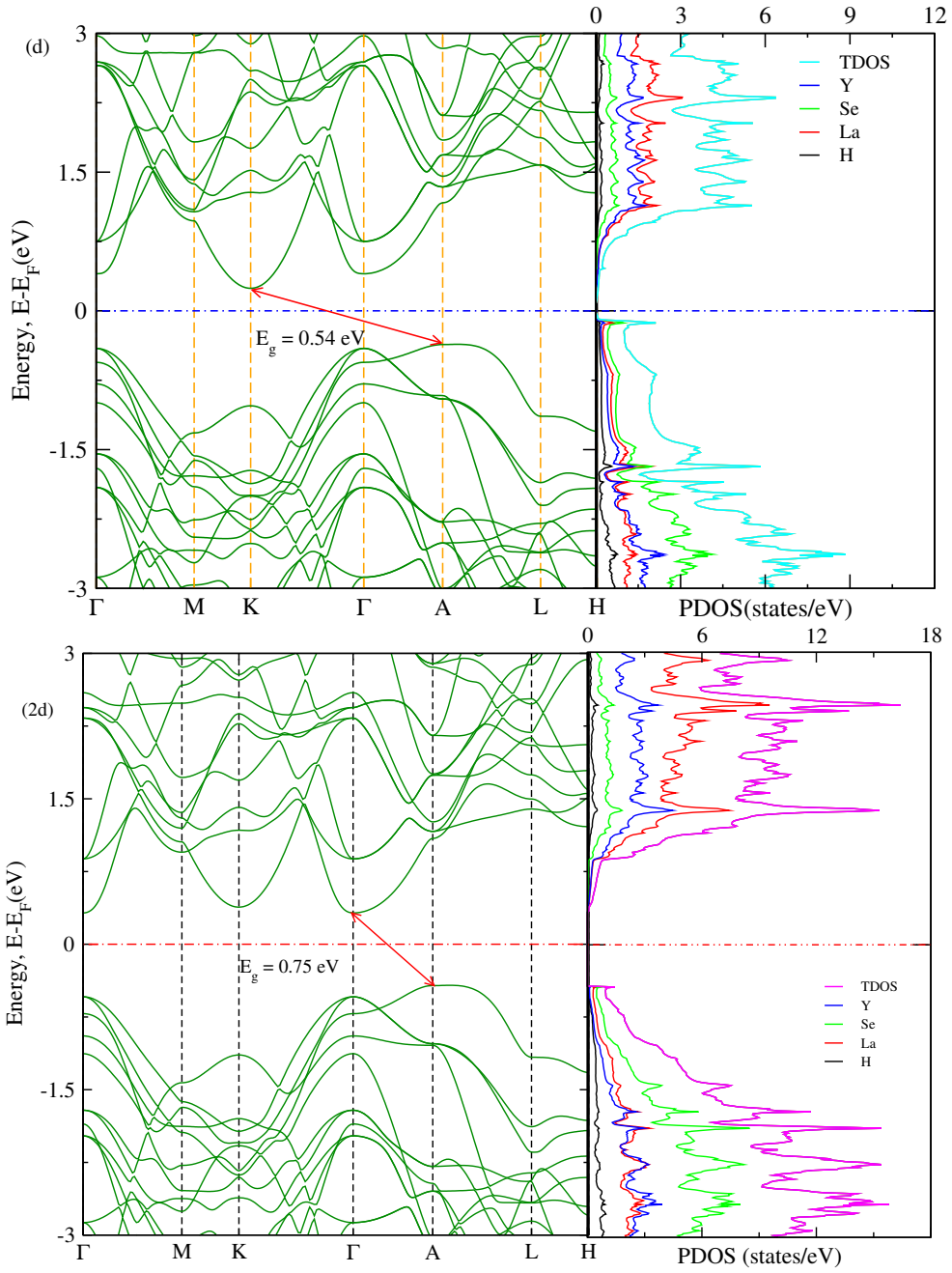
(d)
Energy, E-E$_F$(eV)
3
1.5
0
-1.5
-3
E$_g$ = 0.54 eV
Γ
M
K
Γ
A
L
H
0
3
6
9
12
TDOS
Y
Se
La
H
PDOS(states/eV)
(2d)
Energy, E-E$_F$(eV)
3
1.5
0
-1.5
-3
E$_g$ = 0.75 eV
Γ
M
K
Γ
A
L
H
0
6
12
18
TDOS
Y
Se
La
H
PDOS (states/eV)

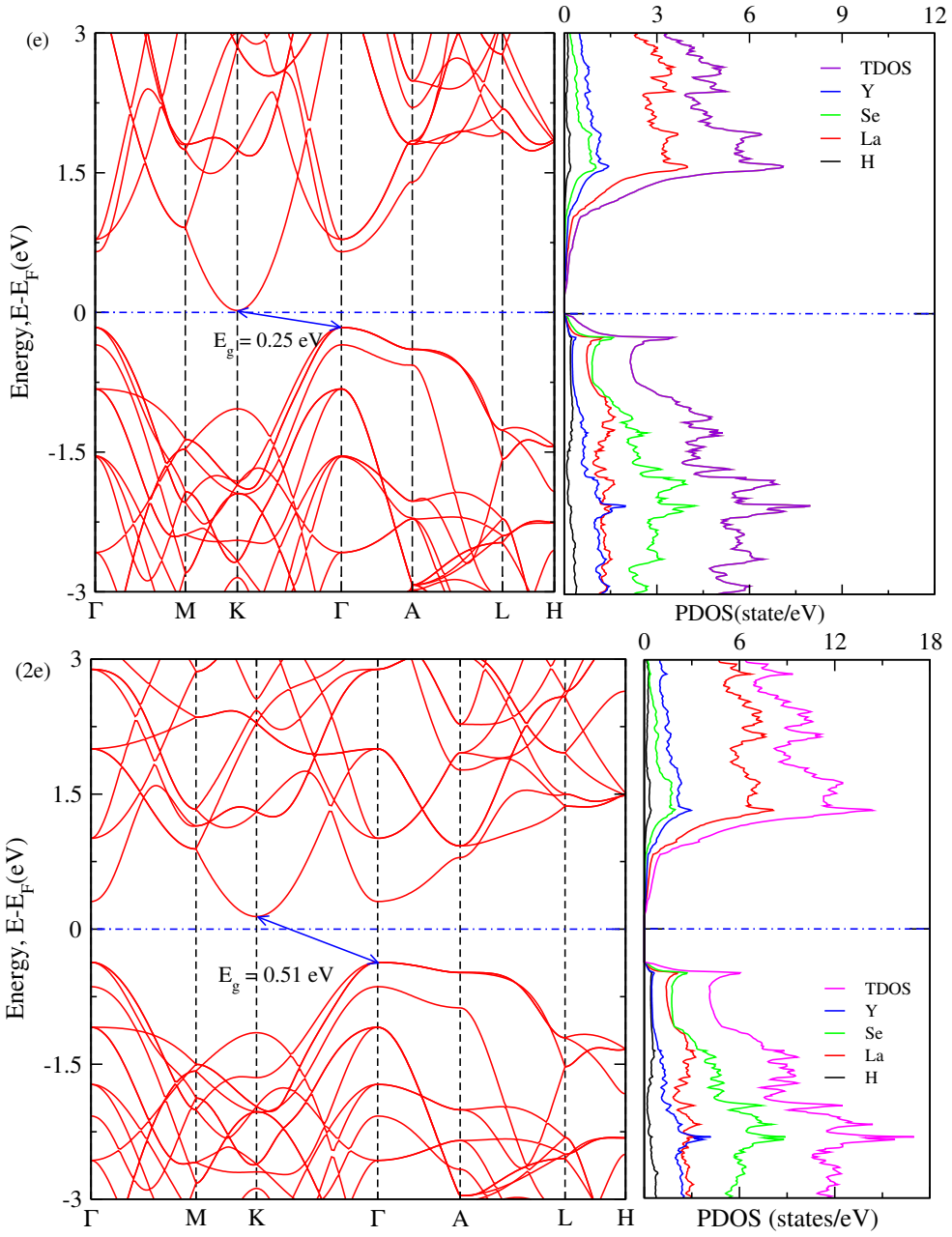
(e)
Energy,E-E$_F$(eV)
E$_g$ = 0.25 eV
Γ M K Γ A L H
PDOS(state/eV)
TDOS
Y
Se
La
H
(2e)
Energy, E-E$_F$(eV)
E$_g$ = 0.51 eV
Γ M K Γ A L H
PDOS (states/eV)
TDOS
Y
Se
La
H

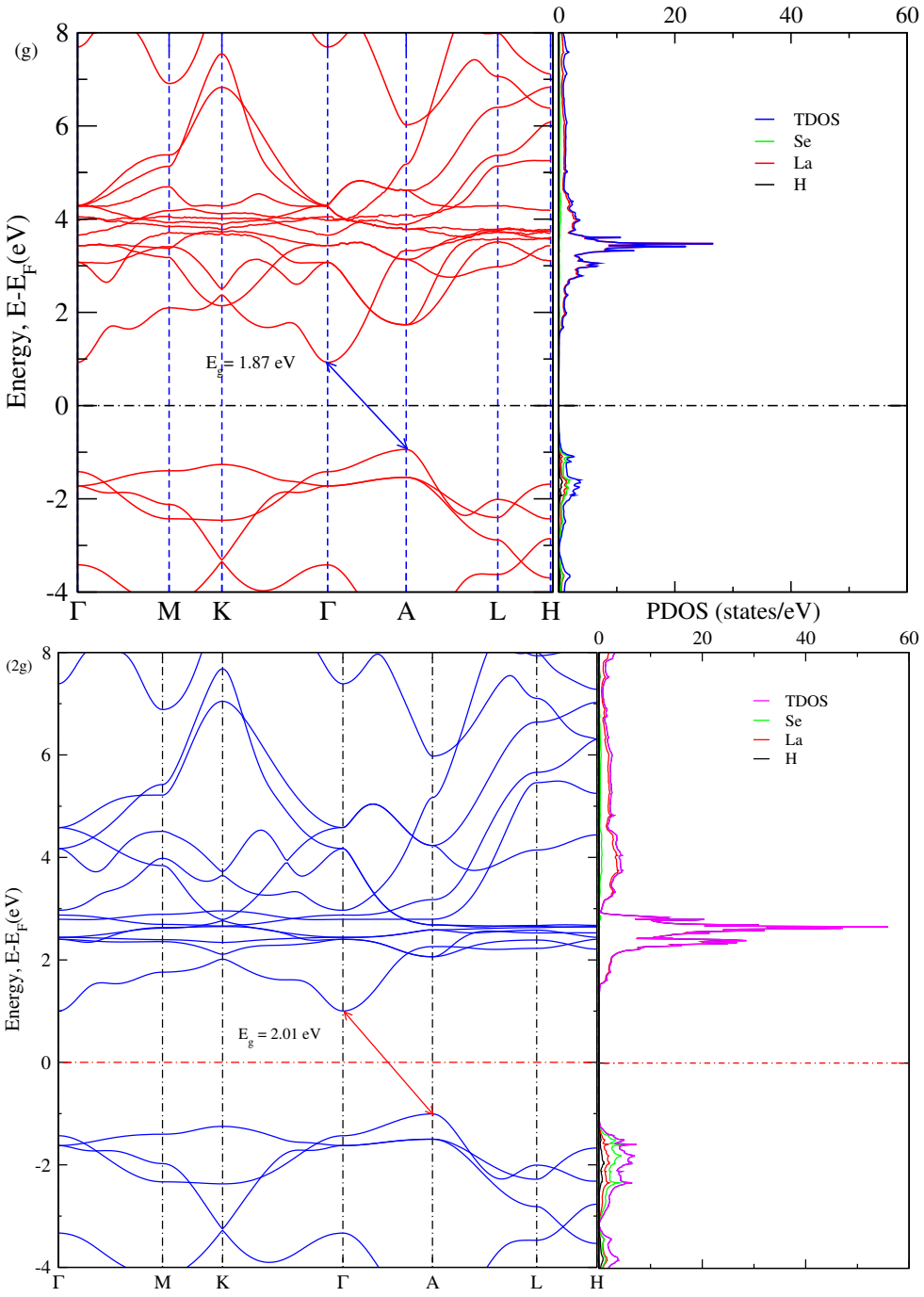

Figure A.1: Band structures and Density of states calculated using the GGA [(a) - (g)] and GGA+U [(2a) - (2g)] approximations for (a) pure YHSe, (b) $La_{0.125}Y_{0.875}HSe$, (c) $La_{0.25}Y_{0.75}HSe$, (d) $La_{0.375}Y_{0.625}HSe$, (e) $La_{0.5}Y_{0.5}HSe$, (f) LaHSe.